STUDY OF SURFACE HALF-METALLICITY OF FULL-HEUSLER COMPOUNDS USING *AB INITIO* APPROACH

A THESIS SUBMITTED IN PARTIAL FULFILLMENT OF THE REQUIREMENTS FOR THE DEGREE OF DOCTOR OF PHILOSOPHY

LALRINKIMA

MZU REGISTRATION NO.: 3443 of 2010-11

Ph.D REGISTRATION NO.: MZU/PH.D./1261 of 14.08.2018

DEPARTMENT OF PHYSICS

SCHOOL OF PHYSICAL SCIENCES

NOVEMBER, 2022

STUDY OF SURFACE HALF-METALLICITY OF FULL-HEUSLER COMPOUNDS USING *AB INITIO* APPROACH

BY

Lalrinkima

Department of Physics

Name of Supervisor: Dr. Lalthakimi Zadeng

Name of Joint Supervisor: Dr. Dibya Prakash Rai, PUC

Submitted

In partial fulfillment of the requirement of the Degree of Doctor of Philosophy in Physics of Mizoram University, Aizawl

Dr. Lalthakimi Zadeng
Phone: 9862770341(M)

Mizoram University
Department of Physics
(A DST-FIST Supported Department)
School of Physical Sciences
Aizawl 796 004 Mizoram
E-mail : kimizadeng@gmail.com

Date: _____ November 2022

Certificate

This is to certify that the thesis entitled 'Study of Surface Half-Metallicity of Full-Heusler Compounds Using *Ab Initio* Approach*'* submitted by Shri Lalrinkima, for the degree of Doctor of Philosophy of the Mizoram University, Aizawl, embodies the record of original investigations carried out by him under my supervision. The thesis presented is worthy of being considered for the award of the Ph. D. degree. This work has not been submitted for any degree to any other University.

(Dr. LALTHAKIMI ZADENG)

Supervisor

(Dr. DIBYA PRAKASH RAI)

Jt. Supervisor, PUC

Declaration

Mizoram University

November, 2022

*I, **Lalrinkima**, hereby declare that the subject matter of this thesis is the record of work done by me, that the contents of this thesis did not form basis of the award of any previous degree to me or to do the best of my knowledge to anybody else, and that the thesis has not been submitted by me for any research degree in any other University/ Institute.*

This is being submitted to the Mizoram University for the degree of Doctor of Philosophy in Physics.

(LALRINKIMA)
Candidate

(Prof. ZAITHANZAUVA PACHUAU)
Head

(Dr. LALTHAKIMI ZADENG)
Supervisor

(Dr. DIBYA PRAKASH RAI)
Jt. Supervisor, PUC

Acknowledgement

As the time flies, now its time for me to say ‘thank you’ to all the people who have helped, assisted and encouraged me during my Ph.D work.

First and foremost, I would like to express my sincere thank to my Supervisor Dr. Lalthakimi Zadeng, Assistant Professor, Department of Physics, Mizoram University, for her beneficial guidance, an enlighten supervision and valuable counselling throughout my Ph.D degree course.

I can’t thank enough to My Joint Supervisor Dr. Dibya Prakash Rai, Department of Physics, Pachhunga University College. He who ignited my research paveway and still upskill me towards the real researcher world. It is less likely that I will forget when he formed like a teacher, father, brother even a friend in need upon me. I couldn’t have done it without him.

I thank to Prof. Diwakar Tiwari, Dean, School of Physical Sciences for his encourage in fullfilment of my work. I will not forget all the support I received from Prof. Zaithanzauva Pachuau, Head of Department, Department of Physics and all the Teaching Faculties of the Department of Physics, Mizoram University.

I would also like to thank Dr. Lalhriatzuala, Department of Physics, Pachhunga University College, who not only lend me his workstation but also give a valuable lessons. I am grateful to all the faculty in the Department of Physics, Pachhunga University College, for their strong cooperation only; Physical Sciences Research Centre (Where I conducted all my research work) could be established. This is also the place where I worked with helpful and dedicated my fellow research scholars like Kamal Bhujel, Bhanu Chettri, Y.T. Singh, Lalmuanchhana, R. Zosiamliana and Bernard Lalroliana-whos’ help and assistancy for me are priceless. And would also express my hearty gratitude to all the research scholars in the Department of Physics, Mizoram University - Mr. Laihnuna, Ms Vanzarmawii, Mr. Lalbiaktluanga, Mr. J. Lalramnghaka for their valuable information and motivation.

I, do acknowledge the Department of Science and Technology (DST), New Delhi, Government of India for INSPIRE Fellowship vide Dy. Order No. DST/INSPIRE Fellowship/2018/IF180550.

I am expressing my sincere thanks to my wife Elizabeth Lalhmingchhuani and my family, for their support, patience and optimistic back-up. With their endless motivation and prayer can only make me to crawl out of the hard time.

Last but not the least, I give thank to the Almighty God who assured me a good health during my course of study.

Dated: ____ November, 2022

Department of Physics,
Mizoram University, Aizawl. (**LALRINKIMA**)

			Pages
Title of the Thesis			i
Certificates			ii
Declaration			iii
Acknowledgement			iv
Contents			vi
List of Figures			ix
List of Tables			xiv
Dedication			xvi
CHAPTER 1	:	**Introduction**	
1.1	:	Introduction and Evolution of Spintronic	1
1.2	:	Half metallic materials	4
1.3	:	Heusler Compounds	5
1.3.1	:	Crystal structure of full Heusler Compounds	6
1.3.2	:	Generalized magnetic properties-Slater Pauling rule	7
1.3.3	:	Half metallicity in full Heusle compounds	7
1.4	:	Review on thin film/surface properties of full Heusler compounds	10
CHAPTER 2	:	**Theoretical formalism and Methodology**	
2.1	:	Density Functional Theory (DFT) Formalism	15
2.2	:	Hohenberg - Kohn (H-K) Theorem	16
2.3	:	Kohn-Sham Equation	18
2.4	:	Exchange - Correlation Energy	20
2.4.1	:	The Exchange Energy	21
2.4.2	:	The Correlation Enegy	21
2.5	:	Approximations: Functionals for $E_{XC}[n]$	22
2.5.1	:	Local Density Approximation (LDA)	22
2.5.2	:	Generalized Gradient Approximation (GGA)	23
2.5.2.1	:	The GGA of Perdew and Wang (PW91)	24
2.5.2.2	:	The GGA of Perdew, Burke and Ernzerhof (PBE)	24
2.5.2.3	:	Revision of PBE (revPBE or RPBE)	25

2.6	:	DFT+U	25
2.7	:	DFT based Simulation Packages	26
2.7.1	:	Quantum Espresso	26
2.7.2	:	MedeA (VASP)	27
2.7.3	:	QuantumATK Q-2019.12	27
2.8	:	Ab-initio Pseudopotential	28
CHAPTER 3	:	**Structural, Electronic, Magnetic,-properties, Mechanical and Thermodynamical stability of bulk X_2YZ type full Heusler Compounds**	
3.1	:	Fe_2IrSi	34
3.1.1	:	Results and Discussions	35
3.1.1.1	:	Structural	35
3.1.1.2	:	Electronic and Magnetic Properties	36
3.1.1.3	:	Mechanical and Thermodynamical Stability	45
3.2	:	Ti_2XSi (X=Mn, Co)	48
3.2.1	:	Results and Discussions	49
3.2.1.1	:	Structural	49
3.2.1.2	:	Electronic and Magnetic Properties	50
3.2.1.3	:	Mechanical and Thermodynamical Stability	52
3.3	:	Mn_2CoSi	55
3.3.1	:	Results and Discussions	55
3.3.1.1	:	Structural	55
3.3.1.2	:	Electronic and Magnetic Properties	56
3.3.1.3	:	Mechanical and Thermodynamical Stability	59
3.4	:	Pressure Dependence Half Metallicity of Fe_2CoAl	60
3.4.1	:	Structural Properties	61
3.4.2	:	Electronic and Magnetic Properties	64
CHAPTER 4	:	**Sructural Stability and Electronic Properties of Full Heusler Surface films**	
4.1	:	Ti_2XSi (X=Mn, Co) Surfaces [001]	72

4.1.1	:	Results and Discussions	73
4.1.1.1	:	Structural Properties	73
4.1.1.2	:	Surface Stability	73
4.1.1.3	:	Surface Electronic and Magnetic Properties	77
4.2	:	Fe_2CoAl Surfaces [111]	80
4.2.1	:	Results and Discussions	82
4.2.1.1	:	Spin Degree of Freedom dependent Ground State Energy	82
4.2.1.2	:	Elelctronic and Magnetic Properties	82
4.2.13	:	Perpendicular Magnetocrystalline anisotropy Energy	87
4.3	:	Mn_2CoSi – Surface Half metallicity at MnSi termination of [001] Mn_2CoSi	88
4.3.1	:	Results and Discussions	90
4.3.1.1	:	Structural Optimization and Stability	90
4.3.1.2	:	Electronic and Magnetic Properties	92
CHAPTER 5	:	**X_2YZ type Heusler and Semiconductor Heterojunction Interface for Spin Injection Properties**	
5.1	:	Mn_2CoSi|CaS|Mn_2CoSi MTJ Device	96
5.2	:	Result and Discussions	97
5.2.1	:	Spin Dependent Transport Properties	98
5.2.2	:	Spin Injected Polarized Current	106
CHAPTER 6	:	**Conclusion**	107
References	:		112
Brief bio-data of the author	:		135
List of Publications and Activities	:		137
Particulars of Candidate	:		141

Lists of Figures

Figure No.	Titles of the Figures	Page
1.1	Conventional density of states structure for half metallic materials (Red 'up-arrow' and Blue 'down-arrow' indicates spin up and spin down states respectively	9
1.2	Schematic illustration of the formation and origin of band gap in spin-down channel	9
2.1	General flow chart for self-consistent cycle in density functional theory based simulation	28
2.2	The graphical representation of norm-conserving ultrasoft pseudopotential as implemented in Quantum ATK Q-2019.12	31-33
3.1	The crystal structure of regular (a) and inverse (b) full-Heusler Fe_2IrSi. (c) Relative energy (E-E_0) per unit cell versus lattice constant profile of the various magnetic configurations calculated	37
3.2	Calculated total and partial density of states [(a) and (b)] and band structure along the high symmetry points of the Brillouin zone	39
3.3	Calculated total and partial density of states: (a) SOC (b) SOC+U (U_{Ir} = 1.0 eV and U_{Fe} = 3.52 eV)	40
3.4	Variation of the partial and total magnetic moment obtained using GGA+U (U_{Fe} = 3.52 eV, U_{Ir} = 0.0 eV to 3.0 eV) for the XA phase of full-Heulser Fe_2IrSi	40
3.5	Calculated exchange coupling parameter J_{ij} as a function of distance the R using GGA+U (U_{Fe} = 3.52 eV) for (a) U_{Ir} = 0.0 eV and (b) U_{Ir} = 1.0 eV and Calculated (c) exchange-coupling parameter $J_{Fe} = \sum_i J_{Fe,i}$ for the Fe atom and (d) Curie temperature T_C within the mean-field approximation as a function of U_{Ir} with the GGA+U (U_{Fe} = 3.52 eV)	43

3.6	Calculated phonon band structure along the various high symmetry points in the first Brillouin zone, the density and the projected phonon density of states, and the Raman spectra of inverse full-Heusler Fe_2IrSi	47
3.7	Total Density of States (upper panel) and partial atomic resolved density of states (lower panel) of the bulk: (a) Ti_2MnSi (b) Ti_2CoSi compounds (↑-spin-up and ↓-spin-down)	51
3.8	Phonon dispersion relation and phonon DOS of (a) Ti_2MnSi and (b) Ti_2CoSi	54
3.9	Spin polarized density of states: (a) and (b) from GGA and GGA+U approximation respectively using projector augmented-wave based VASP calculation, (c) and (d) using GGA and GGA+U respectively using norm-conserving pseudopotential based ATK calculation	57
3.10	Calculated spin resolved electronic band structure of Mn_2CoSi from (a) GGA and (b) GGA+U approximation	58
3.11	Calculated phonon dispersion relation curve and phonon partial DOS contribution from atomic site	60
3.12	Variation of total energy as a function of lattice constant a (Å): (a) direct phase, (b) inverse phase (AMF1, AFM2 and FM configurations are represented by black, red and blue lines, respectively), (c) ground state energy as a function of volume in $Å^3$ for FM and (d) pressure in GPa as a function of volume in $Å^3$	62
3.13	(a) Total DOS calculated using GGA+U, (b) partial DOS of Fe1-d, Fe2-d, Co-d and Al-p calculated with GGA+U at different pressures	64
3.14	(a) Partial DOS of Fe1 (d-e_g,d-t_{2g}), (b) partial DOS of Fe2 (d-e_g,d-t_{2g}), (c) partial DOS of Co (d-e_g,d-t_{2g}) and (d) partial DOS of Al-p at different pressures	66
3.15	Band energies of Fe_2CoAl calculated with GGA+U at (a) P =0	

	GPa, (b) P =5 GPa, (c) P =10 GPa, (d) P =20 GPa and (e) P =60 GPa	67
3.16	Calculated total and partial magnetic moments [(a) and (b)], variation of (c) cohesive energy and (d) energy band gap as a function of pressure	69
3.17	(a) Exchange interaction J_{ij} (meV) and (b) Curie temperature T_C MFA (K) as a function of pressure	69
3.18	Exchange interaction J_{ij} (meV) between (a) Al and Fe1, (b) Fe1and Fe1, (c) Fe2 and Fe1 and (d) Co and Fe1 at different pressure	70
4.1	Conventional Slab model for (a)TiSi (b)TiMn terminal of 001 Ti_2MnSi and (c) TiSi, (d)TiCo terminal from Ti_2CoSi compounds	74
4.2	Calculated surface energies (eV/Å^2) as a function of chemical potentials of (a) μ_{Ti} andμ_{Mn} (eV) for 001-surface of Ti_2MnSi and (b) μ_{Ti} and μ_{Co} (eV) for 001- surface of Ti_2CoSi	75
4.3	Spin resolved partial density of states: (a) TiSi(TMS), (b) TiMn(TCS), (c) TiSi(TCS) and (d) TiCo(TCS) terminal surfaces	78
4.4	Calculated Band structures of Ti_2MnSi (001)[(a)TiSi (b)TiMn-terminal] and Ti_2CoSi (001)[(c)TiSi (d)TiCo terminal]	79
4.5	Conventional slab model (Side-view) for (a) Ferromagnetic Co-terminal (b) Antiferromagnetic (AFM1) Al-terminal and (c) Antiferromagnetic (AFM2) Fe-terminal	83
4.6	Calculated partial DOS of Fe_2CoAl-111 surfaces from GGA and GGA+U: (a) Al-terminal, (b) Co-terminal and (c) Fe-terminal	84
4.7	Calculated band structures of Fe_2CoAl-111 surfaces: (a) Al-terminal (GGA), (b) Al-terminal (GGA+U), (c) Co-terminal (GGA), (d) Co-terminal (GGA+U), (e) Fe-terminal (GGA) and (f) Fe-terminal (GGA+U)	84

4.8	Atomic resolved magnetic moment (a) Al-terminal (b) Co-terminal and (c) Fe-terminal	85
4.9	Calculated Atomic resolved magnetocrystalline anisotropy energy (MAE) of 111- plane of Fe_2CoAl (a) Al-terminal and (b) Co-terminal and (c) Fe-terminal	87
4.10	Conventional slabs model (side view) of (a) MnCo and (b) MnSi-terminated surface of |001| Mn_2CoSi	89
4.11	Top three layers atomic displacement of the relaxed structure from the unrelax position (a) MnSi-terminal's surface relaxation from conjugate gradient (CG) method (b) MnSi-terminal's surface relaxation from BFGS (c) MnCo-terminal's surface relaxation from CG method	91
4.12	Spin resolved DOS for MnSi-terminal: (a) From MedeA(VASP) (b) From QuantumATK 2019.12 calculations and (c) MnCo-terminal from MedeA (VASP)	93
4.13	Calculated band structures along high symmetry point of MnSi-terminal : (a) Spin-up (b) Spin-down and MnCo-terminal: (c) Spin-up (d) Spin-down	94
5.1	The modeled MTJ device and initial spin degree of freedom for (a) parallel configuration (P) and (b) antiparallel configuration (AP); L.E (R.E) →Left (Right) Electrode and E.E→ Electrode Extension layer upto dashed - ↕ for both the left and right electrodes	97
5.2	Transmission coefficient (in log scale) as a function of bias voltage for parallel P and antiparallel AP-configuration within electron energy range - 4 to 4 eV, direction of blue and red arrow indicate spin-up and spin-down states	100
5.3	The equilibrium $K_{\parallel}$ (k_A, k_B) resolved transmission spectrum (full view of 2D Brillouin Zone) for parallel configuration (P) [(a) spin-up, (b) spin-down] and antiparallel configuration (AP) [(c) spin-up, (d) spin-down	103

5.4	The equilibrium $K_{\parallel}$ (k_A, k_B) resolved transmission spectrum (Zoom-in view around Γ-point) at Fermi level for parallel configuration (P) [(a) spin-up, (b) spin-down] and antiparallel configuration (AP) [(c) spin-up, (d) spin-down]	104
5.5	I-V characteristic curve for spin polarized current (in nA) and bias voltage V (a) Parallel (b) Anti-parallel; inset: zoom-in view for I-V curve.	105
5.6	Spin injection efficiency as a function of Bias voltages	106

Lists of Tables

Table No.	Title of the Table	Page
1.1	Structural order of regular and inverse Heusler structures	6
3.1	Magnetic moment of each atom in the *XA* and $L2_1$ structures, and the total energy (E_T) for the various magnetic configurations (MG) in full- Heusler Fe_2IrSi obtained with DFT. E_T is with respect to the nonmagnetic (NM) ground state, i.e., $\Delta E = E_T^{NM} - E_T^{FM/AFM}$	38
3.2	Calculated elastic tensor ($\boldsymbol{C_{ij}}$), degree of elastic anisotropy ($\boldsymbol{A_e}$), bulk modulus ($\boldsymbol{B_M}$), modulus of rigidity (G), B/G, Young's modulus ($\boldsymbol{Y_M}$), and the Poisson ratio ($\boldsymbol{\nu}$) at various onsite Coulomb potentials for the Ir atom	46
3.3	Calculated melting temperature TM, Debye temperature $\boldsymbol{D_b}$, sound velocity $\boldsymbol{v_s}$, longitudinal velocity $\boldsymbol{v_l}$ and transverse velocity $\boldsymbol{v_t}$ at various onsite Coulomb potentials for the Ir atom	47
3.4	The calculated optimized lattice constant a (Å), total and atomic partial magnetic moment with available literature	49
3.5	Estimated Bulk modulus (K) and Shear modulus (G) of Ti_2XSi (X= Mn, Co) from Voigt and Reuss approximation.	53
3.6	Calculated elastic tensor ($\boldsymbol{C_{ij}}$), degree of elastic anisotropy ($\boldsymbol{Ae}$), modulus of rigidity ($\boldsymbol{G_R}$), Young's modulus ($\boldsymbol{Y_M}$), and the Poisson ratio ($\boldsymbol{\nu}$) for Ti_2XSi (X = Mn, Co)	53
3.7	The calculated optimized lattice constant a (Å), total and atomic partial magnetic moment with available literature	56
3.8	Calculated Bulk modulus (**K**) and Shear modulus (**G**) from Voigt and Reuss approximation, elastic tensor ($\boldsymbol{Cij}$), degree of elastic anisotropy ($\boldsymbol{A_e}$), modulus of rigidity ($\boldsymbol{G_R}$), Young's modulus ($\boldsymbol{Y_M}$), and the Poisson ratio ($\boldsymbol{\nu}$) for Mn_2CoSi	59
3.9	Magnetic configurations (MC) of the individual atoms Fe1, Fe2,	

	Co, and Al, and total ground state energy E_T in Rydberg	63
3.10	Total and partial magnetic moments (in μB) calculated with GGA+U along with the Curie temperature; T_C^{cal} (Linear relation approach) and T_C^{MFA} (Mean field approach) in K	63
4.1	The relaxed atomic displacement (d_{i-f}(Å)) and the atomic displacement (% of d_{i-f}) in percentage of optimized bulk lattice constant a	65
4.2	Calculated atomic magnetic moment (in μ_B) of surface(s), sub-surface(s-1) central layer (C.L) and corresponding calculated values in their respective bulk structure	76
4.3	Magnetic Configuration on magnetic atomic sites (six Fe- and three Co-atoms) and energy difference (E_{FM}-E_{AFM}) in Rydberg for Al-terminated surface	81
4.4	Magnetic Configuration on magnetic atomic sites (six Fe- and four Co-atoms) and energy difference (E_{FM}-E_{AFM}) in Rydberg for Co-terminated surface	81
4.5	Magnetic Configuration on magnetic atomic sites (seven Fe- and three Co-atoms) and energy difference (E_{FM}-E_{AFM}) in Rydberg for Fe-terminated surface	81
4.6	Comparison between surface/subsurface atomic sites magnetic moment (in μ_B) with their corresponding moment in the bulk Fe_2CoAl	86
4.7	Calculated atomic magnetic moment (in $\boldsymbol{\mu_B}$) of surface (s), sub-surface (s1) central layer (C.L) and corresponding calculated values in their respective bulk structure	91
5.1	The calculated spin polarized quantum conductance (in Siemen) for parallel magnetization (G↑↑, G↓↓) and anti-parallel magnetization (G↑↓, G↓↑) configurations and total spin polarized current I_P^{Total} , I_{AP}^{Total} (in n*A*) for P and AP configurations and TMR ratio	101

This Thesis is Dedicated

to

My Grandparents
RS Dokhuma (1946-2009)
&
Zoliani (1948-2014)

1

Introduction

This chapter consists; subsection 1.1 as introduction and evolution of spintronic, the details description about half metallic materials and why the Heusler compounds are favour over other family of half metals are presents in subsection 1.2. In subsection 1.3, the background history and concept of full Heusler compounds has been elaborate. And the theoretical formalism and background of density functional theory (DFT) has also been discussed in the last subsection of chapter 1.4.

1.1 Introduction and Evolution of Spintronic

The neoteric opportunity for the development of unrealized materials and their implementation in technological device fabrication are significant. Conventionally, semiconductor electronic devices worked based on the electron charge transfer that is operated with a high level of energy consumption. In present day technological world, the interest of magnetic materials and the utilization of electron-spin degree of freedom is the great concern in view of spintronic application. Alternatively, the usage of an electron spin-based electronic so called spintronic (Bader & Parkin, 2010; Fert, 2008; Gregg *et al.*, 2002; Wolf *et al.*, 2001; Žutić *et al.*, 2004) which utilizes the spin degrees of freedom, can give diverse functionality and new capabilities, including faster switching time and lower power consumption. Researchers believed that future spin based electronic devices would outclass the customary charge-based electronic devices ecologically and in terms of low power consumption and efficiency. The spin functionality of the electrons was successfully implemented in a device as giant-magneto-resistance (GMR) in 1988(Wolf *et al.*, 2001). The spintronic devices solely rely on the spin polarization at the Fermi energy (Hashemifar *et al.*) of the material (Aliev, 1991; Coey *et al.*, 2005; de Groot *et al.*, 1983; Dietl *et al.*, 2008; Fert, 2008; Ishida *et al.*, 1995; Sadoc *et al.*, 2007; Y. Wang *et al.*, 2016; Wurmehl *et al.*, 2006; Xiao *et al.*, 2014). When giant magneto resistance (GMR) was discovered by Albert Fert's group in 1988(Baibich *et al.*, 1988; Wolf *et al.*, 2001), the first steps on the road to deployment of the spin degree of freedom of the electrons had been

initiated e.g. utilized in high performing disk drives read heads HDD (Terris & Thomson, 2005) and magnetic random access memory MRAM (Bhatti *et al.*, 2017). A GMR device consists of sandwich structure of alternate layers of ferromagnetic (FM) and non-magnetic (Zheng *et al.*) metals (FM|NM|FM) multilayer whose resistance depends on the relative orientation of the magnetic layers(Fullerton & Schuller, 2007; Hirohata & Takanashi, 2014). If the ferromagnetic layers have their moment all aligned then the device has very low resistance, alternatively, if alternate layers are anti-aligned, then the device has high resistance and as the alignment changes so does the resistance (Wolf & Treger, 2000).

The crucial measurement of magnetic spin transport in GMR devices is an MR ratio, which can be expressed as (Elphick *et al.*, 2021):

$$MR\ ratio = \Delta R/R = (R_{AP} - R_P) / R_P \qquad (1.1)$$

Where R_P and R_{AP} indicated the resistance measured in parallel and antiparallel configuration of spin source magnetization, respectively. To the best of my knowledge, the maximum GMR ratio in current-in-plane (CIP) geometry at room temperature had been reported as 65% in $[Co(0.8) / Cu(0.83)]_{60}$ junction (S. S. P. Parkin *et al.*, 1991).

A couple of decades passed by, other than non-magnetic (Zheng *et al.*) GMR, the efficiency of magnetoresistance (MR) measurement have been increased by replacing non-magnetic (Zheng *et al.*) layer with oxides as spacer or tunneling barrier in Magnetic Tunneling Junction (MTJ). Large tunneling magnetoresistance (TMR) at room temperature was observed in $Fe|Al_2O_3|Fe$ junction (Miyazaki & Tezuka, 1995). In 2007, Wei *et al.,* demonstrated 80% and 107% tunneling magnetoresistance at room temperature and at 4.2 K respectively for $Co_{40}Fe_{40}B_{20}|AlO(0.6nm)|Co_{40}Fe_{40}B_{20}$ MTJ device (Wei *et al.*, 2007). According to theoretical prediction, when the amorphous AlO_x is replaced by an epitaxial MgO in Fe|MgO|Fe junction device; the TMR ratio have been drastically increased over 1000%; due to the coherent tunneling via Δ_1 band matched at the interface (Butler *et al.*, 2001; Mathon & Umerski, 2001). The TMR is measured based on the spin polarization of a ferro/ferrimagnetic layer and can be written as (Julliere, 1975):

$$TMR = 2P_1P_2 / (1-P_1P_2) \qquad (1.2)$$

Where P_1 and P_2 are the spin polarization of ferro/ferrimagnetic layer 1 and layer 2 respectively. An infinite TMR ratio could be possible for coherent tunneling with the spacer since P_1 and P_2 can be 100%. Experimentally, giant TMR ratio upto 180% in single crystal Fe|MgO|Fe MTJ at room temperature had been reported (Yuasa *et al.*, 2004). MTJ device consisting of |100| oriented MgO tunnel barrier with CoFe as an electrodes exhibited large TMR value up to ~ 220% at room temperature (S. S. Parkin *et al*., 2004). In 2008, Ikeda and his co-workers experimentally achieved largest ever report on tunneling magnetoresistance of 604% at 300K by suppressing Ta diffusion as Ta|$Co_{20}Fe_{60}B_{20}$|MgO| $Co_{20}Fe_{60}B_{20}$|Ta pseudo spin valve (Ikeda *et al.*, 2008). The larger the TMR ratio the more is the areal density of HDD.

In 2018, Hirohata *et al.,* presented the target requirements for 1 *Gbit*, 10 *Gbit* MRAM and 2 *Tbit/in*^{2} HDD application (Hirohata *et al.*, 2018). For 1 Gbit MRAM, the junction cell diameter should be < 65nm, a resistance area product (RA) < $30\Omega.\mu m^2$ and MR ratio > 100% (Sun & Ralph, 2008), the target requirement was successfully fulfilled by achieving RA = $18\Omega.\mu m^2$ with TMR = 124% at room temperature (Ikeda *et al.*, 2010b). For 10 Gbit MRAM requirement, junction cell diameter < 20*nm* with RA < $3.5\Omega.\mu m^2$ and MR ratio > 100% (Schmidt *et al.*, 2000). Nagamine *et al.,* partially satisfied the requirement of 10 Gbit MRAM using in-plane CoFeB|MgO|CoFeB MTJ by accomplishing ultralow resitance area = $0.4\Omega.\mu m^2$ with TMR = 57% at room temperature (Nagamine *et al.*, 2006), further improvement had been carried out to meet 10 *Gbit* MRAM requirement by achieving high magnetoresistance ~ 110 – 150% with resistance area RA = 2 – 5 $\Omega.\mu m^2$ using p-SAF structure of Co/Ru/Pt superlattice (Yakushiji *et al.*, 2015). Unfortunately, to the best of my knowledge, there is no reported work that satisfied the requirement for 2 *Tbit/in*^{2} HDD from MTJ devices, even the implementation with the nano-oxide layer (NOL) (Fuke *et al.*, 2007). Ther$_{ef}$ore, an improvement of these junctions devices are crucial and challenging (Takagishi *et al.*, 2010). To meet the require criteria for 2 Tbit/in^2 HDD or more, a half-metallic ferromagnet (HMF) have to be 100% spin polarization at the E_F at room temperature that leads to an infinite MR ratio. Full Heusler compounds Co_2MnSi exhibit half metallicity with 93^{+7}_{-11}% spin polarization at room temperature in a bulk form as well as in-situ film (Jourdan *et al.*, 2014). Therefore, Heusler alloys films can be the most promising material for room

temperature half-metallicity due to the high Curie temperature, stability and excellent lattice matching with semiconductor.

1.2 Half Metallic Materials

The termed half metal is coined by de Groot and his collaborators in 1983; after they predicted the spin up bands in NiMnSb compound shown metallic property while the spin down bands revealed the semiconducting behavior at Fermi level (de Groot *et al.*, 1983). Ferromagnetic (FM)/Anti-ferromagnetic (AFM) Half metallic materials are having 100% spin polarization at Fermi level (Hashemifar *et al.*) in their electronic structure. Generally, the majority (spin up) channel exhibits metallic nature whereas the minority (spin down) channel shown a finite band gap with semiconducting behavior at the Fermi level (Hashemifar *et al.*) (Fert, 2008; Galanakis *et al.*, 2002).

Since the half metallicity is the key factor in spintronic application includes giant magneto-resistance (GMR) and magnetic random access memory (MRAM) (Felser *et al.*, 2015) (Galanakis *et al.*, 2014), spin injectors, spin computer applications and spin-transfer torque device (Ikeda *et al.*, 2010a; Nistor *et al.*, 2009; Vadapoo *et al.*, 2016). In recent decades, researcher fascinated toward the exploration and investigation on half metallic materials. Among half metallic materials family Heusler compounds outclass other classes of other half metals like oxides (CrO_2, Fe_3O_4) and manganite $La_{0.7}Sr_{0.3}MnO_3$ (Soulen Jr *et al.*, 1998), perovskite Sr_2FeReO_6 (Kato *et al.*, 2004) pyrite CoS_2 (Shishidou *et al.*, 2001) pnictide CrAs (Fong *et al.*, 2004) etc., due to their higher Curie temperature. It has been identified from the theoretical and the experimental work that Zincblende magnetic semiconductors also exhibit half-metallicity but they have low Curie Temperature (below room temperature) (Dietl *et al.*, 2000). The thin film of rutile CrO_2 and perovskite $La_{0.7}Sr_{0.3}MnO_3$ shows half metallic nature with almost 100% spin polarization at low temperature as obtained from Andreev reflection measurement (Soulen Jr *et al.*, 1998), but no experimental report on half metallicity at room temperature. Majority of Heusler compounds show high spin polarization at Fermi level (Hashemifar *et al.*), due to the presence of conducting electrons that give dispersed bands around the E_F at one of the spin channels whereas other spin channel exhibit semi-conducting with a

band gap. The half metallic character in Heusler compounds is attributed to the hybridization between the *d-d* orbitals of the transition elements (Galanakis & Mavropoulos, 2007). The transition metal based Heusler compounds exhibit high magnetic moment in the absence of applied magnetic field. Half metallic ferromagnets (HMF) with high Curie temperature is the ideal requirement for spintronic devices due to enabling devices fabrication at room temperature with the absence of magnetic phase transition. Extensive theoretical and experimental studied had been carried out for some full Heusler compounds due to their half metallicity and high Curie temperature (T_C) such as Co_2CrGa, Mn_2CoZ(Z=Al,Ga,Si,Sb), CoFeMnSi, Fe_2CoSi and FeCoCrSi, Co_2FeAl, Fe_2CoAl. The Curie Temperature (T_C) of some well-known Co-based full Heusler compounds are calculated using ab-initio approach based on atomistic spherical wave approximation (ASW) (Kübler *et al.*, 2007) are Co_2VGa (T_C = 368 K), Co_2CrGa (T_C = 362 K), Co_2MnAl (T_C = 609 K), Co_2MnSi (T_C =990 K), Co_2MnSn (T_C = 889 K), Co_2FeSi (T_C = 1183 K). Gasi *et al.,* also reported high T_C for some Fe based inverse full Heusler compounds (Gasi *et al.*, 2013) ; Fe_2CoGe (T_C = 925 K), Fe_2NiGe (T_C = 750 K), Fe_2NiGa (T_C = 845 K), Fe_2CuGa (T_C = 798 K), Fe_2CuAl (T_C = 875 K) and Fe_2CoAl (T_C = 987 K) (Siakeng *et al.*, 2018). So, in this regard Heusler compounds have comparatively high Curie temperature well above the room temperature for practical applications.

1.3 Heusler Compounds

Heusler compounds are originated from the work of a German mining engineer Friedrich Heusler. In 1903, Heusler discovered a sequence of ferromagnetic compounds such as Cu_2MnAl, CuMnSb, Cu_2MnSn (Heusler, 1903) consisting of diamagnetic, paramagnetic elements (Cu, Mn, Al, etc) which were then considered as nonmagnetic element in those time. Antiferromagnet was revealed after Neel's induction of anti-ferromagnetism in his work later on 1940s (Néel, 1948). Manganese is now known to be antiferromagnet in nature. Up today, the extensive studied by theoretical calculation and experimental work continuously revealed thousands of Heusler compounds with various diverse functional properties such as half metallicity, high Curie temperature, low magnetic damping, spin gapless

semiconductor, thermoelectric, topological insulator, Weyl semimetal and magnetic skyrmion in Heusler compounds. A part from half metallicity, the nature of high Curie temperature of Heusler compounds revealed to be one of the most potential candidates for spintronic application. Within this section (1.3), I do elaborate full Heusler compounds in subsection-wise by presenting the detail description of crystal structure of full Heusler compounds, generalized magnetic properties–Slater-Pauling rule and Half-metallicity in full Heusler compounds.

1.3.1 Crystal Structure of Full Heusler compounds

Generally, full Heusler compounds can be assembled into a family of binary (X_3Z), full/ternary (X_2YZ), and quaternary (X_1X_2YZ) compounds The ternary Heulser compounds have been shown to exist in a chemical formula of X_2YZ with stoichiometric composition 2:1:1, where X and Y are mainly transition metals and Z is the main group element. There can be two ordered structures in full Heusler compounds depending on the atomic arrangement in the manner of their electronegativity: the conventional direct or regular full Heusler (Cu_2MnAl-type) crystallized in a centro-symmetric cubic $L2_1$ structure consisting of four interpenetrating face centred cubic lattices with space group 225 ($Fm\bar{3}m$ symmetry) (Bradley *et al.*, 1934; Heusler, 1903; Heusler *et al.*, 1903) and the inverse full Heulser (Hg_2CuTi type) materialized in *XA* structure with having space group 216 ($F\bar{4}3m$) where the electronegativity of the Y-atom is higher than that of the X-atom or the Y-atom valence electrons is more than that of X-atom (Felser *et al.*, 2015; Galanakis *et al.*, 2006; Graf *et al.*, 2011). The Wyckoff positions of the constituent atoms are presented in Table 1.1

Table 1.1: Structural order of regular and inverse Heusler structures.

	4*a*	4*b*	4*c*	4*d*
	(0, 0, 0)	(½ , ½, ½)	(¼ , ¼ , ¼)	(¾ , ¾ , ¾)
Regular ($L2_1$)	*Z*	*Y*	*X*	*X*
Inverse (XA)	*Z*	*X*	*Y*	*X*

1.3.2 Generalized magnetic properties - Slater-Pauling Rule

The magnetic nature of full Heusler compounds can be generalized according to Slater-Pauling rule, in terms of their valence electron (Graf *et al.*, 2011; Pauling, 1938; Slater, 1936). An integer numbers of electrons Z↑ and Z↓ per unit cell revealed the presence of a gap at the Fermi level E_F where Z↑ is the number of spin-up electrons and Z↓ represents number of electrons with spin-down. Since both Z↑ and Z↓ are integer numbers, their difference must be an integer resulting an integer magnetic moment i.e., $M_t = (Z\uparrow - Z\downarrow)$. The linear relation of spontaneous magnetization attributed to be the extension of the Slater-Pauling rule which stated that in ferromagnet the sum of the number of spin-up electrons Z↑ and spin-down electrons Z↓ per atom must be equal to the total number of valence electrons per atom i.e., $Z_t = (Z\uparrow + Z\downarrow)$. The magnetization M_t and valence electrons Z_t can be linearly related by reshuffling those above relations that results in $M_t = (Z_t - 2Z\downarrow)$ μ_B/atom. For 100% spin polarization full Heusler compounds, it was revealed that the four atoms in the unit cell have a constant number of 12 electrons minority spin (Z↓). So, for full Heusler compounds the linearly dependent magnetization with valence electron becomes $M_t = (Z_t - 24)$ μ_B/atom and $M_t = (Z_t - 18)$ for half Heusler compounds (Galanakis *et al.*, 2002; Galanakis *et al.*, 2006). Systematic theoretical calculation had been performed to sketch out the generalized Slater-Pauling rule for inverse Heusler compounds (Skaftouros *et al.*, 2013) by presenting three linear relation curves for $M_t = Z_t - 18$, $M_t = Z_t - 24$ and $M_t = Z_t - 28$. An extensive review on theoretical calculation and experimental studies for Co based and some direct full Heusler within bulk structure have been reported (Elphick *et al.*, 2021). It can be noted from that reviews, almost all theoretical predictions and experiment measured were in well agreed with the Slater-Pauling rule.

1.3.3 Half Metallicity in Full Heusler compounds

One of the most approved properties in full Heusler compounds is half metallic nature with high T_C. For those systems, the spin polarization at E_F is predicted to be 100% by attaining semiconducting band structure with a finite band

gap in minority spin channel (Spin down) while an alternate spin channel (Spin up) exhibited metallic character. The degree of spin polarization can be measured as (Julliere, 1975; Soulen Jr *et al.*, 1998):

$$P = \frac{P\uparrow(E_F) - P\downarrow(E_F)}{P\uparrow(E_F) + P\downarrow(E_F)} \qquad (1.3)$$

Where $P\uparrow(E_F)$ and $P\downarrow(E_F)$ represent density of states for spin up electrons (Majority states) and spin down electrons (Minority states) at the Fermi level E_F. For Co-based full Heusler compounds the theoretical mechanism for the formation and origin of band gap in spin down channel was proposed (Galanakis *et al.*, 2002). It was explained that the formation of minority band gap is attributed to *d-d* hybridization between the constituent transition elements. He first considered the hybridization between Co-Co atoms and then hybridized states with Mn-atom. The five *d* orbitals split into threefold degenerate d_{xy}, d_{yz}, d_{zx} and twofold degenerate $d_{3z^2-r^2}$, $d_{x^2-y^2}$ states which were represented by d_1, d_2, d_3, d_4, and d_5 respectively. When two Co atoms hybridized, d_4 and d_5 orbitals form double degenerated bonding 2xe_g and antibonding 2xe_u orbitals and d_1, d_2, d_3 orbitals formed triple-degenerated bonding 3xt_{2g} and antibonding 3xt_{1u} orbitals. Due to orbitals symmetry representation, one Co's e_g orbital can couple only with e_g orbitals at other Co site and similar procedure is applied for t_{2g} orbitals. Then again, a coupled doubly degenerate 2xe_g from Co-Co hybridized with d_4, d_5 orbitals from Mn atom forming a double-degenerated bonding e_g states with the same representation that is very low in energy and an antibonding one that is unoccupied and above the Fermi level. While, 3xt_{2g} orbitals hybridized with d_1, d_2, d_3 of Mn atom resulting three bonding states which are occupied and three states with unoccupied antibonding state. Since Mn does not have *u* representing orbitals, therefore 2xe_u and 3xt_{1u} from Co-Co orbitals failed to couple. So, the Fermi level falls between those two antibonding; highest occupied 3xt_{1u} and lowest unoccupied 2xe_u states from Co-Co hybridization. The strength of Co-Co hybridization determined the energy split between these two states, so the width of the band gap.

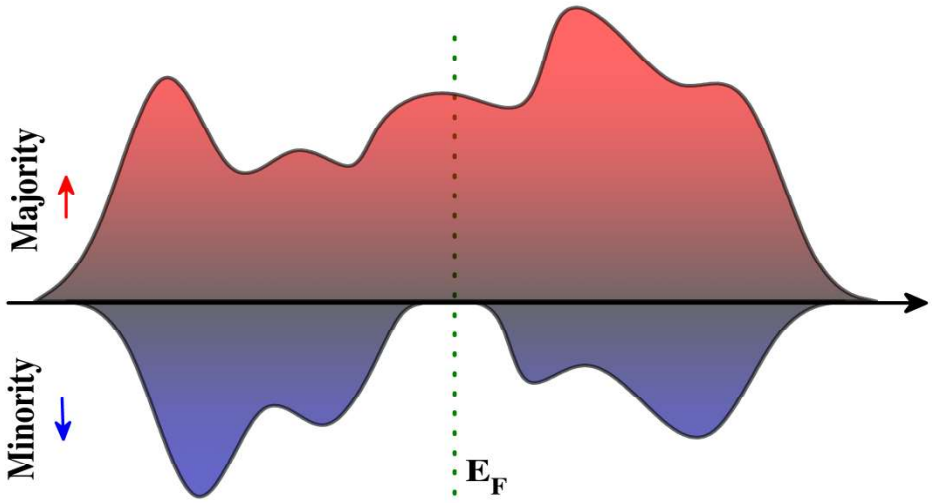

Figure 1.1: Conventional density of states structure for half metallic materials (Red 'up-arrow' and Blue 'down-arrow' indicates spin up and spin down states respectively.

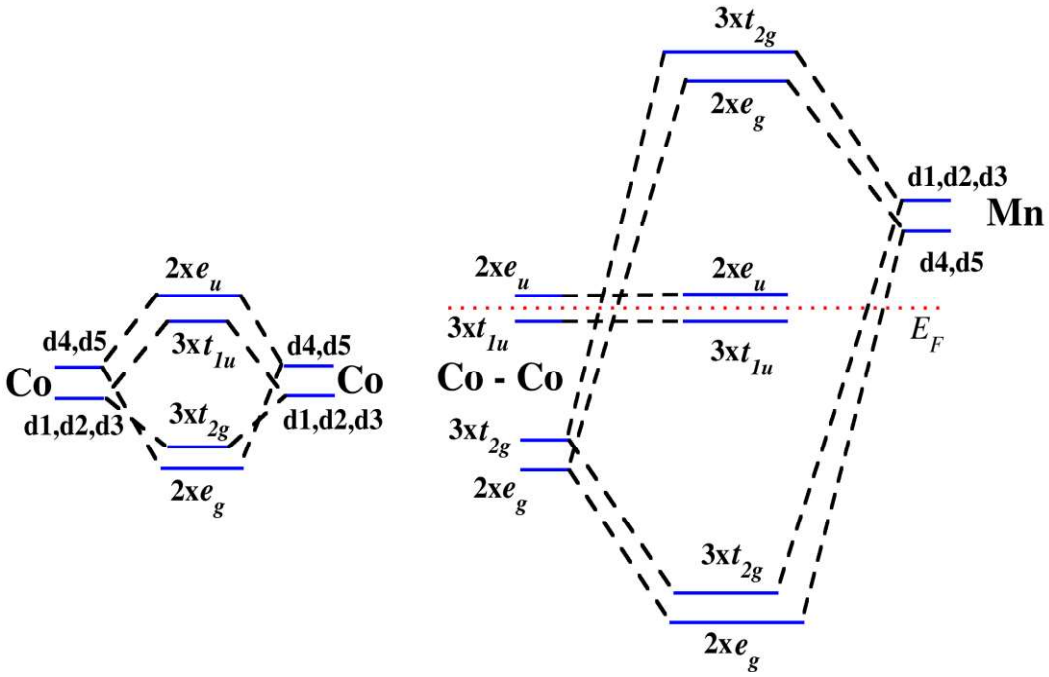

Figure 1.2: Schematic illustration of the formation and origin of band gap in spin-down channel (Galanakis *et al.*, 2002).

1.4 Review on Thin film/surface properties of full Heusler compounds

The preservation of half metallicity in the realm of nanoscale especially on the surface (slab)/ thin film is highly desirable for spintronic fabrication. However, retaining half metallicity on the surfaces are always a big question and challenging. There were several reports in which the surface half metallicity is lost due to broken translational symmetry that leads to breaking of metallic bonds results in spreading of free charges on the surface. One of the pioneer work on the first principle calculation of Heusler surfaces/thin film structure had been performed a couple of decades ago. The electronic and magnetic properties of the surface (001) of the half Heusler alloys NiMnSb, CoMnSb, PtMnSb and of the full Heusler alloys Co_2MnGe, Co_2MnSi and Co_2CrAl had been studied using full potential version of the screened Korringa-Kohn-Rostoker (KKR) Green function method by I.Galanakis (Galanakis, 2002). The MnSb-terminated surfaces of the half Heusler compounds present properties similar to those of their bulk compounds although the half metallicity is lost. In contrast, the CrAl-terminated (001) surface of Co_2CrAl shows a spin polarization of about 84%.

An authentic first principle calculation predicted |001| surface of Co_2MnSi preserved half metallicity at non-natural MnMn terminated surface (Hashemifar *et al.*, 2005), but it might be needed to deploy spin polarized STM technique to confirm the prediction. By using Pseudopotential method calculation in Co2MnSi|GaAs|001| interfacial structure, half metallic character is preserved in SiMn|As where Mn atom is welded As sub-lattice and MnMn|As where Mn atoms occupied hollow and bridge sites between As atoms at the junction (Ghaderi *et al.*, 2007).

Zheng et al. performed first principle calculation within all electron method of full-potential linearized augmented plane-wave (FLAPW) method as implemented in WIEN2k package to explore the structural stability, electronic and magnetic properties of Cr_2CoGa (001) surface. In that work, both Cr_1Co- and Cr_2Ga-terminated (001) surfaces are considered (Zheng *et al.*, 2018). It is found that the Cr_2Ga-terminated (001) surface is more stable than the Cr_1Co-terminated (001) surface over the whole effective chemical potential. Nearly half-metallicity is destroyed at the Cr_1Co-terminated (001) surface and the calculated surface spin polarization is only 60%. Interestingly, the Cr_2Ga-terminated (001) surface retains the half-metallicity and

the spin polarization at the surface (91%) is a little higher than that in the bulk (86%). So, the structure stable, and nearly half-metallic Cr_2Ga-terminated (001) surface makes Cr_2CoGa thin films useful in spintronic applications.

Zhu and Others also performed (Zhu *et al.*, 2015) the calculation of surface electronics states of 18 valence electron half Heusler semiconductors – CoTiSb, CoNbSn and NiTiSn by deploying simulation package VASP (Vienna Ab-Initio Simulation Package) treating the electron exchange-correlation interaction by the generalized gradient approximation (GGA). Various physical properties – half metallicity, weak to strong spin polarization of the conduction electrons and non-magnetic metallic and semiconducting states are realized in CoTiSb, CoNbSn and NiTiSn depending on the compound and surface type, which indicates that the class of 18 valence electron semiconductors constitutes a promising platform with unprecedented flexibility for future spintronics materials.

The (111), (110) and (001) surfaces and the interfaces half-metallicity with *CdS* (111) substrate of the quarternary Heusler alloy CoRuMnSi (Khalaf Al-zyadi *et al.*, 2018) were explored by carrying out a first principle calculation based on density functional theory. Investigation showed that the half-metallicity can be preserved for the Si-terminated |111| surface and subsurface while the half-metallicity is destroyed at Co-, Ru- and Mn-terminated |111| surfaces and sub-surfaces. Regrettably, the surfaces states ruin the gap in the spin-down channel at both MnSi and CoRu-terminated |001| surfaces and sub-surfaces. Remarkably, the |110| surfaces and sub-surfaces have a nearly half metallic property with a high spin polarization. For the interface of CoRuMnSi/CdS 111|, the half-metallicity is destroyed at Si-Cd and Si-S configurations. Recently, in Fe_2MnAl compound P|111| terminated surface half metallicity is predicted theoretically (Paudel & Zhu, 2019). Out of four termination in Sc_2CoSi|001|, ScSi-termination retained half metallicity with 100% spin polarization (Amiri *et al.*, 2019). Nearly half metallicity had been reported for TiSn-terminal of Ti_2CoSn|001| exhibited nearly half metallic character with 94.2% spin polarization (Yan *et al.*, 2016) and TiGe-terminal of Ti_2FeGe|001| surface shown 96.67% spin polarization (Hu & Zhang, 2017). Co_2VAl is one of the most explore compound due to the tendency of preserving bulk half metallicity in thin films and interface realm. First principle calculation revealed that; energetically favourable V and Al-terminal

maintained bulk half metallic character in $Co_2VAl|111|$ thin film (Han *et al.*, 2013) and continue maintained half metallicity at V-S interface in $Co_2VAl|PbS|001|$ heterostructure (Han *et al.*, 2015) and VAl-terminated surface engaged half metallicity with 100% spin polarization in $Co_2VAl|001|$ structure (Khosravi *et al.*, 2014). In $Co_2MnGe|111|$ surfaces, Ge and CoMn surfaces exhibited stable surface half metallic nature whereas only Ge-As interface possessed interfacial half metallicity with 100% spin polarization in $Co_2MnGe|GaAs|001|$ heterostructure (Han *et al.*, 2017).

Besides the theoretical and experimental studies on surfaces and interfaces half metallicity, a large number of rigorous works from theoretical and experimental have been carried out and presented on Heusler based MTJ devices to study spin current injection to semiconductor, tunnelling magnetoresistance (TMR), spin waves, anisotropic magnetoresistance (AMR). For efficient spin injection, theoretically proposed two approach as spin injector with (1) HMF and (2) DMS, in a diffusive regime (Schmidt *et al.*, 2000). From Andreev reflection measurement, the transport spin polarization of $Co_{2.4}Mn_{1.6}Ga$ was measured to be ~50%, but the injected electrons spin polarization to $|001|$ $In_{0.2}Ga_{0.8}As$ quantum well (QW) was measured to be 13% at 5 K (Hickey *et al.*, 2005), this may be due to slightly mismatching lattice between spin injector and semiconductor. The efficient injection from Co_2FeSi to Cu lateral spin valve (LSV) was estimated to be 0.27 (Kimura *et al.*, 2012). Experimentally, demonstrated that injected carriers had been measured to have 78 *ps* spin lifetime and 167*nm* spin diffusion length and junction magnetoresistance (JMR) 325% at room temperature in Hanle device $Mn_2CoSi|SiO_2|$p-Si heterostructure (Maji & Nath, 2019).

Featuring spintronic devices regime, in 2001 GMR ratio had been measured less than 1% at room temperature with Co2MnGe/NM/Co2MnGe trilayers epitaxially grown on GaAs (001). For current-perpendicular to plane (CPP)-GMR, a large magnetoresistance (MR) ratio of 28.8% was observed RT for an epitaxial $Co_2MnSi|Ag|Co_2MnSi$ device (Iwase *et al.*, 2009), a pseudo spin-valve (PSV) consisting of $Co_2FeGe_{0.5}Ga_{0.5}$ (CFGG) layers with Ag spacer (CFGG|Ag|CFGG) gave rise to MR ratio of 41.7% and 9×10^{-3} $\Omega\mu m^2$ resistance area (RA) at 300 K (Takahashi *et al.*, 2011). Further enhancement of MR ratio of 82% and RA = 31 $m\Omega\mu m^2$ at room

temperature had been demonstrated with by inserting of NiAl with thickness 0.21*nm* at the interface of CFGG|Ag|CFGG pseudo spin valve (Jung *et al.*, 2016) . $Co_2Fe_{1-x}Mn_xSi$ (CFMS) based CPP-GMR device had been measured an MR ratio of 58% at RT for fully epitaxial $Co_2Fe_{0.4}Mn_{0.6}Si(4nm)|Ag(3nm)|Co_2Fe_{0.4}Mn_{0.6}Si(2nm)$ device (Sakuraba *et al.*, 2012), an improvement MR ratio had also reported by replacing the spacer Ag with Ag_3Mg achieving 63% MR ratio and 25 $m\Omega\mu m^2$ in CFMS|Ag_3Mg|CFMS at room temperature (Kubota *et al.*, 2017). To the best of our knowledge, no further improvement of MR ratio had been made in GMR since this report, even though a hard effort still been given for further improvement.

Heusler compounds with MgO spacer based magnetic tunneling junction (MTJ) device have yielded a reasonably high TMR ratio at room temperature; for fully epitaxial MTJ $Co2Cr_{0.6}Fe_{0.4}Al|MgO|Co_{50}Fe_{50}$ a TMR value of 90% at RT and 240% at 4.2 K was observed (Marukame *et al.*, 2006). Highly oriented |001| and B2-ordered $Co_2FeAl_{0.5}Si_{0.5}$ as spin injector and MgO fabricated on thermally oxidized Si substrate as a spacer in CFAS|MgO|CFAS MTJ structure, TMR ratio had been measured to be 125% at room temperature and 196 at 7K (W. Wang *et al.*, 2008) which was less than 175% at RT for $L2_1$ ordered $Co_2FeAl_{0.5}Si_{0.5}$ based CFAS|MgO|CFAS spin-valve type MTJ (Tezuka *et al.*, 2006). Co_2MnGe (CMG) with tunnel barrier MgO also exhibited a relatively high tunnel magnetoresistance of 83% at RT (Hakamata *et al.*, 2007). The experimental demonstration for Co_2MnSi based MTJ device with MgO tunnel barrier (CMS|MgO|CMS) usually exhibited comparatively large tunneling magnetoresistance than that of other explored Heusler alloys. For Mn concentration (α = 1.29) at RT fully epitaxial CMS|MgO|CMS MTJ had been shown to have 236% TMR ratio (Ishikawa *et al.*, 2009), whereas it had refined to behave 354% at 290 K by employing CoFe buffer layer (Liu *et al.*, 2012). TMR result can increased to 429% at 290 K for CMS|MgO|CMS MTJ when it had been lightly doped with Fe (Liu *et al.*, 2015). Even though, Heusler based MTJ with MgO barrier yielded a very high TMR value that beyond the fabrication requirement for 10 Gbit MRAM and 2 $Tbit/in^2$ HDD but due to large resistance area product (RA) it is not possible for further improvement in fabrication. The main factor in this case is due to the lattice mismatching at the interface with MgO. To minimize RA, searching

an alternative tunneling barrier also one of the potential opportunity in Heusler based MTJ.

In this Thesis, motivated by the fascinating development and implementation of spin based electronic in the current worldwide research activities. We have studied mainly electronic and magnetic properties of full Heusler compounds as well as their functional properties such as mechanical and thermodynamical stability in bulk crystal and surface\thin films using *ab-initio* (First principle calculation) based on the density functional theory (DFT). The detail formalism of density functional theory (DFT), methodology and the simulation computer code/programme will be discussed in Chapter 2. We approach DFT calculation within generalized gradient approximation (GGA); by the availability of the Hubbard potential U value in literature, the bulk calculation is extended to GGA+U approximation within the frame work of DFT. The Structural, Electronic, Magnetic properties, mechanical and thermodynamical stability of bulk X_2YZ type full Heusler Compounds are presented in Chapter 3. Unfortunately, to the best of our knowledge, we do not came across the validity of DFT+U approach for open system or non-periodic system like thin film/surfaces and interface property calculation since the onsite Hubbard interaction is treated as isotropic projection in the current DFT approximation. However, we report surface electronic properties and stability of various full Heusler compounds in Chapter 4. Specifically, the thermodynamical stability of thin film is computed for the compounds which were not experimentally reported for thin film characterization. Realization of material in a device is the main goal for theoretical investigation and experimental demonstration. Regarding to this, we modelled the magnetoresistance tunnelling junction (MTJ) device based on half metallic ferrimagnet inverse Heusler compound as spin injection source and Calcium chalcogen as a spacer. The spin quantum transport property is calculated and the related physical properties are also discussed in Chapter 5. All the interesting work done based on this thesis and the possible impact of findings for current and futuristic work will be drawn out and concluded in Chapter 6, which is orderly followed by References, List of publication, Brief Bio-data of the author and Particulars of the Candidate.

2

Theoretical Formalism and Methodology

2.1 Density Functional Theory (DFT) Formalism

The collection of non-interacting systems that effect the external field and unambiguously described the behaviour of the solids crystalline systems. However solving them from analytical approach is very complex and not possible. To understand all these issues and problems one must use an ab-initio method, i.e. first principle approach. These techniques are essentially based on the approximations of quantum mechanics accounting the electron density in-stead of its wave function. This umbrella of ab-initio is called density functional theory (DFT) developed by Kohn and Sham (Kohn & Sham, 1965)which is based and rely on the Hohenberg-Kohn Theorem (Hohenberg & Kohn, 1964). Density functional theory is the most widely used and adopted conceptual framework to approach many-body system; an atom, a molecule or a solid. According to Born-Oppeinheimer approximation (Born & Oppenheimer, 1927), the nuclear degrees of freedom take shape in the form of a potential *v(r)* upon electrons and its wave function depends only on the position of the electrons (Staroverov *et al.*, 2003, 2004; Tao *et al.*, 2003). For more than one electron i.e. system with many-body electron, the Schrodinger's equation can be written as (Capelle, 2006)

$$H = [T + V + U]\psi \tag{2.1}$$

$$\left[\sum_i^N \left(-\frac{\hbar^2 \nabla_i^2}{2m} + v(\boldsymbol{r_i})\right) + \sum_{i<j} U(\boldsymbol{r_i}, \boldsymbol{r_j})\right] \Psi(\boldsymbol{r_1}, \boldsymbol{r_2} \ldots \boldsymbol{r_N}) = E\Psi(\boldsymbol{r_1}, \boldsymbol{r_2} \ldots \boldsymbol{r_N}) \tag{2.2}$$

Where *N* is the number of electrons and $U(r_i, r_j)$ is the electron-electron interactions. The Coulomb interaction operator would be same for any system of particles interacting via the coulomb interaction, so does the kinetic energy operator will be same for all non-relativistic system (Kohn, 1999).

$$\widehat{U} = \sum_{i<j} U(\boldsymbol{r_i}, \boldsymbol{r_j}) = \sum_{i<j} \frac{q^2}{|\boldsymbol{r_i} - \boldsymbol{r_j}|} \tag{2.3}$$

The kinetic energy operator,

$$\hat{T} = -\frac{\hbar^2}{2m}\sum_i \nabla_i^2 \tag{2.4}$$

For system with many-body system like solid or a molecule, it depends on the potential $v(\boldsymbol{r_i})$ (Pople, 1999):

$$\hat{V} = \sum_i v(\boldsymbol{r_i}) = \sum_{ik} \frac{Q_k q}{|\boldsymbol{r_i} - \boldsymbol{R_k}|} \tag{2.5}$$

The observables can be evaluated in quantum mechanics by plug-in specified potential $v(\boldsymbol{r_i})$ into the Schrodinger's equation, solving for the wave function Ψ. The expectation values of specific operators yielded its corresponding observables. The electron density $n(\boldsymbol{r})$ (number of electrons per volume at point ($\boldsymbol{r}$) can also be obtained from that way. The relation between electron density $n(r)$ and many-electron wave function can be written as:

$$n(\boldsymbol{r}) = N\int d^3r_1 \int d^3r_2 \ldots . \int d^3r_N \Psi^*(\boldsymbol{r_1}, \boldsymbol{r_2} \ldots \boldsymbol{r_N})\Psi(\boldsymbol{r_1}, \boldsymbol{r_2} \ldots \boldsymbol{r_N}) \tag{2.6}$$

2.2 Hohenberg-Kohn (H-K) Theorem

Hohenberg-Kohn theorem (Hohenberg & Kohn, 1964) is the backbone of density functional theory (DFT). It stated that for a given ground state electron density $n_0(\boldsymbol{r})$, the ground state wave function $\Psi_0(\boldsymbol{r_1}, \boldsymbol{r_2} \ldots \boldsymbol{r_N})$ can be evaluated. This implies that the ground state wave function Ψ_0 is a functional of ground state density n_0 (March, 1982).

$$\Psi_0(\boldsymbol{r_1}, \boldsymbol{r_2} \ldots \boldsymbol{r_N}) = \Psi[n_0(\boldsymbol{r})] \tag{2.7}$$

As an out-turn, any observable $\hat{S}$ ground state expectation value is also a functional of ground state (GS) density $n_0(\boldsymbol{r})$:

$$S_0 = S[n_0] = \langle \Psi[n_0] | \hat{S} | \Psi[n_0] \rangle \tag{2.8}$$

One of the most important observable is ground state energy, according to the previous line: GS energy is a functional of $n_0(\boldsymbol{r})$

$$E_0 = E_0[n_0] = \langle \Psi[n_0] | \hat{H} | \Psi[n_0] \rangle \tag{2.9}$$

Where $\hat{H} = \hat{T} + \hat{U} + \hat{V}$ (Laird *et al.*, 1996)

$$E_0 = E_0[n_0] = \langle \Psi[n_0] | \hat{T} + \hat{U} + \hat{V} | \Psi[n_0] \rangle \quad (2.10)$$

For any arbitrary density n, if n is not the ground state density n_0 in potential $v(r)$, the corresponding wave function cannot be the ground state wave function Ψ_0. From variational principle (Laird *et al.*, 1996), the energy eigenvalue from that Hamiltonian operator should be higher than the GS energy. The energy functional can be written as:

$$E[n] = \langle \Psi[n] | \hat{T} + \hat{U} + \hat{V} | \Psi[n] \rangle \quad (2.11)$$

$$= \langle \Psi[n] | \hat{T} + \hat{U} | \Psi[n] \rangle + \int d^3 r n(\boldsymbol{r}) v(\boldsymbol{r}) \quad (2.12)$$

$\because V[n] = \int v(\boldsymbol{r}) n(\boldsymbol{r}) d^3 r,$ it is solely depends on $v(\boldsymbol{r})$ and non-universal functional.

$$E[n] = T[n] + U[n] + V[n] = F[n] + V[n] \quad (2.13)$$

Where $F[n] = T[n] + U[n]$ (2.14)

$T[n]$ and $U[n]$ are the universal functional. To approximate the density functional for the total internal energy functional $F[n]$. Fermi and Thomas (Fermi, 1927; Lieb, 1991; Thomas, 1927) introduced Fermi-Thomas functional $T_{TF}[n]$ to approximate the total kinetic energy $T[n]$; and the electrostatic energy of classical repulsive gas $J[n]$ for internal potential energy $U[n]$:

$$T \approx T_{TF}[n] = \frac{3}{5}(3\pi^2)^{2/3} \left(\frac{\hbar^2}{2m_e} \right) \int n^{5/3}(\boldsymbol{r}) dr. \quad (2.15)$$

$$U \approx J[n] = \frac{1}{2} \left(\frac{e_c^2}{4\pi\epsilon_0} \right) \iint \frac{n(\boldsymbol{r_1}) n(\boldsymbol{r_2})}{|\boldsymbol{r_1} - \boldsymbol{r_2}|} dr_1 dr_2. \quad (2.16)$$

Re-writing equation (2.13), we get:

$$E[n] = T_{TF}[n] + J[n] + V[n] \quad (2.17)$$

The energy functional of any arbitrary particle density n from equation (2.17) is so called *Thomas-Fermi Model*.

2.3 Kohn-Sham Equation

To refine H-K theorem on DFT, more accurate kinetic energy functional is essential. Kohn and Sham introduced the Kohn-Sham method (Kohn & Sham, 1965) by rewriting many interacting electron system as non-interacting Kohn-Sham particles, it behaves like non-interacting electrons i.e. the internal potential energy $U = 0$. Therefore, the internal electronic energy functional $F[n]$ can be written in terms of non-interacting kinetic energy T_S, the electrostatic energy of repulsive gas $J[n]$ and the exchange-correlation energy $E_{xc}[n]$. From Equation (2.14), we get (Armiento, 2002):

$$F[n] = T_S[n] + J[n] + E_{xc}[n] \tag{2.18}$$

We can now have the Kohn-Sham based ground state energy functional from Thomas-Fermi model, in terms of equation (2.18). We get

$$E_0[n_0] = T_S[n_0] + J[n_0] + E_{xc}[n_0] + V[v, n_0] \tag{2.19}$$

Deploying variational principle, the energy minimum which is functional of electron density can be represented in stationary condition:

$$\frac{\delta T_S[n_0]}{\delta n} + \frac{\delta E_{xc}[n_0]}{\delta n} + \frac{\delta J[n_0]}{\delta n} + \frac{\delta V[v, n_0]}{\delta n} = 0 \tag{2.20}$$

The ground state energy of non-interacting Kohn-Sham particles E_S and the potentials $v_{eff}(r)$ in which the system is influenced, by under variational principle, we get:

$$E_S = T_S[n_0] + V\left[v_{eff}, n_0\right] \tag{2.21}$$

The stationary condition becomes:

$$\frac{\delta T_S[n_0]}{\delta n} + \frac{\delta V\left[v_{eff}, n_0\right]}{\delta n} = 0 \tag{2.22}$$

From equation (2.20) and (2.22), the stationary condition of both interacting particle system and non-interacting K-S particles can be compared by (Armiento & Mattsson, 2003; Capelle, 2006):

$$\frac{\delta V[v_{eff}, n_0]}{\delta n} = \frac{\delta E_{xc}[n_0]}{\delta n} + \frac{\delta J[n_0]}{\delta n} + \frac{\delta V[v, n_0]}{\delta n} \tag{2.23}$$

Evaluating the functional both sides yielded

$$v_{eff}(\boldsymbol{r}) = v_{xc}(\boldsymbol{r}) + \left(\frac{e_c^2}{4\pi\epsilon_0}\right) + \int \frac{n(\boldsymbol{r}')}{|\boldsymbol{r} - \boldsymbol{r}'|} d\boldsymbol{r}' + v(\boldsymbol{r}) \tag{2.24}$$

Where, $v_{xc}(\boldsymbol{r})$ represent the exchange-correlation potential. The relation between the ground state energies of non-interacting particle system and interacting particles can be expressed as:

$$E_0 = E_S - J[n_0] + E_{xc}[n_0] - V_{xc}[v_{xc}, n_0] \tag{2.25}$$

The most informative conclusion that can be drawn from Kohn-Sham theory was that the ground state electron density of fully interacting system is the same with non-interacting particles system if the effective potential $v_{eff}(r)$ is known (March, 1982; Perdew *et al.*, 2003; R, 2005).

The Kohn-Sham orbital equation for non-interacting particles can be solved for one particle Kohn-Sham orbitals $\Phi_i(r)$ and its corresponding energies $\mathcal{E}_i$,

$$-\left(\frac{\hbar^2}{2m}\right)\nabla^2\phi_i(\boldsymbol{r}) + v_{eff}(\boldsymbol{r})\phi_i(r) = \mathcal{E}_i\phi_i(\boldsymbol{r}) \tag{2.26}$$

A single particle wave function depends upon the co-ordinate and the spin function, $\psi_i(\boldsymbol{r}, \sigma) = \phi_i(\boldsymbol{r}) + \chi_i(\sigma)$. The GS wave function of many-non interacting particle system is Slater-determinant (Slater, 1929). The many-particle electron density can be expressed as:

$$n(\boldsymbol{r}) = \sum_i^N |\phi_i(\boldsymbol{r})|^2 \tag{2.27}$$

And the total energy of the system consisting of N number of particles,

$$E_s = \sum_i^N \varepsilon_i \tag{2.28}$$

Equation (2.24) to (2.28) are called the Kohn-Sham equation, the central line for K-S based DFT formalism. From these equations the ground state observables are evaluated with the process named 'self-consistent cycle'. Since the stationary condition can be achieved with correct electron density $n(\boldsymbol{r})$. But, it is impossible to know the correct electron density $n(\boldsymbol{r})$ to start up solving Kohn-Sham equation for stationary conditions. One has to start with a trial electron density, put the trial density in Eqn. (2.24), to get the effective potential. Second, using that output effective potential, solve the Kohn-Sham orbital equation using Eqn. (2.26). For the last step, solve the K-S orbital equation of Eqn. (2.27) to produce new many-particle density. Repeat the process called 'iteration' until it converges or until it reaches the stationary condition through correct electron density. The iteration sequence of K-S based DFT can be summarized below:

$$n_{trial} \xrightarrow{Eqn.(2.24)} v_{eff} \xrightarrow{Eqn.(2.26)} \phi_i \xrightarrow{Eqn.(2.27)} n_{new1}$$

2.4 Exchange-Correlation Energy

From Eqn. (2.18), the exact exchange-correlation energy can be written as;

$$E_{xc}[n] = F[n] - T_S[n] - J[n] = (T[n] - T_S[n]) + (U[n] - J[n]) \tag{2.29}$$

The exchange-correlation energy $E_{xc}[n]$ explicitly counts for the kinetic energy difference between non-interacting and interacting particle system and correction to the electrostatic energy arose from non-classical quantum interactions. The exchange-correlation energy $E_{xc}[n]$ is the integral of exchange-correlation energy per electron, it can be expressed as:

$$E_{xc}[n] = \int n(\boldsymbol{r})\varepsilon_{xc}([n];\boldsymbol{r})d\boldsymbol{r} \tag{2.30}$$

$\mathcal{E}_{xc}([n];\boldsymbol{r})$ indicates the exchange-correlation energy per electron.

The $E_{xc}[n]$ can be separated into its component energy i.e. $E_c([n];\boldsymbol{r})$ and $E_x([n];\boldsymbol{r})$.

$$E_x[n] = \int n(\boldsymbol{r})\mathcal{E}_x([n];\boldsymbol{r})d\boldsymbol{r} \tag{2.31}$$

$$E_c[n] = \int n(\boldsymbol{r})\mathcal{E}_c([n];\boldsymbol{r})d\boldsymbol{r} \tag{2.32}$$

2.4.1 The Exchange Energy:

The expressions for local and conventional exchange energy per particles $\mathcal{E}_x([n];\boldsymbol{r})$ and exchange hole $\hat{n}_x(r,r')$ are shown below, respectively:

$$\widehat{\mathcal{E}}_x([n];\boldsymbol{r}) = \frac{1}{2}\left(\frac{e_c^2}{4\pi\epsilon_0}\right)\int \frac{\hat{n}_x(\boldsymbol{r},\boldsymbol{r}')}{|\boldsymbol{r}-\boldsymbol{r}'|}d\boldsymbol{r}' \tag{2.33}$$

$$\hat{n}_x(\boldsymbol{r},\boldsymbol{r}') = -\frac{1}{2}\frac{|n_1(\boldsymbol{r},\boldsymbol{r}')|^2}{n(\boldsymbol{r})} \tag{2.34}$$

Where, $\hat{n}_1(\boldsymbol{r},\boldsymbol{r}')$ is the first order spin-less density matrix. The exchange hole sum rule is satisfied and revealed the non-positivity constraint as presented as:

$$\int \hat{n}_x(\boldsymbol{r},\boldsymbol{r}')d\boldsymbol{r}' = -1, \quad \therefore \hat{n}_x(\boldsymbol{r},\boldsymbol{r}') \leq 0.$$

Unconventional exchange hole is termed when the total exchange energy can be obtained by any function n_x in Eqn. (2.33) that integrates in Eqn. (2.31).

2.4.2 The Correlation Energy:

The correlation energy per particle is given by (Armiento & Mattsson, 2003):

$$\widehat{\mathcal{E}}_c([n];\boldsymbol{r}) = \frac{1}{2}\left(\frac{e_c^2}{4\pi\epsilon_0}\right)\int \frac{\hat{n}_c(\boldsymbol{r},\boldsymbol{r}')}{|\boldsymbol{r}-\boldsymbol{r}'|}d\boldsymbol{r}' \tag{2.35}$$

$$\hat{n}_c(\boldsymbol{r},\boldsymbol{r}') = \hat{n}_{xc}(\boldsymbol{r},\boldsymbol{r}') - \hat{n}_x(\boldsymbol{r},\boldsymbol{r}') \tag{2.36}$$

The correlation sum rule follows:

$$\int \hat{n}_c\,(\boldsymbol{r},\boldsymbol{r}')d\boldsymbol{r}' = 0$$

That being said, for any function n_c that results the total correlation energy using Eqn. (2.32) and (2.35) is unconventional correlation hole.

2.5 Approximation: functionals for $\mathbf{E_{xc}[n]}$

The complexity and being an unknown variable, the exchange-correlation energy made difficulty in K-S equation for exact solution. One must need to approximate the functional for exchange-correlation energy $E_{xc}[n]$ for many-electrons systems (Capelle & Vignale, 2001; Perdew & Levy, 1985). There are several types of approximation in terms of their locality, namely local functional, semi-local functional, orbital functional and other non-local functional (Capelle, 2006; Capelle & Vignale, 2002).

2.5.1 Local Density Approximation (LDA):

When the exchange-correlation energy per particle $\mathcal{E}_{xc}([n];\boldsymbol{r})$ is depends on the locality of the electron density $n(\boldsymbol{r})$, that is the position or co-ordinates; the exchange-correlation term can be approximate in local density approximation (LDA). Kohn and Sham proposed local density approximation back in 1965 (Kohn & Sham, 1965), it was the first functional for exchange-correlation energy that implemented in DFT framework. Since by then, there are large numbers of development for $\mathcal{E}_{xc}([n];\boldsymbol{r})$ functional still today. The LDA for $E_x[n]$ is given by

$$E_x^{LDA}\big(n(r)\big) = -\frac{3}{4\pi}\left(\frac{9\pi}{4}\right)^{1/3}\left(\frac{e_c^2}{4\pi\epsilon_0 a_0}\right)\frac{1}{r_s} \tag{2.36}$$

The expression of $E_c[n]$ for LDA came up with; high density and weak correlations and low density and strong correlation respectively, as presented below:

$$E_c^{LDA}\big(n(r)\big) = \left(\frac{e_c^2}{4\pi\epsilon_0 a_0}\right)(c_1 lnr_s + c_1 + c_2 r_s lnr_s + c_3 r_s + \cdots), \qquad r_s \ll 1 \tag{2.37}$$

$$E_c^{LDA}\big(n(r)\big) = \left(\frac{e_c^2}{4\pi\epsilon_0 a_0}\right)\left(\frac{d_0}{r_s} + \frac{d_1}{r_s^{3/2}} + \frac{d_2}{r_s^4} + \cdots\right), \qquad r_s \gg 1 \tag{2.38}$$

Within LDA approximation, error cancellation is happened systematically due to the fact that for any density $n(r)$, LDA exchange-correlation hole satisfies their corresponding sum rule. That can be possible only when errors in exchange hole

cancel with it counterpart in correlation hole. LDA overestimates exchange energy while underestimates the correlation energy, approximating a reasonably good exchange energy. In LDA, the inhomogeneous (Electrons interaction with nuclei by means of varying fields) and Coulomb interacting (Electron-electron interaction) many body system is solved into two solutions: solution of homogeneous interacting part results the uniform exchange energy while the solution of inhomogeneous non-interacting produces the particle density. Therefore, we can express the general representation of exchange-correlation term for LDA as:

$$E_{xc}^{LDA}[n] = \int d^3r \mathcal{E}_{xc}^{homo}\big(n(r)\big)$$

Since LDA is the pioneer exchange-correlation functional that implemented in DFT, it is therefore scripted in most of all quantum DFT packages. However, exact $E_{xc}^{LDA}[n]$ account for local density, it is not accurate enough for rapidly varying electron density system.

2.5.2 Generalized Gradient Approximation (GGA):

Local density functional method had not much essential in rapidly varying density i.e. spatially inhomogeneous system. A generalized gradient approximation (GGA) refined the existing method of LDA by introducing not only local density but also gradient of the density (Perdew, Burke, & Ernzerhof, 1996). The general form density gradient based exchange-correlation functional can be written as:

$$E_{xc}^{GGA}[n] = \int d^3r\, f(n(r), \nabla n(r))$$

A GGA is not just meant to be a terminated power expansion valid only for low density gradient $\nabla n(r)$, but rather some expression that aims to give a generally applicable efficient approximation of the exchange-correlation energy per particle for all values of gradients $\nabla n(r)$. The perception of GGA is solely rely through the local value of the density $n(r)$ and the density gradient $\nabla n(r)$. It should be noticeable that there may be situations when this limited view does not distinguish between physically different situations. For instance, certain points in the inter-shell regions of an atom focus the same points as where the electron density decays exponentially. In

such condition, the gradient approximation must employ averaged interpretation of what the values of $n(r)$ and $\nabla n(r)$ mean. Many functional for GGA scheme had been developing since a couple of decades ago; developing and searching for more accurate refinement of GGA functional still ongoing task. In the next line, we list out only most widely used and globally adopted GGA functional that implemented in most of the DFT based quantum simulation packages. A real space cut-off technique had introduced to further improvement and refinement of the slowly varying density in generalized expansion approximation (Perdew, 1985, 1986; Perdew, Burke, & Wang, 1996; Perdew *et al.*, 1992)

2.5.2.1 The GGA of Perdew and Wang (PW91):

PW91 is a non-empirical functional based that introduced the real-space cutoff technique for installing to a numerical GGA (Wang *et al.*, 1990). When the dimensionless gradient $\nabla n(r) \to 0$, i.e. within the scale of slowly varying and high density limits, the PW91 parameterization is opted for to reproduce a second-order gradient extension approximation. PW91 corrects on LDA functional for certain chemical and physical properties of materials. However, PW91 is subservient to LDA for systems such as defective solids, electronic surfaces/thin film, vacancy systems. PW91 failed to describe the correct uniform scaling upon high density limit. It sometime gives contrived jiggle in the exchange-correlation potential for small and large density gradient $\nabla n(r)$.

2.5.2.2 The GGA of Perdew, Burke and Ernzerhof (PBE):

This functional was developed in 1996 (Perdew, Burke, & Ernzerhof, 1996), PBE functional had a form with a non-empirical functional with parameters satisfying specific set of exact constraints search in exchange-correlation functional. PBE provides a better description of linear response limit instead of forging a second-order gradient extension approximation for slowly varying densities. Therefore, contrived jiggle in the exchange-correlation potential is absent in PBE, so it had been suited for pseudopotential. However, there is similarity between PBE and PW91 action for slowly varying densities. PBE failed to validate the non-uniform scaling of E_x in limits where the reduced gradient $\nabla n(r) \to \infty$ a scaling limit that PW91 validated.

2.5.2.3 Revisions of PBE (revPBE or RPBE):

It had been reflected that the PBE exchange functional may be too strict for enforcing the local Lieb–Oxford bound. Zhang *et al.,* proposed general feature of the functional by introducing revPBE (Zhang & Yang, 1998) that switched one of the PBE parameters into an empirical value by fitting to total atomic energies from helium to argon and totally disregard the bound. More or less, there had been further improvement upon PBE for certain properties such as chemisorption energy of atoms and molecules on transition-metal surfaces (Hammer *et al.*, 1999). Furthermore, Hammer *et al.,* reintroduced local Lieb-Oxford bound revised by presenting a further revised revPBE functional (RPBE). However, despite being a revised functional, RPBE and revPBE did not always improve on PBE (Zhang & Yang, 1998): some material properties are in larger deviation or not agreed with experimental results as compared to PBE.

2.6 DFT+U

In order to properly treating the electron-electron interaction in many-electrons DFT energy functional, an additional term Hubbard potential (U) usually added as DFT+U (Dudarev *et al.*, 1998; Liechtenstein *et al.*, 1995). The formalism presented below are going to be based on spin-polarize system. The approximate energy of DFT+U conceivably written as the sum of approximates energy from DFT and energy from Hubbard term:

$$E_{DFT+U} = E_{DFT} + E_U \tag{2.39}$$

E_{DFT} represent approximated energy from DFT and E_U can be expressed as:

$$E_U = \frac{1}{2} \sum_{I\sigma B_1 B_2} U^I \left(\delta_{B_1 B_2} - n^{I\sigma}_{B_1 B_2}\right) n^{I\sigma}_{B_2 B_1} \tag{2.40}$$

Where I is the atomic site index, $B_1$and B_2 are the magnetic quantum numbers associated with a specific angular momentum and U^I is the effective on-site Hubbard

parameters. In the Hubbard manifold scheme, the atomic occupation matrices $n^{I\sigma}_{B_1B_2}$ are based on the projection of the Kohn-Sham states wave function $u^{\sigma}_{v,\boldsymbol{k}}(\boldsymbol{r})$:

$$n^{I\sigma}_{B_1B_2} = \frac{1}{N_{\boldsymbol{k}}}\sum_{\boldsymbol{k}}^{N_{\boldsymbol{k}}}\sum_{j} O^{\sigma}_{j,\boldsymbol{k}}\langle u^{\sigma}_{j,\boldsymbol{k}}|\hat{P}^{I}_{B_2B_1\boldsymbol{k}}|u^{\sigma}_{j,\boldsymbol{k}}\rangle \qquad (2.41)$$

k the sampled points in the Brillouin zone, $O^{\sigma}_{j,\boldsymbol{k}}$ the occupations of KS states j and σ indicate the band and spin notation in KS wave function. Whereas, the projector on the Hubbard manifold;

$$\hat{P}^{I}_{B_2B_1\boldsymbol{k}} = |\odot^{I}_{B_2\boldsymbol{k}}\rangle\langle\odot^{I}_{B_1\boldsymbol{k}}| \qquad (2.42)$$

Where, $\odot^{I}_{B_2(B_1)\boldsymbol{k}}$ represent the localized orbitals of I^{th} atom at position R_I.

2.7 DFT based Simulation packages

In this sub-section, we briefly discuss about the background of DFT based simulation packages or codes that are being deployed throughout all the DFT calculation in this thesis.

2.7.1 Quantum Espresso

Quantum Espresso (Giannozzi *et al.*, 2009)is globally adopted and a well-known open source code that integrated suite of simulation program written for electronic-structure calculation and modeling for materials. It was developing based on DFT, using a plane wave basis set and the atomic core can be describe by different choice of pseudopotentials (PPs) such as norm-conserving pseudopotentials (NC-PPs) (Hamann *et al.*, 1979), ultrasoft-pseudopotentials (US-PPs) (Vanderbilt, 1990) or projector augmented wave (PAW) (Blöchl, 1994). It had been subjected to work well in the framework of different exchange-correlation functionals; local density approximation (LDA), generalized gradient approximation (GGA), on-site Hubbard potential (U) can be included to extend functional for correct treatment of electron-electron interaction and some meta-GGA and hybrid functionals. The detail description of workflow,

implementation of algorithm and numerical method can be found somewhere in literature (Giannozzi *et al.*, 2017) by the code developer group.

2.7.2 MedeA(VASP)

MedeA Software is a proprietary electronic structure simulation package based on DFT, which is own and developed by Material Design. It was build and developed as graphical user interface (GUI) within a plane wave method based Vienna Atomistic Simulation Package (VASP) (Kresse & Furthmüller, 1996). The distinguished between source code VASP and MedeA is the latter output is given via GUI which make it ease of use.

2.7.3 QuantumATK Q-2019.12

QuantumATK Q-2019.12 (Smidstrup *et al.*, 2019) is a powerful code for atomic scale, nanoscale modeling, electronic structure calculation, etc. within the framework of density functional theory (DFT) with various method for atomic core treatment such as semi-empirical, classical force field potential, numerical linear combination of atomic orbitals (LCAO) and plane wave method. For a close or periodic system the density matrix is solved by diagonalizing the Kohn-Sham Hamiltonian using Davidson scheme while for an open system it is solved using non-equilibrium Green's functions (NEGFs).

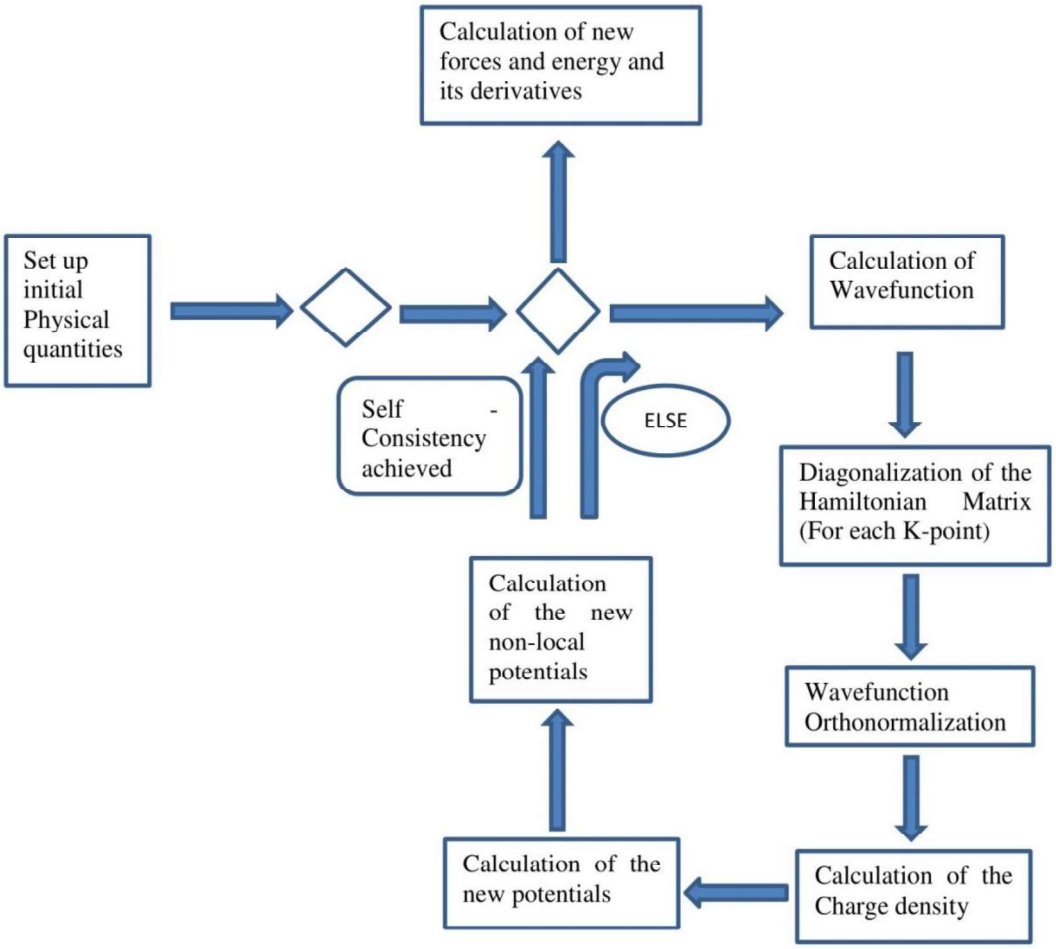

Figure 2.1: General flow chart for self-consistent cycle in density functional theory based simulation.

2.8 Ab-initio Pseudopotential Method

The many-electron Schrödinger equation can be significantly simplified when the electrons systems are grouped into two groups: valence-electrons and inner nucleus-electrons. The electrons in the inner region are tightly bound and do not play a reasonable character in the chemical bonding of atoms; they also fragmentarily shield the core region; creating a half-rigid like core with the core. The chemical nature of bonding is almost completely due to the valence electrons, especially in metals and semiconductors. This segregation suggests that inner nucleus-electrons can

be ignored in a large number of electron system cases, henceforth reducing the atom into an ionic core that interacts with the valence electrons. The implementation of an effective interaction that estimated the potential experienced by the valence electrons is so call the pseudopotential.

The widely adopted two types of approaches had been implemented and developed in ab initio calculations: the all-electron (full-potential) approach and the pseudopotential (valence-electrons) approach. The eigenvalues/ eigenstates and wave functions of all the electrons in the system (including core electrons) are treated in the all-electron (full potential) approximation, it is very much possible to have been estimating an impressive results for the equilibrium (zero-temperature) equation of state for condensed materials of solids within the framework of the density-functional theory (DFT) formalism. The well-known methods employed in the all-electron (full potential) approach are the Green's-function method [Korringa-Kohn-Rostoker (KKR)] (Kohn & Rostoker, 1954; Korringa, 1947), the augmented-plane-wave method (APW) (Loucks & Slater, 1967), and the linear muffin-tin orbital method (LMTO) (Andersen, 1975), which were designed to have shape constraints. Where the charges density have been constraint spherically within these methods, work-well for approximation for the study of the equilibrium equations of state and its derivatives of closed-packed solids. However, for to study the general ground state structural and physical properties in which tributary of the charge density on the angular is a crucial factor for the establishment of small total energy differences between rather different structures, the relevancy of the spherical averaging approach is insubstantial. Unlike all-electron method, the linear combination of atomic orbitals method (LCAO) (Hess, 1972) has no shape constraints, but often the bounded basis set adopted is insufficient to reveal accurate structure balancing. Even for non-shape constraints in the plane-wave method (PW), the strong oscillation of the wave functions in the core region make its operation in the all-electron (full-potential) approximation is close to impractical. This most likely would indispensable too large basis set to be practically implemented

The two applicable and efficient techniques to improve the aforementioned methods for to study of the various ground state physical properties. First, to eliminate

the spherical averaging charge density constraints in full-potential methods which are restricted by their utilization. This problem is complicated and demanding, even though experts attempts (Janak & Williams, 1981) had been made in this regard; unfortunately no fruitful result have been made. Secondly, to reconstruct the all-electron Schrodinger equations into an effective equations more appropriate for the implementation of the methods containing no spherical constraints like the plane wave (PW) method, the linear combination of atomic orbitals method (LCAO) method, or the mixed-basis method (Louie *et al.*, 1979) using both PW and LCAO basis functions. In general, it is convenient to deploy an effective ab initio pseudopotential to reproduce the interaction between the valence electrons and the cores (nuclei plus core electrons) such that core wave functions have to be exclude explicitly and the valence wave functions no more extending to have strong oscillations in the core region. This pseudopotential approach has its fundamental in the well-known certitude that the valence electrons play the governing role in chemical bonding and has as its aim the precise simulation of the all-electron approach. The conclusive success of this approach can be partially due to the pronouncement that the valence and core states are thoroughly separated in energy as well as in real space for many elements (Yin & Cohen, 1982).

The norm-conserving ultrasoft-pseudopotential basis sets opted for our calculation can be graphically represent as shown below in Figure 2.2. Unfortunately, to the best of our knowledge, we do not come across the graphical representation of the basis sets for projector augmented wave method.

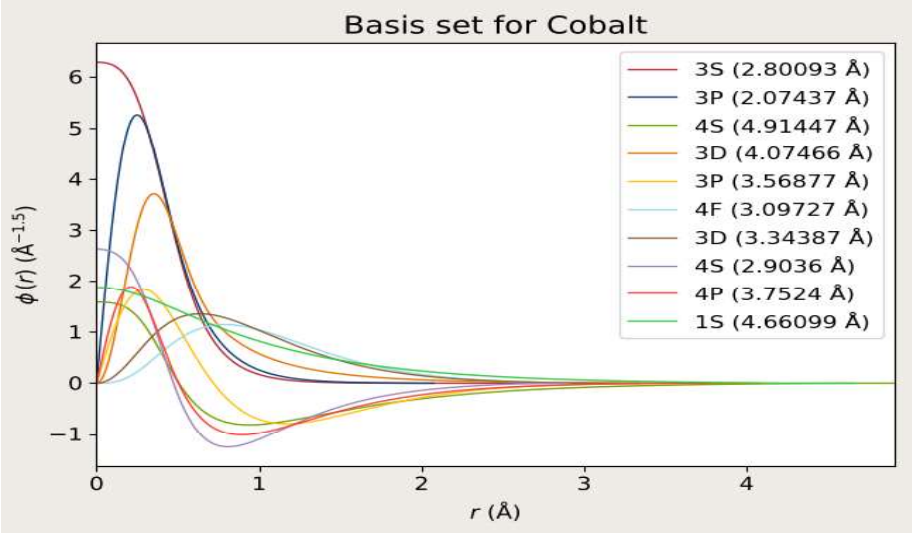
Basis set for Cobalt
3S (2.80093 Å)
3P (2.07437 Å)
4S (4.91447 Å)
3D (4.07466 Å)
3P (3.56877 Å)
4F (3.09727 Å)
3D (3.34387 Å)
4S (2.9036 Å)
4P (3.7524 Å)
1S (4.66099 Å)
$\phi(r)$ (Å$^{-1.5}$)
r (Å)

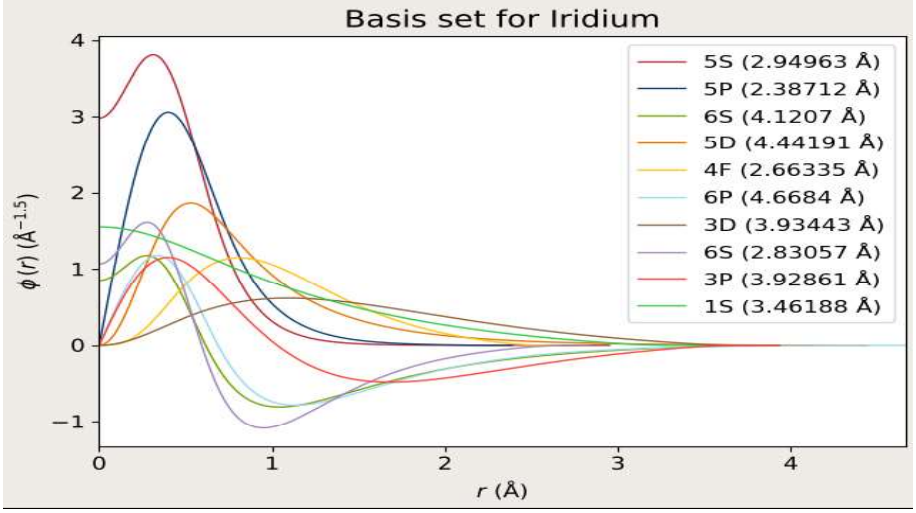
Basis set for Iridium
5S (2.94963 Å)
5P (2.38712 Å)
6S (4.1207 Å)
5D (4.44191 Å)
4F (2.66335 Å)
6P (4.6684 Å)
3D (3.93443 Å)
6S (2.83057 Å)
3P (3.92861 Å)
1S (3.46188 Å)
$\phi(r)$ (Å$^{-1.5}$)
r (Å)

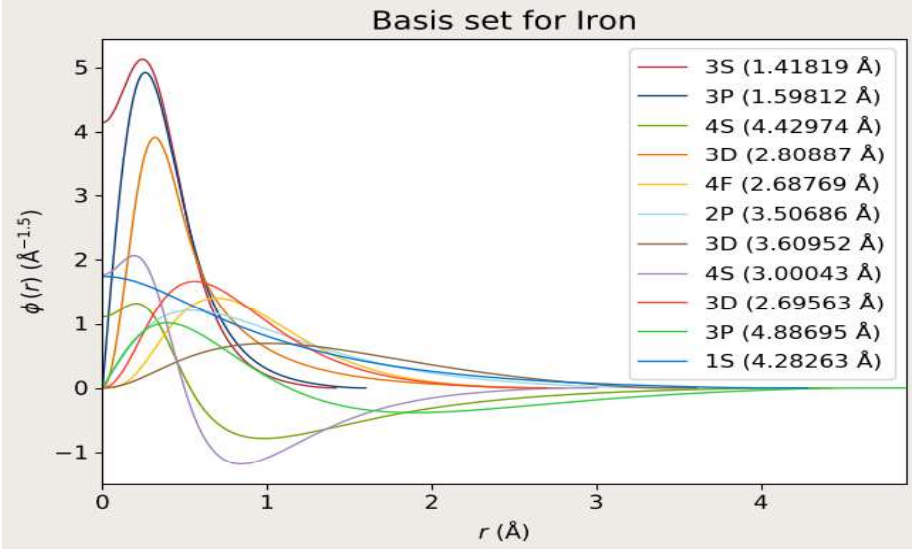
Basis set for Iron
3S (1.41819 Å)
3P (1.59812 Å)
4S (4.42974 Å)
3D (2.80887 Å)
4F (2.68769 Å)
2P (3.50686 Å)
3D (3.60952 Å)
4S (3.00043 Å)
3D (2.69563 Å)
3P (4.88695 Å)
1S (4.28263 Å)
$\phi(r)$ (Å$^{-1.5}$)
r (Å)

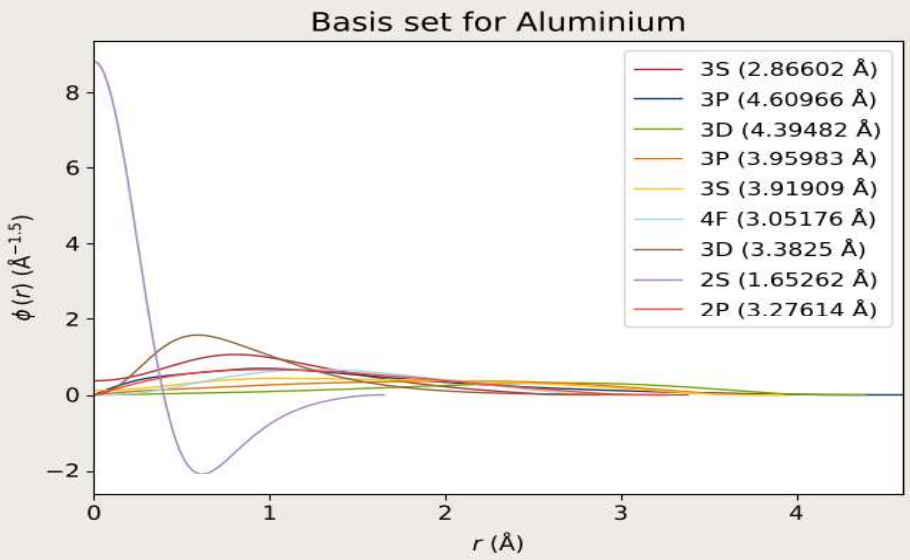
Basis set for Aluminium
3S (2.86602 Å)
3P (4.60966 Å)
3D (4.39482 Å)
3P (3.95983 Å)
3S (3.91909 Å)
4F (3.05176 Å)
3D (3.3825 Å)
2S (1.65262 Å)
2P (3.27614 Å)
$\phi(r)$ (Å$^{-1.5}$)
r (Å)

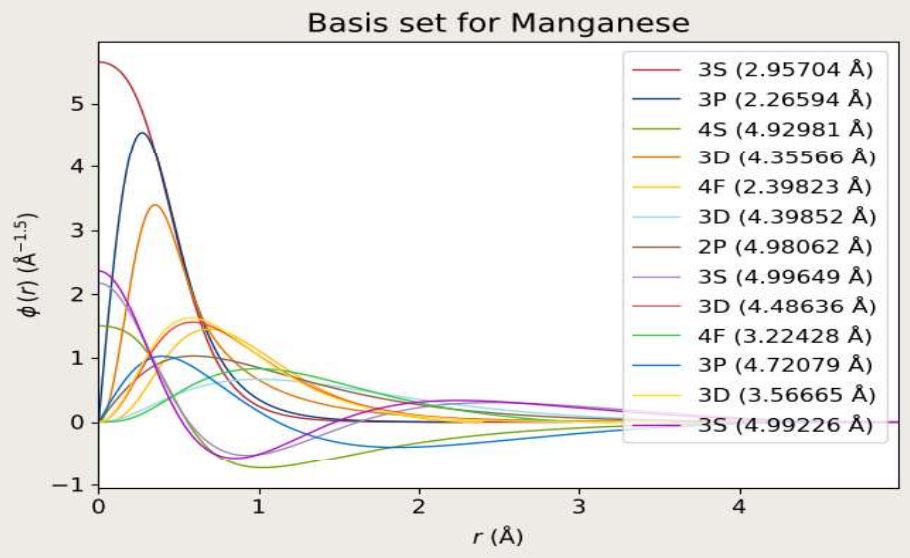
Basis set for Manganese
3S (2.95704 Å)
3P (2.26594 Å)
4S (4.92981 Å)
3D (4.35566 Å)
4F (2.39823 Å)
3D (4.39852 Å)
2P (4.98062 Å)
3S (4.99649 Å)
3D (4.48636 Å)
4F (3.22428 Å)
3P (4.72079 Å)
3D (3.56665 Å)
3S (4.99226 Å)
$\phi(r)$ (Å$^{-1.5}$)
r (Å)

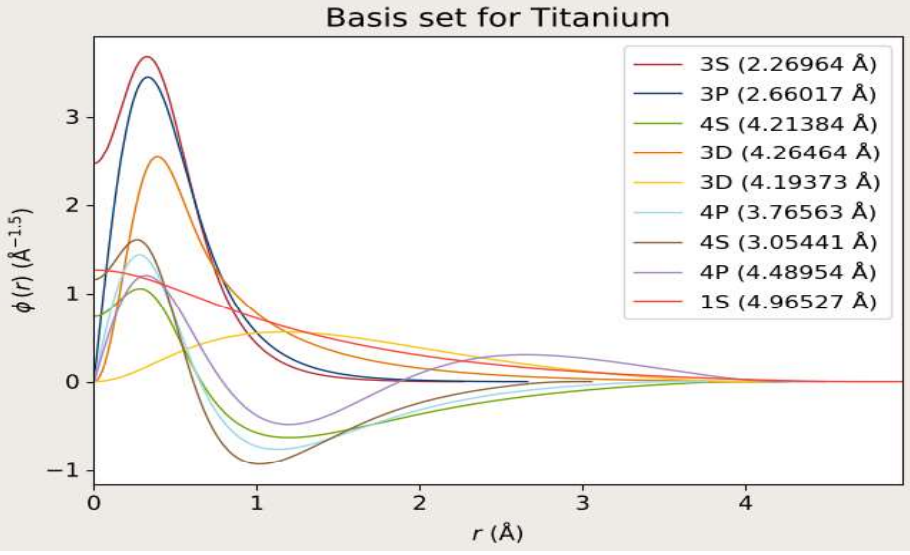
Basis set for Titanium
3S (2.26964 Å)
3P (2.66017 Å)
4S (4.21384 Å)
3D (4.26464 Å)
3D (4.19373 Å)
4P (3.76563 Å)
4S (3.05441 Å)
4P (4.48954 Å)
1S (4.96527 Å)
$\phi(r)$ (Å$^{-1.5}$)
r (Å)

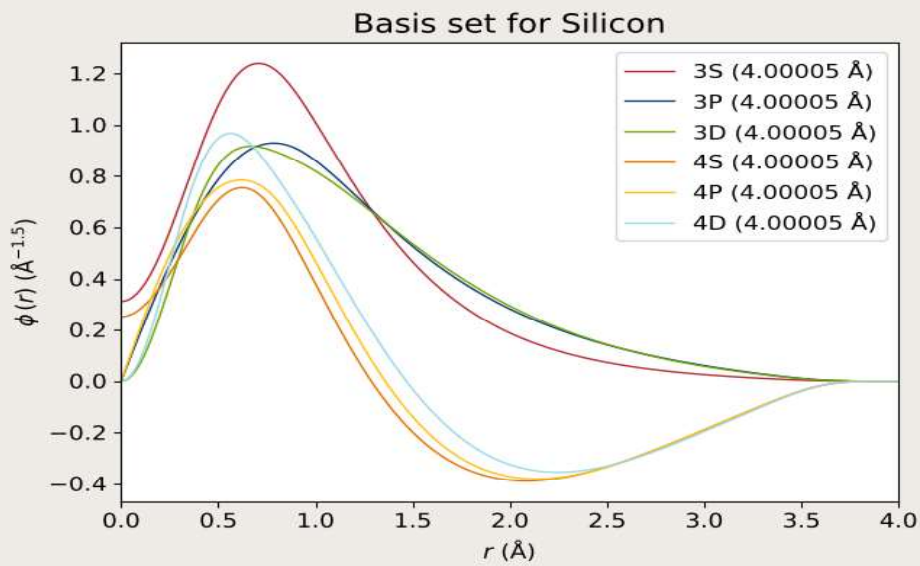

Figure 2.2: The graphical representation of norm-conserving ultrasoft pseudopotential as implemented in Quantum ATK Q-2019.12

3

Structural, Electronics, Magnetic, Mechanical and Thermodynamical stability of bulk X_2YZ type full-Heusler compounds.

In this chapter, we present the first principle (ab-initio) DFT calculation of the structural, electronic, magnetic, mechanical properties and thermodynamic stability of bulk X_2YZ type full Heusler compounds will be discussed. Since regular or direct type full Heusler had been more explored theoretically and experimentally, we are a bit focussing on the inverse type full Heusler compounds. We rigorously studied the aforementioned physical properties of Fe_2IrSi, Ti_2MnSi, Ti_2CoSi, Mn_2CoSi; appropriate comparison of our work with available theoretical literature and experimental report also presented. For Fe_2CoAl, we presented pressure dependence half metallicity by adopting all the ground state properties from our previous work.

3.1 Fe_2IrSi

To study the physical properties of inverse full-Heusler Fe_2IrSi, we performed first-principles density functional theory (DFT) (Hohenberg & Kohn, 1964; Kohn & Sham, 1965) calculations using the generalized gradient approximation (GGA) exchange–correlation functional of Perdew–Burke–Ernzerhof (PBE) (Perdew *et al.*, 1996) and screened Coulomb interactions (DFT+U) from the Dudarev approach (Dudarev *et al.*, 1998). The effective Coulomb potential is $U_{eff} = U_{Fe/Ir} - J_{Fe/Ir}$. The effective interactions on the spin and orbital polarized Ir d orbital are treated as a free parameter and U_{Ir} varies from 0 to 3.0 eV. However, J_{Ir} is not available in the literature so $J_{Ir} = 0$ eV is considered. We also varied $U_{Fe} = 3.0 - 5.0$ and adopted $J_{Fe} = 0.50$ eV for the exchange coupling parameter as J_{3d} varies from 0.36 to 6.0 eV (Şaşıoğlu *et al.*, 2013; Zipporah *et al.*, 2017). The result of electronic structures has a negligible impact within $U_{Fe} = 3.0 - 5.0$ eV and $U_{Ir} = 1.0$ eV. Therefore, we have estimated the interaction parameter $U_{Fe} = 3.52$ eV on Fe-d electrons and $U_{Ir} \approx 1.0$ eV on Ir-d electrons. Interestingly, this value of $U = 3.52$ eV for Fe in Fe_2IrSi is close to

U_{Fe} = 3.8 eV in Co_2FeAl (D. Rai *et al.*, 2012) and 3.1 - 3.83 eV for other 3d-electrons (Şaşıoğlu *et al.*, 2013). In our calculations, we used the Quantum Espresso electronic structure suite (Giannozzi *et al.*, 2009). The electronic structure is obtained using a plane-wave basis set formalism with a cutoff energy of 100 Rydberg and 16×16×16 k-points were used to sample the Brillouin zone.

3.1.1 Results and Discussions

3.1.1.1 Structural

The ground state crystal structure of full-Heusler Fe_2IrSi i.e., whether Fe_2IrSi prefers $L2_1$ or XA symmetry [Figure 3.1(a)&(b)]. The experimental work of Krishnamurthy et al. studied the $L2_1$ crystal structure of Fe_2IrSi (Krishnamurthy *et al.*, 2003). Consider a full-Heusler alloy with the chemical formula X_2YZ. In the regular, full-Heusler system, the electronegativity of the X atom is greater than that of the Y atom and vice versa for the inverse full-Heusler alloy. From this chemistry point of view, we expect Fe_2IrSi to be an inverse alloy because the Fe atom is less electronegative than the Ir atom. For full structural optimization of the lattice parameters, the energy and charge convergence criteria were set to 10^{-3} eV and 0.0001e, respectively. The Hellmann–Feynman forces experienced by all atoms in the cell are lower than 10^{-3} $eV/Å^{-1}$. The initial structures (both for $L2_1$ and XA) were constructed using the experimental lattice constant a = 4.99 Å (Krishnamurthy *et al.*, 2003). The most energetically stable structure is the one with the lowest ground state energy. We consider ferromagnetic (FM) and antiferromagnetic (AFM) configurations, respectively. The equilibrium lattice constant of each magnetic configuration is obtained by computing the total energy at the various lattice constants around the experimental lattice constants. We fit the calculated total energy (per unit cell)–lattice constant profile to the Murnaghan equation of state for both the $L2_1$ and XA structures. The obtained data are presented in Figure 3.1(c). The calculated total energy difference $\Delta E = E_T^{NM} - E_T^{FM/AFM}$ and the corresponding magnetic moment for each atomic species are presented in Table 3.1, where NM denotes the nonmagnetic state. From the energetic analysis, the XA phase with the FM configuration has the lowest ground state energy. This is due to the involvement of transition metal atoms

in Heusler with larger numbers of valence electrons and their interatomic distance. As it is well-known from the Bethe–Slater curve (Cardias *et al.*, 2017; Slater, 1930) when the late transition metal atoms like Fe, Co etc., are at a certain interatomic distance the overlap of the wave functions is such that the ferromagnetic coupling is favored. In order to get antiferromagnetic coupling they should be much closer. In Fe_2IrSi the interatomic distance is comparable to Fe-bulk and thus ferromagnetism is favored. Also, magnetism of Fe dominates that of Ir giving rise to an itinerant-electron ferromagnet like behavior. Thus the exchange interaction *J* increases with the number of conduction electrons, in fact the latter produce *J* via the Zener and de Gennes ferromagnetism mechanism (de Gennes, 1960; Kübler *et al.*, 2007; Zener, 1951) this favors ferromagnetism and dominates all other possible mechanisms. We predict the lattice constant to be ~ 5.84 Å. We note that the predicted lattice parameter is closer to structurally similar Fe-based Heusler compounds with a lattice constant of $\geq 5.80 \pm 0.61$ Å (Endo *et al.*, 1995; Gasi *et al.*, 2013; Khovaylo *et al.*, 2017)

3.1.1.2 Electronic and magnetic properties

The calculated electronic properties of inverse full-Heusler Fe_2IrSi employing various approximations. The electronic structure is studied using the Quantum Espresso electronic structure codes (Giannozzi *et al.*, 2009). We determine the degree of the spin polarization at the Fermi energy E_F as

$$P = [N_{\uparrow}(E_F) - N_{\downarrow}(E_F)] / [N_{\uparrow}(E_F) + N_{\downarrow}(E_F)] \quad (3.1)$$

where $N_{\uparrow}(E_F)$ and $N_{\downarrow}(E_F)$ are the number of density of states at E_F for spin-up and spin-down channels, respectively.

Employing the GGA functional, we predict a metallic solution in both channels [Figure 3: (a) and (c)] with ~ 45% spin polarization. The dispersive band around E_F in the spin-down channel is due to the Fe_2-*d* (↓) (*d-eg* + *d-t2g*) and the Fe1-*d* dominates that of the spin-up channel. The Fe1-*d* band lies at higher energy in both occupied and unoccupied states as compared with the Fe2-*d* bands, which fail to give the signature *d-d* hybridization between Fe1-*d* and Fe2-*d* orbitals as in the case of other half-metallic Heusler compounds (Felser *et al.*, 2015; Galanakis *et al.*, 2014; Kandpal *et al.*, 2006; Liechtenstein *et al.*, 1987; Wurmehl *et al.*, 2006)

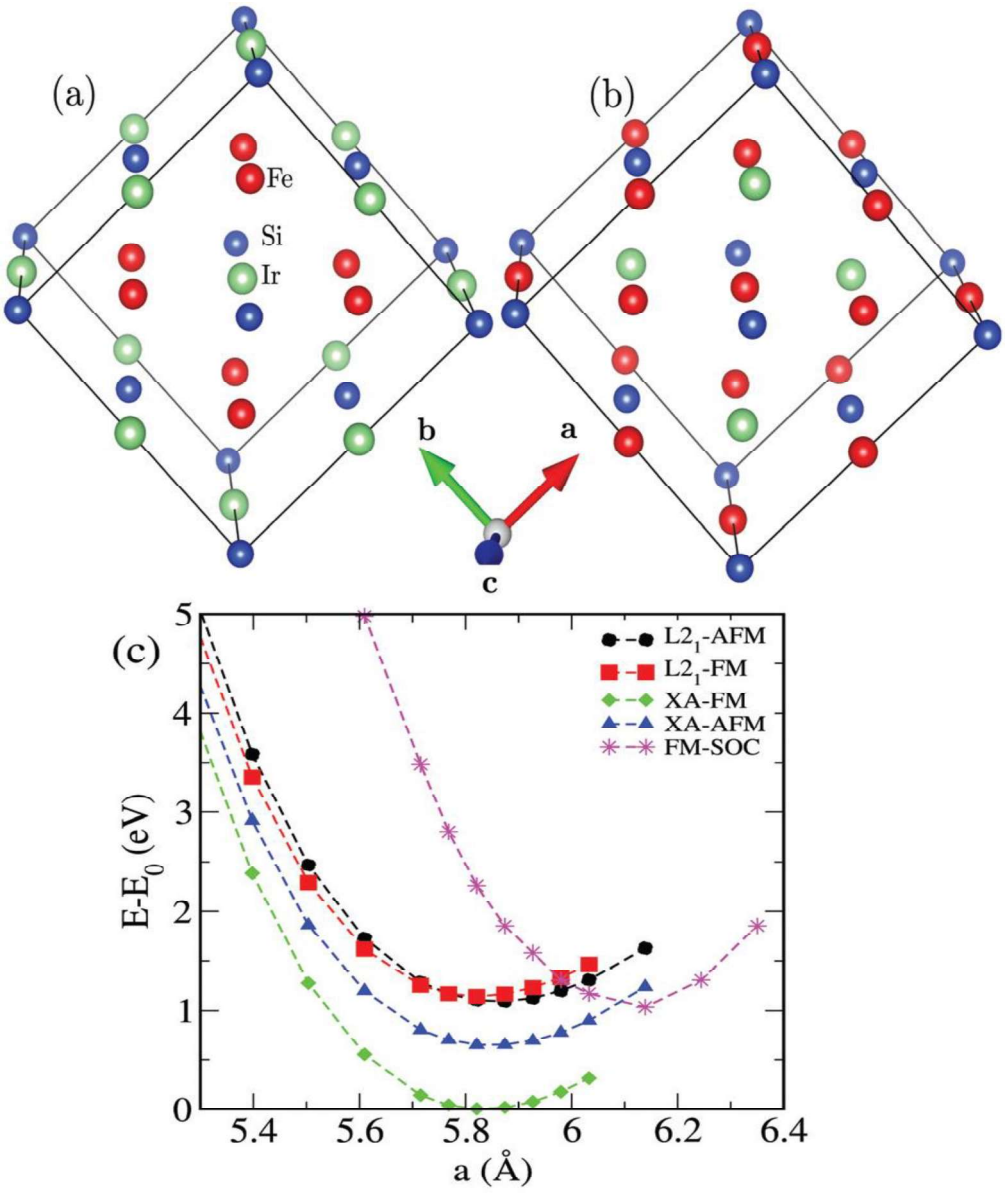

Figure 3.1: The crystal structure of regular (a) and inverse (b) full-Heusler Fe_2IrSi. (c) Relative energy (E-E_0) per unit cell versus lattice constant profile of the various magnetic configurations calculated

Table 3.1: Magnetic moment of each atom in the XA and $L2_1$ structures, and the total energy (E_T) for the various magnetic configurations (MG) in full- Heusler Fe_2IrSi obtained with DFT. E_T is with respect to the nonmagnetic (NM) ground state, i.e., $\Delta E = E_T^{NM} - E_T^{FM/AFM}$

MG	Fe1	Fe2	Ir	Si	Δ*E* (eV)
XA Phase					
FM	1.89	2.88	0.30	-0.03	1.60
AFM	-2.47	2.08	-0.20	-0.07	0.91
$L2_1$ Phase					
FM	2.01	2.01	0.62	-0.07	0.89
AFM	-2.29	-2.29	0.0	0.0	0.98

This may be as a result of the insufficient treatment of electronic excitations, especially the highly polarizing Fe-d orbitals within the GGA approximation. To account for the electron–electron correlation effects, we employ the GGA+U functional [Figure 3.2; (b) and (d)]. Accounting for the electron–electron interactions, we predict a semiconducting behavior in the spin-down channel with an energy band gap of ~ 0.78 eV. Interestingly, the variation of U_{Ir} parameter has an insignificant impact on the electronic band structures. This is not surprising since the large extensions of the Ir-d orbital support decreased itinerancy of the d electrons associated with the Ir atom. Hence, electron–electron correlation effects emanate mainly from the strongly polarizing Fe-*d* states. The origin of the energy bandgap in the spin-down channel is due to *d*–*d* hybridization, which results in the dominance of the doubly degenerated eu and the triple t_{2u} orbitals that lie above the E_F (Galanakis *et al.*, 2014). The predicted semiconducting half-metallic behavior within our GGA+U calculations in inverse full-Heusler Fe_2IrSi has a characteristic spin polarization of ~ 99.8% at the E_F. We have also used spin-orbit coupling (SOC) along with GGA and GGA+U (U_{Ir} = 1.0 eV and U_{Fe} = 3.52 eV). The results of the density of states obtained from GGA + SOC and GGA+U + SOC is presented in Figure 3.3 [(a) and (b)], respectively. With

the implementation of SOC the half metallicity is lost and the system behaves like a magnetic metal. More bands are crossing the Fermi level with the majority of contributions from the Fe1-*d*, Fe2-*d* and Ir-*d* orbitals in the spin down channel.

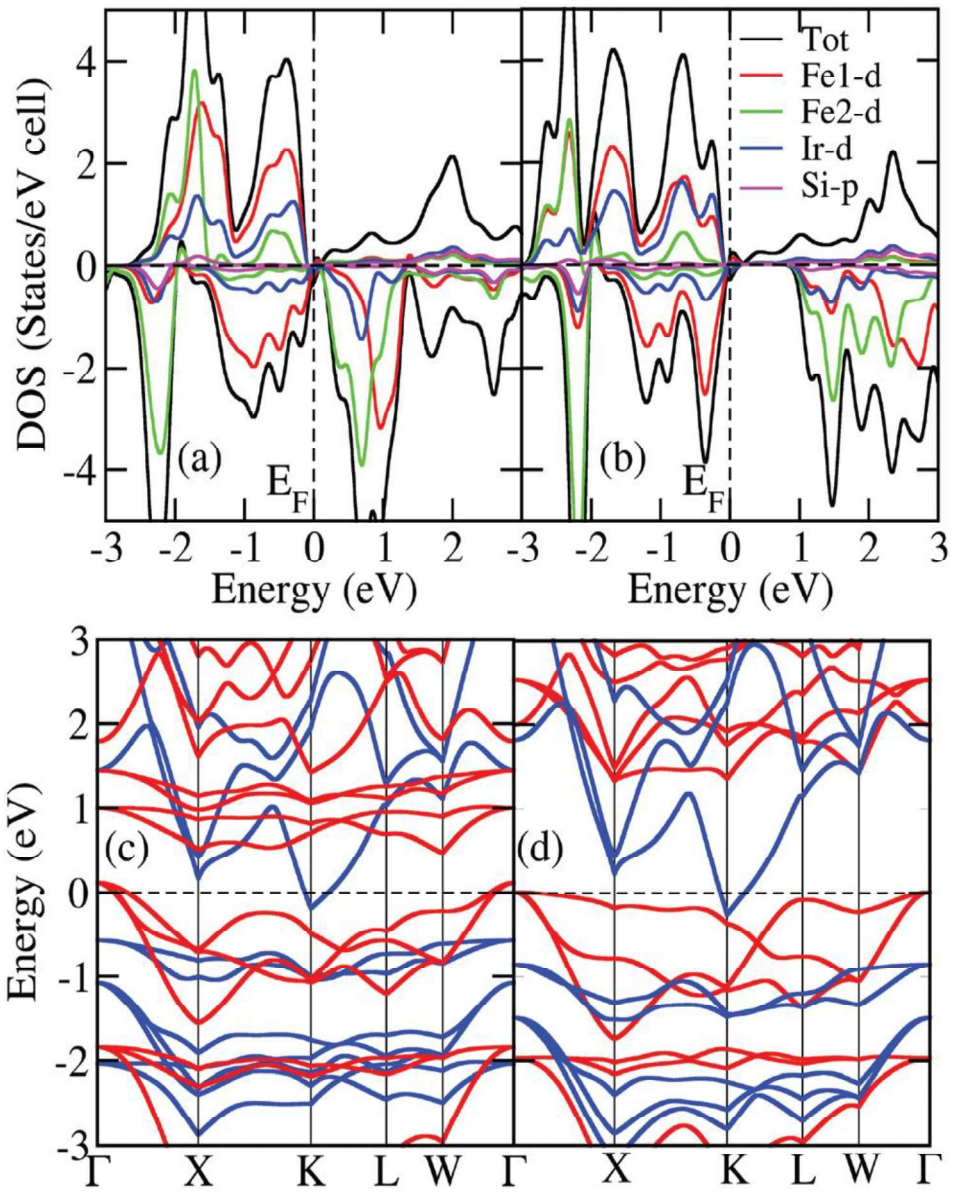

Figure 3.2: Calculated total and partial density of states [(a) and (b)] and band structure along the high symmetry points of the Brillouin zone [(c) and (d)] of inverse full-Heusler Fe_2IrSi with GGA (left panel) and GGA+U (right panel). The horizontal dashed-line in [(c) and (d)] depicts the Fermi energy E_F, which has been set to zero at the top of the valence band. The blue and red curves in (c and d) correspond to the up and down spin channels, respectively.

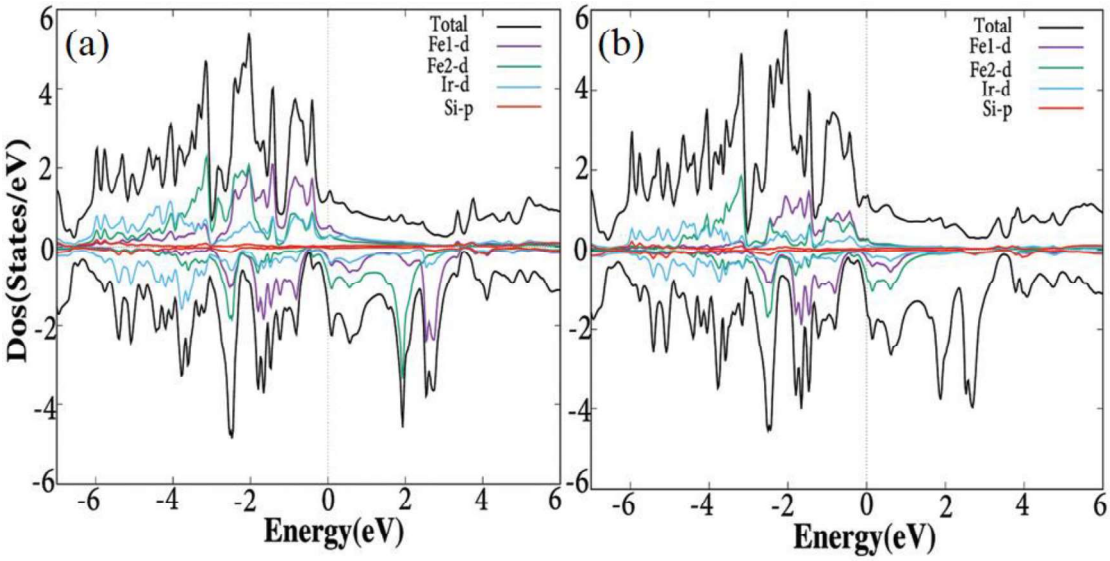

Figure 3.3: Calculated total and partial density of states: (a) SOC (b) SOC+U (U_{Ir} = 1.0 eV and U_{Fe} = 3.52 eV).

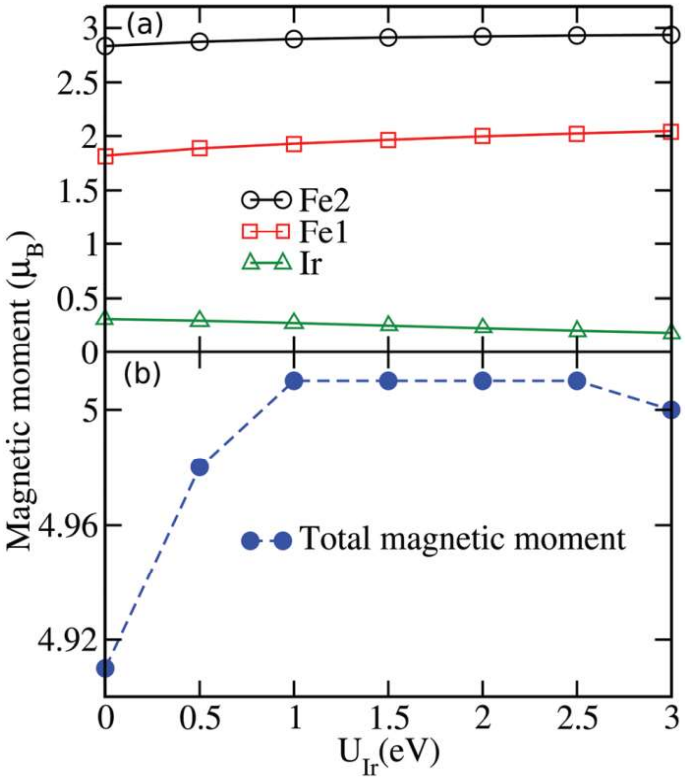

Figure 3.4: Variation of the partial and total magnetic moment obtained using GGA+U (U_{Fe} = 3.52 eV, U_{Ir} = 0.0 eV to 3.0 eV) for the XA phase of full-Heulser Fe_2IrSi.

The magnetic properties of Heusler compound depend mainly on the total number of valence electrons per unit cell (Felser *et al.*, 2015; Kandpal *et al.*, 2006; Liechtenstein *et al.*, 1987; Slater, 1930) as determined by the Slater Pauling (SP) rule (Pauling, 1938; Skaftouros *et al.*, 2013; Slater, 1936). The predicted total magnetic moment of the studied Heusler alloy follows the SP rule (Skaftouros *et al.*, 2013); $M_t = (Z_t - 24)$ μ_B, where Mt is the total magnetic moment and Z_t is the total valence electrons. Since, Fe_2IrSi has 29 valence electrons, the corresponding total magnetic moment (M_t) is expected to be an integer number of 5.0 μ_B according to the SP rule. In the *L2₁* phase, we observe ~ 0.62 μ_B for the Ir atom in the FM configuration and it is practically zero in the AFM configuration (see Table 3.1). In the *XA* structure, our simulation reveals that the Ir atom is ferromagnetically and antiferromagnetically coupled to the Fe atoms with an average magnetic moment of ~ |0.25| μ_B in the FM and AFM states, respectively. The Si atom acquired a small but finite average magnetic moment, which depends weakly on U and antiferromagnetic coupling. As evident from Figure 3.4 and Table 2, Fe1 and Fe2 have strikingly different magnetic moments; this is due to the different local coordination of their neighboring atoms. From the analysis of the magnetic coupling, we have gained a better understanding of the origin of the induced magnetic moment at the Ir-site. The ferromagnetic interatomic exchange interactions between the eight nearest neighbor 3d electrons of the Fe atom and the Ir-5d states are the main source of the induced magnetic moment on the Ir-site. This observation is supported by the significant contribution of the 5d states to the density of states at the E_F. Our calculated GGA value, Mt = 4.91 μ_B, is within the numerical uncertainty of the expected value of 5.0 μ_B. The variation of the atomic moment obtained with the GGA and GGA+U is presented in Figure 3.4(a). Observe that the magnetic moment of Fe1 and Fe2-atoms follows the same increasing trend as U_{Ir} value is increased, while that of Ir-atoms decreased slightly. The total magnetic moment as a function of U is presented in Figure 3.4(b). If we include electron– electron interactions, the total magnetic moment increased to ~ 5.01 μ_B and is almost independent of U_{Ir} > 0.80 eV, in good agreement with the SP-rule.

To gain further insights into the magnetic properties, we compute the strength of the magnetic interaction based on the Heisenberg model (Liechtenstein *et al.*, 1987)

using the SPR-KKR code. The Hamiltonian of the extended Heisenberg model for a spin system is given by equation (3.1),

$$H = -\sum_{ij} e_i e_j J_{ij} \qquad (3.2)$$

here J_{ij} is the isotropic exchange-coupling related to unit vectors e_i and e_j pointing along the direction of the magnetic moment on the sites *i* and *j*, respectively. Using SPR-KKR code we have computed the strength of the magnetic interaction J_{ij} by mapping the full system within a Heisenberg Hamiltonian model. The interaction between the atoms at *i* and *j* sites (pair exchange interaction parameter) as a function of distance is given by

$$J_{ij} = \frac{1}{4\pi}\int^{E_F} d(E) Tr_L\{\Delta_i T_{\uparrow}^{ij} \Delta_j T_{\downarrow}^{ji}\} \qquad (3.3)$$

where $\Delta_{i/j} = t_{ij\uparrow}^{-1} - t_{ij\downarrow}^{-1}, t_{\uparrow\downarrow}^{-1}$ is the atomic *t*-matrix of the magnetic impurities at site i for the spin up/down state $T_{\uparrow\downarrow}^{ij}$, is the scattering path operator between *ij* sites for the spin up/down state, and Tr_L is the trace over the orbital variables of the scattering matrices. The site *i* is assumed to be at the center of a cluster of radius R^C = max $|R_i - R_j|$. J_{ij} is then calculated with respect to the atom at i defined by a cluster of radius Rc. We choose Fe2 as the center atom and use $R^C \approx 4.5$ Å. Other choices of $R^C \geq 2.5$ Å have negligible effect on J_{ij}. The calculated J_{ij} as a function of distance is presented in Figure 3.5 [(a) and (b)]. Beyond 2 Å, J_{ij} is almost constant for all the atoms. We also present in Figure 3.5(c) the calculated J_{ij} as a function of U_{Ir}; the variation in J_{ij} with U_{Ir} is rather small. With J_{ij} obtained, we calculate the T_C^{MFA} within a mean-field approximation (MFA)

$$\frac{3}{2} K_B T_C^{MFA} \langle e^{\mu} \rangle = \sum_{v} J_0^{\mu,v} \langle e^{v} \rangle \qquad (3.4)$$

where $\langle e^{v} \rangle$ is the average *z* component of the unit vector e_r^v pointing in the direction of the spin moment and K_B is the Boltzmann constant. The Curie temperature (T_C) can be obtained from the largest Eigenvalue matrix of $J_0^{\mu,v}$ (Anderson, 1963; Şaşıoğlu *et al.*, 2013). The variation of calculated T_C with respect to U_{Ir} is presented in Figure 3.5 [(d)]. We observe a linear increase of T_C as the exchange interaction J_{ij} increases as

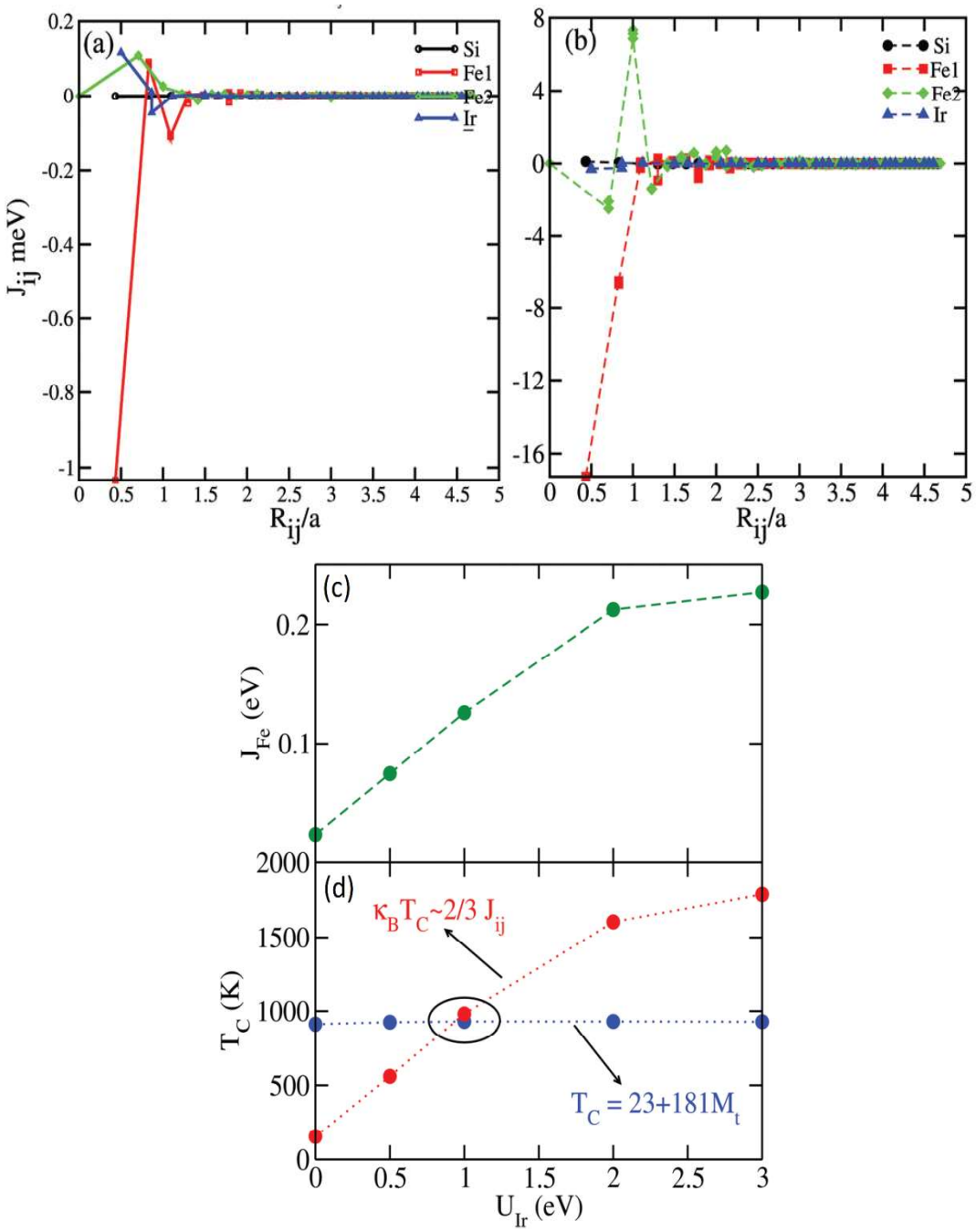

Figure 3.5: Calculated exchange coupling parameter J_{ij} as a function of distance the R using GGA+U (U_{Fe} = 3.52 eV) for (a) U_{Ir} = 0.0 eV and (b) U_{Ir} = 1.0 eV and Calculated (c) exchange-coupling parameter $J_{Fe} = \sum_i J_{Fe,i}$ for the Fe atom and (d) Curie temperature T_C within the mean-field approximation as a function of U_{Ir} with the GGA+U (U_{Fe} = 3.52 eV). Also plotted in figure (b) is the approximate relation T_C = 23 + 181M_t proposed by Wurmehl et al. (Wurmehl *et al.*, 2006)

denoted by the red dotted line in Figure 3.5(d). At $U_{Ir} \approx 1$ eV, the T_C approaches a linear trend $T_C^{cal} = 23 + 181M_t$ [Figure 3.5(d)], in agreement with the proposal of Wurmhel et al. (Chen *et al.*, 2006; Wurmehl *et al.*, 2006). The crossing point $U_{Ir} \approx 1$ eV is also consistent with the point where the critical magnetic moment [lower panel of Figure 3.4] is observed. Hence, $U_{Ir} \approx 1$ eV seems to be the optimal interaction strength of the Ir atom in the studied material. At the crossing point in Figure 3.5(d), we obtain $T_C \approx 911.7$ K. The linear trend, which is independent of U_{Ir}, is due to the negligible dependence of the total magnetic moment on U_{Ir}. The crossing point of the mean-field approach and the linear relation could be said to depict the optimal T_C. Within the nearest-neighbor (NN) interactions and assuming that the exchange energy and spin magnetic moments are the same in both ferro- and antiferromagnetic states, i.e., $|S_1| = |S_2| = S \sim \frac{3}{2}$ as the localized spin, which is the total moment on Fe^{2+} and $J_{AFM} = J_{FM} = J$, we estimate $J = \frac{\Delta E}{NS^2} \approx 153{:}33$ meV, where $\Delta E \approx 0.69$ eV is the total energy difference between the ferro- and antiferromagnetic configurations and $N = 2$ is the total number of magnetic atoms. Using this, we obtain a NN mean-field Curie temperature $T_C^{MF} \approx 1186.29$ K. This value is larger than the one obtained using the exchange-coupling parameter within the KKR that accounted for the interactions beyond the NN. Beyond the NN, interactions are generally known to decrease the T_C. Overall we note, however, that mean-field theory usually overestimates T_C; it employs the average of the magnon energies in estimating the T_C, and, as such, does not take into account the local variations of the crystal lattice which could significantly affect the exchange coupling parameter. Nevertheless, the high T_C value suggests that the inverse full-Heusler Fe_2IrSi alloy could be a suitable material for spintronic and optoelectronic applications.

3.1.1.3 Mechanical and thermodynamic stability

The elastic properties determine the mechanical stability of solid materials and further confirm the dynamical stability. The elastic properties are keys to ascertaining the stability of the material under applied external forces and serve as a guide on the potential device applications. In this regard, we compute the elastic parameters of the inverse full-Heusler Fe_2IrSi alloy by fitting the Murnaghan equation of states with the relaxation of atomic positions on the application of small strains using the Quantum Espresso code. The shear modulus G is obtained as the average of the Voigt–Reuss approximation: G = $(G_V + G_R)/2$, where $G_V = (C_{11} - C_{12} + 3C_{44})/5$, and $G_R = 5(C_{11} - C_{12})\,C_{44}/[4C_{44} + 3(C_{11} - C_{12})]$. The Young's modulus is obtained using $Y_M = 9B_M G/(3B_M + G)$, the bulk modulus as $B_M = (C_{11} + 2C_{12})/3$, and the Poisson ratio as $v = (3B_M - Y_M)/6B_M$. The calculated moduli of elasticity along with the elastic tensor C_{ij} are presented in Table 3.2; they satisfy the criteria of mechanical stability for a cubic structure, i.e., $C_{11} - C_{12} > 0$, $C_{44} > 0$, $(C_{11} + 2C_{12}) > 0$. Significant is the large elastic anisotropy A_e of the Fe_2IrSi alloy obtained from Equation (3.5). This may be due to the intrinsic crystal lattice distortion, which seems to be a generic feature of Heulser alloys.

$$A_e = \frac{2C_{44} - C_{12}}{C_{11}} - 1 \qquad (3.5)$$

Our calculations show an inverse relationship between the onsite Coulomb potential and the degree of anisotropy. This shows that accounting for electron–electron interactions in the *d*-electrons enhances the stability of the crystal structure. The calculated B/G ratio reveals a decrease in the ductility of Fe_2IrSi with an increase in U_{Ir}. However, at the critical U_{Ir} = 1.0 eV, we obtain a Pugh's modulus ratio (B/G) of ~ 3.41, which is well above the critical value of ~1.75 for ductility and even higher than the ~ 2.75 reported for Fe_2CoAl (Siakeng *et al.*, 2018). The thermodynamical properties can be characterized by calculating the melting temperature T_M, the Debye temperature D_b, and the average sound velocity v_s. The average velocity (v_s) is obtained from Equation 3.6

$$v_s = \left[\frac{1}{3}\left(\frac{1}{v_l^3} + \frac{2}{v_t^3}\right)\right]^{-1/3} \qquad (3.6)$$

Where $v_l = \sqrt{\frac{3B+4G}{3\rho}}$ (Longitudinal velocity), $v_l = \sqrt{\frac{G}{\rho}}$ (Transverse velocity) and ρ is the density. We present the calculated thermodynamical properties in Table 3.3. A theoretical value of T_M has been determined as T_M (K) = [553 + (5.91) C_{11}] $\pm$ 300 K (Khandy *et al.*, 2019). Our calculations show that inverse full-Heusler Fe_2IrSi exhibits a high $T_M \approx 2000 \pm 300$ K, which supports its stability at high temperatures. Concerning the calculated bulk and shear modulus, the longitudinal v_l, transverse v_t, and the average sound velocities v_s are also determined and presented in Table 3.3. Further, we obtain the Debye temperature $D_b = \frac{h}{K_B} v_s \left(\frac{3nN_A\rho}{4\pi M}\right)^{1/3}$, where h is Planck constant, N_A is the Avogadro number, n is the number of atoms in the unit cell, M is the molecular mass, and ρ is the density.

Table 3.2: Calculated elastic tensor ($\boldsymbol{C_{ij}}$), degree of elastic anisotropy ($\boldsymbol{A_e}$), bulk modulus ($\boldsymbol{B_M}$), modulus of rigidity ($\boldsymbol{G}$), $\boldsymbol{B/G}$, Young's modulus ($\boldsymbol{Y_M}$), and the Poisson ratio ($\boldsymbol{v}$) at various onsite Coulomb potentials for the Ir atom

U_{Ir} (eV)	C_{11} (GPa)	C_{12} (GPa)	C_{44} (GPa)	A_e	B_M (GPa)	G (GPa)	B/G	Y_M (GPa)	v
0	246.418	205.792	127.639	6.29	219.334	62.85	3.49	170.458	0.35602
0.5	242.025	205.246	128.728	7.00	217.506	61.23	3.55	166.003	0.35565
1	248.454	206.112	130.133	6.15	220.226	64.55	3.41	174.742	0.35361
1.5	244.963	198.477	130.948	5.63	215.639	69.28	3.11	186.432	0.34543
2	244.103	183.339	130.792	4.30	203.594	73.48	2.77	195.735	0.33193
2.5	244.877	178.150	129.780	3.89	200.392	75.70	2.65	200.871	0.32668
3	259.298	190.877	128.246	3.75	213.684	75.86	2.67	202.763	0.33647

Table 3.3: Calculated melting temperature T_M, Debye temperature D_b, sound velocity v_s , longitudinal velocity v_l and transverse velocity v_t at various onsite Coulomb potentials for the Ir atom

U_{Ir} (eV)	T_M (K)	D_b(K)	v_s (Kms^{-1})	v_l (Kms^{-1})	v_t (Kms^{-1})
0	2009.33±300	327.730	2.590	4.410	2.316
0.5	1983.37±300	321.533	2.579	4.411	2.305
1	2021.36±300	332.730	2.599	4.474	2.322
1.5	2000.73±300	347.643	2.794	4.434	2.513
2	1995.65±300	359.922	2.778	4.315	2.513
2.5	2000.22±300	366.755	2.788	4.418	2.507
3	2085.45±300	368.730	2.889	4.426	2.603

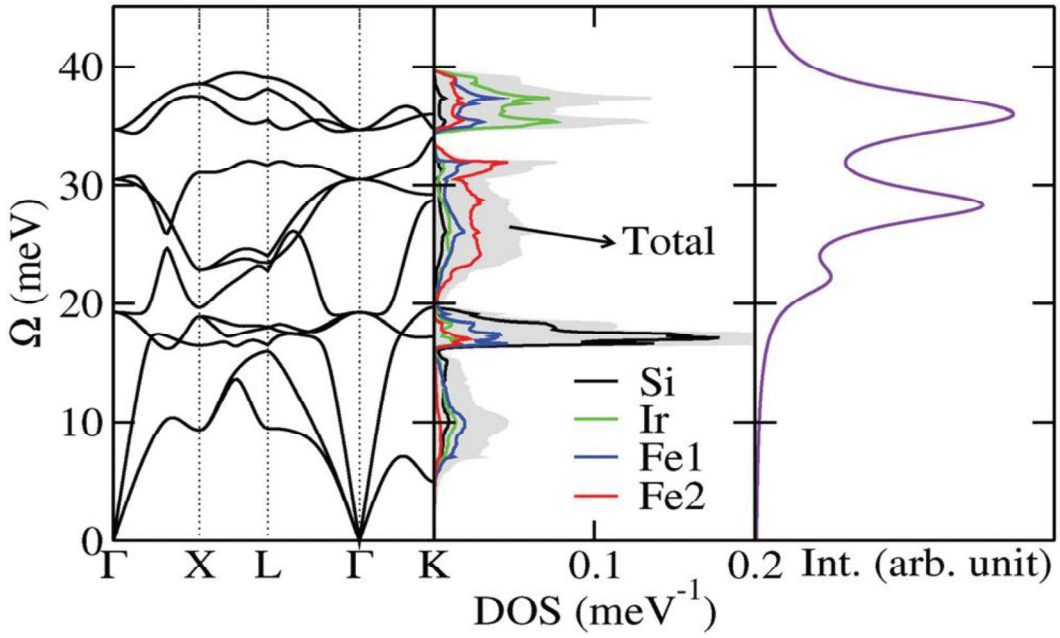

Figure 3.6: Calculated phonon band structure along the various high symmetry points in the first Brillouin zone, the density and the projected phonon density of states, and the Raman spectra of inverse full-Heusler Fe_2IrSi

To determine the dynamical stability of the predicted inverse full-Heusler alloy, we calculated the phonon and vibrational properties using density functional perturbation theory. The forces are calculated with Quantum Espresso (Giannozzi *et al.*, 2009) . The calculated phonon dispersion along the high symmetry points of the Brillouin zone, the corresponding phonon density and projected density of states, and the Raman spectra are presented in Figure 3.6. We do not observe any imaginary frequency in the phonon dispersion, which confirms the dynamical stability. The atoms contribute to all the frequency scales with Si dominating at the mid-frequency regime of ~20 meV. Surprisingly, there is a large density of Ir atoms in the high-frequency regime of ~36 meV of the optical branch. This trend deviates from the simple trend observed in the diatomic linear chain model where the frequency scale of the acoustic (optical) phonon modes are dominated by atoms with larger (smaller) masses (Ekuma *et al.*, 2019). Inverse full Fe_2IrSi belongs to the point group $T_d(\bar{4}3m)$ with four atoms in the primitive cell; this implies that there will be twelve normal vibrational modes at the zone center (Γ point). The irreducible representation of the vibrational modes at the Γ point is $\Gamma = 4T_2$. The first three low-frequency curves, which are the triply degenerate T_2 modes are the usual acoustic modes characterized by the transverse acoustic (TA), longitudinal acoustic (LA), and the out-of-plane transverse acoustic mode (ZA), respectively. The remaining nine curves belong to the optical mode. Using group theory analysis (Kroumova *et al.*, 2003) with the Raman spectra, we predict Raman active modes at ~ 20.80, 28.31, and 36.11 meV, which are all triply degenerate. We also observed a strong coupling between the acoustic and the optical branches; this may be due to the heavy Ir atom, which is a predominant feature of electron-phonon coupling

3.2 Ti_2XSi (X = Mn, Co)

The first principles calculations are performed using DFT based on the projector augmented wave (PAW) method which constitute the core ionic interaction as implemented and programmed in Vienna *ab-initio* Simulation Package (VASP). All electron interactions were treated using the electron correlation exchange energy within the generalized gradient approximation (GGA) within Perdew-Burke-

Ernzerhof (PBE) formalism. A plane wave cut off energy of 300 eV and an explicit k-mesh of 8×8×8 were used within the Monkhorst pack grid to integrate the first Brillouin zone. The self-consistent field calculation steps were performed till the energy difference reaches less than 10^{-5} eV.

3.2.1 Results and Discussions

3.2.1.1 Structural

With having face centre cubic space group 216 (F43m), X_2YZ inverse full Heusler Ti_2MnSi and Ti_2CoSi are predicted to be crystallized in XA structure with atomic position at Wyckoff position; X-atom at (1/4,1/4,1/4) and (1/2,1/2,1/2), Y-atom at (3/4,3/4,3/4) and p-element at (0,0,0) . The equilibrium lattice parameter, total magnetic moment and atomic resolved magnetic moment of bulk structure of Ti-based inverse full Heusler Ti_2XSi (X= Mn, Co) calculated from GGA are presented in Table 3.4. Unfortunately, to the best of our knowledge we did not come across the experimental data to compare. However, our calculated equilibrium lattice constants are in well-agreement with the previous theoretical reports with relatively negligible deviation.

Table 3.4 The calculated optimized lattice constant *a* (Å), total and atomic partial magnetic moment with available literature.

Compounds	a_0	μ_B(Ti1)	μ_B(Ti2)	μ_B(X)	μ_B(Si)	μ_B(Total)
Ti_2MnSi	6.0084	1.042	0.63	-0.814	0.009	1.0145
	5.997*					1.050**
Ti_2CoSi	6.0022	1.545	0.795	0.407	0.012	3.0227
	6.02**					3.00**
	6.03***					3***

* (Fang *et al.*, 2014), ** (Mokhtari *et al.*, 2020), *** (Zhang *et al.*, 2020)

3.2.1.2 Electronic and magnetic properties

In order to analyze the electronic properties of their bulk systems, we have presented the total and atomic resolved density of states (DOS) for both the bulk structures of Ti_2XSi with XA phases are HMF having finite band gap in the minority spin channel, while the spin up channel is characterized by the metallicity with dispersed bands around the Fermi level (E_F) as shown in Figure 3.7[(a) and (b)]. The blend of semiconducting and metallic behavior in Ti_2XSi validated the half metal ferromagnet characteristic with ≋100% spin polarization at E_F. The calculated electronic and magnetic properties of Ti_2XSi are in close agreement with the previous reports (Mokhtari *et al.*, 2020; Zhang *et al.*, 2020). There are some reports of possessing spin gapless semiconducting (SGS) behavior in Ti_2CoSi (Amiri *et al.*, 2019; Zhang *et al.*, 2020). In Figure 3.7(b), due to the presence of a minuscule electronic states (0.25 States/eV) in majority spin (↑) channel at around E_F, mainly contributed by the *d*-orbital states of Co; exhibiting a half metal ferromagnetic character contrary to a SGS behavior of Ti_2CoSi. Our calculated electronic structure of Ti_2CoSi is well agreed with the available results, where 0.13 States/eV and 0.02 States/eV in the spin up channel reported within GGA and *mBJ* approximation, respectively (Mokhtari *et al.*, 2020). Interestingly, a highly dominant states of Ti(1)-*d* orbital in the majority spin channel at around E_F (-1eV to -0.1eV) is followed by unanticipated strong coupled hybridization of *d-d* orbitals which results an energy gap at around -1.3 to -1 eV. Below that energy range, the *d*-orbital states of Co atom imaged the total density of states for both the spin channel (Up or down) as shown in Figure 3.7(b). The formations of band gap in full Heusler rely on the *d-d* hybridization of the transition elements. In Ti-based inverse Heusler, the shaping of *d-d* band gap commenced from the coupling between the 2xe_g and 3xt_{2g} degenerated states of *d*-orbitals of the two inequivalent Ti atoms that prompting the bonding (3xt_{2g}, 2xe_g) states and an anti-bonding (3xt_u, 2xe_u) states. The coupled bonding states of Ti(1)*d-d* Ti(2) further undergone hybridization with the *d*-orbital degenerated states (3xt_{2g}, 2xe_g) of X (Mn,Co) atom that resulted to the bonding states(3xt and 2xe) and anti-bonding states (3xt* and 2xu*).

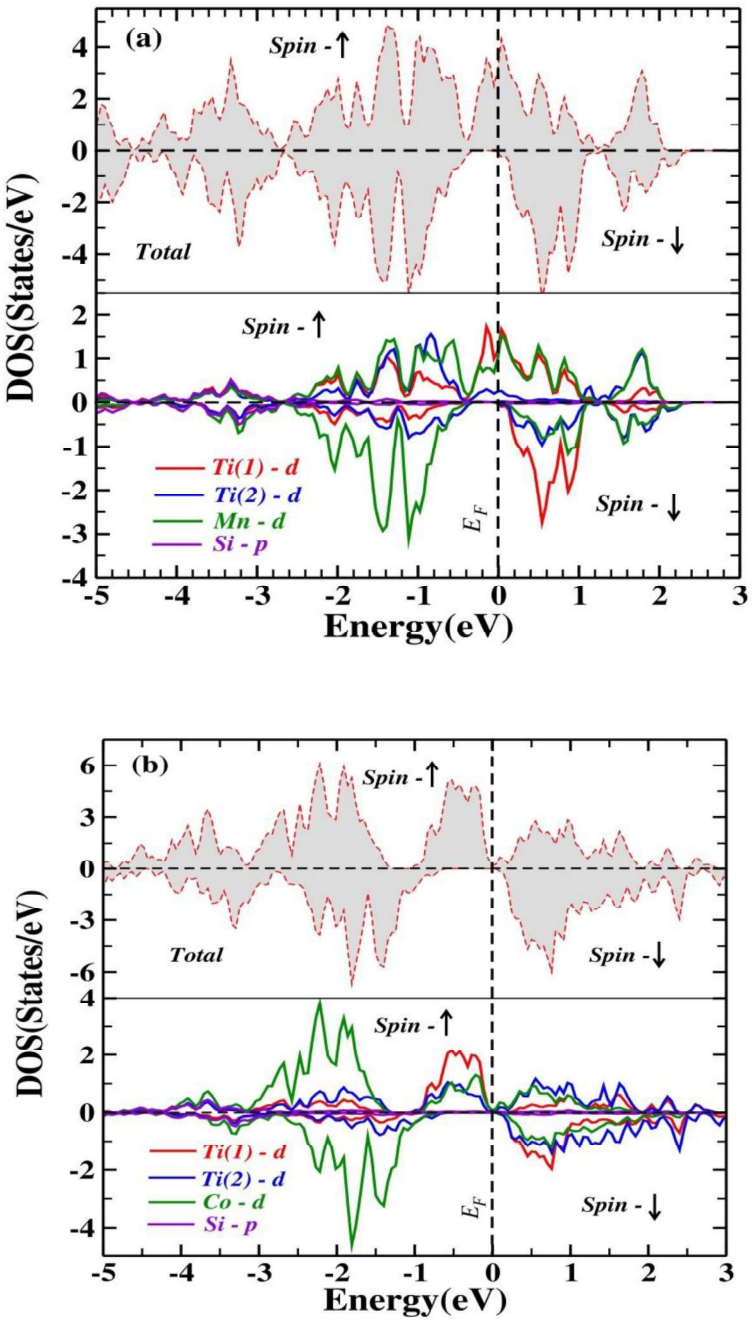

Figure 3.7: Total Density of States (upper panel) and partial atomic resolved density of states (lower panel) of the bulk: (a) Ti_2MnSi (b) Ti_2CoSi compounds (↑-spin-up and ↓-spin-down).

The energy difference between the bonding state 3x*t* and anti-bonding state 3x*t** induced from the hybridization of degenerated Mn *d* orbitals and bonding states of Ti-Ti coupled is the so called *d-d* band gap. The spin polarization at the Fermi level E_F is calculated using the applied formula given in Equation 3.1. In spite of having the chemical formula of X_2YZ type Heusler alloys (Gilleßen & Dronskowski, 2010; D. P. Rai *et al.*, 2010), the Ti-based inverse Full Heusler alloys Ti_2XSi follow the Slater-Pauling rule given by Equation 3.7 (Skaftouros *et al.*, 2013)

$$\mu_t = Z_t - 18 \qquad (3.7)$$

where total magnetic moment is denoted by μ_t and Z_t is the total number of valence electrons. Hence, the calculated magnetic moment per unit cell are associate well with the Slater-Pauling rule with an integer number 1 for Ti_2MnSi with 19 valence electrons and an integer 3 for Ti_2CoSi with 21 valence electrons. Thus, the total magnetic moments associated with Ti_2MnSi and Ti_2CoSi are expected to be $1\mu_B$ and $3\mu_B$, respectively. In Table 3.4, we have observed that the moment of Mn atom is anti-parallel to both the Ti atoms in Ti_2MnSi alloy. Therefore, a presence of non-zero magnetic moment despite having anti-ferromagnetic coupling between Mn-Ti revealed that Ti_2MnSi is a ferrimagnetic half metal, consistent with the previous report (Fang *et al.*, 2014). While the parallel alignment of moment of Co atom with the neighboring Ti atoms revealed the ferromagnetic character of Ti_2CoSi alloy. Further analyzing the total and atomic partial moment, the sum of the local atomic magnetic moment is usually smaller than the total magnetic moment of the unit cell; the differences correspond to the contribution of the interstitial region.

3.2.1.3 Mechanical and Thermodynamical Stability

To investigate of elastic property which determines the mechanical stability of solid materials and further confirms the dynamical stability. The elastic properties are keys to ascertaining the stability of the material under applied external forces and serve as a guide on the potential device applications. In this regard, we compute the elastic parameters of the inverse full-Heusler Ti_2MnSi and Ti_2CoSi compounds. The shear modulus G is obtained as the average of the Voigt–Reuss approximation: G =

$(G_V + G_R)/2$, where $G_V = (C_{11} - C_{12} + 3C_{44})/5$, and $G_R = 5(C_{11} - C_{12})\, C_{44}/[4C_{44} + 3(C_{11} - C_{12})]$. The Young's modulus is obtained using $Y_M = 9K_M G/(3K_M + G)$, the bulk modulus as $K_M = (C_{11} + 2C_{12})/3$, and the Poisson ratio as $v = (3K_M - Y_M)/6K_M$. The calculated moduli of elasticity along with the elastic tensor C_{ij} are presented in Table 3.5 and 3.6; they satisfy the criteria of mechanical stability for a cubic structure, i.e., $C_{11} - C_{12} > 0$, $C_{44} > 0$, $(C_{11} + 2C_{12}) > 0$. Interestingly, a large difference in the studied Ti-base inverse Heusler; a larger elastic anisotropy A_e of the Ti_2CoSi compare to Ti_2MnSi attributed to the presence of stronger intrinsic lattice distortion in Ti_2CoSi alloy that can be obtained from Equation (3.8), which seems to be a generic feature of Heulser alloys.

$$A_e = 5\frac{B^V}{B^R} + \frac{K^V}{K^R} - 1 \qquad (3.8)$$

Table 3.5: Estimated Bulk modulus (**K**) and Shear modulus (**G**) of Ti_2XSi (X= Mn, Co) from Voigt and Reuss approximation.

Compounds	**Averaging Scheme**	***Bulk Modulus* (GPa)**	***Shear Modulus* (GPa)**
Ti_2MnSi	**Voigt**	K_V = 212.22	G_V = 47.338
	Reuss	K_R = 212.22	G_R = 29.552
Ti_2CoSi	**Voigt**	K_V = 165.23	G_V = 64.168
	Reuss	K_R = 165.23	G_R = 63.373

Table 3.6: Calculated elastic tensor ($\boldsymbol{C_{ij}}$), degree of elastic anisotropy ($\boldsymbol{A_e}$), modulus of rigidity ($\boldsymbol{G_R}$), Young's modulus ($\boldsymbol{Y_M}$), and the Poisson ratio ($\boldsymbol{v}$) for Ti_2XSi (X = Mn, Co)

Alloy	$\boldsymbol{C_{11}}$ **(GPa)**	$\boldsymbol{C_{12}}$ **(GPa)**	$\boldsymbol{C_{44}}$ **(GPa)**	$\boldsymbol{A_e}$	$\boldsymbol{G_R}$ **(GPa)**	$\boldsymbol{Y_M}$ **(GPa)**	$\boldsymbol{v}$
Ti_2MnSi	233.51	201.57	68.25	3.01	38.45	132.19	0.397
Ti_2CoSi	239.38	128.15	69.87	5.06	63.77	170.44	0.328

For further confirmation of the ground state thermodynamical stability of the compounds have been studied by calculating frequency dependent phonon dispersion relation based on linear response method in combination with density functional perturbation theory. The phonon band structures and corresponding density of states for Ti_2XSi (X = Mn, Co) are presented in Figure 3.8 [(a) and (b)]. Twelve vibrational modes, that is composed of three acoustic modes and nine optical modes are generated at any q-point due to the presence of 4 atoms in the primitive cell which follows N×3, where N is the number of atoms in the unit cell. We observed a strong coupling between optical and acoustic branches at around 20-30 meV frequency. The optical band gap is nearly open in between 50-55 meV range in both the systems. The low lying acoustic branch for Ti_2CoSi may be due to the dominant features of out of plane transverse acoustic mode (ZA). The absence of an imaginary phonon modes confirmed the thermodynamical stability of the inverse Heusler Ti_2XSi (X = Mn, Co) compounds.

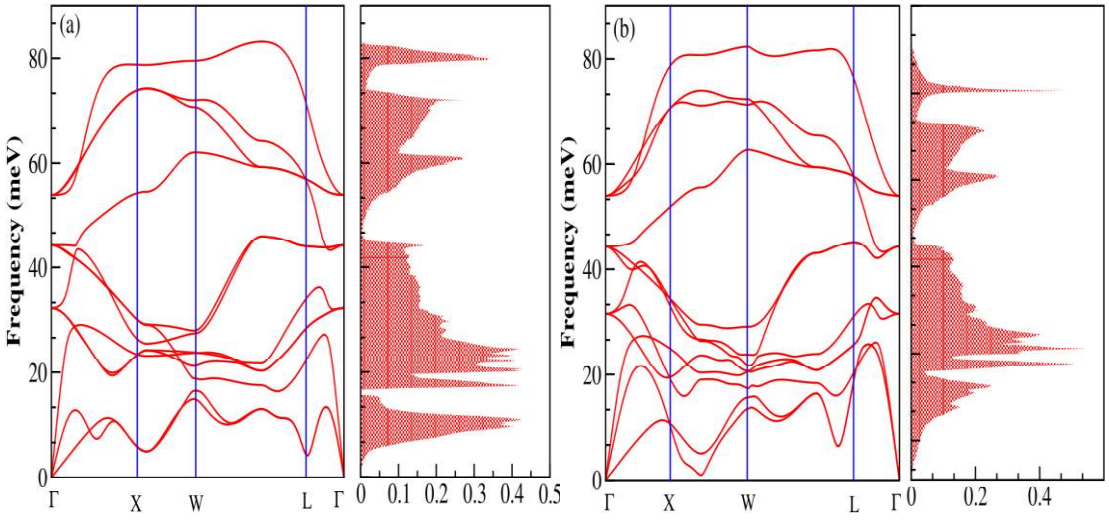

Figure 3.8: Phonon dispersion relation and phonon DOS of (a) Ti_2MnSi and (b) Ti_2CoSi

3.3 Mn_2CoSi

An ab-initio spin polarized DFT calculations of the bulk and surface electronic structures were performed using MedeA-VASP (Kresse & Furthmüller, 1996) based on the programmed where the core ionic interaction was shaped by the projector augmented wave (PAW) method and linear combination atomic orbital (LCAO) method as implemented in QuantumATK Q-2019.12 Simulation package (Smidstrup *et al.*, 2019). Deploying correlation exchange functionals within the generalized gradient approximation (GGA)-Perdew-Burke-Ernzerhof (PBE) formalism (Perdew *et al.*, 1996) for describing all the electron interactions. In order to accurate treatment of strongly correlated electron-electron interactions of 3d electrons, a simplified on site Hubbard potential (U_{eff}) is deployed as GGA+U approximation within the framework of DFT. Adopted fully screened Coulombs interaction U_{Co} = 1.83 eV, J_{Co} = 0.53 eV, U_{Mn}=1.71 eV and J_{Mn}=0.46 eV for $U_{(eff)}$Co − 3d= U_{Co} - J_{Co} = 1.3 eV and $U_{(eff)}$Mn − 3d = U_{Mn} - J_{Mn} = 1.25 eV (Şaşıoğlu *et al.*, 2013). For numerical accuracy of VASP simulation, a plane-wave cut off energy was set at 300 eV. A plane wave basis set is integrated for the first Brillouin zone with an accurate Monkhorst pack grid (Monkhorst & Pack, 1976) of 12×12×12. The self-consistent field calculation steps were performed till the energy difference reaches less than 10^{-5} eV. Where a norm-conserving pseudopotential based LCAO is configured to a density mesh cutoff 95 Hatree in tune with 8×8×8 desity k-point sampling.

3.3.1 Results and Discussions

3.3.1.1 Structural

Face Centre Cubic (FCC) inverse Heusler Mn_2CoSi alloy crystallized in XA-structure (Hg2CuTi-type) belongs to F43m (225) - space group. The atomic positions are described by the wyckoff postision of 4a (0, 0, 0), 4b (1/2, 1/2, 1/2), 4c (1/4, 1/4, 1/4), and 4d (3/4, 3/4, 3/4) where Mn atoms located at 4b and 4d, Co and Si atoms occupied 4aand 4c respectively. The calculated optimized lattice constants, magnetic

moments of inverse Mn_2CoSi Heusler bulk structure calculated from GGA and GGA+U approximations as well as previous theoretical and experimental reported literatures are presented in Table 3.7. Despite two different basis sets approach, both the optimized lattice constants from PAW method (VASP) and LCAO method (ATK) are closely agreed within the theoretical reported values but slightly smaller as compared with the experiment data with absolute uncertainty about 3.1% for the former and 2.88% for the later method. However, all the calculated lattice values presented are within the range 5.4 Å - 5.9 Å of where Xing et al., had been maintained perfect half metallicity for Mn_2CoSi.

Table 3.7: The calculated optimized lattice constant a (Å), total and atomic partial magnetic moment with available literature.

Approach		a_0	μ_B(Mn1)	μ_B(Mn2)	μ_B(Co)	μ_B(Si)	μ_B(Total)
VASP	GGA	5.61	-0.488	2.562	0.879	0.04	2.99
	GGA+U		-1.185	3.019	1.122	0.022	3.00
ATK	GGA	5.623	-0.752	3.005	0.847	-0.096	3.003
	GGA+U		-1.985	3.881	1.296	-0.194	2.997
Exp.		5.79[a]					
Others		5.63[b] 5.65[c] 5.558[d]					3.00[c] 3[d]

[a] (Maji & Nath, 2019), [b] (Singh *et al.*, 2013), [c] (Xing *et al.*, 2008), [d] (On *et al.*, 2021)

3.3.1.2 Electronic and Magnetic Properties

The calculated spin polarized density of states (DOS) from GGA and GGA+U approximation are presented in Figure 3.8 [VASP calculation (a) and (b)], [QuantumATK calculation (c) and (d)]. We estimated the minority (spin-↓) band gap of 0.63 eV (a) and 0.67 eV (c) from GGA, 0.83 eV (b) and 0.89 eV (d) from GGA+U approximation respectively. As it can be seen in Figure 3.8, a similar pattern of

electronic structure is found for projector augmented wave based VASP calculation and using norm-conserving pseudopotential based ATK. Therefore, we generalized

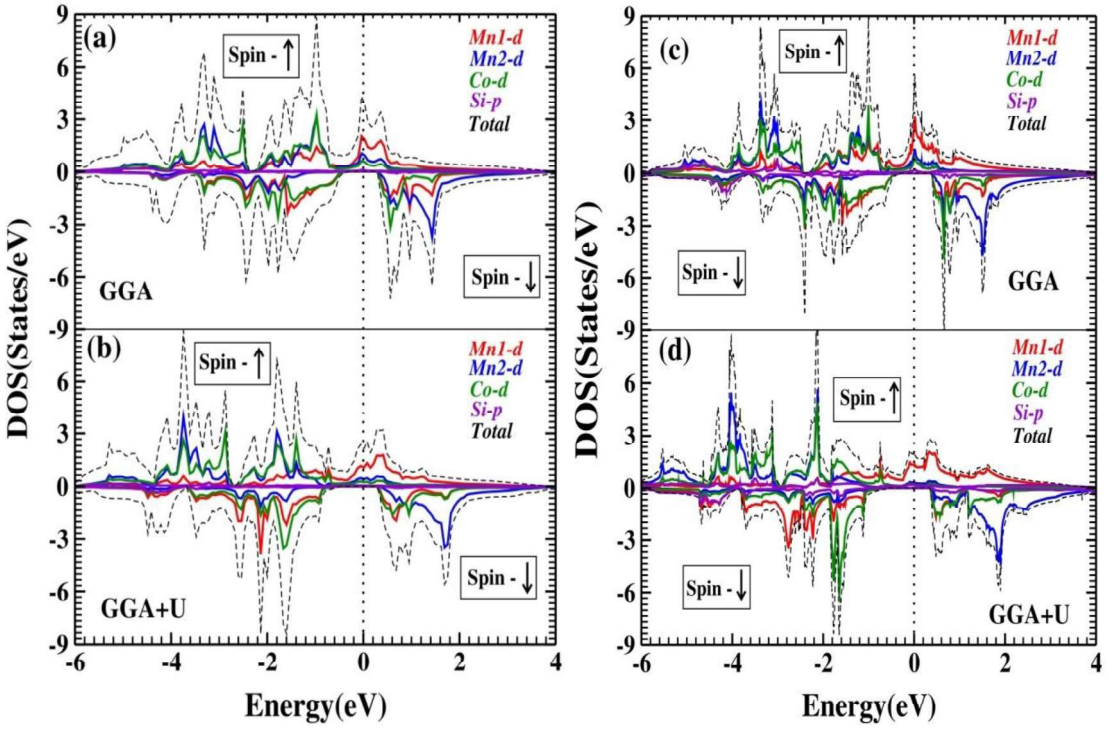

Figure 3.9 Spin polarized density of states: (a) and (b) from GGA and GGA+U approximation respectively using projector augmented-wave based VASP calculation, (c) and (d) using GGA and GGA+U respectively using norm-conserving pseudopotential based ATK calculation

the electronic analysis from Figure 3.8 (a) and (b). In GGA calculation, For Mn2-atom the minority spin (↓) band gap is originated from the strong covalent hybridization between Mn2-*d* states and its neighbor atoms, Mn1-*d* and Co-*d* states, wider band gap of Mn2-atom as compared to Mn1 and Co atoms indicated that Mn2-atom undergone larger exchange splitting which induced large localized spin moment that leads to high polarization of d-states further away from the Fermi level E_F. The strong hybridized Mn2-*d* and Co-*d* states occupied the bonding majority spin (↑) states, where as the bonding minority spin (↓) states mainly contributed from Mn1-*d* and Co-*d* hybridized t_{1u} states. An overlapping doubly degenerated e_u states of Mn1-*d* and Co-*d* atoms occupied at the edges of minority conduction bands in minority spin

channel where the antibonding *d*-states of Mn2 dominantly located at higher energy states which implied reasonably strong *d-d* hybridization occurs only between Mn1 and Co atoms. As it can be found the discussion of the origin of band gap somewhere in literature, since the T_d symmetry is a subgroup of O_h symmetry, there would be no coupling between Mn2-*d* states and degenerate e_u and t_{1u} states due to crystal symmetry reason. It can be reasonably concluded that the half metallic band gap is determined by a narrower *d-d* band gap of Mn1 and Co atom over a wider covalent Mn2-d band gap. Interestingly, instead of e_g-t_{2g} splitting of *d-d* band gap in full Heusler alloys, Mn_2CoSi band gap is predicted due to the energy splitting of e_u-t_{1u} from *d-d* hybridization of Mn1 and Co atoms.

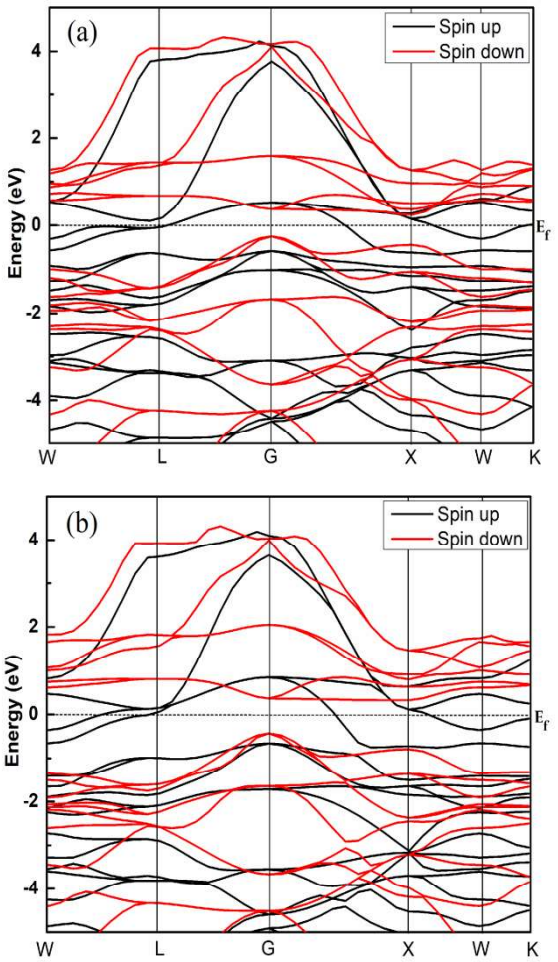

Figure 3.10: Calculated spin resolved electronic band structure of Mn_2CoSi from (a) GGA and (b) GGA+U approximation.

3.3.1.3 Mechanical and Thermodynamical Stability

Table 3.8: Calculated Bulk modulus (**K**) and Shear modulus (**G**) from Voigt and Reuss approximation, elastic tensor ($\boldsymbol{C_{ij}}$), degree of elastic anisotropy ($\boldsymbol{A_e}$), modulus of rigidity ($\boldsymbol{G_R}$), Young's modulus ($\boldsymbol{Y_M}$), and the Poisson ratio ($\boldsymbol{v}$) for Mn_2CoSi

Averaging Scheme	***Bulk Modulus* (GPa)**	***Shear Modulus* (GPa)**
Voigt	K_V = 216.98	G_V = 122.03
Reuss	K_R = 216.98	G_R = 104.03

$\boldsymbol{C_{11}}$ (GPa)	$\boldsymbol{C_{12}}$ (GPa)	$\boldsymbol{C_{44}}$ (GPa)	$\boldsymbol{A_e}$	$\boldsymbol{G_R}$ (GPa)	$\boldsymbol{Y_M}$ (GPa)	$\boldsymbol{v}$
308.91	171.01	157.41	5.86	104.03	269.08	0.29331

To study the mechanical stability of face centre cubic inverse Heusler Mn_2CoSi, the calculated the elastic constant matrix is analized to further confirm the independency of external physical deformation. The shear modulus G is obtained as the average of the Voigt–Reuss approximation: G = $(G_V + G_R)/2$, where $G_V = (C_{11} - C_{12} + 3C_{44})/5$, and $G_R = 5(C_{11} - C_{12})\,C_{44}/[4C_{44}+3(C_{11} - C_{12})]$. The Young's modulus is obtained using $Y_M = 9K_M G/(3K_M + G)$, the bulk modulus as $K_M = (C_{11}+2C_{12})/3$, and the Poisson ratio as $v = (3K_M - Y_M)/6K_M$. The calculated moduli of elasticity along with the elastic tensor C_{ij} are presented in Table 3.8; they satisfy the criteria of mechanical stability for a cubic structure, i.e., $C_{11} - C_{12} > 0$, $C_{44} > 0$, $(C_{11}+ 2C_{12}) > 0$. The elastic anisotropy A_e is calculated from Equation 3.8. The significant large A_e attributed to the strong intrinsic crystal lattice distortion. Young's modulus (Y_M) can provide an information about the stiffness of a material, larger the values harder to deform. Poisson's ratio ($\boldsymbol{v}$) is an important parameter to describe the nature of atomic bonding

in the crystal. The $\boldsymbol{v} \sim 1$ refers to covalent bonding, moreover our calculated value 0.29331 predict metallic bonding.

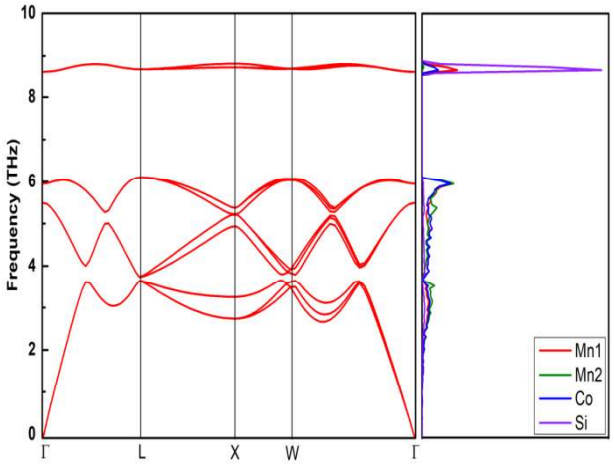

Figure 3.11: Calculated phonon dispersion relation curve and phonon partial DOS contribution from atomic site.

We observed twelve modes of vibrational modes like other system consist of four atoms in the primitive cell. The three acoustic branches are splitted out from the lower modes of optical branch. We observed that a wide optical band gap at around 6 – 8.5 Tetrahertz along high symmetry Γ – L point. The dominant states at higher optical branch arises from Si atom while at the mid-range energy Co-atom is more pronounce, after looking carefully the acoustic modes vibration is greatly influenced by the vibration of Mn2 atom. The all-positive modes of vibration confirmed the thermodynamical stability of Mn_2CoSi compounds.

3.4 Pressure dependence half metallicity in Fe_2CoAl

We have performed first-principles Density Functional Theory (DFT) calculations. All electron–electron interactions were considered according to the generalized gradient approximation (GGA) within the Perdew–Burke–Ernzerhof (PBE) parametization. A screened Coulomb interaction along with the conventional

GGA (GGA+U or DFT+U) in order to deal with strongly correlated 3d electrons the first Brillouin zone (BZ) was integrated by taking a 10×10×10 k-mesh grid within the Monkhorst package.

3.4.1 Structural properties

Our first-principles calculations start with the optimization of both the $L2_1$ (direct) and XA (inverse) structures with different magnetic configurations. The initial magnetic configurations set for our calculations are ferromagnetic FM (Fe1↑, Fe2↑, Co↑), antiferromagnetic AFM1 (Fe1↑, Fe2↓, Co↑), and AFM2 (Fe1↑, Fe2↑, Co↓) (Table 3.9). The variations in total energy versus the lattice constant a (Å) for both the direct and inverse phases with the FM, AFM1 and AFM2 magnetic configurations are shown in Figure 3.11. The XA-structure (inverse) with the FM configuration is energetically favorable with the minimum energy as shown by the blue line and the diamonds [Figure 3.11(b)]. The ground state energy and pressure as a function of volume are also presented in Figure 3.11 (c) and (d). The calculated lattice constant is 5.73 Å and is consistent with previously reported values of 5.70 Å (Matsushita *et al.*, 2017), 5.71 Å (Gilleßen & Dronskowski, 2010), 5.766±0.05 Å (Popiel *et al.*, 2004) and 5.732 Å (Jain *et al.*, 2013). This result also agrees well with the results for several other analogous Fe-based inverse Heusler alloys whose lattice parameters vary from 5.5 to 6.2 Å (Aguilera-Granja *et al.*, 2019; Dahmane *et al.*, 2016; Endo *et al.*, 1995; Friák *et al.*, 2018; Gasi *et al.*, 2013; Ghosh & Ghosh, 2019; Jiang *et al.*, 2018; Luo *et al.*, 2007; Meinert *et al.*, 2014; Siakeng *et al.*, 2018). Further, the cohesive energy has been calculated from Equation (3.9). The cohesive energy results are presented in Figure 3.15 (c) and confirm the ground state stability of each system under different applied pressures.

$$E_C = \frac{E_{Fe1} + E_{Fe2} + E_{Co} + E_{Al} - E_T}{4} \qquad (3.9)$$

Where, E_{Fe1}, E_{Fe2}, E_{Co}, E_{Al} and E_T are the individual energies of Fe1, Fe2, Co, and Al, and the total energy of the system, respectively, n = 4 denotes the total number of atoms in the unit cell.

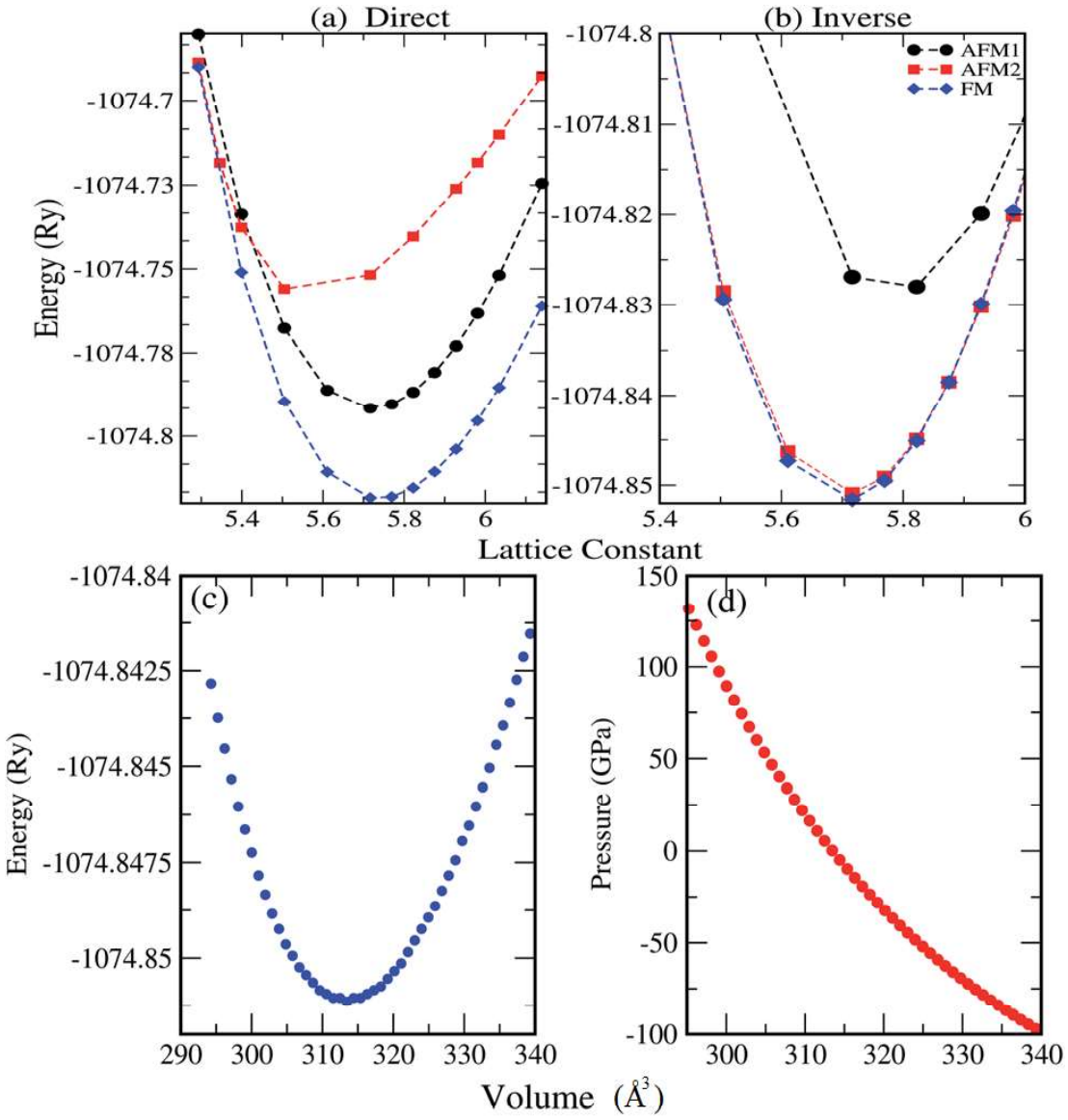

Figure 3.12: Variation of total energy as a function of lattice constant *a* (Å): (a) direct phase, (b) inverse phase (AMF1, AFM2 and FM configurations are represented by black, red and blue lines, respectively), (c) ground state energy as a function of volume in Å^3 for FM and (d) pressure in GPa as a function of volume in Å^3.

Table 3.9: Magnetic configurations (MC) of the individual atoms Fe1, Fe2, Co, and Al, and total ground state energy E_T in Rydberg.

Structure	MC	Fe1	Fe2	Co	Al	E_T
Inverse	FM	↑	↑	↑	0	-1074.852
	AFM1	↑	↓	↑	0	-1074.829
	AFM2	↑	↑	↓	0	-1074.8509
Direct	FM	↑	↑	↑	0	-1074.818
	AFM1	↑	↓	↑	0	-1074.792
	AFM2	↑	↑	↓	0	-1074.758

Table 3.10: Total and partial magnetic moments (in μ_B) calculated with GGA+U along with the Curie temperature; T_C^{cal} (Linear relation approach) and T_C^{MFA} (Mean field approach) in K.

$P(GPa)$	M_{Total}	M_{Fe1}	M_{Fe2}	M_{Co}	T_C^{cal}	T_C^{MFA}
0.0	4.440	2.126	1.011	1.109	826.640	1164.30
5.0	4.030	2.158	0.989	1.075	752.430	1134.90
10.0	3.999	2.171	0.990	1.051	746.819	1130.60
20.0	3.990	2.165	1.010	1.018	745.190	1127.20
30.0	4.00	2.155	1.016	0.995	747.000	1124.20
40.0	3.996	2.152	1.009	0.979	744.828	1146.30
50.0	4.009	2.137	1.025	0.978	748.629	1173.50
60.0	3.988	2.121	1.028	0.964	746.276	1190.40
70.0	3.981	2.105	1.024	0.957	743.561	1187.00

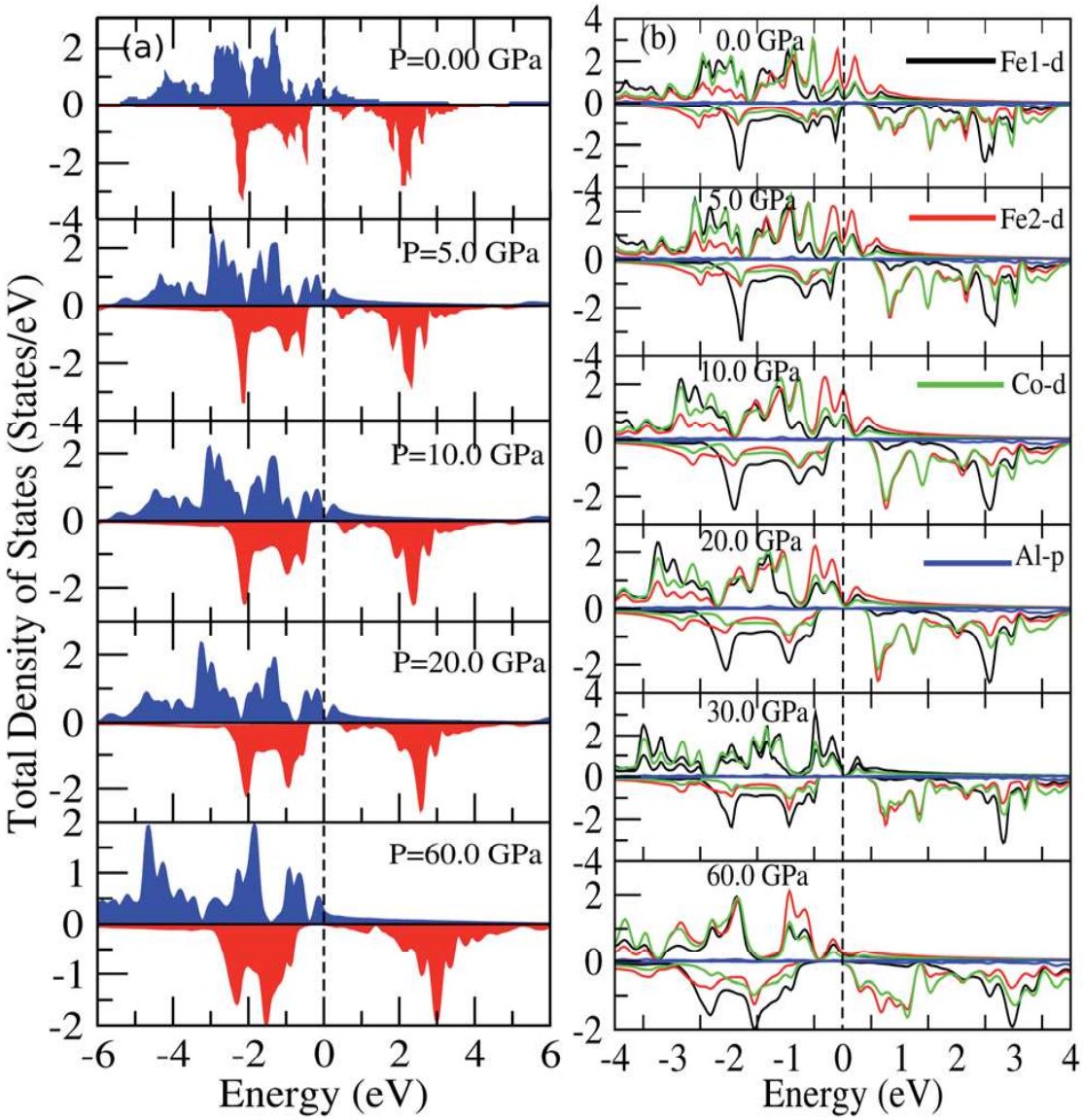

Figure 3.13: (a) Total DOS calculated using GGA+U, (b) partial DOS of Fe1-d, Fe2-d, Co-d and Al-p calculated with GGA+U at different pressures.

3.4.2 Electronic and magnetic properties

We have investigated the electronic properties of Fe_2CoAl by calculating the total density of states (TDOS) and energy bands at different pressures using GGA+U [Figure 3.12 – 3.14]. We have already reported the inadequacy of GGA in deriving the electronic properties in our previous work (Siakeng *et al.*, 2018). On the other hand, GGA+U has predicted a band gap in the spin down channel but this is well

above the Fermi level (E_F). We have observed the presence of some band edges at the E_F, mostly originating from Fe1-*d* (t_{2g}), Fe2-*d* (e_g, t_{2g}) and Co-*d* (e_g, t_{2g}) [Figure 3.13 (a)–(d)]. However, the Fe1-*d* (e_g) state is hardly seen in the picture as it lies far below the E_F in the spin up channel [Figure 3.13(a)]. Hence, we have proceeded with our calculations by using GGA+U along with the application of compressive pressure. Interestingly, on the application of compressive pressure (5 GPa), the E_F is pushed upward within the band gap [Figure 3.12 (a) and (b)]. The halfmetallic band gap is attributed to the *d*–*d* hybridization between Fe2-*d* and Co-*d* followed by Fe1-*d* states to give bonding–antibonding states as in the case of other full-Heusler alloys (Chen *et al.*, 2006; Felser *et al.*, 2015; Galanakis *et al.*, 2014; Kandpal *et al.*, 2006; Liechtenstein *et al.*, 1987; Wurmehl *et al.*, 2006). The bonding states at the top of the valence band form the valence band maximum (VBM) and the lowest antibonding states in the conduction region form the conduction band minimum (CBM). On the other hand, the spin up channel is still conducting. This hybrid characteristic of being semiconducting in the spin down channel and conducting in the spin up channel results in peculiar half-metal ferromagnetic (HMF) behaviour. We have also noticed widening of the band gap with increasing compressive pressure, as this facilitates hybridization due to shortening of the bond lengths. The energy band gap increases from 0.0 eV to 0.72 eV on increasing the pressure from 0 to 30 GPa [Figure 3.15(d)]. This result can also be confirmed by the energy band structure which exhibits the indirect nature of the band gap as measured along the L–X symmetry and denoted by the green circles [Figure 3.14]. In Figure 3.12 and 3.13, we observe a large band gap of ~0.72 eV at 30 GPa with the E_F pinned exactly in the middle of the band gap, providing more evidence of half-metallicity.

A further increase in applied pressure (say beyond 30 GPa) decreases the band gap with drifting of the upper band edge (CBM) towards lower energy (specifically towards the E_F). This can be seen in Figure 3.12(b) and 3.13 (a)-(d) in which the Fe1-d state has moved towards higher energy in the conduction band, taking part less in the *d*–*d* hybridization, and the coupled Fe2-*d*–Co-*d* bands are pushed towards lower energy (i.e. towards the E_F) in the spin down region.

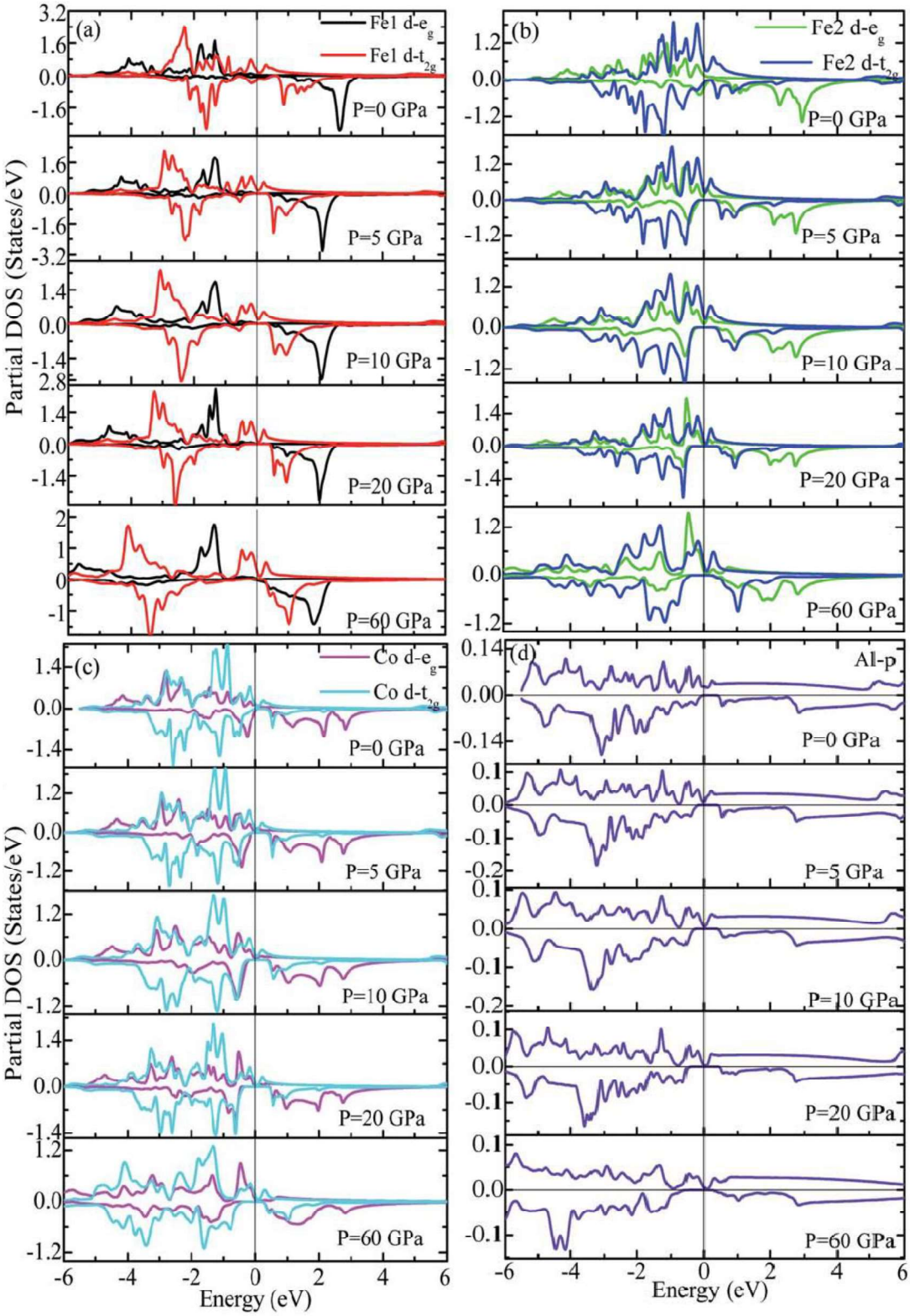

Figure 3.14: (a) Partial DOS of Fe1 (d-e_g, d-t_{2g}), (b) partial DOS of Fe2 (d-e_g, d-t_{2g}), (c) partial DOS of Co (d-e_g, d-t_{2g}) and (d) partial DOS of Al-p at different pressures.

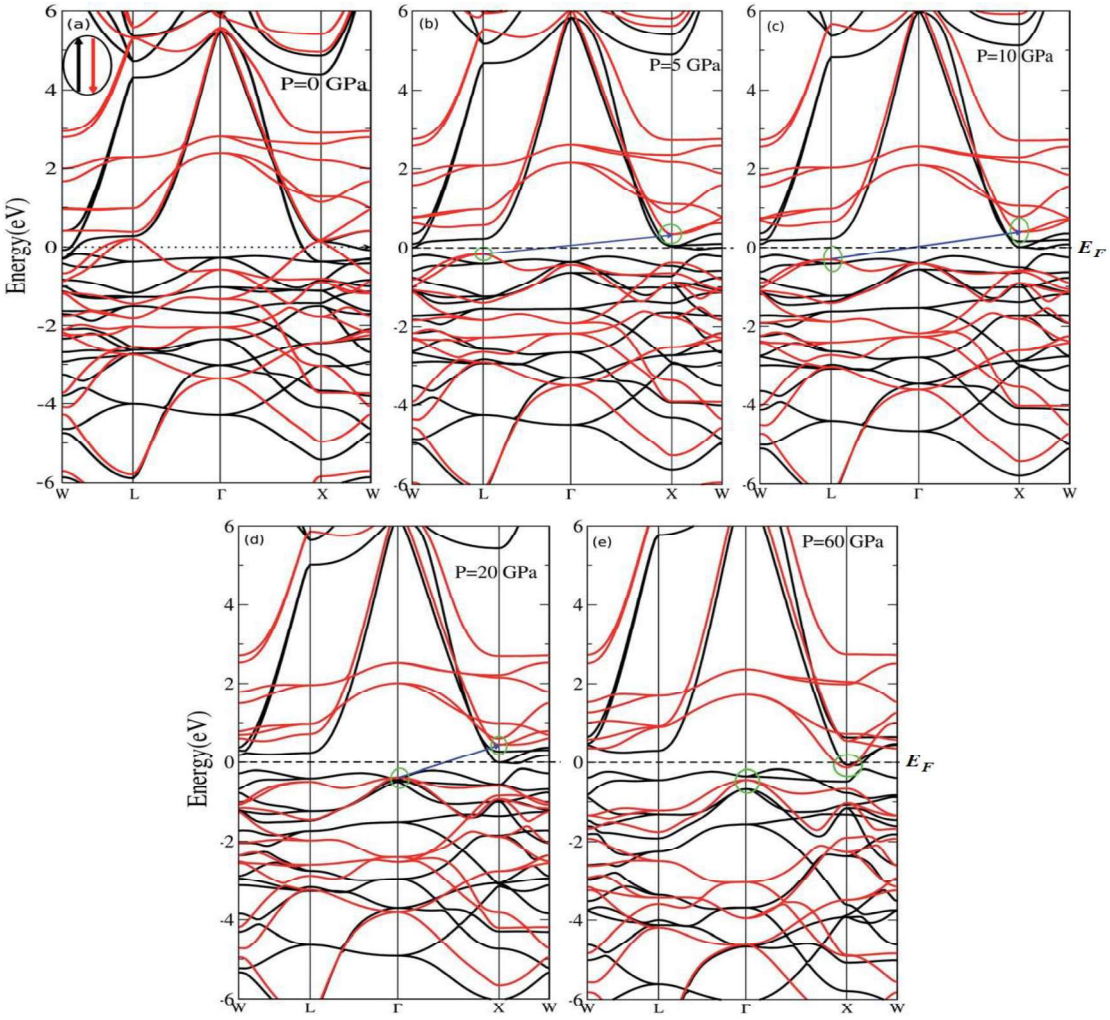

Figure 3.15: Band energies of Fe_2CoAl calculated with GGA+U at (a) P =0 GPa, (b) P =5 GPa, (c) P =10 GPa, (d) P =20 GPa and (e) P =60 GPa.

It looks like the E_F shifts from the lower to the upper edge of the half metallic band gap in the spin down channel on increasing the pressure, a typical feature of band flip. At 60 GPa the CBM (upper edge of the band gap) appears at the E_F, thus diminishing the half-metallic behaviour and increasing the metallicity. The robustness of the half-metallicty is measured in terms of spin polarization at the E_F. The degree of spin polarization in the vicinity of the E_F can be analyzed by P = [N↑(E_F) - N↓(E_F)]/[N↑(E_F) + N↓(E_F)], where N↑(E_F) and N↓(E_F) are the numbers of states at E_F for the spin up and spin down channels, respectively. Our GGA+U calculation with pressure

has significantly improved the spin polarization by more than 45%. At 5 GPa we estimated ~ 98% spin polarization. On varying the pressure, 5 < P < 60 GPa, we have achieved perfect half-metallic behaviour in our Fe_2CoAl system. The projection of E_F inside the band gap in the spin down channel and the finite value of the electron density around E_F in the spin up channel at 5 < P < 60 GPa results in 100% spin polarization. The analysis of the charge density shows the presence of metallic bonding between the atoms and no sign of covalent bonds. As reported elsewhere, the magnetic properties of perfect half-metallic ferromagnet (HMF) Heusler alloys (HAs) can be predicted from the total number of valence electrons present in the unit cell. The total magnetic moment can be derived from the Slater–Pauling (SP) rule (Felser *et al.*, 2015; Kandpal *et al.*, 2006; Skaftouros *et al.*, 2013; Wurmehl *et al.*, 2006) as given by $M_t = (Z_t - 24)\ \mu_B$, where M_t is the total magnetic moment and Z_t is the total number of valence electrons. The total number of valence electrons in our Fe_2CoAl system is $2 \times 8 + 9 + 3 = 28$. So the expected value of the total magnetic moment is $M_t = 4.0\ \mu_B$ which results in the half-metallicity. The total magnetic moment obtained from GGA sharply deviates from the Slater–Pauling rule.

However, on treating the system within GGA+U and applying pressures (0-70 GPa), the total magnetic moment M_t varies around 4.0 μ_B. The highest $M_t = 4.440\ \mu_B$ and the lowest $M_t = 3.981\ \mu_B$, calculated at 0 GPa and 70 GPa, respectively [Table 3.10]. The M_t values at 0 and 70 GPa do not comply with the SP rule. Also, at 60 GPa Mt = 3.988 μ_B and $\Delta\ \mu_B$ = ~ 0.012 or ~ 0.3%. At applied pressures of 5 < P < 60 GPa, the M_t value is ~ 4 μ_B. Thus, we can claim that the M_t values are in accordance with the SP rule at 5 < P < 60 GPa. We also present the variation of the partial magnetic moments calculated with GGA and GGA+U under different pressures in Figure 3.15(b) and their numerical values are tabulated in Table 3.10. Further understand the magnetic interactions and magnetic properties, we have calculated the magnetic exchangeenergy by modeling the pair exchange interaction parameter J_{ij}. The J_{ij} parameter is computed using the Heisenberg model (Liechtenstein *et al.*, 1987). The calculated exchange parameters J_{ij} for a central Fe1 atom interacting with all other atoms (Al–Fe1, Fe1–Fe1, Fe2–Fe1 and Co–Fe1) as a function of R_{ij}/a at different pressures are shown in Figure 3.17(a) – (d).

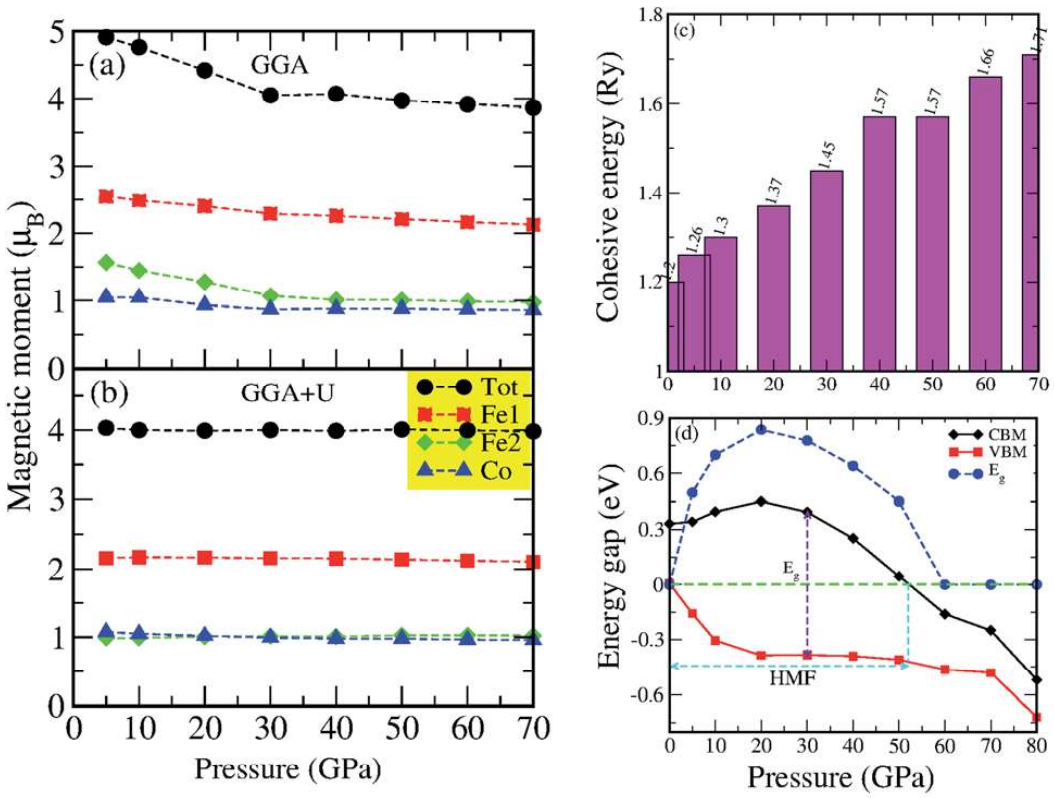

Figure 3.16: Calculated total and partial magnetic moments [(a) and (b)], variation of (c) cohesive energy and (d) energy band gap as a function of pressure.

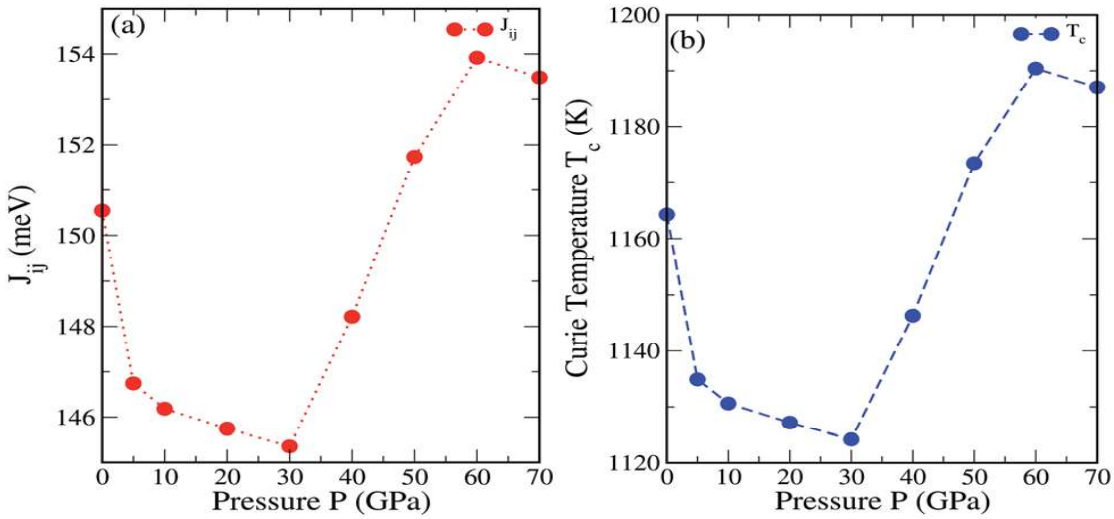

Figure 3.17: (a) Exchange interaction J_{ij} (meV) and (b) Curie temperature T_C^{MFA} (K) as a function of pressure.

The J_{ij} below R_{ij}/a = -1 (below 1) shows a finite stable value. Meanwhile, the J_{ij} values above R_{ij}/a = -1 (above 1) either remain close to 0 meV or fluctuate around 0 meV. The variation of the total J_{ij} along with the calculated T_C^{MFA} as a function of R_{ij}/a under different pressures are shown in Figure 3.16 (a) and (b). We can see that on increasing the pressure up to 30 GPa the J_{ij} parameter decreases systematically. This leads to a decrease in T_C^{MFA}. As shown in Figure 3.17(c) the J_{ij} value is governed by a strong interaction between Fe1 and Fe2. The lowest calculated value of T_C^{MFA} = 1124.20 K at 30 GPa is mainly attributed to the low value of J_{ij} due to the short range (R_{ij}/a < ~1) interaction between Fe1 and Fe2 [inset (blue line) in Figure 3.17(c)]. For the Al–Fe1, Fe1–Fe1 and Co–Fe1 interactions, the J_{ij} values are intermediate at 30 GPa [Figure 3.17(a)–(d)]. On increasing the pressure beyond 30 GPa there occurs a linear increase in T_C^{MFA} , which reaches a maximum at 60 GPa. Our results for T_C^{MFA} contradict with the results of Rambabu et al. for Co_2CrX (X = Al, Ga, In) below 30 GPa, whereas at high pressure, i.e., above 30 GPa they follow a similar trend (Rambabu *et al.*, 2020).

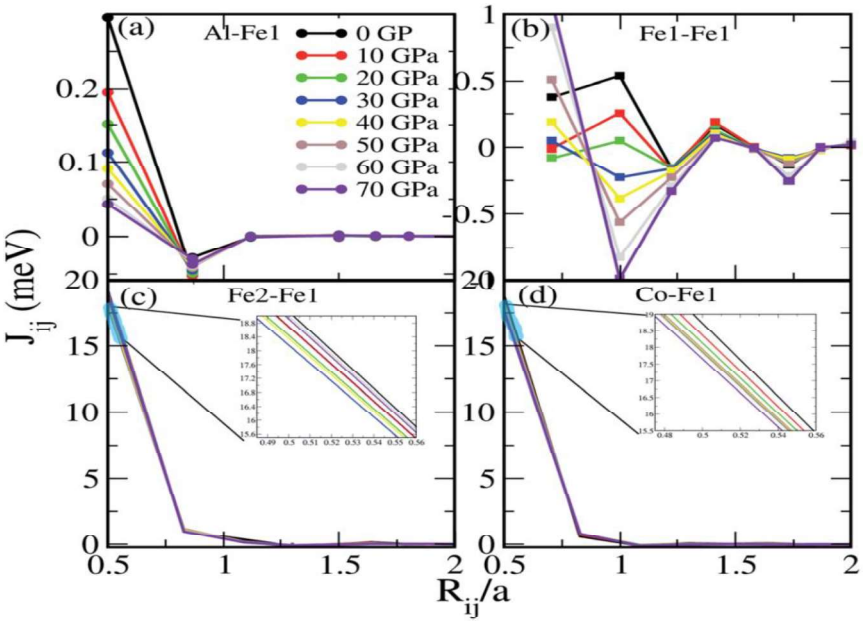

Figure 3.18: Exchange interaction J_{ij} (meV) between (a) Al and Fe1, (b) Fe1and Fe1, (c) Fe2 and Fe1 and (d) Co and Fe1 at different pressure.

The calculated T_C values obtained from the mean field approximation are tabulated in Table 3.10. The other method to estimate the T_C in relation to the total magnetic moment (M_t) of HMF-HAs is given by T_C^{cal} = 23+181 M_t (Chen *et al.*, 2006; Wurmehl *et al.*, 2006). As we have already discussed the inefficiency of GGA in derivingthe half-metallicity, estimating T_C by taking the Mt obtained from GGA is not justifiable. Therefore, we have taken the M_t values calculated with GGA+U and substituted in the aforementioned above relation to obtain the T_C^{cal} . The estimated values of T_C^{cal} are presented in Table 3.10. The T_C^{cal} values vary from 826.640 K to 743.561 K on varying the pressure from 0 to 70 GPa. These results are in good agreement with the T_C*s* of other analogous Fe-based inverse full-Has (Gasi *et al.*, 2013). We have noted that the T_C obtained from linear relation appears to be independent of interaction strength as the variation of the total magnetic moment (M_t) is very small. Referring to Table 3.10, the T_C values calculated with the MFA look much higher as compared to those calculated with linear relation. The large values of T_C^{MFA} may arise due to inability to include the magnetic percolation effect within the mean field approximation.

4

Structural Stability and Electronic properties of Full Heusler Surface films

In order to fabricate technological device, it is necessary to preserve materials functional properties in nanoscale regime. Mostly, the functional diverse properties exhibited in the bulk form are destroyed at surface/thin film and interface realm. This is due to the breakdown of translational symmetry when cleavage to thin film. In this chapter, to ensure the preservation of surface half metallicity; we present the theoretical investigation of surface properties mainly focusing electronic property of full Heusler compounds from first principle calculation. Interestingly, for TiSi terminated 001 plane of Ti_2MnSi and MnSi terminated of Mn_2CoSi inverse full Heusler exhibited half metallic character with 100% spin polarization. Meanwhile, TiMn and MnCo-terminals are found to behave metallic character, respectively from the aforementioned compound. Regarding, surface stability, some studied compounds are already grown in thin film and optimistically utilized in experimental study. For those compounds, we do not perform stability calculation. However, the thermodynamic stability is predicted for unexplored materials and presented in this chapter.

4.1 Ti_2XSi (X=Mn,Co) Surfaces [001]

The first principles calculation were performed using DFT based on the projector augmented wave (PAW) method which constitute the core ionic interaction as implemented and programmed in Vienna *ab-initio* Simulation Package (VASP). All electron interactions were treated using the electron correlation exchange energy within the generalized gradient approximation (GGA) within Perdew-Burke-Ernzerhof (PBE) formalism. A plane wave cut off energy of 460 eV and an explicit k-mesh of 12 × 12 × 1 were used within the Monkhorst pack grid to integrate the first Brillouin zone. The self-consistent field calculation steps were performed till the energy difference reaches less than 10^{-5} eV.

4.1.1 Results and Discussion

4.1.1.1 Structural Properties

We have adopted the optimized bulk structure of $Ti_2(X)Si$ as presented in the previous chapter (i.e. Chapter 3) and cleaved the [001] surfaces using supercell method. The surface [001] consists of two natural terminations; alternating planes of TiSi and TiMn terminals for Ti_2MnS (TMS), while TiSi and TiCo terminated surfaces for Ti2CoSi (TCS). We acquired each slabs with 13 diatomic layers and applied a vacuum of 15 Å on both the sides of the identical phases along the z-axis to prevent the unphysical interaction between the periodic slabs. The in-plane lattice parameter of these slabs: $a\sqrt{2}/2$, where a = 6.0084 Å is the optimized lattice constant of bulk Ti_2MnSi and 6.0022 Å for Ti_2CoSi. By considering the interfaces of both the sides of the slab, we have relaxed the top four layers of each slab with fixed core layers (5-layers). The results of relaxed parameters are presented in Table 4.1 in terms of atomic displacement (fourth column) and percentage of atomic displacement with respect to the bulk's lattice constant a (fifth column). The inward relaxation of both surface atoms (Ti, Si) are seen only in TiSi (TMS) terminal surface while the surface Ti-atom of other terminals are relaxed outward. The outward relaxation may be attributed to the metallicity of the surfaces, in which the surface layers tried to rearrange the displaced valence electron density (Chis & Hellsing, 2004). The higher variation of atomic displacement among transition elements may be attributed to the *d-d* re-hybridization after reducing symmetry of the surfaces. In addition, Ti-X terminated surfaces for each compound give rise to strong relaxation due to the breaking of the bonds at the surface. One can noticed that TiSi(TMS) terminal surface generate the smallest relaxation among these terminals which is followed by TiSi(TCS) terminated surface. Consequently, TiSi(TMS) terminal surface is found to be the most stable surface structure out of the studied surfaces.

4.1.1.2 Surface stability: ab-initio thermodynamic

As the surface stability is an important aspect in realization of thin films growth, we further study the stability of the adopted relaxed surfaces by calculating the surface energy as a function of the constituent atomic chemical potential within

the framework of *ab-initio* thermodynamics (Faregh *et al.*, 2019; Han *et al.*, 2013; Hashemifar *et al.*, 2005). The surface energy can be calculated as follows:

$$\gamma = \frac{1}{2A}\left[G - \sum_i (N_i \mu_i)\right] \tag{4.1}$$

Where A and G are the surface area and total energy of the relaxed slab respectively. N_i and μ_i; the total number and chemical potential of the constituent i^{th} atom in the slab. Since the chemical potential of the constituent elements in the compounds are not independent, the sum of the chemical potentials are equal to the total energy of the bulk Ti_2XSi; $G_{Ti_2XSi}$where $X = Mn, Co$:

$$2\mu_{Ti} + \mu_{(X)} + \mu_{Si} = G_{Ti_2(X)Si}\ (X = Mn, Co) \tag{4.2}$$

By rearranging the Eq. (4.2) and substituting the μ_{Si} in Eq. (4.1), we obtained the surface energy as a function of μ_{Ti} and $\mu_{(X)}$. The maximum value of chemical potential for Ti and X (Mn,Co) can be obtained from the total energy of their bulk structure;

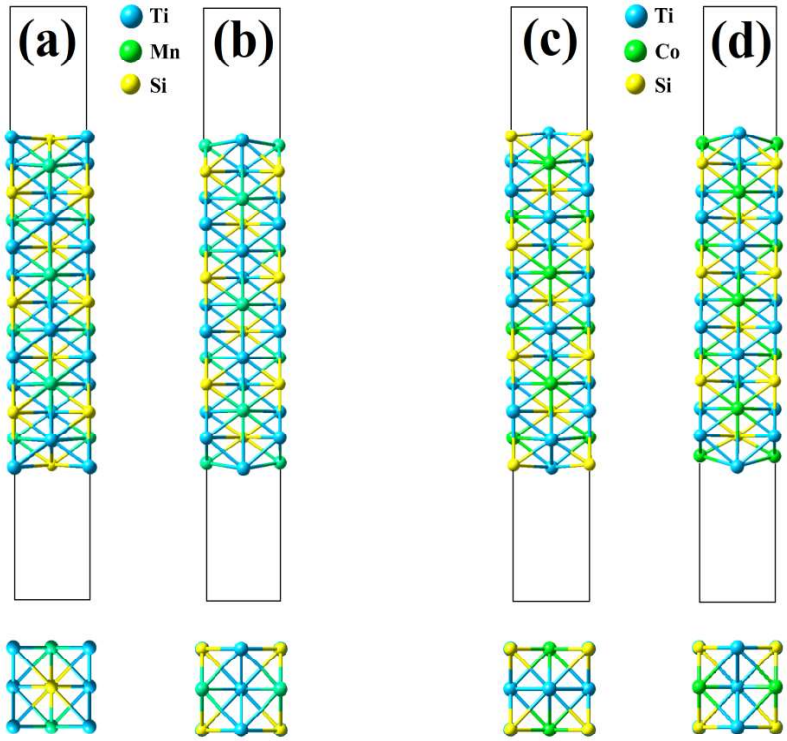

Figure 4.1: Conventional Slab model for (a)TiSi (b)TiMn terminal of 001 Ti_2MnSi and (c) TiSi, (d)TiCo terminal from Ti_2CoSi compounds.

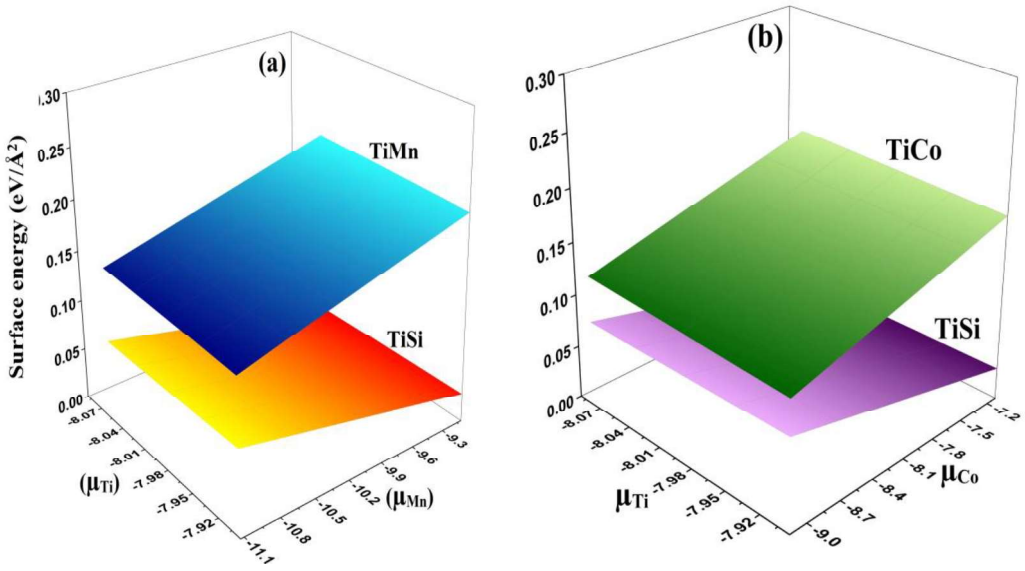

Figure 4.2: Calculated surface energies (eV/Å^2) as a function of chemical potentials of (a) μ_{Ti} andμ_{Mn} (eV) for 001-surface of Ti_2MnSi and (b) μ_{Ti} and μ_{Co} (eV) for 001- surface of Ti_2CoSi.

the minimum allowed chemical potentials were set on to a certain extent that by diminishing μ_{Ti} and $\mu_{(X)}$ till Ti and X(Mn,Co) leave the structure and T_2Si and X (Mn, Co)Si were formed. Whereas the boundary condition of μ_{Ti} and $\mu_{(X)}$ are given by:

$$\frac{1}{2}\left(G_{Ti_2(X)Si} - G_{(X)Si} \leq \mu_{Ti} \leq G_{Ti}\right) \tag{4.3}$$

$$G_{Ti_2(X)Si} - G_{Ti_2Si} \leq \mu_{(X)} \leq G_{(X)} \tag{4.4}$$

Where $G_{(X)Si}$, G_{Ti}, G_{Ti_2Si} and $G_{(X)}$ are the total energy of the bulk (X)Si, Ti, T_2Si and (X), respectively. To obtain the allowed chemical potentials for μ_{Ti} and $\mu_{(X)}$, we adopted the available data of the above mentioned total energies except G_{Ti} from the authentic web i.e. www.materialsproject.org (Jain *et al.*, 2013) those data were obtained from the similar computational approaches.

In Figure 4.2, we have presented the surface energies of different slabs as a function of μ_{Ti} and $\mu_{(X)}$ within the allowed ranges. TiSi terminal surface possibly favorable than Ti(X) terminal surfaces from their respective compounds due to the presence of lower surface energies which agrees well with the smaller structural relaxation as discussed in the preceding subsection. Interestingly, the TiX terminated surfaces

Table 4.1: The relaxed atomic displacement (d_{i-f}(Å)) and the atomic displacement (% of d_{i-f}) in percentage of optimized bulk lattice constant *a*

Alloy	**Terminal**	**Layer**	$\boldsymbol{d_{i-f}}$(Å)	**% of** $\boldsymbol{d_{i-f}}$
Ti_2MnSi	*TiSi*	Ti/Si (s)	-0.005/-0.130	-0.083/-2.16
		Ti/Mn(s-1)	0.040/-0.075	0.670/-1.250
		Ti/Si(s-2)	-0.015/0.005	-0.250/0.080
		Ti/Mn(s-3)	0.020/-0.035	0.330/-0.580
	TiMn	Ti/Mn(s)	0.205/-0.120	3.410/-1.990
		Ti/Si(s-1)	-0.010/-0.035	-0.17/-0.58
		Ti/Mn(s-2)	0.015/-0.060	0.25/-0.99
		Ti/Si(s-3)	0.005/-0.005	0.083/-0.083
Ti_2CoSi	*TiSi*	Ti/Si(s)	0.062/-0.088	1.04/-1.47
		Ti/Co(s-1)	0.083/-0.057	1.39/-0.95
		Ti/Si(s-2)	-0.005/0.016	-0.09/0.26
		Ti/Co(s-3)	0/0.026	0 /0.43
	TiCo	Ti/Co(s)	0.213/-0.374	3.55/-6.24
		Ti/Si(s-1)	0.010/0.042	0.17/0.69
		Ti/Co(s-2)	0.021/0	0.35 /0.000
		Ti/Si(s-3)	0.042/-0.005	0.69/-0.09

Table 4.2: Calculated atomic magnetic moment (in μ_B) of surface(s), sub-surface(s-1) central layer (C.L) and corresponding calculated values in their respective bulk structure.

Terminal	**Ti_2MnSi**			
	Ti	Mn	Si	C.L
TiSi	1.112(s)	-1.182(s-1)	-0.033(s)	0.605(Ti)
				0.009(Si)
TiMn	-1.324(s)	2.738(s)	-006(s-1)	0.957(Ti)
				-1.001(Mn)
Bulk	1.042(Ti1)	-0.814	0.009	
	0.63(Ti2)			
	Ti_2CoSi			
	Ti	Co	Si	C.L
TiSi	0.997(s)	0.263(s-1)	-0.022(s)	0.780(Ti)
				0.011(Si)
TiCo	1.13(s)	0.012(s)	-0.006(s-1)	1.532(Ti)
				0.394(Co)
Bulk	1.545(Ti1)	0.407	0.012	
	0.795(Ti2)			

shown strong molecular attraction as their chemical potentials μ_{Mn} and μ_{Co} increases. From the practical point of view; the instability of the surfaces can be handled by deploying non-equilibrium epitaxial thin film growth technique.

4.1.1.3 Surface electronic and magnetic properties

To analyze the surface electronic structures, we have presented the calculated DOS and energy band structures of TiSi, TiMn-terminals of Ti_2MnSi (001) slab and TiSi, TiCo-terminasl of Ti_2CoSi (001) surface in Figure 4.3 and 4.4, respectively. In order to gain the detail insight of the surface electronic configuration, the atomic partial DOS of surface layer (s) were presented. The second layer(s-1) and central layer for each particular film as well as their respective bulk electronic DOS were also displayed in Figure 4.3. In Ti_2MnSi (001) surface, we can noticed that the bulk half metallic character is degenerated in TiMn terminal with complete metallic character as seen in Figure 4.3 (b), while it is preserved in TiSi terminal with the presence of distinct band gap in the spin down channel and the overlapped of the valence and the conduction bands with the E_F crossing over it in the spin up states are as shown in Figure 4.3(a). TiSi termination of Ti_2CoSi (001) surfaces, exhibit the spin gapless semiconducting phase (SGS) over the half metal [see Figure 4.4(c)]. Furthermore, one can observed from Figure 4.3(c) and Figure 4.4(c), the presence of surface delocalized states derived from *d*-orbitals of the surface Ti(s) and Co(s-1) atoms around the Fermi level destroyed the HMF nature. This may be attributed to the electrostatic potential declined towards the vacuum region which has lifted these states up to the E_F as the Ti(s) atom relaxed towards vacuum (Hashemifar *et al.*, 2005). For TiCo termination, the weak hybridization between the *d* states of Ti(s) and Co(s) may induce zero energy splitting which results surface states at the E_F due to the lowering of symmetry at the surface. Hence, the half metallic properties are lost. However, it is clearly seen that the partial DOS contributed from the central layer atoms of all terminals are well matches with the bulk electronic properties as displayed in bottom panel of Figure 4.3(a, b, c and d). These figures demonstrated that the chosen slab thickness were sufficient enough to investigate the surface electronic property. 100% spin polarization is an ideal factor for spin injected device applications.

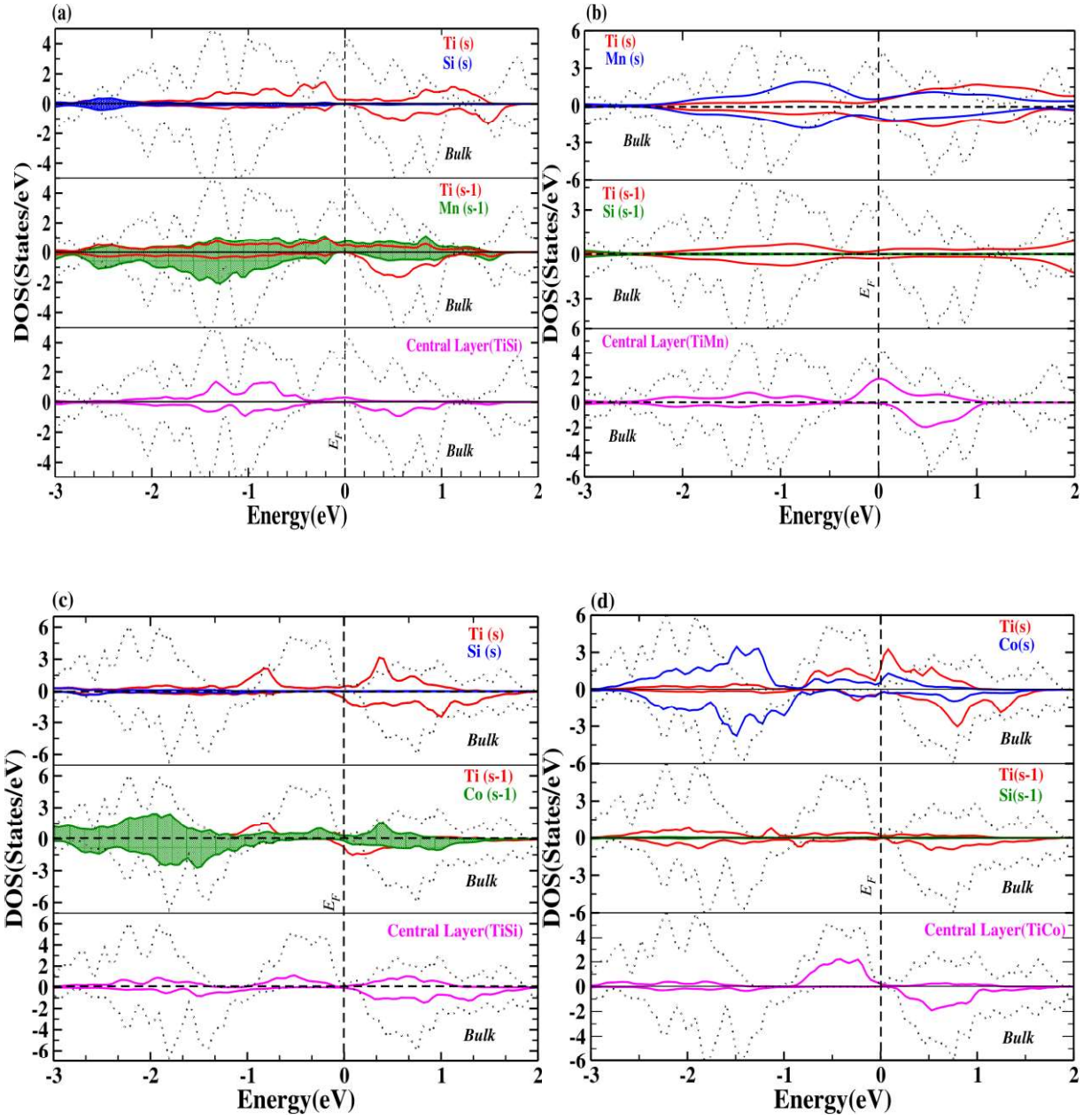

Figure 4.3: Spin resolved partial density of states: (a) TiSi(TMS), (b) TiMn(TCS), (c) TiSi(TCS) and (d) TiCo(TCS) terminal surfaces.

We further calculate the spin polarization of all terminal surfaces using Equation 3. It was found that an excellent 100% spin polarization for TiSi terminal in Ti_2MnSi surface only, whereas TiMn terminal shows the metallic character. For TiSi terminal of Ti_2CoSi surface, we have found the flip of spin polarization of -33.4% due to the

presence of spin gapless semiconducting like behavior with more dense states at the spin down channel. Meanwhile, we report 89.1% spin polarization of TiCo terminal surface. To explore the surface effect of the magnetic properties, the calculated atomic magnetic moment of the surface, sub-surface (s-1) and central layer (C.L) atoms for each terminals surface and corresponding calculated moment in their respective bulk structures are presented in Table 4.2. By comparing the corresponding partial moments in the bulk structure, we have observed the enhanced magnetic moment of the surface atoms. The increased in the magnetic moment of surface atoms may be due to the release of the free electrons owing to the breaking of translations

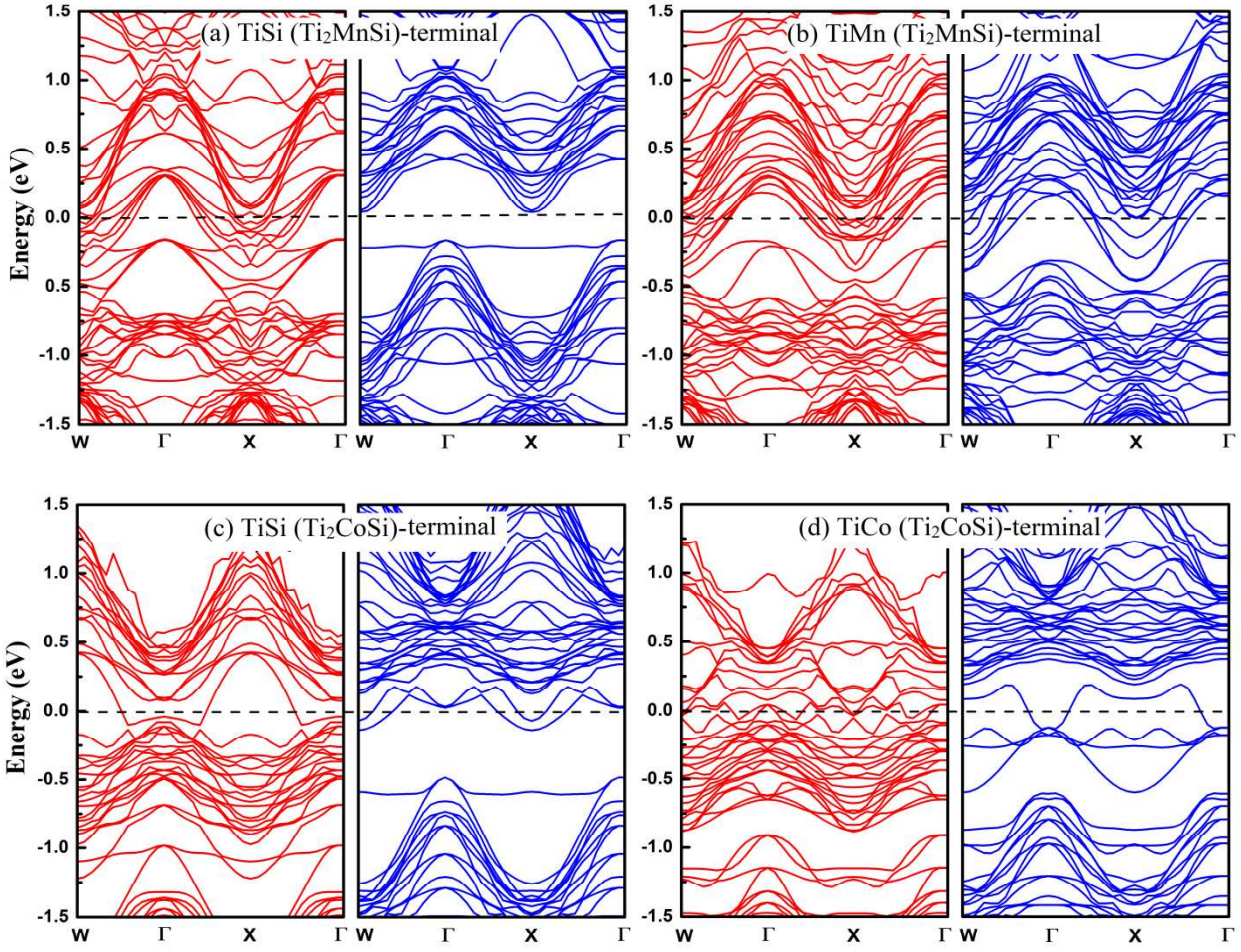

Figure 4.4: Calculated Band structures of Ti_2MnSi (001)[(a)TiSi (b)TiMn-terminal] and Ti_2CoSi (001)[(c)TiSi (d)TiCo terminal]

symmetry (breaking of bond) during the surface formation (Hashemifar *et al.*, 2005; Hu & Zhang, 2017). However, the value of bulk atomic sites moment are nearly retained in the central region. The antiparallel spin moment of Si atom in each surface and sub-surface layer may be attributed to the Ruderman-Kittel-Kasuya-Yosida (RKKY) exchange interaction between Mn atoms (Hu & Zhang, 2017; Kim *et al.*, 2021; Ruderman & Kittel, 1954; Şaşıoğlu *et al.*, 2008). For TiMn termination, the occurrence of anti-ferromagnetic super-exchange (Şaşıoğlu *et al.*, 2008) between the surface atoms Ti and Mn possibly enhancing spin moment value as compared to the bulk phase.

4.2 Fe_2CoAl surfaces

Different FCA surface slabs with orientations [(001), (110), (111)] have been cleavage from the cubic bulk Fe_2CoAl with lattice constant a =5.703 Å (Siakeng *et al.*, 2018). A vacuum of 15 Å is applied along the z-axis to avoid periodic layer interactions. We have performed the first principles DFT (Kohn & Sham, 1965) calculation using Quantum Espresso (QE) (Giannozzi *et al.*, 2009) package considering the electron exchange energy within the generalized gradient approximation (GGA) proposed by Perdew–Burke–Ernzerhof (PBE) (Perdew *et al.*, 1996). We used 250 Rydberg for the kinetic cut off energy and a mesh of 16×16×1 within Monkhorst pack (Monkhorst & Pack, 1976) for K-point to integrate the first Brillouin zone. Structural relaxation was achieved with a force tolerance of 0.0136eV/Å. We deployed the force theorem (Li *et al.*, 2014) as implemented in QE; by performing the self-consistent-field calculation (SCF) without the spin–orbit coupling (SOC) within the scalar pseudopotentials method we obtained the charge density and spin magnetic moment. Then, two types non-SCF calculations are executed with the spin polarized fully relativistic pseudopotentials with SOC. In which we have considered spin moment with angle 0° in xy-plane for parallel and 90° in z-axis for perpendicular direction. The difference of the band energy between the two spin moment directions (90° and 0°) is the total MAE.

Table 4.3: Magnetic Configuration on magnetic atomic sites (six Fe- and three Co-atoms) and energy difference (E_{FM}-E_{AFM}) in *Rydberg* for Al-terminated surface.

Config.	**Fe1**	**Fe2**	**Fe3**	**Fe4**	**Fe5**	**Fe6**	**Co1**	**Co2**	**Co3**	***E_{FM} -E_{AFM}(Ry)***
FM	↑	↑	↑	↑	↑	↑	↑	↑	↑	**0.00**
AFM1	↑	↑	↑	↑	↑	↑	↓	↓	↓	**0.009**
AFM2	↑	↓	↑	↓	↑	↓	↑	↓	↑	**−0.040**
AFM3	↑	↑	↓	↓	↑	↑	↑	↑	↓	**−3.889**
AFM4	↓	↓	↑	↑	↓	↓	↓	↓	↑	**−2.438**
AFM5	↑	↓	↓	↑	↓	↓	↑	↓	↓	**−0.004**
AFM6	↓	↑	↑	↓	↑	↑	↓	↑	↑	**−0.004**

Table 4.4: Magnetic Configuration on magnetic atomic sites (six Fe- and four Co-atoms) and energy difference (E_{FM}-E_{AFM}) in *Rydberg* for Co-terminated surface.

Config.	**Fe1**	**Fe2**	**Fe3**	**Fe4**	**Fe5**	**Fe6**	**Co1**	**Co2**	**Co3**	**Co4**	***E_{FM} -E_{AFM}(Ry)***
FM	↑	↑	↑	↑	↑	↑	↑	↑	↑	↑	**0.00**
AFM1	↑	↑	↑	↑	↑	↑	↓	↓	↓	↓	**−4.762**
AFM2	↑	↓	↑	↓	↑	↓	↑	↓	↑	↓	**−6.889**
AFM3	↑	↑	↓	↓	↑	↑	↑	↑	↓	↓	**−5.101**
AFM4	↓	↓	↑	↑	↓	↓	↓	↓	↑	↓	**−3.690**
AFM5	↑	↓	↓	↑	↓	↓	↑	↓	↓	↑	**−4.798**
AFM6	↓	↑	↑	↓	↑	↑	↓	↑	↑	↓	**−4.797**

Table 4.5: Magnetic Configuration on magnetic atomic sites (seven Fe- and three Co-atoms) and energy difference (E_{FM}-E_{AFM}) in *Rydberg* for Fe-terminated surface.

Config.	**Fe1**	**Fe2**	**Fe3**	**Fe4**	**Fe5**	**Fe6**	**Fe7**	**Co1**	**Co2**	**Co3**	***E_{FM} - E_{AFM}(Ry)***
FM	↑	↑	↑	↑	↑	↑	↑	↑	↑	↑	**0.00**
AFM1	↑	↑	↑	↑	↑	↑	↑	↓	↓	↓	**−0.314**
AFM2	↑	↓	↑	↓	↑	↓	↑	↑	↓	↑	**3.551**
AFM3	↑	↑	↓	↓	↑	↑	↓	↑	↑	↓	**−0.678**
AFM4	↓	↓	↑	↑	↓	↓	↑	↓	↓	↑	**2.586**
AFM5	↑	↓	↓	↑	↓	↓	↑	↑	↓	↓	**3.520**
AFM6	↓	↑	↑	↓	↑	↑	↓	↓	↑	↑	**−2.105**

4.2.1 Results and Discussions

4.2.1.1 Spin degree of freedom dependent Ground state energy

Among the three different slab orientations (001, 110 and 111) the 111-surface slab with thirteen atomic monolayers have been found to be the most stable with the minimum ground state energy. We have performed the magnetic configuration dependent ground state energy calculation from the 111-surface slab. The 111-surface slabs of Fe_2CoAl are again categorized with three different terminal atoms like Fe-, Co- and Al-terminals as shown in Figure 4.5 (a), (b) and (c). The seven magnetic configurations are considered including one ferromagnetic (FM) and six types of antiferromagnetic (AFM) orientations as shown in Table 4.3, Table 4.4 and Table 4.5 for each Fe-, Co and Al-terminal, respectively. In terms of their minimum ground state energy with corresponding magnetic configurations; Al-terminal is stable with AFM1-configuration, Fe-terminal with AFM2 configuration and Co-terminal with FM configuration.

4.2.1.2 Electronic and magnetic properties

In Figures 4.6 and 4.7, we have presented the spin-resolved partial density of states (DOS) and energy band structures of three terminal 111-surface slab of Fe_2CoAl, calculated from GGA and GGA+U (U_{Fe} = 3.82 eV and U_{Co} = 3.89 eV) (Rai *et al.*, 2012) to study the electronic properties. For each terminal, we considered the surface, subsurface-1 and subsurface-2 atomic layers to reveal the electronic properties. We observed a metallic behavior in both the spin channels with dispersed bands around the Fermi level due to the breaking of metallic bonding when the non-periodic surface slab is cleavage from the periodic bulk system and also the DOS decreases from GGA to GGA+U calculation in all cases [Figure 4.6(a), (b) and (c)]. In Al-terminated surface, as shown in Figure 4.6(a), all the Fe1-d, Al-p and Fe4-d spin-up and spin-down states are dispersed around the Fermi level (EF) within GGA and GGA+U calculation. The higher occupation of Fe4-d states prior to Fe1-d states around the E_F in the spin-down channel may be due to the absence of *d-d* hybridization between Fe4-d and Fe1 -d states. A higher peak of Fe4-d spin down states likely reveals the surface reconstruction (Galanakis, 2002; Paudel & Zhu, 2019).

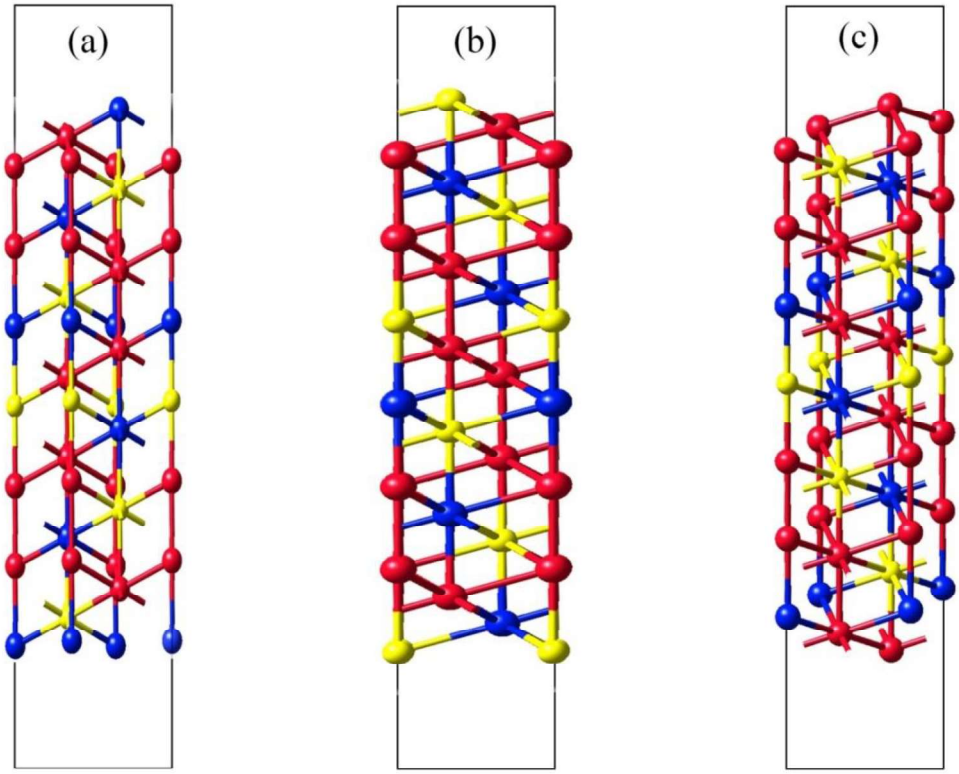

Figure 4.5: Conventional slab model (Side-view) for (a) Ferromagnetic Co-terminal (b) Antiferromagnetic (AFM1) Al-terminal and (c) Antiferromagnetic (AFM2) Fe-terminal.

Interestingly, we observed a small spin-down band gap (0.19 eV) between 0.55 eV–0.74 eV in the conduction band from GGA calculation. By treating electron-electron interactions in GGA+U calculation, free electrons abruptly reduced which results lesser population states. The presence of small hybridization between Co1-*d* and Fe1-*d* in spin-down states results in coupled states at the E_F in FM Co-terminated surface, the similar trend of results are obtained for AFM1 Al-terminated and AFM2 Fe-terminal electronic structure. We have calculated the total spin polarization degree for each terminal using the relation equation (1) (Soulen *et al.*, 1998)

$$P = \frac{N_{\uparrow}(E_F) - N_{\downarrow}(E_F)}{N_{\uparrow}(E_F) + N_{\downarrow}(E_F)} \tag{4.5}$$

where $N_{\uparrow}(E_F)$ and $N_{\downarrow}(E_F)$ are the densities of states at E_F for spin-up and spin-down channels respectively.

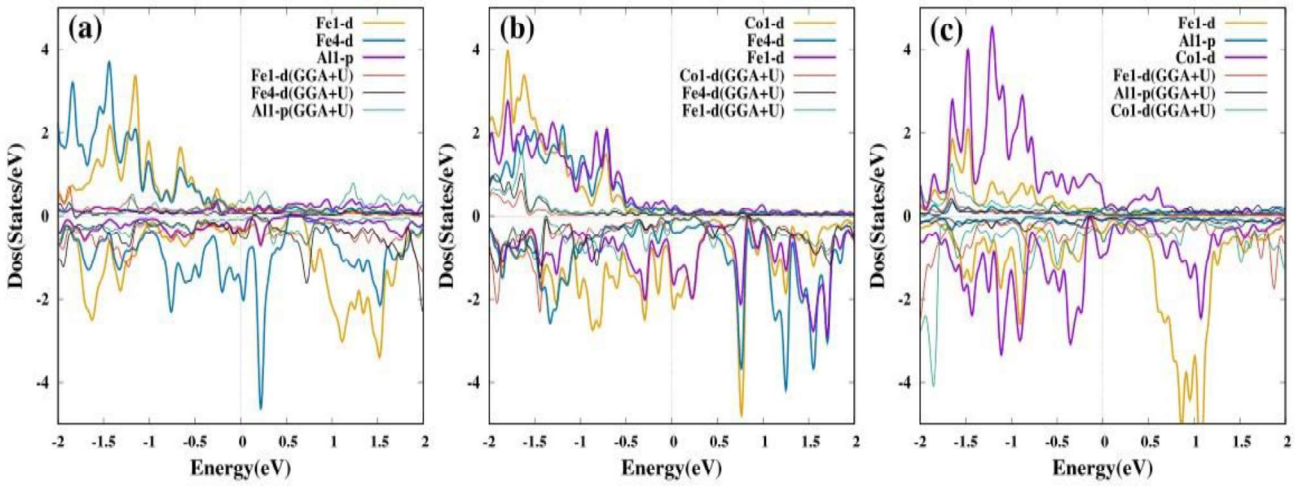

Figure 4.6: Calculated partial DOS of Fe_2CoAl-111 surfaces from GGA and GGA+U: (a) Al-terminal, (b) Co-terminal and (c) Fe-terminal

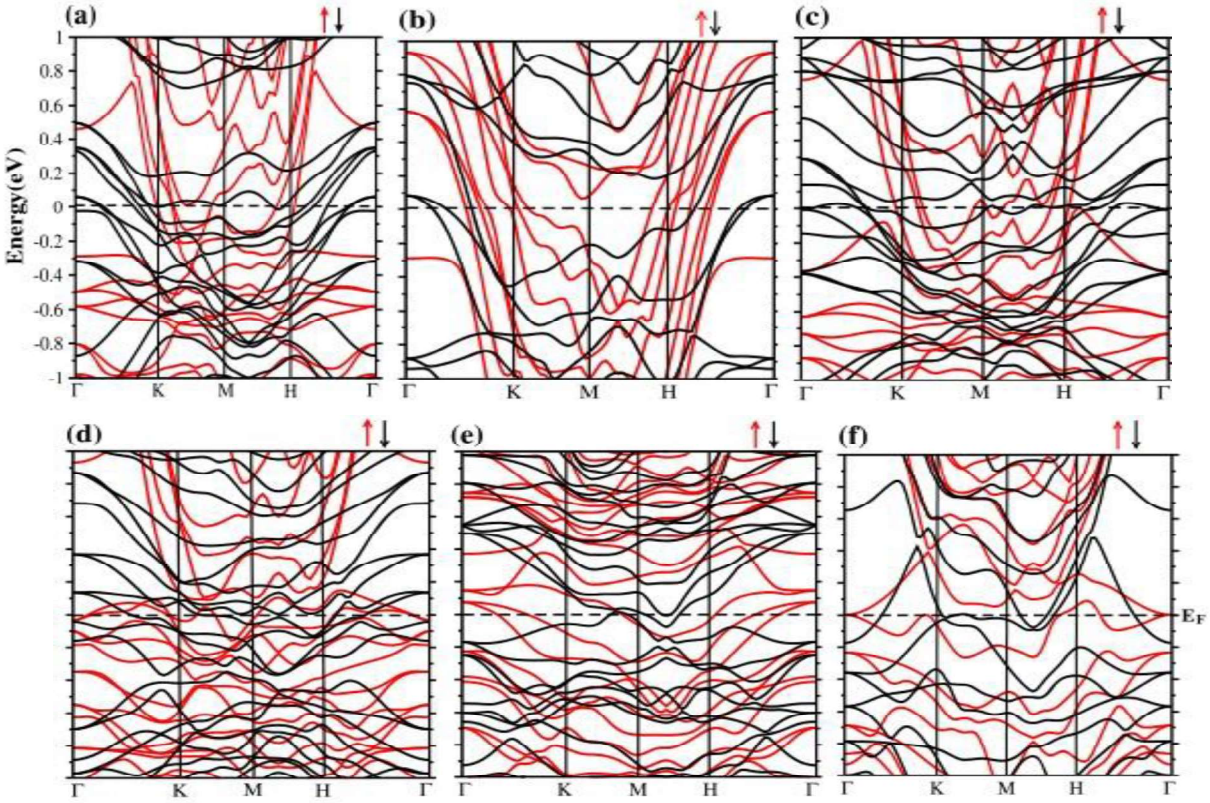

Figure 4.7: Calculated band structures of Fe_2CoAl-111 surfaces: (a) Al-terminal (GGA), (b) Al-terminal (GGA+U), (c) Co-terminal (GGA), (d) Co-terminal (GGA+U), (e) Fe-terminal (GGA) and (f) Fe-terminal (GGA+U).

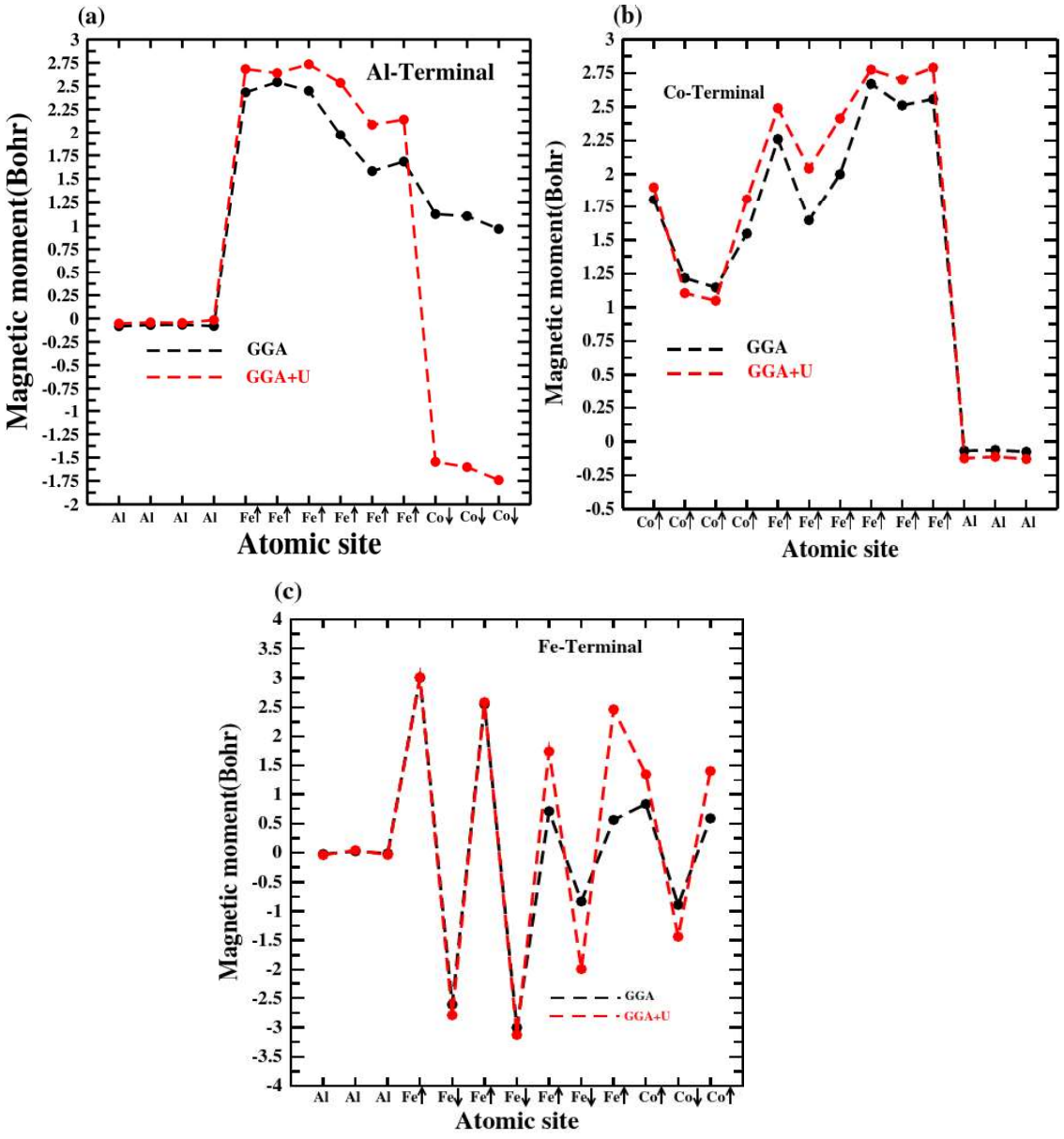

Figure 4.8: Atomic resolved magnetic moment (a) Al-terminal (b) Co-terminal and (c) Fe-terminal.

We estimated the polarization degree 65% (GGA) and 21.7% (GGA+U) for Al-terminal, 62.4% (GGA) and 36.5% (GGA+U) for Co-terminal, where a comparatively low polarization degree with 40% (GGA) and 5% (GGA+U) for Fe-terminal. The calculated total magnetic moments are found to be 18.9μ_B (GGA) and 20.46μ_B (GGA+U) for ferromagnetic Co-terminal and comparatively higher than

Table 4.6: Comparison between surface/subsurface atomic sites magnetic moment (in μ_B) with their corresponding moment in the bulk Fe_2CoAl.

	Atomic site	$\mu_B(GGA)$	$\mu_B(GGA+U)$
Al-terminal	Fe-4	2.45	2.68
	Fe-1	2.43	2.53
Co-terminal	Co-1	1.80	1.90
	Fe-4	2.67	2.77
	Fe-1	2.25	2.48
Fe-terminal	Fe-1	3.00	3.01
	Co-1	0.83	1.35
Bulk	Fe-1	2.56	2.76
	Fe-2	1.64	2.16
	Co	1.18	0.89

antiferromagnetic Al-terminal [5.32μ_B (GGA) and 9.73μ_B (GGA+U)] and Fe-terminal [0.03μ_B (GGA) and 3.5μ_B (GGA+U)] calculation partial magnetic moments of the corresponding magnetic moment of the bulk Fe_2CoAl (Siakeng *et al.*, 2018) is shown in Table 4.6. The moment of Fe4 atoms in sub-surface1 for Al- and Co-terminals are comparable with the moment of Fe1 site in the bulk whereas, the Fe1 moment of the sub-surface2 are likely within the range of Fe1 and Fe2 site in the bulk structure. But, the values of magnetic moment of Co1 atom in Co-terminal surface is fractionally higher as compared to that of the Co1 atom at sub-surface1 of the Fe-terminal and the bulk within both GGA and GGA+U calculation in calculation. The atomic sites magnetic moments from GGA and GGA+U are also presented in Figure 4.8. The anti-parallel configured three Co-atoms of Al-terminal experienced parallel magnetization along with Fe-atoms from GGA calculation this may be due to the strong coupling between Co-atoms and Fe-atoms within the core-region of the slab. The magnetic atoms (Fe and Co) in the FM Co-terminal shows parallel magnetization as expected where the moment of magnetic atoms in the AFM2 Fe-terminal oscillate around zero.

4.2.1.3 Perpendicular Magnetocrystalline anisotropy Energy

We calculated the energy required to switch the magnetization direction from easy (xy) axis to the perpendicular direction (z) of the crystal axis for each terminal, which is usually termed as perpendicular magnetocrystalline anisotropy energy (MAE). We estimated the total in-plane MAE values 0.034 meV/cell and 0.68 meV/cell for the two antiferromagnetic Al(AFM1)- and Fe-(AFM2) terminated surfaces respectively, whereas the out-plane total MAE -0.087 meV/cell for ferromagnetic Co-terminated surface.

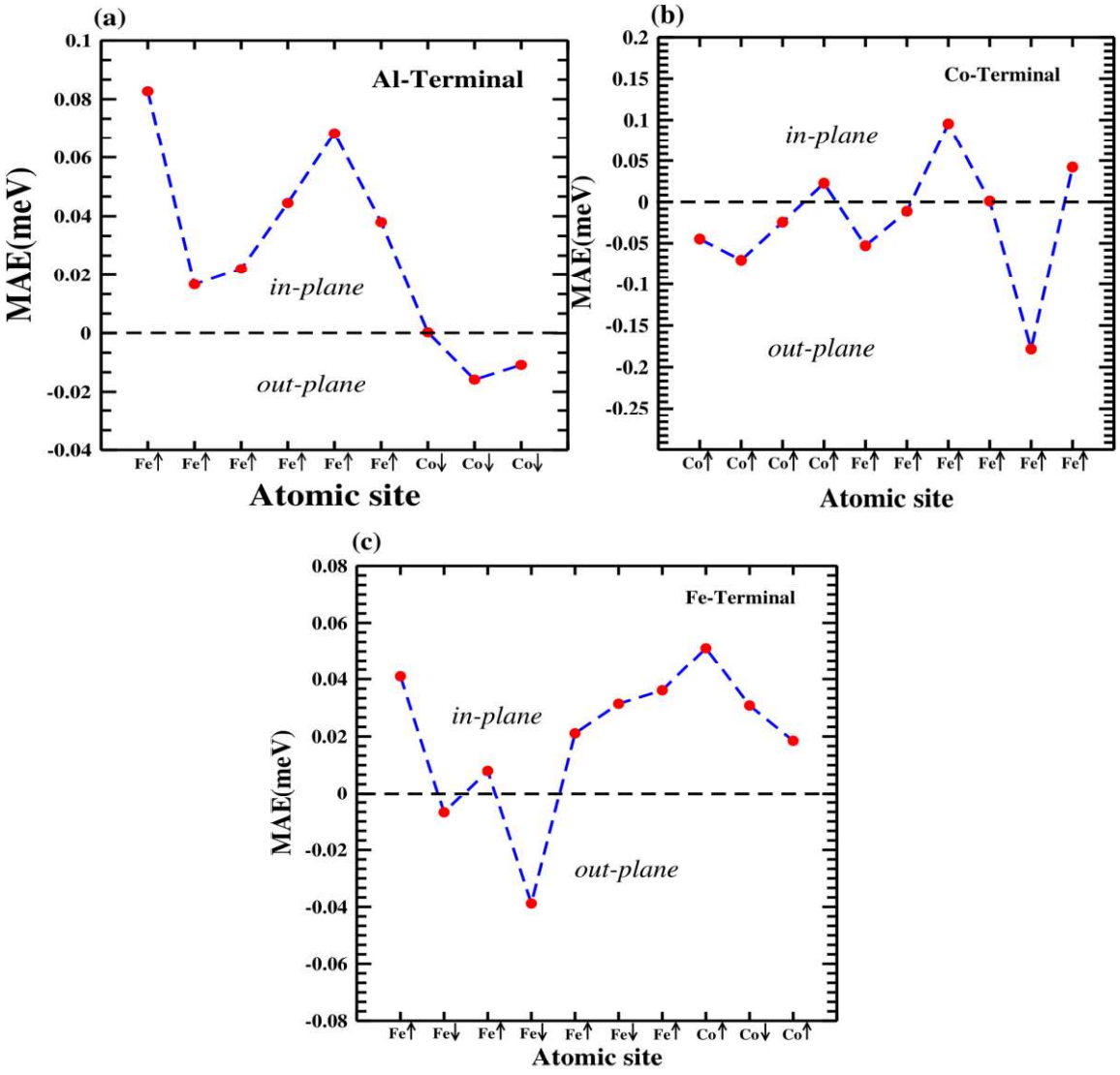

Figure 4.9: Calculated Atomic resolved magnetocrystalline anisotropy energy (MAE) of 111-plane of Fe_2CoAl (a) Al-terminal and (b) Co-terminal and (c) Fe-terminal.

The distribution of total MAE over an atomic site *i* is given by Equation 4.6 (Li *et al.*, 2014)

$$MAE_i = \int^{E_F^1} (E - E_F) n_i^1(E) dE - \int^{E_F^2} (E - E_F) n_i^2(E) dE \quad (4.6)$$

where E_F is the Fermi energy of obtained from non-SCF calculation with SOC and subtracted from all the eigen values to produce correct local decomposition of MAE. Figure 4.9 shows the atomic resolved MAE for different terminals. In case of antiferromagnetic Al-terminal (AFM1) and Fe-terminal (AFM2), we have noticed the dependence of total MAE on the atomic resolved surface and sub-surfaces. In case of Co-terminal, the out of plane favor the surface atomic site whereas the sub-surfaces are ferromagnetic. The major contribution to the total out-plane MAE is neither dominated by surface nor by sub-surface atoms rather from the core-region. This may be due to the cancellation between surface and sub-surface atomic moments (Li *et al.*, 2014). Usually the cubic bulk structure exhibit negligibly small MAE per atom, but it is possible to get higher measurable values of MAE (more likely in meV) in nanostructures (Gambardella *et al.*, 2003; Rusponi *et al.*, 2003) due to reducibility of dimension or miniature in size scale. Unfortunately, we do not have sufficient reported data to compare our results.

4.3 Mn_2CoSi- Surface half metallicity at MnSi termination of [001] Mn_2CoSi

An ab-initio spin polarized DFT calculations of the bulk and surface electronic structures were performed using MedeA-VASP based on the programmed where the core ionic interaction was shaped by the projector augmented wave (PAW) method and linear combination atomic orbital (LCAO) method as implemented in QuantumATK Q-2019.12 Simulation package. Using correlation exchange functionals within the generalized gradient approximation (GGA)-Perdew-Burke-Ernzerhof (PBE) formalism for describing all the electron interactions. For numerical accuracy of VASP simulation, a plane wave cut off energy of 400 eV and with an accurate 12×12×1 k-mesh Monkhorst pack grid were used to integrate a plane wave

basis set for the first Brillouin zone. The self-consistent field calculation steps were performed till the energy difference reaches less than 10^{-5} eV. Structural relaxation was attained via conjugate gradient (CG) algorithm as integrated in VASP by minimizing the energy and atomic forces with a force tolerance of 0.02 eV/A. For a norm-conserving pseudopotential based LCAO is configured to a density mesh cutoff 120 Hatree with 12×12×1 k-point sampling for the surfaces calculation. Two natural terminated viz., MnSi and MnCo relaxed thin film of Mn_2CoSi (001)-having 13 diatomic layers [Figure 4.10 (a) and (b)] have been analyzed to validate the surface electronic properties

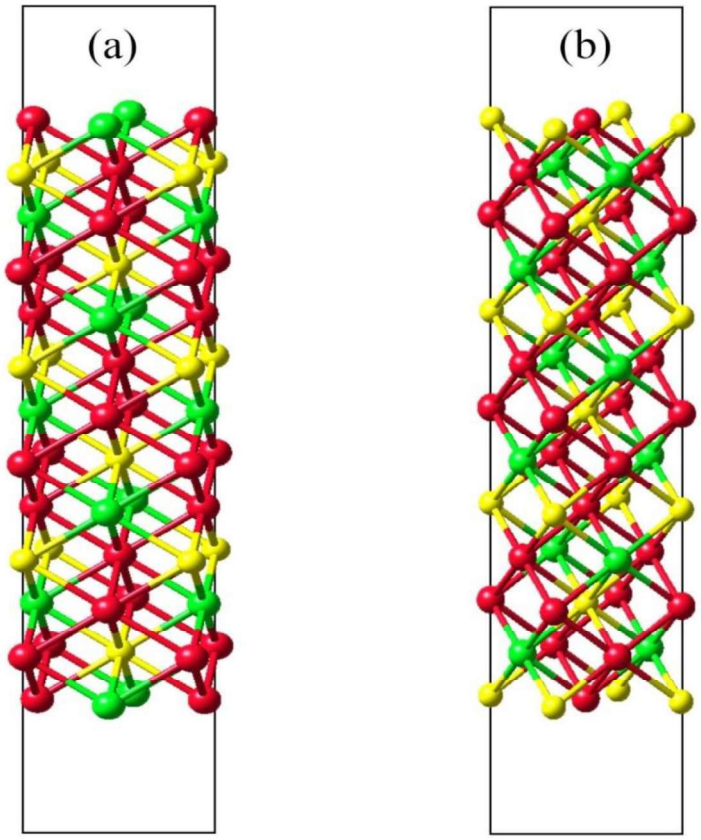

Figure 4.10: Conventional slabs model (side view) of (a) MnCo and (b) MnSi-terminated surface of |001| Mn_2CoSi

4.3.1 Results and Discussions

4.3.1.1 Structural Optimization and Stability

We exfoliated two ideal termination; MnSi and MnCo from the optimized bulk structure using (1 × 1) supercell method. Modelling the slabs with 13 diatomic layers and to prevent the adjacent slabs interplay a vacuum of 15 Å had been applied on both the sides of the slabs. The generated in-plane lattice parameter of these slabs are estimated with $a\sqrt{2}/2$, where a, the equilibrium lattice constants. In all the structural relaxation the top five layers are relaxed with the core three layers fixed. The relaxed structures are presented in Figure 4.11 in terms of surface(s), sub-surface (s1) and the second sub-surface (s2) atomic displacement with respect to their unrelaxed position. In MnSi terminal, a minimal inward relaxation have been observed for Si(s) and outward relaxation for Mn(s) resulting surface buckling around 0.26 Å, this may be due to the surface and near surface layer tend to rearrange the valence displaced electrons (Chis & Hellsing, 2004; Hashemifar *et al.*, 2005) which drove the ionic force towards vacuum and resulting outward relaxation of Mn(s) atom in MnSi-terminated surface. Despite of two algorithm approach a symmetric pattern of relaxation for MnSi terminated surface are achieved within conjugate gradient method and BFGS method. Both the surface Mn(s) and Co(s) atoms are relaxed inward for MnCo-terminal surface. The calculated surface energy, relaxation energy and pressure exerted by the system according to their respective volume presented in Table 4.7, where $\gamma(\text{eV}) = (E_{slab} - \text{N}E_{bulk})/2\text{A}$ (Galanakis *et al.*, 2002) and ΔE_{relax} accounted for the change in energy during structural relaxation. It can be clearly seen that MnSi terminated surface is energetically favorable as compared to MnCo terminated surface due to lower surface energy and energy change involved during structural relaxation, so for that we do not performed calculations on MnCo terminated surface for norm-conserving pseudopotential based approach. The negative values of pressure exerted by the systems during relaxation indicated that structural compressed relaxation in both the terminal surfaces. Therefore, we adopted only MnSi terminated surface for our interface calculations. Since Nath et al., successfully growth thin film of Mn_2CoSi on p-Si substrate via SiO_2 as a spacer for efficient spin injection at room temperature (Maji & Nath, 2019), therefore it may be reasonable to exclude thermodynamic stability calculation from first principle method.

Table 4.7: Calculated atomic magnetic moment (in μ_B) of surface (s), sub-surface (s1) central layer (C.L) and corresponding calculated values in their respective bulk structure.

Plane	**γ(eV)**	**ΔE_{relax}**	**P(GPa)**
MnSi	-2.4	-0.27	-1.17
MnCo	-2.31	-0.34	-1.1

	medeA-VASP (Units are in μ_B)				**QuantumATK (Units are in μ_B)**			
	Mn	Si	Co	C.L	Mn	Si	Co	C.L
MnSi	3.54(s)	-0.08(s)	0.8(s1)	2.6(Mn)	4.12(s)	-0.35(s)	0.79(s1)	2.9(Mn)
				0.004(Si)				-0.13(Si)
MnCo	0.46(s)	-0.014(s1)	0.94(s)	-0.46(Mn)	-	-	-	-
				0.89(Co)	-	-	-	-

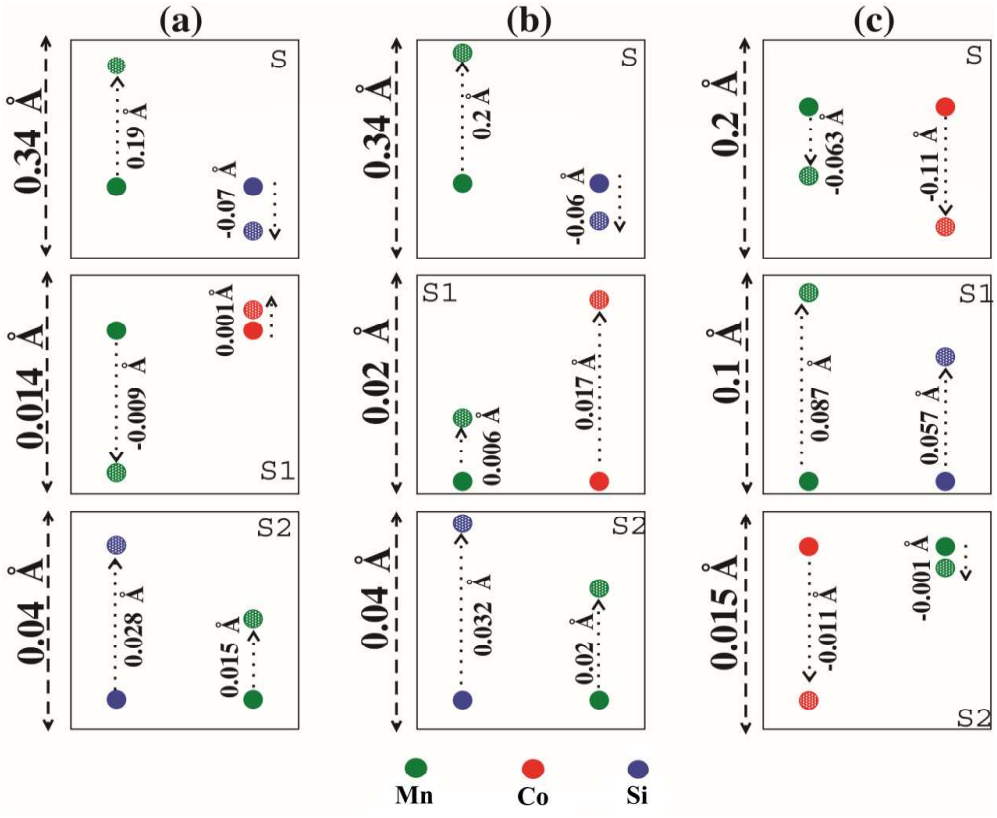

Figure 4.11: Top three layers atomic displacement of the relaxed structure from the unrelax position (a) MnSi-terminal's surface relaxation from conjugate gradient (CG) method (b) MnSi-terminal's surface relaxation from BFGS (c) MnCo-terminal's surface relaxation from CG method. [Arrow indicates direction of atomic relaxation]

4.3.1.2 Electronic and magnetic properties

The surface electronic structure can be analyzed from the spin polarized partial density of states and band structures calculation that are presented in Figure 4.12 and Figure 4.13, respectively. Firstly, we performed surface electronic study for both the slabs MnSi- and MnCo-terminated surface using VASP simulation package that are presented in Figure 4.12 (a), (c). The bulk half metallic structure is preserved in MnSi terminated surface with a minority spin (↓) gap at around E_F with a metallic nature in majority spin (↑) channel. For MnCo-terminal, the half metallicity is destroyed with the surface dispersed states in minority spin (↓) channel mainly derived from Mn(s) and Co(s)-*d* delocalized states as presented in Figure 4.12 (c) and Figure 4.13 [MnCo (Spin-down) panel], this may be attributed to the weak *d-d* re-hybridization after losing half of their respective nearest neighbor atoms which in turn may did not induced sufficient energy splitting of hybridized e_u-t_{1u} states at around E_F. We further confirmed half metallicity of MnSi-terminal using QuantumATK Q-2019.12 simulation package as shown in Figure 4.12(b). We estimated a nearly similar electronic structure for MnSi terminated surface except the p-orbital states of Si is slightly more pronounce in low energy regime of bonding states within linear combination of atomic orbitals calculation. It is worth to note that due to a natural surface lattice plane of 001 MnSi-terminal, the surface Mn atom is exactly Mn1 site atom of the bulk crystal having Mn2 site and Co atoms as its nearest neighboring atom. Even after the reduction of co-ordination number, Mn(s)-d states governed a sufficiently strong *d- d* re-hybridization with sub-surface atoms; Co(s1)-d states, which induced and energy splitting between the bonding and antibonding states. We can also perceived a well-defined band gap characterized by the subsurface atoms Co(s1) and Mn(s1) as shown in the middle panel of Figure 4.12 (a) and (b), this may possibly indicated that a negligible surface effect on strong covalent hybridization between Mn(s1) and Co(s1) and Mn(s) $d-d$ states which turned out energy splitting between e_u-t_{1u} states to open up band gap around E_F. It can be learned from Figure 4.13, a minority direct band gap rather than bulk's indirect gap along high symmetry Γ - point is observed.

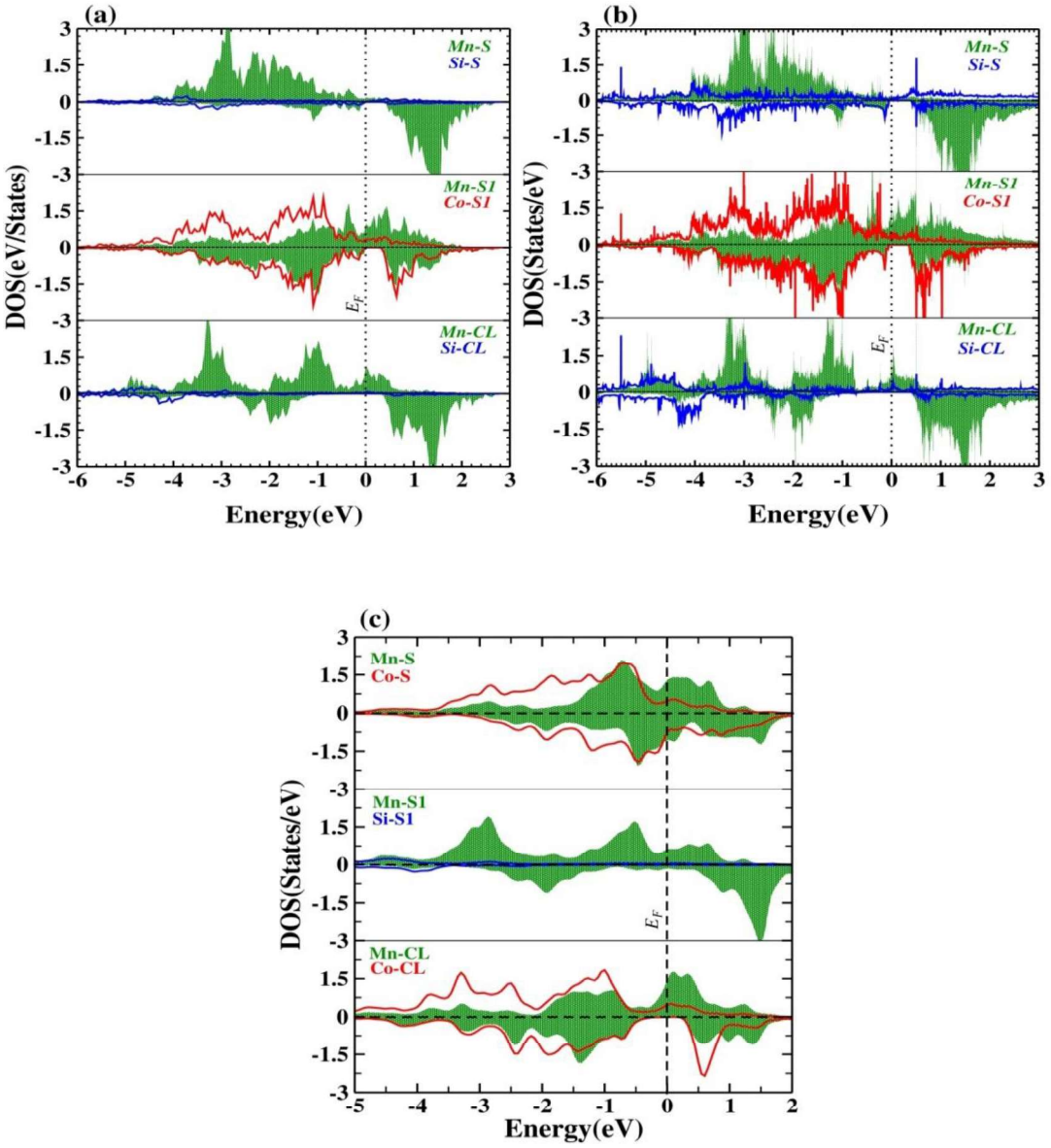

Figure 4.12: Spin resolved DOS for MnSi-terminal: (a) From MedeA(VASP) (b) From QuantumATK 2019.12 calculations and (c) MnCo-terminal from MedeA (VASP).

Nonetheless, bulk half metallic nature is well maintained in the central region atoms as shown in Figure 4.12 [each bottom panel in (a), (b) and (c)] in accordance with their respective bulk like band gap in both MnSi and MnCo terminated slabs. This reasonably meant that the slab thickness is sufficient enough to image out the bulk nature within central region.

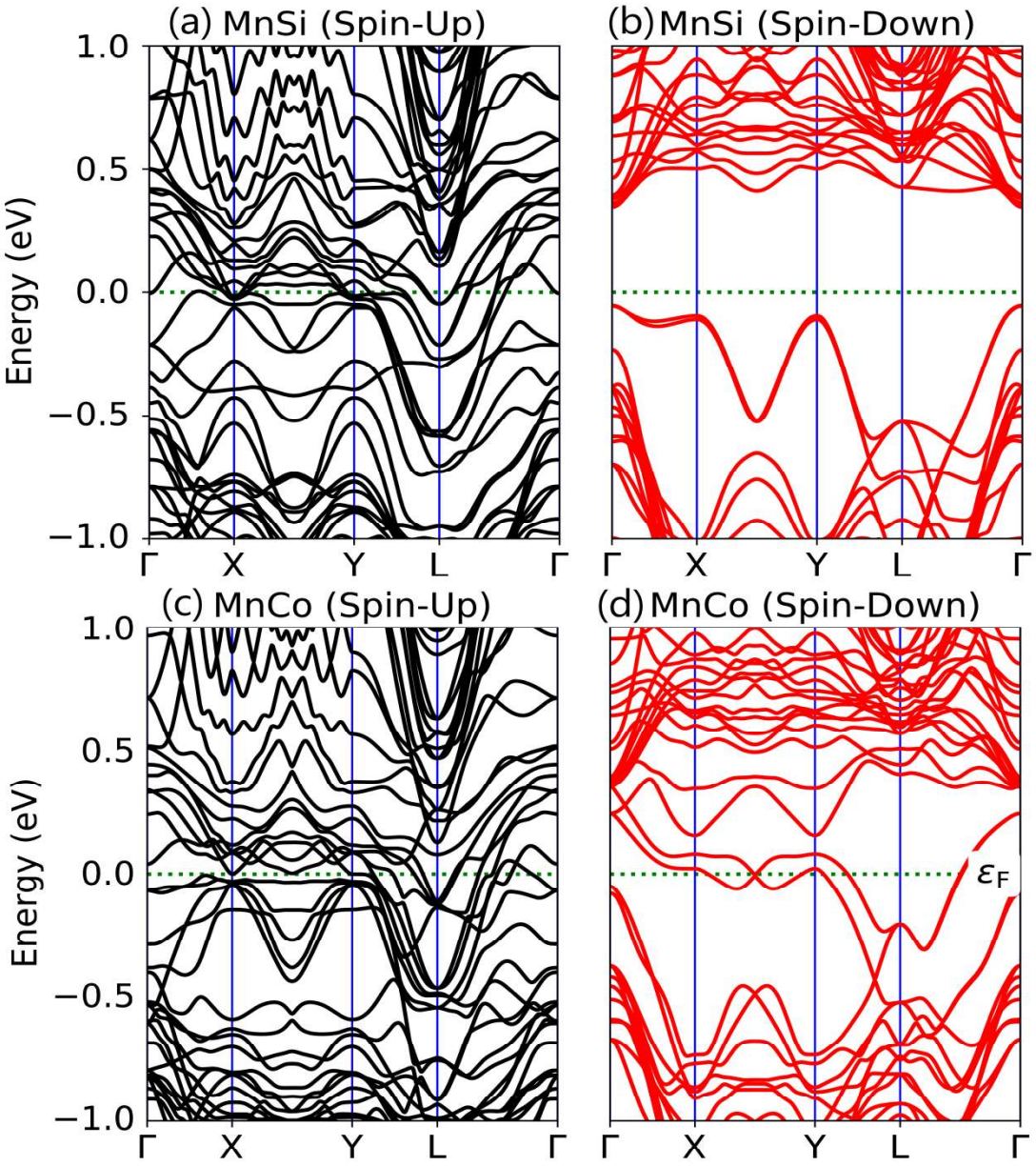

Figure 4.13: Calculated band structures along high symmetry point of MnSi-terminal : (a) Spin-up (b) Spin-down and MnCo-terminal: (c) Spin-up (d) Spin-down

The calculated atomic resolved magnetic moment for the surface and subsurface atoms are presented in Table 4.7, the enhancement of localized spin moment of surface atom Mn(s) in MnSi terminated surface is revealed from both the calculation approach. The presence of broken translational symmetry at the non

periodic surface tends to rearrange the displaced valence electrons that leads to a strong intra-atomic exchange interaction, induced a larger localized spin magnetic moment of Mn(s) as compared to the respective magnetic moment in bulk. The anti-parallel spin moment of surface Si(s) atom had slightly increases which may be due to the direct exchange between p-orbital from Si(s) and dorbital of the subsurface Mn(s1) atoms. The subsurface Co atom has less experienced surface effect with a negligibly variation from the bulk value. In MnCo surface, the Mn2 site of the bulk structure is terminated and unexpectedly a parallel spin is observed between Mn(s) and Mn(s1), so for that reason it can be obvious that the antiparallel moment induced in Si(s1) arises from the second subsurface Mn atom. The complexity of surface and subsurface atoms magnetic structure may be due to the presence of competition between direct exchange and antiferromagnetic superexchange interaction. The higher value of calculated spin moment within QuantumATK approach is depends on the incorporated basis sets which generally resulting higher deviation as compared to PW method.

5

X_2YZ-type Heusler and Semicondutor hetero-junction Interface for spin injection properties

5.1 $Mn_2CoSi|CaS|Mn_2CoSi$ MTJ Device

In this chapter, quantum spin transport character is investigated using Mn2CoSi (001) with semicoductor CaS (001) MTJ device. The selection of CaS semiconductor is mainly due to the fact that, to minimize the resistance area product in the interface structure which in turn attributed to the similar crystallization cubic structure and the theoretical and experimental lattice parameter were within the range of 5.4Å- 5.72Å (Bayrakci *et al.*, 2009; Charifi *et al.*, 2005; Luo *et al.*, 1994; Salam & Manal, 2018; Straub & Harrison, 1989) which are closely matching with our calculated Mn2CoSi lattice parameter (5.62Å), we adopted CaS lattice 5.69Å) (Ekbundit *et al.*, 1996) for our calculation. The interface structure is modeled by matching the two in-plane lattice using the co-incidence site lattice method as implemented in QuantumATK. Grid size; search through the grid given by $nV_1 + mV_2$. The vectors V_1 and V_2 are the basis of the first lattice. The integers n and m run from - n^{max} to n^{max} and - m^{max} to m^{max} where n^{max} = 6 and m^{max} = 6. Scanning the rotation angle between the two surfaces a large step size calculation time at the risk of missing relevant matches; scan angle from 0° to 180° with an increment of 4°. Using first surface straining method, strains within the tolerance of $1e^{-06}$ are considered equal. With the mean absolute strain of 0.92%; two probe symmetric electrode of Mn2CoSi (001) with a barrier of CaS(001) MTJ device is designed. Both the left and right principal layer electrode length are configured to be 11.224Å with symmetric atomic termination, the length of central region lattice is 47.536Å where the in-plane lattice is 3.97Å through-out the device. The atomic positions of central region are fully relaxed. The optimized distance between Mn-Ca is found to be 2.5Å. The spin dependent transport properties have been studied from unbiased voltage and with an application of some finite bias voltages.

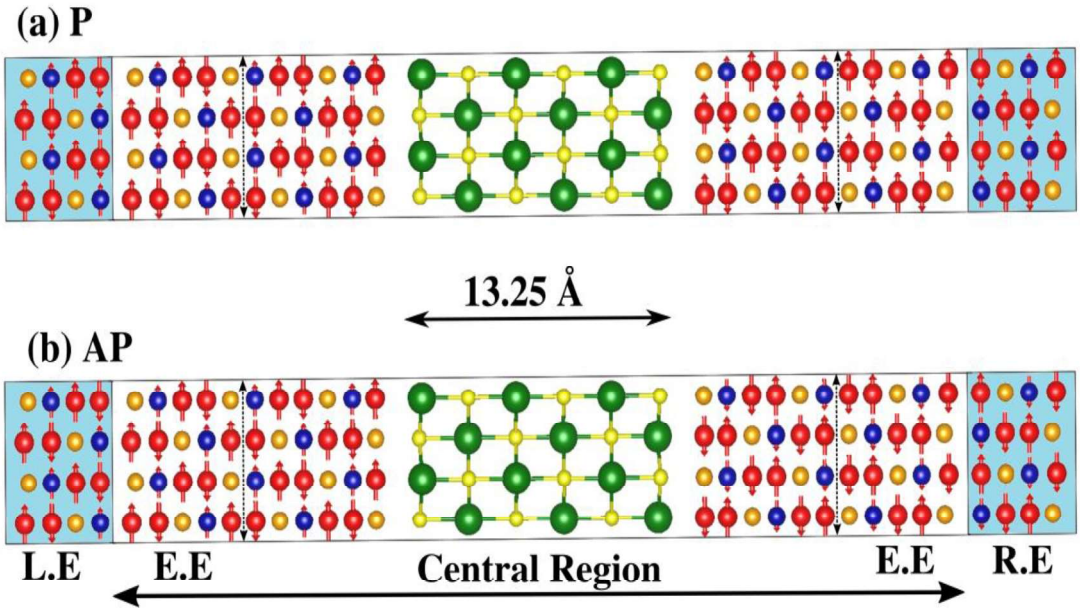

Figure 5.1: The modeled MTJ device and initial spin degree of freedom for (a) parallel configuration (P) and (b) antiparallel configuration (AP); L.E (R.E) →Left (Right) Electrode and E.E→ Electrode Extension layer upto dashed - ↕ for both the left and right electrodes.

5.2 Results and Discussions

The quantum transport calculation is based on the combination of non-equilibrium Green function-density functional theory (NEGF-DFT) formalism (Stradi *et al.*, 2016) as implemented in QuantumATK-2019.12. The K-point is sampled 10×10×200 Monkhorst-Pack (MP) grid to converge the density matrix. For transmission coefficients calculation; 200×200 MP is used to integrate the 2D full Brillouin zone along the transverse Bloch wave vectors $K_{\parallel}$ (k_A,k_B). The transmission coefficient T at electron energy ∈ is obtained from the retarded Greens function (Petersen *et al.*, 2008);

$$T(\epsilon) = Tr[G(\epsilon)\Gamma^{L}(\epsilon)G^{\dagger}(\epsilon)\Gamma^{R}(\epsilon)] \quad (5.1)$$

Where, $G(\epsilon) = \left[(\epsilon + i\delta_{+})S - H - \sum^{L}(\epsilon) - \sum^{R}(\epsilon)\right]^{-1}$ is the retarded Greens function matrix for the central region. And $\Gamma^{L(R)} = \frac{1}{i}\left(\sum^{L(R)} - \left(\sum^{L(R)}\right)^{\dagger}\right)$: the broadening functions of the electrodes. The electrical current is given by the Landauer formula:

$$I = \frac{2e}{h}\int_{-\infty}^{\infty} d\epsilon T(\epsilon)\left[f\left(\frac{\epsilon-\mu_L}{k_B T_L}\right) - f\left(\frac{\epsilon-\mu_R}{k_B T_R}\right)\right] \quad (5.2)$$

e the electron charge, h the Planck's constant and $f_{L,R} = \left[1 + exp\left\{\frac{\epsilon-\mu_{L(R)}}{k_B T_{L(R)}}\right\}\right]^{-1}$ is the Fermi-Dirac distribution. The chemical potential of the left (right) electrode is denoted as $\mu_{L(R)}$. The tunneling magnetoresistance ratio (TMR) is calculated using the optimistic approach;

$$TMR(Optimistic) = \frac{G_P - G_{AP}}{G_{AP}} \quad (5.3)$$

Where G_P and G_{AP} are the conductance in parallel and antiparallel configuration respectively.

According to Fermi golden rule the probability of electron tunnelling from a metal electrode to a semiconducting one (in ML/insulator/MR) taking into account the wave functions in the electrodes given by

$$P_{L,R} = \frac{2\pi}{\hbar}\left|M_{L,R}(\epsilon, V_b)\right|^2 f_L(\epsilon)\rho_k^L(\epsilon)[1 - f_R(\epsilon)]\rho_k^R(\epsilon) \quad (5.4)$$

where $P_{L,R}$ is the electron tunneling probability from the left electrode (M_L) to the right electrode (M_R), $f_L(\epsilon)$ and $f_R(\epsilon)$ are the occupation probabilities in the L and R electrodes and $M_{L,R}$ (E,Vb) is the transfer matrix element. Concerning the above equation, the current density passing from L to R) during the tunneling process, is written as:

$$J_{L,R} = -\frac{4\pi e}{\hbar}\sum_k \int_{\mu_L}^{\mu_R} \left|M_{L,R}(\epsilon, V_b)\right|^2 f_L(\epsilon)\rho_k^L(\epsilon)[1 - f_R(\epsilon)]\rho_k^R(\epsilon)d\epsilon \quad (5.5)$$

Similarly, the current density from ($M_L \rightarrow M_R$) electrode is given by:

$$J_{R,L} = -\frac{4\pi e}{\hbar}\sum_k \int_{\mu_L}^{\mu_R} \left|M_{L,R}(\epsilon, V_b)\right|^2 f_R(\epsilon)\rho_k^R(\epsilon)[1 - f_L(\epsilon)]\rho_k^L(\epsilon)d\epsilon \quad (5.6)$$

Considering $M_{L,R} = M_{R,L}$, the net current density is $J = J_{L,R} - J_{R,L}$ is

$$J = -\frac{4\pi e}{\hbar}\sum_k \int_{\mu_L}^{\mu_R} \left|M_{L,R}(\epsilon, V_b)\right|^2 \rho_k^L(\epsilon)\rho_k^R(\epsilon)[f_L(\epsilon) - f_R(\epsilon)]\, d\epsilon \quad (5.7)$$

Fermi-Dirac distribution functions and the product $\left|M_{L,R}(\epsilon,V_b)\right|^2\rho_k^L(\epsilon)\rho_k^R(\epsilon)$ depends on the band structure of the electrodes and the barrier characteristics.

With the above equation, the quantum conductance *dJ/dV* is given by;

$$G=\frac{dJ}{dV_b}=-\frac{2\pi e}{\hbar}\sum_k\int_{\mu_L}^{\mu_R}\left|M_{L,R}(\epsilon,V_b)\right|^2\rho_k^L(\epsilon)\rho_k^R(\epsilon)\frac{df_R(\epsilon)}{dV_b}d\epsilon \qquad (5.8)$$

When T→0, $\frac{df_R(\epsilon)}{dV_b}$ approaches a delta-Dirac function; for constant $M_{L,R}$ and an infinitesimal V_b ,then we have;

$$G\infty\left|M_{L,R}(\epsilon,V_b)\right|^2\rho_k^L(\mu_L)\rho_k^R(\mu_R) \qquad (5.9)$$

This equation shows that the probability of tunnelling conductance is directly related to the density of states (DOS) of the electrons in the metallic electrodes at the Fermi level. This model can be used in describing electron spin tunnelling.

5.2.1 Spin Dependent Transport Properties

The antiferromagnetic coupling between two inequivalent Mn-sub lattices led to the ferrimagnet MTJ configuration. Firstly, the initial spin degree of freedom is constrained to be antiferromagnetic configuration, so the two symmetric electrodes (Say AFM1 and AFM2) have antiferromagnetic coupling sub-lattices magnetic structure separately. For AFM coupling spin source, the presence of complex magnetic structure complicates the spin transport phenomena. The spin channel of left electrode will be an opposite channel at right electrodes. In that sense, the transmission coefficients will be low and the corresponding resistance will be high. The calculated transmission coefficients are at zero-bias condition and at various finite bias voltages is presented. From Figure 5.2 it can be seen that the calculated spin transports property at equilibrium condition revealed that, for parallel configuration a small transmission coefficient at Fermi level E_F and K-dependent transmission peak at around 1.8eV above the Fermi level is observed for majority spin states which originated from the conduction Δ1 bands composed of Mn-d states and Si-p states (Miura *et al.*, 2007) along Γ-point, whereas a drastic fall of transmission probability near the Fermi level is observed in the minority spin channel because there are no minority-spin Bloch states in the electrode region due to the half metallic

minority gap of the electrode that lead to coherent tunneling. However, for anti-parallel configuration the transmission localized peak is surrounded by zero-transmission regions. An identical transmission curves are observed for spin-up and spin-down

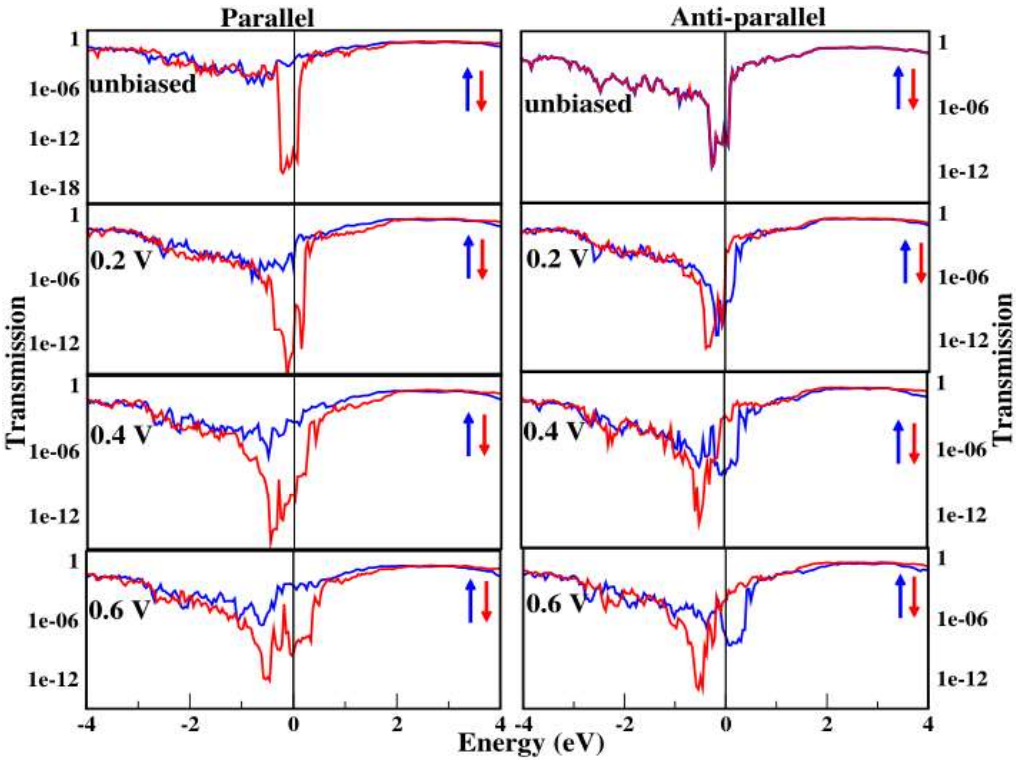

Figure 5.2: Transmission coefficient (in log scale) as a function of bias voltage for parallel P and antiparallel AP-configuration within electron energy range - 4 to 4 eV, direction of blue and red arrow indicate spin-up and spin-down states

states due to the mirror symmetry of the device. In time inversion symmetry, the transmission from left to right is always identical to the transmission from right to left electrodes. The spin up (spin-down) component of the transmission probability corresponds to spin-up (spin-down) electrons from the left (right) electrode propagation into the right(left) electrode. Due to the anti-symmetric spin, the up electrons in the left electrode and the down electrons in the right electrode are both majority channels. At equilibrium, because of the mirror symmetry of the device, the spin polarized transportation or conductance of the left majority channels into the

right minority channels ($G^{\uparrow\downarrow}$) and the spin polarized transportation of the right majority channels into the left minority channels ($G^{\downarrow\uparrow}$) are more or less identical. Thus, it is worth note that for symmetric devices, the equivalence of the two spin channels is a crucial validation for antisymmetric calculations at zero bias. The zoom in view of $K_{\parallel}$ (k_A,k_B) resolved transmission coefficient contour plots around Γ-point are presented in Figure 5.4 [for P (a) spin up (b) spin down and for AP (c) spin up (d) spin down], the full 2D Brillouin zone view are presented in Figure 5.3. For P configuration, a circular pattern of polarized transmission around the Γ-point were observed for both spin up and spin down states; that exactly the main contribution for spin down transmission [Figure 5.4 (b) and Figure 5.3 (b)], while for spin up in addition transmission around Γ-point, it can be seen that transmission contributed from some special point in the vicinity of the 2D BZ edges [Figure 5.4(a) and Figure 5.3 (a)] The In Table 5.1, we present our calculated spin polarized conductance with respect to applied bias; it can be noted that an extremely large difference in conductance of the order of three magnitude for parallel configuration and anti-parallel configuration which results large tunneling magnetoresistance ≈ 1.5×10^4% at equilibrium condition. Whereas, the TMR for finite bias voltage are calculated using the relation (Feng *et al.*, 2019; Montes *et al.*, 2016):

$$TMR = \left|\frac{I_P^{Total} - I_{AP}^{Total}}{I_{AP}^{Total}}\right| \times 100\% \qquad (5.4)$$

Table 5.1: The calculated spin polarized quantum conductance (in Siemen) for parallel magnetization ($G^{\uparrow\uparrow}$, $G^{\downarrow\downarrow}$) and anti-parallel magnetization ($G^{\uparrow\downarrow}$, $G^{\downarrow\uparrow}$) configurations and total spin polarized current I_P^{Total} , I_{AP}^{Total} (in *n*A) for P and AP configurations and TMR ratio.

Bias voltage	$\mathbf{G^{\uparrow\uparrow}}$	$\mathbf{G^{\downarrow\downarrow}}$	$\mathbf{G^{\uparrow\downarrow}}$	$\mathbf{G^{\downarrow\uparrow}}$	$\boldsymbol{I_P^{Total}}$	$\boldsymbol{I_{AP}^{Total}}$	**TMR ratio**
0	1.54×10^{-7}	1.17×10^{-10}	4.53×10^{-10}	4.51×10^{-10}			$\approx1.5\times10^4$%
0.2	1.43×10^{-7}	1.05×10^{-10}	3.14×10^{-10}	3.35×10^{-8}	22.84	3.13	≈ 628%
0.4	8.64×10^{-8}	2.61×10^{-10}	3.42×10^{-9}	1.75×10^{-7}	15.45	23.79	≈ 54%
0.6	1.26×10^{-7}	1.16×10^{-10}	3.75×10^{-10}	5.08×10^{-8}	79.08	12.56	≈ 529%

For a finite bias, the conductance for majority spin states had less experienced on external field for both P and AP configuration. Interestingly, for AP configuration, the conductance rapidly evolved when bias voltage is applied, even faster increase as compare to P-configuration due to the increase in conductance for AP is proportional (Zhang *et al.*, 1997) to $\rho_L^M \rho_R^M + \rho_L^m \rho_R^m$ and $\rho_L^M \rho_R^m + \rho_L^m \rho_R^M$ for P configuration, where $\rho_{L,R}^M$ the density of itinerant electrons states for majority spin at left(right) and $\rho_{L,R}^M$ the itinerant electrons density for minority spin at left(right) electrode. The polarized conductance increased with the orders of two magnitudes for 0.2V and 0.6V bias that results smaller difference in conductance between parallel and anti-parallel configuration. As this mechanism was revealed by Mavropoulos et al., (Mavropoulos *et al.*, 2000) this is due to if the spin complexity nature such as non-collinear spin, thermal spin fluctuation and spin−orbit interactions are included in spin transport calculation, the minority spin interface states can contribute to the conductance, which give rise to a regular finite conductance for MTJ device with anti-parallel magnetization. The resulting suppression of the magnetoresistance is accounted for bias induced spin excitations localized at the interfaces between the magnetic electrodes and the tunnel barrier (Zhang *et al.*, 1997). Zhang et al., interpreted the decay of TMR with bias voltage by considering that inelastic scattering by magnon excitations at the ferromagnet/insulator interface controlled the voltage dependence (Zhang *et al.*, 1997). In a finite bias, electrons which had tunneled across the barrier arrive at the adjacent electrode as itinerant tunnel excited electrons called hot electrons with energy higher than the Fermi energy of that electrode assuming that no inelastic scattering had occurred. These higher energy electrons may then lose their energy by emitting a magnon and hence spin flipping. Bias induced further magnons emission resulting reduced TMR values (Miura *et al.*, 2007). Surprisingly, it can be pointed out from Table 1 [$G^{\uparrow\downarrow}$ and $G^{\downarrow\uparrow}$] that an unusual oscillating conductance behavior (Lee, 2010; Tanaka *et al.*, 2011; Yuasa *et al.*, 2002) can be seen between 0.4 V and 0.6 V which results an oscillating TMR even negative spin polarization indicating negative TMR behavior (Jeong *et al.*, 2016). This oscillating tunneling conductance under bias voltage may be attributed to the non-monotonic energy dependence of transmission coefficients and further split in the molecular field of the

electrode (Panfilenok *et al.*, 2008) and also reasonably to account the mechanism proposed by Ma et al., that insufficient thickness of spacer SC to the extent so that the entire structure size is likely not compatible with electronic coherence length (Ma *et al.*, 2004), so does oscillate TMR (Itoh *et al.*, 2004).

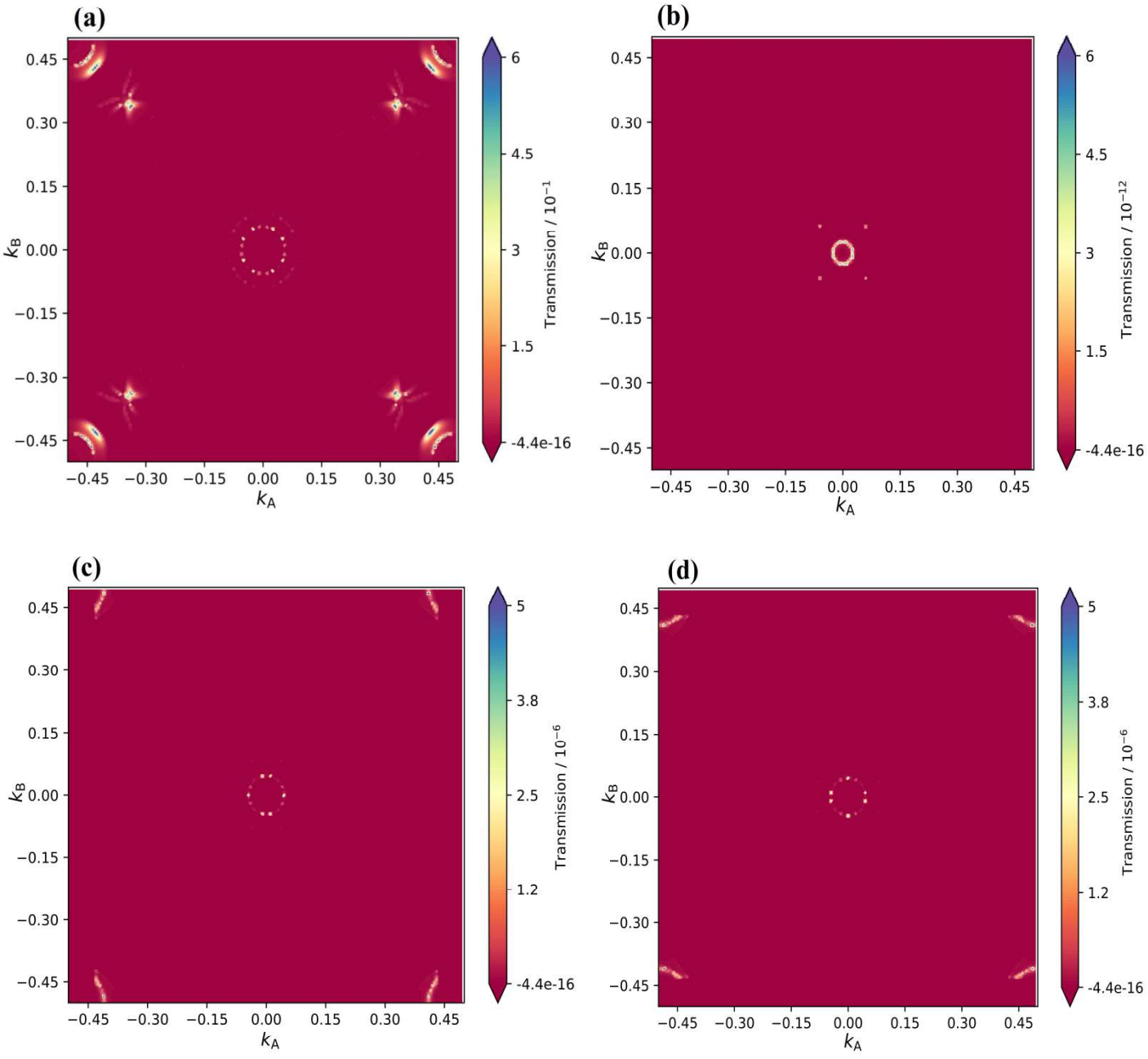

Figure 5.3: The equilibrium $K_{\parallel}$ (k_A, k_B) resolved transmission spectrum (full view of 2D Brillouin Zone) for parallel configuration (P) [(a) spin-up, (b) spin-down] and antiparallel configuration (AP) [(c) spin-up, (d) spin-down]

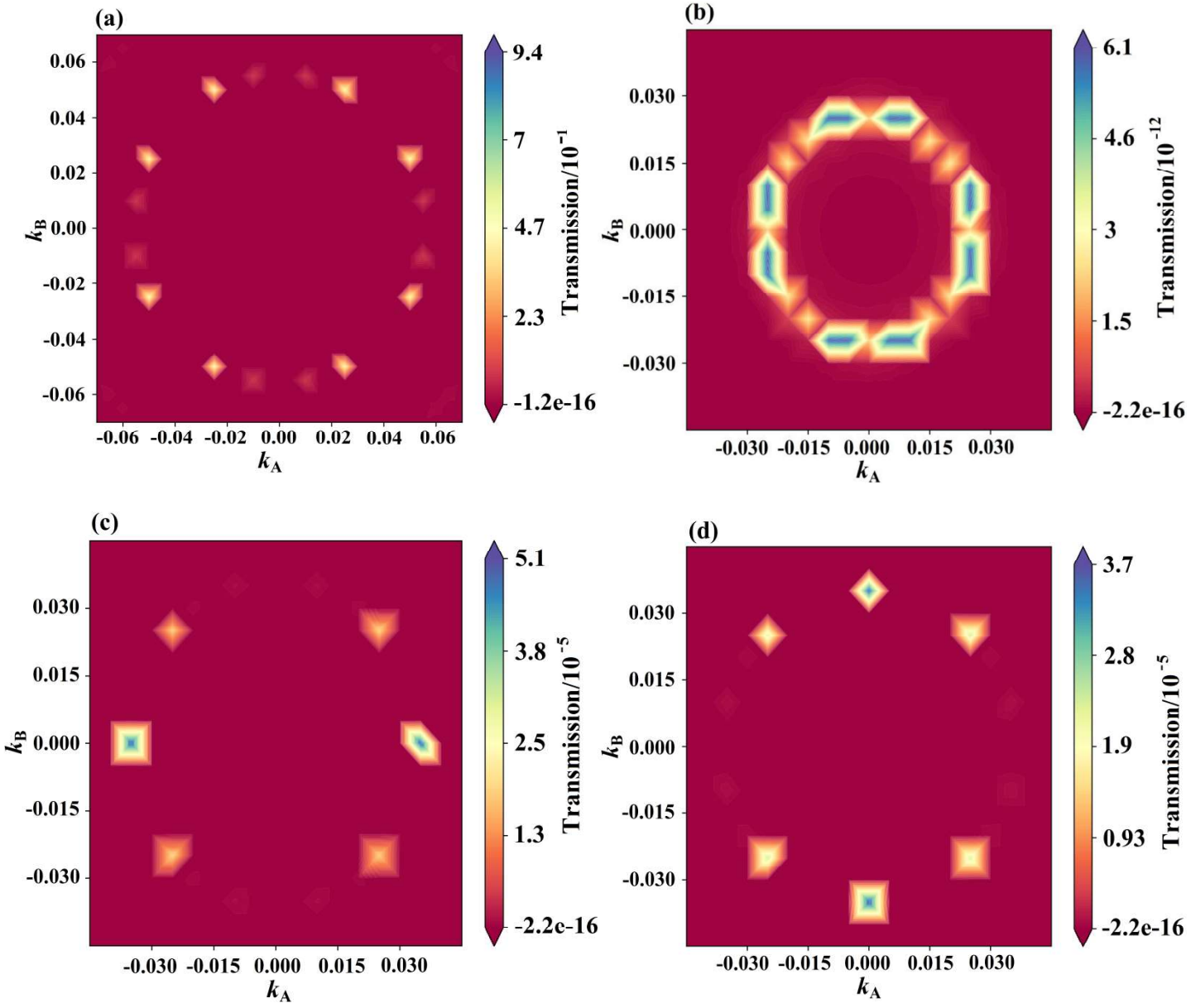

Figure 5.4: The equilibrium $K_{\parallel}$ (k_A,k_B) resolved transmission spectrum (Zoom-in view around Γ-point) at Fermi level for parallel configuration (P) [(a) spin-up, (b) spin-down] and antiparallel configuration (AP) [(c) spin-up, (d) spin-down]

5.2.2 Spin Injected Polarized Current

The calculated spin polarized current for spin up and spin down currents in PC and APC are presented in Figure 5.5[(a) and (b)]. The spin up current $I_P^{\uparrow}$ increase with bias voltage for parallel configuration while negligible change in spin down current $I_P^{\downarrow}$, but the $I_P^{\uparrow}$ and $I_P^{\downarrow}$ variation pattern are identical for P and AP configuration [inset of Figure 4].

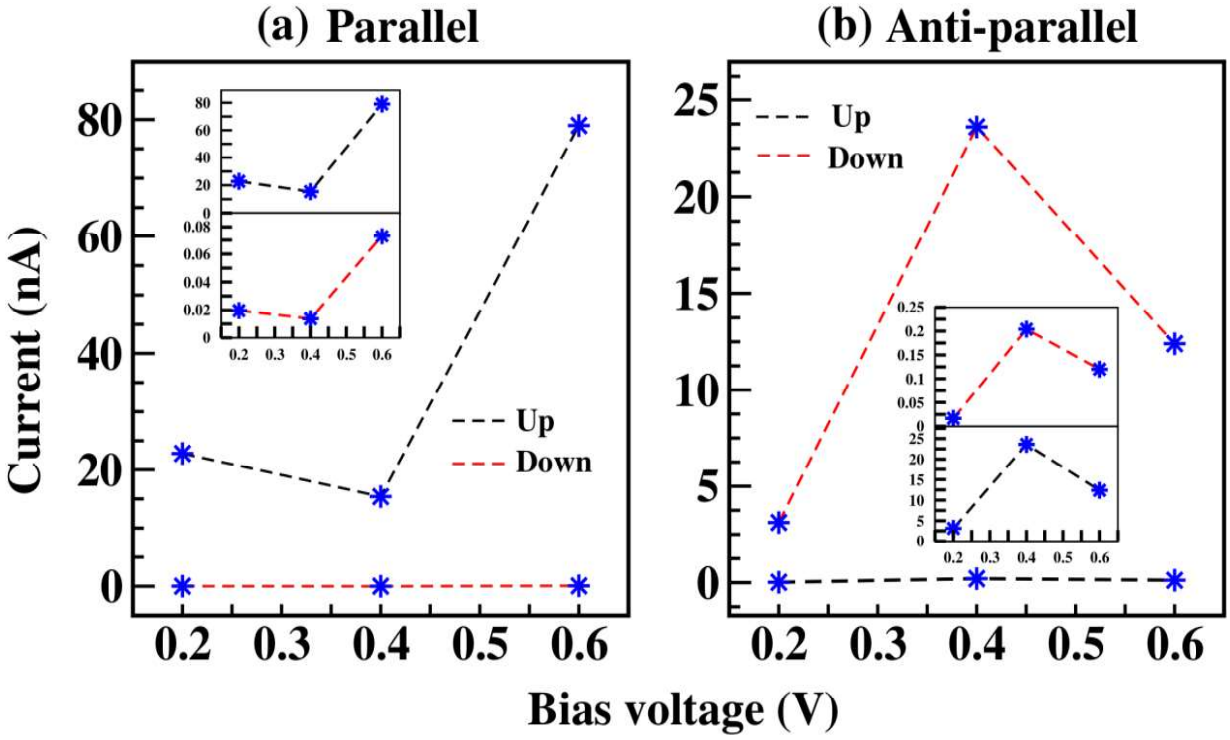

Figure 5.5: I-V characteristic curve for spin polarized current (in *nA*) and bias voltage V (a) Parallel (b) Anti-parallel; inset: zoom-in view for I-V curve.

The spin injection efficiency (SIE) is evaluated based on spin up and spin down currents as

$$SIE = \left|\frac{I^{\uparrow} - I^{\downarrow}}{I^{\uparrow} + I^{\downarrow}}\right| \times 100\%$$

Despite the oscillating behavior of TMR, it is very worth to note that the spin injection efficiency do not change with increasing bias voltage for P configuration. This can be clear from the inset of Figure 4 that the polarized current variation under bias condition is identical and hence the stable spin injection efficiency is observed. For AP configuration, a miniature change in SIE is observed [Figure 5.6]; however it is within 98 - 99% throughout the bias voltages.

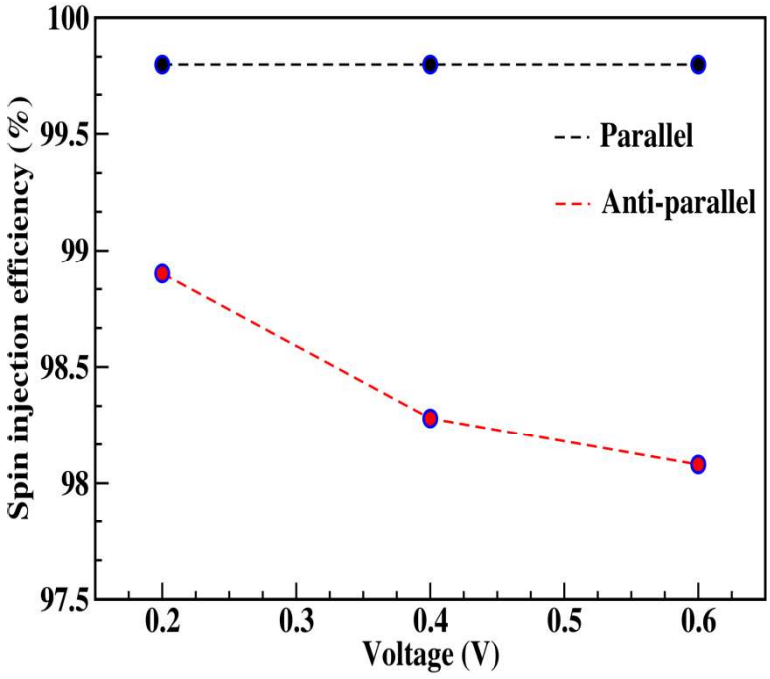

Figure 5.6: Spin injection efficiency as a function of Bias voltages

6

Conclusion

This chapter will give the conclusive ideas out from the thesis titled, “Study of surface half metallicity of full Heusler compounds using ab-initio approach”. Since, the theoretical investigation, modelling or computational exploration of the material always been the first prior pavement for realization of materials in practical application. The extensive investigation of full Heusler compounds from ab-initio (First principle) calculation had been performed rigorously to study mainly electronic and magnetic properties within different phases such as bulk symmetric, non-periodic slab or thin film and an extended the study to spin quantum transports in device realm by modelling Heusler electrode based magnetoresistance tunnelling junction (MTJ) device. The following conclusions are composed from the first principle calculation that had been carried out in this thesis:

- The XA phase of Fe_2IrSi with ferromagnetic configuration exhibited its lowest form of ground state energy from our theoretical energetic analysis. The absence of imaginary frequency in phonon dispersion curve revealed its dynamical stability and we observed a strong coupling between the acoustic and the optical branches; this may be due to the heavy Ir-atom, which is a predominant feature of electron-phonon coupling. We predicted metallic nature in both the spin channel with ~ 45% spin polarization from GGA calculation in inverse full-Heusler Fe_2IrSi. The dispersive bands around E_F in the spin down channel is due to the Fe2-d(↓) [d-e_g+d-t_{2g}] states. The predicted semiconducting half-metallic behavior within our GGA+U calculations has a characteristic of indirect band gap along Γ-X symmetry point in minority channel with a spin polarization of ~ 99.9% at the E_F. We, appropriately treat relativistic effect since the presence of 4d-element (Ir-atom) by deploying spin−orbit coupling (SOC) along with GGA and GGA+U (U_{Ir} =1.0eV and U_{Fe} =3.52eV). With the implementation of SOC the half metallicity is lost and the system behaves like a magnetic metal. The predicted magnetic moment for 29 valence electrons system Fe_2IrSi strongly obeyed Slater-Pauling rule M_t= (Z_t - 24) with the total magnetic

moment with 5.01μ_B. The calculated elastic and mechanical properties confirm both dynamical and structural stability with a melting temperature of ~ 2000±300 K, which supports a promising application of inverse full-Heusler Fe_2IrSi in devices operating above room temperature.

- The prediction for crystallization of Ti_2XSi (X=Mn, Co) inverse Heusler in XA phase is well agreed with available previous reports. The blend of semiconducting minority channel and metallic majority channel behavior in Ti_2XSi validate the half metallic characteristic with ≅100% spin polarization at E_F. Both the compounds followed Slater-Pauling rule with a moment of 1.01μ_B and 3.02μ_B for Ti_2MnSi and Ti_2CoSi respectively. The presence of non-zero magnetic moment despite having anti-ferromagnetic coupling between Mn-Ti revealed that Ti_2MnSi is a ferrimagnetic half metal, whereas Ti_2CoSi is predicted to be ferromagnetic half metal. The calculated elastic constants matrix and non-negative twelve modes of phonon dispersion relation revealed the mechanical and thermodynamical stability of Ti_2XSi (X=Mn, Co) compounds.

- A first principles density functional theory calculation based on PAW and LCAO method revealed the ferrimagnet half-metallic nature of the bulk Mn_2CoSi(MCS) within GGA and GGA+U exchange-correlation potential. The higher accuracy treatment of electron-electron interactions has been incorporated with the inclusion of the on-site Hubbard potential as GGA+U which enhanced the band gap. The calculated lattice constant from the aforementioned two method are slightly smaller as compared with the experiment report with absolute uncertainty about 3.1% for the former and 2.88% for the later method.

- The values obtained from GGA and GGA+U under applied pressures. We have shown that the strong correlation mainly comes from the Fe-3d and Co-d states, and the inclusion of electron–electron interactions within GGA as the GGA+U formalism is essential to describe the electronic properties. The implementation of GGA+U along with compressive pressure (5 < P < 60GPa) leads to half-metallic behavior with the opening ofa spin minority band gap. The predicted integer value of the total magnetic moment in the inverse full-Heusler alloy Fe_2CoAl, ~ 4.0μ_B at 30 GPa, is in accordance with the Slater–Pauling rule, which supports the half-metallicity. The T_C calculated from equation (4) is 747 K at 30 GPa, in good

agreement with the results of other Fe-based inverse full-Heusler compounds. However, the results from MFA are overestimated. The calculated cohesive energy confirmed the ground state stability of the system under different applied pressures.

- The non-periodic thin film of 001 surface with four terminated faces have been exfoliated from the optimized bulk Ti_2XSi(X=Mn,Co) structure. Out of the four explored terminal surfaces, TiSi(TMS) is the most stable with lowest surface energy which agrees well with its smallest surface relaxation. However, the TiX(X=Mn/Co) terminated surfaces from both Ti_2MnSi(TMS) and Ti_2CoSi(TCS) compounds are less stable as compared to respective adjacent TiSi terminated surfaces which were revealed by the ab-initio atomistic thermodynamic calculation. We have observed from the electronic structure calculations that for TiMn, TiSi (TCS) and TiCo terminal surfaces, the presence of surface states at the Fermi level destroying their respective bulk half metallic properties. A significant surface half metallicity is observed in TiSi(TMS) terminal surface. We expect that our present work will invigorate the experimental work for the realization of surface half-metallicity in Ti_2MnSi with TiSi termination.

- We have studied the surface electronic and perpendicular magnetocrystalline anisotropy of 111-surface slab of inverse Heusler alloy Fe_2CoAl using the first principles calculation. Adopting the different atomic terminals we have calculated the minimum ground state energy for various magnetic configurations - Ferromagnetic (FM) and antiferromagnetic (AFM). The slab with different atomic-terminals and energetically stable ground states are AFM1: Al-terminal, FM: Co-terminal and AFM2: Fe-terminal. All the terminals are magnetic metals with finite value of total magnetic moments and dispersed bands around EF in both the spin channels from GGA as well as GGA+U approaches. We have observed the decrease in the degree of the total spin polarization from the GGA to GGA+U calculation in all cases. This may be due to the large number of free conducting charges dispersed on the surface and another reason might be the irrelevant choice of the Hubbard potential (U) to incorporate the surface atoms. In fact, we have observed a small spin-down energy gap (0.19 eV) between 0.55 eV – 0.74 eV in Al-terminal within GGA calculation. By varying the cell parameters or doping it may be possibly tuned the Fermi level in the spin band gap to get the surface half-metallicity.

- For Mn_2CoSi surfaces study, among two ideal terminations the energetically favored MnSi-terminal to MnCo-terminal. From the analysis of surface electronic structure via spin resolved partial density and band structure; MnSi-terminal surface is found to be exhibited half metallic nature with a minority gap in the spin down channel while MnCo-terminal revealed the metallic character with a dispersed bands around Fermi level in both the spin channel. This may be attributed to the weak d-d re-hybridization after losing half of their respective nearest neighbor atoms which in turn may did not induced sufficient energy splitting of hybridized e_u-t_{1u} states at around E_F. The surface half metallicity of MnSi-terminal is further confirmed using LCAO method, this most likely attributed to even after the reduction of co-ordination number, Mn(s)-d states governed a sufficiently strong d-d re-hybridization with sub-surface atoms; Co(s1)-d states, which induced and energy splitting between the bonding and antibonding states; perceiving a well-defined band gap characterized by the subsurface atoms Co(s1) and Mn(s1). This may possibly indicated that a negligible surface effect on strong covalent hybridization between Mn(s1) and Co(s1) and Mn(s) d-d states which turned out energy splitting between e_u-t_{1u} states to open up band gap around E_F. The enhancement of localized spin moment of surface atom Mn(s) in MnSi terminated surface is revealed from both the calculation approach. The presence of broken translational symmetry at the non-periodic surface tends to rearrange the displaced valence electrons that leads to a strong intra-atomic exchange interaction, induced a larger localized spin magnetic moment of Mn(s) as compared to the respective magnetic moment in bulk. The anti-parallel spin moment of surface Si(s) atom had slightly increases which may be due to the direct exchange between p-orbital from Si(s) and d orbital of the subsurface Mn(s1) atoms. The subsurface Co atom has less experienced surface effect with a negligibly variation from the bulk value. In MnCo surface, the Mn2 site of the bulk structure is terminated and unexpectedly a parallel spin is observed between Mn(s) and Mn(s1), so for that reason it can be obvious that the antiparallel moment induced in Si(s1) arises from the second subsurface Mn atom. The complexity of surface and subsurface atoms magnetic structure may be due to the presence of competition between direct exchange and antiferromagnetic super exchange interaction.

- The quantum transport in half metallic ferrimagnet Mn_2CoSi based MTJ have been studied with the aim of developing ferrimagnet spintronic material. The spin dependent transport properties have been studied within non-equilibrium Green function-density functional theory [NEGF-DFT]; in view of miniaturization the resistance product area, the lattice matching semiconductor Calcium-Chalcogen (CaS) is used as non-magnetic spacer in our ferrimagnet MTJ device. The spin dependent transmission value is comparatively low which may be due to the only contribution from spin-flip scattering, which is inherently small due to the half-metallic electrode. However, a large TMR value is observed at equilibrium. We found a drastic change is TMR under applied bias voltage, which further oscillates at increasing voltage, which is reasonably attributed to the non-monotonic energy of transmission coefficients which further split in molecular field. We concluded that our proposed half metallic electrode (spin injector) for further study especially in experimental characterization for ferrimagnetic spintronic. It will also be very useful to explore the tunneling anisotropic magnetoresistance, spin texture and spin dynamics for future spintronic application.

References

Aguilera-Granja F, Aguilera-del-Toro RH, & Morán-López JL. (2019). A first principles systematic study of the structural, electronic, and magnetic properties of Heusler X_2MnZ with X = Fe, Co, Ni, Cu, Ru, Rh, Pd, Ag, Pt, Au and Z = Al, Si, Ga, Ge, In and Sn. *Materials Research Express, **6*****(10)**, 106118.

Aliev FG. (1991). Gap at Fermi level in some new d- and f-electron intermetallic compounds. *Physica B: Condensed Matter, **171*****(1)**, 199-205.

Amiri M, Akbari H, Nedaee-shakarab B, Boochani A, Aminian A, Zangeneh Y, & Naderi S. (2019). Thermodynamic Stability, Half-Metallic and Optical Properties of Sc_2CoSi [001] Film: a DFT Study. *Communications in Theoretical Physics, **71*****(4)**, 455.

Andersen OK. (1975). Linear methods in band theory. *Physical Review B, **12*****(8)**, 3060-3083.

Anderson PW. (1963). Theory of Magnetic Exchange Interactions:Exchange in Insulators and Semiconductors. *Solid State Physics, **14***, 99-214.

Armiento R. (2002). Subsystem functionals in density-functional theory: Investigating the exchange energy per particle. *Physical Review B, **66*****(16)**, 165117.

Armiento R, & Mattsson A. (2003). Alternative separation of exchange and correlation in density-functional theory. *Physical Review B, **68*****(24)**, 245120.

Bader SD, & Parkin SSP. (2010). Spintronics. *Annual Review of Condensed Matter Physics, **1*****(1)**, 71-88.

Baibich MN, Broto JM, Fert A, Van Dau FN, Petroff F, Etienne P, Creuzet G, Friederich A, & Chazelas J. (1988). Giant Magnetoresistance of (001)Fe/(001)Cr Magnetic Superlattices. *Physical Review Letters, **61*****(21)**, 2472-2475.

Bayrakci M, Colakoglu K, Deligoz E, & Ciftci YO. (2009). A first-principle study of the structural and lattice dynamical properties of CaX (X=S, Se, and Te). *High Pressure Research, **29*(2)**, 187-203.

Bhatti S, Sbiaa R, Hirohata A, Ohno H, Fukami S, & Piramanayagam SN. (2017). Spintronics based random access memory: a review. *Materials Today, **20*(9)**, 530-548.

Blöchl PE. (1994). Projector augmented-wave method. *Physical Review B, **50*(24)**, 17953-17979.

Born M, & Oppenheimer R. (1927). Zur Quantentheorie der Molekeln. *Annalen der Physik, **389*(20)**, 457-484.

Bradley AJ, Rodgers JW, & Bragg WL. (1934). The crystal structure of the heusler alloys. *Proceedings of the Royal Society of London. Series A, Containing Papers of a Mathematical and Physical Character, **144*(852)**, 340-359.

Butler WH, Zhang XG, Schulthess TC, & MacLaren JM. (2001). Spin-dependent tunneling conductance of Fe|MgO|Fe sandwiches. *Physical Review B, **63*(5)**, 054416.

Capelle K. (2006). A bird's-eye view of density-functional theory. *Brazilian Journal of Physics, **36* (4a)**, 1.

Capelle K, & Vignale G. (2001). Nonuniqueness of the Potentials of Spin-Density-Functional Theory. *Physical Review Letters, **86*(24)**, 5546-5549.

Capelle K, & Vignale G. (2002). Nonuniqueness and derivative discontinuities in density-functional theories for current-carrying and superconducting systems. *Physical Review B, **65*(11)**, 113106.

Cardias R, Szilva A, Bergman A, Marco ID, Katsnelson MI, Lichtenstein AI, Nordström L, Klautau AB, Eriksson O, & Kvashnin YO. (2017). The Bethe-Slater curve revisited; new insights from electronic structure theory. *Scientific Reports, **7*(1)**, 4058.

Charifi Z, Baaziz H, Hassan FEH, & Bouarissa N. (2005). High pressure study of structural and electronic properties of calcium chalcogenides. *Journal of Physics: Condensed Matter, **17*(26)**, 4083-4092.

Chen X-Q, Podloucky R, & Rogl P. (2006). Ab initio prediction of half-metallic properties for the ferromagnetic Heusler alloys Co_2MSi (M=Ti,V,Cr). *Journal of Applied Physics, **100*(11)**, 113901.

Chis V, & Hellsing B. (2004). Surface Relaxation Influenced by Surface States. *Physical Review Letters, **93*(22)**, 226103.

Coey JMD, Venkatesan M, & Fitzgerald CB. (2005). Donor impurity band exchange in dilute ferromagnetic oxides. *Nature Materials, **4*(2)**, 173-179.

Dahmane F, Mogulkoc Y, Doumi B, Tadjer A, Khenata R, Bin Omran S, Rai DP, Murtaza G, & Varshney D. (2016). Structural, electronic and magnetic properties of Fe2-based full Heusler alloys: A first principle study. *Journal of Magnetism and Magnetic Materials, **407***, 167-174.

de Gennes PG. (1960). Effects of Double Exchange in Magnetic Crystals. *Physical Review, **118*(1)**, 141-154.

de Groot RA, Mueller FM, Engen PGv, & Buschow KHJ. (1983). New Class of Materials: Half-Metallic Ferromagnets. *Physical Review Letters, **50*(25)**, 2024-2027.

Dietl T, Awschalom D, & Maria Kaminska HO. (2008). *Spintronics* (1st Ed.): Elsevier.

Dietl T, Ohno H, Matsukura F, Cibert J, & Ferrand D. (2000). Zener Model Description of Ferromagnetism in Zinc-Blende Magnetic Semiconductors. *Science, **287*(5455)**, 1019-1022.

Dudarev SL, Botton GA, Savrasov SY, Humphreys CJ, & Sutton AP. (1998). Electron-energy-loss spectra and the structural stability of nickel oxide: An LSDA+U study. *Physical Review B, **57*(3)**, 1505-1509.

Ekbundit S, Chizmeshya A, LaViolette R, & Wolf GH. (1996). Theoretical and experimental investigation of the equations of state and phase stabilities of MgS and CaS. *Journal of Physics: Condensed Matter, **8*(43)**, 8251-8265.

Ekuma CE, Najmaei S, & Dubey M. (2019). Electronic and vibrational properties of van der Waals heterostructures of vertically stacked few-layer atomically thin MoS2 and BP. *Materials Today Communications, **19***, 383-392.

Elphick K, Frost W, Samiepour M, Kubota T, Takanashi K, Sukegawa H, Mitani S, & Hirohata A. (2021). Heusler alloys for spintronic devices: review on recent development and future perspectives. *Sci Technol Adv Mater, **22*(1)**, 235-271.

Endo K, Matsuda H, Ooiwa K, & Itoh K. (1995). Antiferromagnetism in a Heusler Alloy Fe_2VSi. *Journal of the Physical Society of Japan, **64*(7)**, 2329-2332.

Fang Q-L, Zhang J-M, & Xu K-W. (2014). Magnetic properties and origin of the half-metallicity of Ti_2MnZ (Z=Al, Ga, In, Si, Ge, Sn) Heusler alloys with the Hg_2CuTi-type structure. *Journal of Magnetism and Magnetic Materials, **349***, 104-108.

Faregh RA, Boochani A, Masharian SR, & Jafarpour FH. (2019). The surface effect on the thermodynamic stability, half-metallic and optical properties of Co_2MnGa(001) films: a DFT study. *International Nano Letters, **9*(4)**, 339-348.

Felser C, Wollmann L, Chadov S, Fecher GH, & Parkin SSP. (2015). Basics and prospective of magnetic Heusler compounds. *APL Materials, **3*(4)**, 041518.

Feng Y, Cui Z, Wei M-s, & Wu B. (2019). Spin-polarized quantum transport in Fe_4N based current-perpendicular-to-plane spin valve. *Applied Surface Science, **466***, 78-83.

Fermi E. (1927). Un Metodo Statistico per la Determinazione di alcune Prioprietà dell'Atomo. *Accademia Nazionale dei Lincei, **6***, 602-607.

Fert A. (2008). The present and the future of spintronics. *Thin Solid Films, **517*(1)**, 2-5.

Fong CY, Qian MC, Pask JE, Yang LH, & Dag S. (2004). Electronic and magnetic properties of zinc blende half-metal superlattices. *Applied Physics Letters,* ***84*****(2)**, 239-241.

Friák M, Slávik A, Miháliková I, Holec D, Všianská M, Šob M, Palm M, & Neugebauer J. (2018). Origin of the Low Magnetic Moment in Fe_2AlTi: An Ab Initio Study. *Materials,* ***11*****(9)**.

Fuke HN, Hashimoto S, Takagishi M, Iwasaki H, Kawasaki S, Miyake K, & Sahashi M. (2007). Magnetoresistance of FeCo Nanocontacts With Current-Perpendicular-to-Plane Spin-Valve Structure. *IEEE Transactions on Magnetics,* ***43*****(6)**, 2848-2850.

Fullerton EE, & Schuller IK. (2007). The 2007 Nobel Prize in Physics: Magnetism and Transport at the Nanoscale. *ACS Nano,* ***1*****(5)**, 384-389.

Galanakis I. (2002). Surface properties of the half-and full-Heusler alloys. *Journal of Physics: Condensed Matter,* ***14*****(25)**, 6329-6340.

Galanakis I, Dederichs PH, & Papanikolaou N. (2002). Slater-Pauling behavior and origin of the half-metallicity of the full-Heusler alloys. *Physical Review B,* ***66*****(17)**, 174429.

Galanakis I, & Mavropoulos P. (2007). Spin-polarization and electronic properties of half-metallic Heusler alloys calculated from first principles. *Journal of Physics: Condensed Matter,* ***19*****(31)**, 315213.

Galanakis I, Mavropoulos P, & Dederichs PH. (2006). Electronic structure and Slater–Pauling behaviour in half-metallic Heusler alloys calculated from first principles. *Journal of Physics D: Applied Physics*, ***39*****(5)**, 765-775.

Galanakis I, Özdoğan K, Şaşıoğlu E, & Blügel S. (2014). Conditions for spin-gapless semiconducting behavior in Mn_2CoAl inverse Heusler compound. *Journal of Applied Physics,* ***115*****(9)**, 093908.

Galanakis I, Papanikolaou N, & Dederichs P. (2002). Applicability of the broken-bond rule to the surface energy of the fcc metals. *Surface Science, **511*(1)**, 1-12.

Galanakis I, Şaşıoğlu E, Blügel S, & Özdoğan K. (2014). Voids-driven breakdown of the local-symmetry and Slater-Pauling rule in half-metallic Heusler compounds. *Physical Review B, **90*(6)**, 064408.

Gambardella P, Rusponi S, Veronese M, Dhesi SS, Grazioli C, Dallmeyer A, Cabria I, Zeller R, Dederichs PH, Kern K, Carbone C, & Brune H. (2003). Giant Magnetic Anisotropy of Single Cobalt Atoms and Nanoparticles. *Science, **300*(5622)**, 1130-1133.

Gasi T, Ksenofontov V, Kiss J, Chadov S, Nayak AK, Nicklas M, Winterlik J, Schwall M, Klaer P, Adler P, & Felser C. (2013). Iron-based Heusler compounds Fe_2YZ: Comparison with theoretical predictions of the crystal structure and magnetic properties. *Physical Review B, **87*(6)**, 064411.

Ghaderi N, Hashemifar SJ, Akbarzadeh H, & Peressi M. (2007). First principle study of Co_2MnSi/GaAs(001) heterostructures. *Journal of Applied Physics, **102*(7)**, 074306.

Ghosh S, & Ghosh S. (2019). Half-Metallicity in Quaternary Heusler Alloys with 3d and 4d Elements: Observations and Insights from DFT Calculations. *Physica Status Solidi (b), **256*(8)**, 1900039.

Giannozzi P, Andreussi O, Brumme T, Bunau O, Nardelli B, Calandra M, Car R, Cavazzoni C, Ceresoli D, Cococcioni M, Colonna N, Carnimeo I, Dal Corso A, Gironcoli dS, Delugas P, DiStasio R, Ferretti A, Floris A, Fratesi G, Fugallo G, Gebauer R, Gerstmann U, Giustino F, Gorni T, Jia J, Kawamura M, Ko HY, Kokalj A, Küçükbenli E, Lazzeri M, Marsili M, Marzari N, Mauri F, Nguyen NL, Nguyen HV, Otero-de-la-Roza A, Paulatto L, Poncé S, Rocca D, Sabatini R, Santra B, Schlipf M, Seitsonen A, Smogunov A, Timrov I, Thonhauser T, Umari P, Vast N, Wu X, & Baroni S. (2017). Advanced

capabilities for materials modelling with Quantum ESPRESSO. *Journal of Physics: Condensed Matter, **29*(46)**, 465901.

Giannozzi P, Baroni S, Bonini N, Calandra M, Car R, Cavazzoni C, Ceresoli D, Chiarotti GL, Cococcioni M, Dabo I, Dal Corso A, de Gironcoli S, Fabris S, Fratesi G, Gebauer R, Gerstmann U, Gougoussis C, Kokalj A, Lazzeri M, Martin-Samos L, Marzari N, Mauri F, Mazzarello R, Paolini S, Pasquarello A, Paulatto L, Sbraccia C, Scandolo S, Sclauzero G, Seitsonen AP, Smogunov A, Umari P, & Wentzcovitch RM. (2009). QUANTUM ESPRESSO: a modular and open-source software project for quantum simulations of materials. *Journal of Physics: Condensed Matter, **21*(39)**, 395502.

Gilleßen M, & Dronskowski R. (2010). A combinatorial study of inverse Heusler alloys by first-principles computational methods. *Journal of Computational Chemistry*, ***31*(3)**, 612-619.

Graf T, Felser C, & Parkin SSP. (2011). Simple rules for the understanding of Heusler compounds. *Progress in Solid State Chemistry, **39*(1)**, 1-50.

Gregg JF, Petej I, Jouguelet E, & Dennis C. (2002). Spin electronics a review. *Journal of Physics D: Applied Physics, **35*(18)**, R121-R155.

Hakamata S, Ishikawa T, Marukame T, Matsuda K-i, Uemura T, Arita M, & Yamamoto M. (2007). Improved tunnel magnetoresistance characteristics of magnetic tunnel junctions with a Heusler alloy thin film of Co_2MnGe and a MgO tunnel barrier. *Journal of Applied Physics, **101*(9)**, 09J513.

Hamann DR, Schlüter M, & Chiang C. (1979). Norm-Conserving Pseudopotentials. *Physical Review Letters, **43*(20)**, 1494-1497.

Hammer B, Hansen LB, & Nørskov JK. (1999). Improved adsorption energetics within density-functional theory using revised Perdew-Burke-Ernzerhof functionals. *Physical Review B, **59*(11)**, 7413-7421.

Han H, Bai Z, & Yao KL. (2013). Half-metallicity of bulk and (111) surface for full-Heusler alloy Co_2VAl: A density functional study. *Journal of Alloys and Compounds, **576***, 93-97.

Han H, Feng T, Fan L, Zhao Z, Li M, & Yao KL. (2017). The half-metallicity of (111) surface and (111) interface for Heusler alloy Co_2MnGe thin film. *Journal of Magnetism and Magnetic Materials, **438***, 95-99.

Hashemifar SJ, Kratzer P, & Scheffler M. (2005). Preserving the Half-Metallicity at the Heusler Alloy Co_2MnSi (001) Surface: A Density Functional Theory Study. *Physical Review Letters, **94*(9)**, 096402.

Hess E. (1972). Computational Methods in Band Theory. Edited by P.M. Marcus, J.F Nanak and A.R. Williams 578 Seiten. Preis 28, - Plenum Press, New York - London 1971. *Kristall und Technik, **7*(9)**, K107-K110.

Heusler F. (1903). Über magnetische Manganlegierungen. *Verhandlungen der Deutschen Physikalischen Gesellschaft (in German), **12***, 219.

Heusler F, Starck W, & Haupt E. (1903). *Verh DPG, **5***, 220-223.

Hickey MC, Damsgaard CD, Farrer I, Holmes SN, Husmann A, Hansen JB, Jacobsen CS, Ritchie DA, Lee RF, Jones GAC, & Pepper M. (2005). Spin injection between epitaxial $Co_{2.4}Mn_{1.6}Ga$ and an InGaAs quantum well. *Applied Physics Letters, **86*(25)**, 252106.

Hirohata A, Frost W, Samiepour M, & Kim JY. (2018). Perpendicular Magnetic Anisotropy in Heusler Alloy Films and Their Magnetoresistive Junctions. *Materials (Basel), **11*(1)**.

Hirohata A, & Takanashi K. (2014). Future perspectives for spintronic devices. *Journal of Physics D: Applied Physics, **47*(19)**, 193001.

Hohenberg P, & Kohn W. (1964). Inhomogeneous Electron Gas. *Physical Review, **136*(3B)**, B864-B871.

Hu Y, & Zhang J-M. (2017a). First-principles study on the thermodynamic stability, magnetism, and half-metallicity of full-Heusler alloy Ti_2FeGe (001) surface. *Physics Letters A, **381*(18)**, 1592-1597.

Ikeda S, Hayakawa J, Ashizawa Y, Lee YM, Miura K, Hasegawa H, Tsunoda M, Matsukura F, & Ohno H. (2008). Tunnel magnetoresistance of 604% at 300K by suppression of Ta diffusion in CoFeB/MgO/CoFeB pseudo-spin-valves annealed at high temperature. *Applied Physics Letters, **93*(8)**, 082508.

Ikeda S, Miura K, Yamamoto H, Mizunuma K, Gan HD, Endo M, Kanai S, Hayakawa J, Matsukura F, & Ohno H. (2010a). A perpendicular-anisotropy CoFeB-MgO magnetic tunnel junction. *Nat Mater, **9*(9)**, 721-724.

Ishida S, Fujii S, Kashiwagi S, & Asano S. (1995). Search for Half-Metallic Compounds in Co_2MnZ (Z=IIIb, IVb, Vb Element). *Journal of the Physical Society of Japan, **64*(6)**, 2152-2157.

Ishikawa T, Liu H-x, Taira T, Matsuda K-i, Uemura T, & Yamamoto M. (2009). Influence of film composition in Co_2MnSi electrodes on tunnel magnetoresistance characteristics of Co_2MnSi/MgO/Co_2MnSi magnetic tunnel junctions. *Applied Physics Letters, **95*(23)**, 232512.

Itoh H, Inoue J, Umerski A, & Mathon J. (2004). Quantum oscillation of TMR in tunneling junctions containing a non-magnetic spacer. *Journal of Magnetism and Magnetic Materials, **272-276***, E1467-E1468.

Iwase T, Sakuraba Y, Bosu S, Saito K, Mitani S, & Takanashi K. (2009). Large Interface Spin-Asymmetry and Magnetoresistance in Fully Epitaxial Co_2MnSi/Ag/ Co_2MnSi Current-Perpendicular-to-Plane Magnetoresistive Devices. *Applied Physics Express, **2***, 063003.

Jain A, Ong SP, Hautier G, Chen W, Richards WD, Dacek S, Cholia S, Gunter D, Skinner D, Ceder G, & Persson KA. (2013). Commentary: The Materials Project: A materials genome approach to accelerating materials innovation. *APL Materials, **1*(1)**, 011002.

Jain V, Nehra J, Sudheesh VD, Lakshmi N, & Venugopalan K. (2013). Comparative study of the structural and magnetic properties of bulk and nano-sized Fe_2CoAl. *AIP Conference Proceedings, **1536*(1)**, 935-936.

Janak JF, & Williams AR. (1981). Method for calculating wave functions in a nonspherical potential. *Physical Review B, **23*(12)**, 6301-6306.

Jeong J, Ferrante Y, Faleev SV, Samant MG, Felser C, & Parkin SSP. (2016). Termination layer compensated tunnelling magnetoresistance in ferrimagnetic Heusler compounds with high perpendicular magnetic anisotropy. *Nature Communications, **7*(1)**, 10276.

Jiang D, Ye Y, Gou Q, Wu D, & Wen Y. (2018). First-principles predictions on structural, elastic and half-metallic properties of Fe_2LiAs Heusler compound. *Journal of Magnetism and Magnetic Materials, **458***, 235-240.

Jourdan M, Minár J, Braun J, Kronenberg A, Chadov S, Balke B, Gloskovskii A, Kolbe M, Elmers HJ, Schönhense G, Ebert H, Felser C, & Kläui M. (2014). Direct observation of half-metallicity in the Heusler compound Co_2MnSi. *Nature Communications, **5*(1)**, 3974.

Julliere M. (1975). Tunneling between ferromagnetic films. *Physics Letters A, **54*(3)**, 225-226.

Jung JW, Sakuraba Y, Sasaki TT, Miura Y, & Hono K. (2016). Enhancement of magnetoresistance by inserting thin NiAl layers at the interfaces in $Co_2FeGa_{0.5}Ge_{0.5}$/Ag/$Co_2FeGa_{0.5}Ge_{0.5}$ current-perpendicular-to-plane pseudo spin valves. *Applied Physics Letters, **108*(10)**, 102408.

Kandpal HC, Fecher GH, Felser C, & Schönhense G. (2006). Correlation in the transition-metal-based Heusler compounds Co_2MnSi and Co_2FeSi. *Physical Review B, **73*(9)**, 094422.

Kato H, Okuda T, Okimoto Y, Tomioka Y, Oikawa K, Kamiyama T, & Tokura Y. (2004). Structural and electronic properties of the ordered double perovskites

A_2MReO_6 (A=Sr,Ca; M=Mg,Sc,Cr,Mn,Fe,Co,Ni,Zn). *Physical Review B,* ***69*****(18)**, 184412.

Khalaf Al-zyadi Jabbar M, Kadhim AA, & Yao K-L. (2018). Half-metallicity of the (001), (111) and (110) surfaces of CoRuMnSi and interface half-metallicity of CoRuMnSi/CdS. *RSC Advances,* ***8*****(45)**, 25653-25663.

Khandy SA, Islam I, Gupta DC, Khenata R, & Laref A. (2019). Lattice dynamics, mechanical stability and electronic structure of Fe-based Heusler semiconductors. *Scientific Reports,* ***9*****(1)**, 1475.

Khosravi H, Boochani A, Khodadadi J, Solaymani S, & Sartipi E. (2014). Thermodynamic phase diagram and electronic properties of Co_2VAl〈001〉 film: A first-principles study. *International Journal of Modern Physics B,* ***28***, 1450145.

Khovaylo VV, Voronin AI, Zueva VY, Seredina MA, & Chatterdjee R. (2017). Fe-based semiconducting heusler alloys. *Semiconductors,* ***51***, 718.

Kim T, Cha IH, Kim YJ, Kim GW, Stashkevich A, Roussigné Y, Belmeguenai M, Chérif SM, Samardak AS, & Kim YK. (2021). Ruderman–Kittel–Kasuya–Yosida-type interfacial Dzyaloshinskii–Moriya interaction in heavy metal/ferromagnet heterostructures. *Nature Communications,* ***12*****(1)**, 3280.

Kimura T, Hashimoto N, Yamada S, Miyao M, & Hamaya K. (2012). Room-temperature generation of giant pure spin currents using epitaxial Co_2FeSi spin injectors. *NPG Asia Materials,* ***4*****(3)**, e9.

Kohn W. (1999). Nobel Lecture: Electronic structure of matter---wave functions and density functionals. *Reviews of Modern Physics,* ***71*****(5)**, 1253-1266.

Kohn W, & Rostoker N. (1954). Solution of the Schrodinger Equation in Periodic Lattices with an Application to Metallic Lithium. *Physical Review,* ***94*****(5)**, 1111-1120.

Kohn W, & Sham LJ. (1965). Self-Consistent Equations Including Exchange and Correlation Effects. *Physical Review, **140*(4A)**, A1133-A1138.

Korringa J. (1947). On the calculation of the energy of a Bloch wave in a metal. *Physica, **13*(6)**, 392-400.

Kresse G, & Furthmüller J. (1996). Efficient iterative schemes for ab initio total-energy calculations using a plane-wave basis set. *Physical Review B, **54*(16)**, 11169-11186.

Krishnamurthy VV, Weston JL, Mankey GJ, Suzuki M, Kawamura N, & Ishikawa T. (2003). Magnetism of Ir in Fe_2IrSi from Ir $L_{2,3}$ edge x-ray magnetic circular dichroism spectroscopy. *Journal of Applied Physics, **93*(10)**, 7981-7983.

Kroumova E, Aroyo MI, Perez-Mato JM, Kirov A, Capillas C, Ivantchev S, & Wondratschek H. (2003). Bilbao Crystallographic Server : Useful Databases and Tools for Phase-Transition Studies. *Phase Transitions, **76*(1-2)**, 155-170.

Kübler J, Fecher GH, & Felser C. (2007). Understanding the trend in the Curie temperatures of Co_2-based Heusler compounds: Ab initio calculations. *Physical Review B, **76*(2)**, 024414.

Kubota T, Ina Y, Wen Z, Narisawa H, & Takanashi K. (2017). Current perpendicular-to-plane giant magnetoresistance using an $L1_2$ Ag_3Mg spacer and $Co_2Fe_{0.4}Mn_{0.6}Si$ Heusler alloy electrodes: Spacer thickness and annealing temperature dependence. *Physical Review Materials, **1*(4)**, 044402.

Laird BB, Ross RB, Ziegler T. (1995). *Chemical Applications of Density-functional Theory*: American Chemical Society. *ACS Symposium Series, **629***

Lee BC. (2010). Theory of oscillatory tunneling magnetoresistance. *Journal of Applied Physics, **107*(9)**, 09C708.

Lieb EH. (1991). Thomas-fermi and related theories of atoms and molecules. In Walter Thirring (Ed.), *The Stability of Matter: From Atoms to Stars: Selecta of Elliott H. Lieb* (pp. 191-230). Berlin, Heidelberg: Springer Berlin Heidelberg.

Liechtenstein AI, Anisimov VI, & Zaanen J. (1995). Density-functional theory and strong interactions: Orbital ordering in Mott-Hubbard insulators. *Physical Review B, **52*(8)**, R5467-R5470.

Liechtenstein AI, Katsnelson MI, Antropov VP, & Gubanov VA. (1987). Local spin density functional approach to the theory of exchange interactions in ferromagnetic metals and alloys. *Journal of Magnetism and Magnetic Materials, **67*(1)**, 65-74.

Liu H-x, Honda Y, Taira T, Matsuda K-i, Arita M, Uemura T, & Yamamoto M. (2012). Giant tunneling magnetoresistance in epitaxial $Co_2MnSi/MgO/Co_2MnSi$ magnetic tunnel junctions by half-metallicity of Co_2MnSi and coherent tunneling. *Applied Physics Letters, **101*(13)**, 132418.

Liu H-x, Kawami T, Moges K, Uemura T, Yamamoto M, Shi F, & Voyles PM. (2015). Influence of film composition in quaternary Heusler alloy $Co_2(Mn,Fe)Si$ thin films on tunnelling magnetoresistance of $Co_2(Mn,Fe)Si$|MgO-based magnetic tunnel junctions. *Journal of Physics D: Applied Physics, **48*(16)**, 164001.

Loucks T, & Slater JC. (1967). Augmented Plane Wave Method: A Guide to Performing Electronic Structure Calculations. *Physics Today, **20*(11)**, 92-93.

Louie SG, Ho K-M, & Cohen ML. (1979). Self-consistent mixed-basis approach to the electronic structure of solids. *Physical Review B, **19*(4)**, 1774-1782.

Luo H, Greene RG, Ghandehari K, Li T, & Ruoff AL. (1994). Structural phase transformations and the equations of state of calcium chalcogenides at high pressure. *Physical Review B, **50*(22)**, 16232-16237.

Luo H, Zhu Z, Ma L, Xu S, Liu H, Qu J, Li Y, & Wu G. (2007). Electronic structure and magnetic properties of Fe_2YSi (Y = Cr, Mn, Fe, Co, Ni) Heusler alloys: a theoretical and experimental study. *Journal of Physics D: Applied Physics, **40*(22)**, 7121-7127.

Ma JUN, Sun JIE, & Wang JUN. (2004). Detection of spin injection efficiency by tunneling magnetoresistance. *Modern Physics Letters B, **18*(10)**, 411-418.

Maji N, & Nath TK. (2019). Room temperature electrical spin injection from a new spin gapless ferromagnetic semiconducting inverse Heusler alloy Mn_2CoSi into p-Si via SiO_2 tunnel barrier. *Journal of Applied Physics, **125*(17)**, 173903.

March NH. (1982). Electron density theory of atoms and molecules. *The Journal of Physical Chemistry, **86*(12)**, 2262-2267.

Marukame T, Ishikawa T, Matsuda K-I, Uemura T, & Yamamoto M. (2006). High tunnel magnetoresistance in fully epitaxial magnetic tunnel junctions with a full-Heusler alloy $Co_2Cr_{0.6}Fe_{0.4}Al$ thin film. *Applied Physics Letters, **88*(26)**, 262503.

Mathon J, & Umerski A. (2001). Theory of tunneling magnetoresistance of an epitaxial Fe/MgO/Fe(001) junction. *Physical Review B, **63*(22)**, 220403.

Matsushita YI, Madjarova G, Dewhurst JK, Shallcross S, Felser C, Sharma S, & Gross EKU. (2017). Large magnetocrystalline anisotropy in tetragonally distorted Heuslers: a systematic study. *Journal of Physics D: Applied Physics, **50*(9)**, 095002.

Mavropoulos P, Papanikolaou N, & Dederichs PH. (2000). Complex Band Structure and Tunneling through Ferromagnet|Insulator|Ferromagnet Junctions. *Physical Review Letters, **85*(5)**, 1088-1091.

Meinert M, Geisler MP, Schmalhorst J, Heinzmann U, Arenholz E, Hetaba W, Stöger-Pollach M, Hütten A, & Reiss G. (2014). Experimental realization of a semiconducting full-Heusler compound: Fe_2TiSi. *Physical Review B, **90*(8)**, 085127.

Miura Y, Uchida H, Oba Y, Nagao K, & Shirai M. (2007). Coherent tunnelling conductance in magnetic tunnel junctions of half-metallic full Heusler alloys with MgO barriers. *Journal of Physics: Condensed Matter, **19*(36)**, 365228.

Miyazaki T, & Tezuka N. (1995). Giant magnetic tunneling effect in Fe/Al_2O_3/Fe junction. *Journal of Magnetism and Magnetic Materials*, ***139*****(3)**, L231-L234.

Mokhtari DJ, Jum'h I, Baaziz H, Charifi Z, Ghellab T, Telfah A, & Hergenröder R. (2020). Structural, electronic, magnetic and thermoelectric properties of inverse Heusler alloys Ti_2CoSi, Mn_2CoAl and Cr_2ZnSi by employing Ab initio calculations. *Philosophical Magazine*, ***100*****(12)**, 1636-1661.

Monkhorst HJ, & Pack JD. (1976). Special points for Brillouin-zone integrations. *Physical Review B*, ***13*****(12)**, 5188-5192.

Montes E, Rungger I, Sanvito S, & Schwingenschlögl U. (2016). Tunneling magnetoresistance in Si nanowires. *New Journal of Physics*, ***18*****(11)**, 113024.

Nagamine Y, Maehara H, Tsunekawa K, Djayaprawira DD, Watanabe N, Yuasa S, & Ando K. (2006). Ultralow resistance-area product of 0.4Ω(μm)2 and high magnetoresistance above 50% in CoFeB⁄MgO⁄CoFeB magnetic tunnel junctions. *Applied Physics Letters*, ***89*****(16)**, 162507.

Néel ML. (1948). Propriétés magnétiques des ferrites; ferrimagnétisme et antiferromagnétisme. *Ann. Phys.*, ***12*****(3)**, 137-198.

Nistor LE, Rodmacq B, Auffret S, & Dieny B. (2009). Pt/Co/oxide and oxide/Co/Pt electrodes for perpendicular magnetic tunnel junctions. *Applied Physics Letters*, ***94*****(1)**, 012512.

On VV, Nguyen DK, Hoat DM, Ponce-Pérez R, Rivas-Silva JF, & H. Cocoletzi G. (2021). Pressure effects on the electronic, magnetic, thermoelectric, and thermodynamic properties of Mn_2CoSi half-metallic compound. *International Journal of Quantum Chemistry*, ***121*****(4)**, e26445.

Panfilenok AS, Danilyuk AL, & Borisenko VE. (2008). Oscillations of tunnel magnetoresistance in ferromagnet-insulator-ferromagnet structures. *Technical Physics*, ***53*****(4)**, 479-484.

Parkin SS, Kaiser C, Panchula A, Rice PM, Hughes B, Samant M, & Yang SH. (2004). Giant tunnelling magnetoresistance at room temperature with MgO (100) tunnel barriers. *Nat Mater, **3*****(12)**, 862-867.

Parkin SSP, Li ZG, & Smith DJ. (1991). Giant magnetoresistance in antiferromagnetic Co/Cu multilayers. *Applied Physics Letters, **58*****(23)**, 2710-2712.

Paudel R, & Zhu J. (2019). Investigation of half-metallicity and magnetism of bulk and (111)-surfaces of Fe_2MnP full Heusler alloy. *Vacuum, **164***, 336-342.

Pauling L. (1938). The Nature of the Interatomic Forces in Metals. *Physical Review, **54*****(11)**, 899-904.

Perdew JP. (1985). Accurate Density Functional for the Energy: Real-Space Cutoff of the Gradient Expansion for the Exchange Hole. *Physical Review Letters, **55*****(16)**, 1665-1668.

Perdew JP. (1986). Density-functional approximation for the correlation energy of the inhomogeneous electron gas. *Physical Review B, **33*****(12)**, 8822-8824.

Perdew JP, Burke K, & Ernzerhof M. (1996). Generalized Gradient Approximation Made Simple. *Physical Review Letters, **77*****(18)**, 3865-3868.

Perdew JP, Burke K, & Wang Y. (1996). Generalized gradient approximation for the exchange-correlation hole of a many-electron system. *Physical Review B, **54*****(23)**, 16533-16539.

Perdew JP, Chevary J, Vosko S, Jackson K, Pederson M, Singh D, & Fiolhais C. (1992). Atoms, molecules, solids, and surfaces: Applications of the generalized gradient approximation for exchange and correlation. *Physical Review B, **46*****(11)**, 6671-6687.

Perdew JP, & Levy M. (1985). Extrema of the density functional for the energy: Excited states from the ground-state theory. *Physical Review B, **31*****(10)**, 6264-6272.

Perdew JP, Tao J, & Armiento R. (2003). How to Tell an Atom From an Electron Gas : A Semi-Local Index of Density Inhomogeneity. *Acta Physica et Chimica Debrecina, **36*(25)**.

Petersen DE, Sørensen HHB, Hansen PC, Skelboe S, & Stokbro K. (2008). Block tridiagonal matrix inversion and fast transmission calculations. *Journal of Computational Physics, **227*(6)**, 3174-3190.

Popiel ES, Zarek W, & Tuszynski M. (2004). Moessbauer study of the Hausler-type Fe_2MAl compounds for M = V, Cr, Fe, Co, Ni. *Nukleonika, **49*(suplЗ)**, S49-S52.

Pople JA. (1999). Nobel Lecture: Quantum chemical models. *Reviews of Modern Physics, **71*(5)**, 1267-1274.

R A. (2005). The many-electron energy in density functional theory-From Exchange-Correlation Functional Design to Applied Electronic Structure Calculations. *(Doctoral), Royal Institute of Technology*, SE-106 91 Stockholm, Sweden. (TRITA-FYS 2005:48)

Rai D, Shankar A, Sandeep, Singh L, Jamal M, Hashemifar S, Ghimire M, & Thapa R. (2012). Calculation of coulomb repulsion (u) for 3d transition elements in Co_2YAL type heusler alloys. *Armenian Journal of Physics, **5*(3)**, 105.

Rai DP, Hashemifar J, Jamal M, Lalmuanpuia, Ghimire MP, Sandeep, Khathing DT, Patra PK, Indrajit Sharma B, Rosangliana, & Thapa RK. (2010). Study of Co_2MnAl Heusler alloy as half metallic ferromagnet. *Indian Journal of Physics, **84*(6)**, 717-721.

Rambabu P, Anuroopa B, Manivel Raja M, & Kanchana V. (2020). Enhanced Curie temperature and spin polarization in Co-based compounds under pressure: A first principles investigation. *Solid State Sciences, **105***, 106257.

Ruderman MA, & Kittel C. (1954). Indirect Exchange Coupling of Nuclear Magnetic Moments by Conduction Electrons. *Physical Review, **96*(1)**, 99-102.

Rusponi S, Cren T, Weiss N, Epple M, Buluschek P, Claude L, & Brune H. (2003). The remarkable difference between surface and step atoms in the magnetic anisotropy of two-dimensional nanostructures. *Nature Materials, **2*(8)**, 546-551.

Sadoc A, de Graaf C, & Broer R. (2007). Quantum chemical study of the nature of the ground state and the pressure-induced spin transition in $CaFeO_3$. *Physical Review B, **75*(16)**, 165116.

Sakuraba Y, Ueda M, Miura Y, Sato K, Bosu S, Saito K, Shirai M, Konno TJ, & Takanashi K. (2012). Extensive study of giant magnetoresistance properties in half-metallic Co_2(Fe,Mn)Si-based devices. *Applied Physics Letters, **101*(25)**, 252408.

Salam A, & Manal M. (2018). Theoretical study of CaO, CaS and CaSe via first-principles calculations. *Results in Physics, **10***, 934-945.

Şaşıoğlu E, Galanakis I, Friedrich C, & Blügel S. (2013). Ab initio calculation of the effective on-site Coulomb interaction parameters for half-metallic magnets. *Physical Review B, **88*(13)**, 134402.

Şaşıoğlu E, Sandratskii LM, & Bruno P. (2008). Role of conduction electrons in mediating exchange interactions in Mn-based Heusler alloys. *Physical Review B, **77*(6)**, 064417.

Schmidt G, Ferrand D, Molenkamp LW, Filip AT, & van Wees BJ. (2000). Fundamental obstacle for electrical spin injection from a ferromagnetic metal into a diffusive semiconductor. *Physical Review B, **62*(8)**, R4790-R4793.

Shishidou T, Freeman AJ, & Asahi R. (2001). Effect of GGA on the half-metallicity of the itinerant ferromagnet CoS_2. *Physical Review B, **64*(18)**, 180401.

Siakeng L, Mikhailov GM, & Rai DP. (2018). Electronic, elastic and X-ray spectroscopic properties of direct and inverse full Heusler compounds Co_2FeAl and Fe_2CoAl, promising materials for spintronic applications: a DFT+U approach. *Journal of Materials Chemistry C, **6*(38)**, 10341-10349.

Singh M, Saini HS, Thakur J, Reshak AH, & Kashyap MK. (2013). Disorder dependent half-metallicity in Mn_2CoSi inverse Heusler alloy. *Journal of Solid State Chemistry, **208**,* 71-77.

Skaftouros S, Özdoğan K, Şaşıoğlu E, & Galanakis I. (2013). Generalized Slater-Pauling rule for the inverse Heusler compounds. *Physical Review B, **87*(2)**,* 024420.

Slater JC. (1929). The Theory of Complex Spectra. *Physical Review, **34*(10)**,* 1293-1322.

Slater JC. (1930). Atomic Shielding Constants. *Physical Review, **36*(1)**,* 57-64.

Slater JC. (1936a). The Ferromagnetism of Nickel. *Physical Review, **49*(7)**,* 537-545.

Slater JC. (1936b). The Ferromagnetism of Nickel. II. Temperature Effects. *Physical Review, **49*(12)**,* 931-937.

Smidstrup S, Markussen T, Vancraeyveld P, Wellendorff J, Schneider J, Gunst T, Verstichel B, Stradi D, Khomyakov PA, Vej-Hansen UG, Lee M-E, Chill ST, Rasmussen F, Penazzi G, Corsetti F, Ojanperä A, Jensen K, Palsgaard MLN, Martinez U, Blom A, Brandbyge M, & Stokbro K. (2019). QuantumATK: an integrated platform of electronic and atomic-scale modelling tools. *Journal of Physics: Condensed Matter, **32*(1)**,* 015901.

Soulen Jr RJ, Byers JM, Osofsky MS, Nadgorny B, Ambrose T, Cheng SF, Broussard CTTPR, Nowak J, Moodera JS, Barry A, & Coey JMD. (1998). Measuring the spin polarization of a metal with a superconducting point contact. *Science, **282*(5386)**,* 85-88.

Soulen RJ, Byers JM, Osofsky MS, Nadgorny B, Ambrose T, Cheng SF, Broussard PR, Tanaka CT, Nowak J, Moodera JS, Barry A, & Coey JMD. (1998). Measuring the Spin Polarization of a Metal with a Superconducting Point Contact. *Science, **282*(5386)**,* 85-88.

Staroverov VN, Scuseria GE, Tao J, & Perdew JP. (2003). Comparative assessment of a new nonempirical density functional: Molecules and hydrogen-bonded complexes. *The Journal of Chemical Physics, **119**(23)*, 12129-12137.

Staroverov VN, Scuseria GE, Tao J, & Perdew JP. (2004). Tests of a ladder of density functionals for bulk solids and surfaces. *Physical Review B, **69**(7)*, 075102.

Stradi D, Martinez U, Blom A, Brandbyge M, & Stokbro K. (2016). General atomistic approach for modeling metal-semiconductor interfaces using density functional theory and nonequilibrium Green's function. *Physical Review B, **93**(15)*, 155302.

Straub GK, & Harrison WA. (1989). Self-consistent tight-binding theory of elasticity in ionic solids. *Physical Review B, **39**(14)*, 10325-10330.

Sun JZ, & Ralph DC. (2008). Magnetoresistance and spin-transfer torque in magnetic tunnel junctions. *Journal of Magnetism and Magnetic Materials, **320**(7)*, 1227-1237.

Takagishi M, Yamada K, Iwasaki H, Fuke HN, & Hashimoto S. (2010). Magnetoresistance Ratio and Resistance Area Design of CPP-MR Film for 2-5 Tb/in^2 Read Sensors. *IEEE Transactions on Magnetics, **46**(6)*, 2086-2089.

Takahashi YK, Srinivasan A, Varaprasad B, Rajanikanth A, Hase N, Nakatani TM, Kasai S, Furubayashi T, & Hono K. (2011). Large magnetoresistance in current-perpendicular-to-plane pseudospin valve using a $Co_2Fe(Ge_{0.5}Ga_{0.5})$ Heusler alloy. *Applied Physics Letters, **98**(15)*, 152501.

Tanaka MA, Hori T, Hori S, Kondou K, Kasai S, Ono T, & Mibu K. (2011). Bias-voltage-dependence of magnetoresistance for epitaxial Fe/MgO/Co_2MnSn tunnel junctions. *Journal of Physics: Conference Series, **266***, 012107.

Tao J, Perdew JP, Staroverov VN, & Scuseria GE. (2003). Climbing the Density Functional Ladder: Nonempirical Meta-Generalized Gradient Approximation Designed for Molecules and Solids. *Physical Review Letters, **91**(14)*, 146401.

Terris BD, & Thomson T. (2005). Nanofabricated and self-assembled magnetic structures as data storage media. *Journal of Physics D: Applied Physics, **38*(12)**, R199-R222.

Tezuka N, Ikeda N, Sugimoto S, & Inomata K. (2006). 175% tunnel magnetoresistance at room temperature and high thermal stability using $Co_2FeAl_{0.5}Si_{0.5}$ full-Heusler alloy electrodes. *Applied Physics Letters, **89*(25)**, 252508.

Thomas LH. (1927). The calculation of atomic fields. *Mathematical Proceedings of the Cambridge Philosophical Society, **23*(5)**, 542-548.

Vadapoo R, Hallal A, Yang H, & Chshiev M. (2016). First-principles investigation of magnetocrystalline anisotropy at the $L2_1$ full Heusler|MgO interfaces and tunnel junctions. *Physical Review B, **94*(10)**, 104418.

Vanderbilt D. (1990). Soft self-consistent pseudopotentials in a generalized eigenvalue formalism. *Physical Review B, **41*(11)**, 7892-7895.

Varghese SS, Varghese SH, Swaminathan S, Singh K, & Mittal V. (2015). Two-Dimensional Materials for Sensing: Graphene and Beyond. *Electronics, **4**, 651-687.

Wang W, Sukegawa H, Shan R, & Inomata K. (2008). Large tunnel magnetoresistance in $Co_2FeAl_{0.5}Si_{0.5}$|MgO|$Co_2FeAl_{0.5}Si_{0.5}$ magnetic tunnel junctions prepared on thermally oxidized Si substrates with MgO buffer. *Applied Physics Letters, **93*(18)**, 182504.

Wang Y, Perdew JP, Chevary JA, Macdonald LD, & Vosko SH. (1990). Exchange potentials in density-functional theory. *Physical Review A, **41*(1)**, 78-86.

Wang Y, Shang S-L, Fang H, Liu Z-K, & Chen L-Q. (2016). First-principles calculations of lattice dynamics and thermal properties of polar solids. *npj Computational Materials, **2*(1)**, 16006.

Wei HX, Qin QH, Ma M, Sharif R, & Han XF. (2007). 80% tunneling magnetoresistance at room temperature for thin Al–O barrier magnetic tunnel junction with CoFeB as free and reference layers. *Journal of Applied Physics, **101*(9)**, 09B501.

Wolf SA, Awschalom DD, Buhrman RA, Daughton JM, von Molnár S, Roukes ML, Chtchelkanova AY, & Treger DM. (2001). Spintronics: A Spin-Based Electronics Vision for the Future. *Science, **294*(5546)**, 1488-1495.

Wolf SA, & Treger D. (2000). Spintronics: a new paradigm for electronics for the new millennium. *IEEE Transactions on Magnetics, **36*(5)**, 2748-2751.

Wurmehl S, Fecher GH, Kandpal HC, Ksenofontov V, Felser C, & Lin H-J. (2006). Investigation of Co_2FeSi: The Heusler compound with highest Curie temperature and magnetic moment. *Applied Physics Letters, **88*(3)**, 032503.

Xiao W-Z, Wang L-l, Meng B, & Xiao G. (2014). First-principles insight into the surface magnetism of Cu-doped SnO_2 (110) thin film. *RSC Advances, **4*(75)**, 39860-39865.

Xing N, Li H, Dong J, Long R, & Zhang C. (2008). First-principle prediction of half-metallic ferrimagnetism of the Heusler alloys Mn_2CoZ (Z=Al, Ga, Si, Ge) with a high-ordered structure. *Computational Materials Science, **42*(4)**, 600-605.

Yakushiji K, Kubota H, Fukushima A, & Yuasa S. (2015). Perpendicular magnetic tunnel junctions with strong antiferromagnetic interlayer exchange coupling at first oscillation peak. *Applied Physics Express, **8*(8)**, 083003.

Yan P-L, Zhang J-M, & Xu K-W. (2016). First-principles study on the magnetic and half-metallic properties in bulk and (001) surface of Ti_2CoSn Heusler alloy. *Thin Solid Films, **609***, 19-24.

Yin MT, & Cohen ML. (1982). Theory of ab initio pseudopotential calculations. *Physical Review B, **25*(12)**, 7403-7412.

Yuasa S, Nagahama T, Fukushima A, Suzuki Y, & Ando K. (2004). Giant room-temperature magnetoresistance in single-crystal Fe/MgO/Fe magnetic tunnel junctions. *Nature Materials, **3**(12)*, 868-871.

Yuasa S, Nagahama T, Kawakami T, Ando K, & Suzuki Y. (2002). A large quantum-well oscillation of the TMR effect. *Journal of Physics D: Applied Physics, **35**(19)*, 2427-2431.

Zener C. (1951). Interaction between the *d*-Shells in the Transition Metals. II. Ferromagnetic Compounds of Manganese with Perovskite Structure. *Physical Review, **82**(3)*, 403-405.

Zhang L, Dong S, Du J, Lu Y-L, Zhao H, & Feng L. (2020). First-Principles Forecast of Gapless Half-Metallic and Spin-Gapless Semiconducting Materials: Case Study of Inverse Ti_2CoSi-Based Compounds. *Applied Sciences, **10**(3)*.

Zhang S, Levy PM, Marley AC, & Parkin SSP. (1997). Quenching of Magnetoresistance by Hot Electrons in Magnetic Tunnel Junctions. *Physical Review Letters, **79**(19)*, 3744-3747.

Zhang Y, & Yang W. (1998). Comment on ``Generalized Gradient Approximation Made Simple". *Physical Review Letters, **80**(4)*, 890-890.

Zheng A, Huang H, Gao G, & Yao KJJoMS. (2018). Surface half-metallicity in the Heusler alloy Cr_2CoGa with low magnetic moment. ***53***, 8364-8371.

Zhu Z, Wang H, & Schwingenschlögl U. (2015). Surface Electronic States of 18 Valence Electron Half-Heusler Semiconductors. *Advanced Materials Interfaces, **2**(4)*, 1400340.

Zipporah M, Rohit P, Robinson M, Julius M, Ralph S, & Arti K. (2017). First-principle investigation of structural, electronic and magnetic properties of Co_2VIn and CoVIn Heusler compounds. *AIP Advances, **7**(5)*, 055705.

Žutić I, Fabian J, & Das Sarma S. (2004). Spintronics: Fundamentals and applications. *Reviews of Modern Physics, **76**(2)*, 323-410.

BRIEF BIODATA OF LALRINKIMA

Name	:	Lalrinkima
Father's Name	:	Laldinsanga
Date of Birth	:	29 - 01 - 1992
Address	:	H/No. 45, Near Bazar, Kawn Veng Bilkhawthlir, Mizoram, Pin- 796091.
Subject of Specialization	:	Condensed Matter Physics
Educational Qualification	:	

H.S.L.C	:	2008	First Division	M.B.S.E.
H.S.S.L.C.	:	2010	Second Division	M.B.S.E.
B.Sc. (Physics)	:	2013	First Division	M.Z.U.
M.Sc. (Physics)	:	2017	Distinction	M.Z.U.
Pre-Ph.D Course	:	2018	A^+	M.Z.U.

Working Experience:

- Completed M.Sc. Project work entitled "Determination of Linear Attenuation coefficient (μ) and half value layer of Aluminium sheets placed in X-ray beam generated at $70kV_p$ and $90kV_p$" under the supervision of Prof. R.C. Tiwari at Department of Physics, Mizoram University, Mizoram (796004), 2017.

- Completed online training course on "Research and Publication Ethics" organized by the UGC Human Resource Development Centre, Mizoram University, during 1^{st} – 7^{th} October, 2021.

- Completed research works as Research Assistant on DST-RFBR (Indo-Russia) Sponsored Project entitled, "Modelling and experimental investigation of half metallic epitaxial films based on Heusler alloys for spin-injection Tetrahertz and Far-infrared Photonics", from 6th February 2018 – 6th February 2020 under the Project Principal Investigator Dr. Dibya Praksh Rai, Department of Physics, Pachhunga University College, Aizawl, Mizoram in collaboration with Institute of Microelectronics Technology and High Purity Materials, Russian Academy of Science, Ac. Osipian str. 6, 14432 Chernogolovka, Moscow region, Russia.

- Started research work on "Study of surface half metallicity of full Heusler compounds using ab-initio approach" since August 2018 under the supervision of Dr. Lalthakimi Zadeng, Department of Physics, Mizoram University, Aizawl, Mizoram and Joint Supervision of Dr. Dibya Prakash Rai, Department of Physics, Pachhunga University College, Aizawl, Mizoram, in collaboration with Physical Sciences Research Centre, Pachhunga University College, Aizawl.

LISTS OF PUBLICATIONS AND ACTIVITIES

(I) Journals:

1. **Lalrinkima,** S.M. Kastuar, L. Zadeng, R. Zosiamliana, B. Chettri, Y.T. Singh, L. Zuala, D.P. Rai, C.E. Ekuma (2023). Giant intrinsic magnetoresistance in spin-filtered tunnel junctions with ferromagnetic electrode. *Physical Review B* **107,** 155305. https://doi.org/10.1103/PhysRevB.107.155305. ISSN: 2469-9950 (print); 2469-9969 (online). **IF = 3.908**

2. **Lalrinkima**, Lalthakimi Zadeng, Lalmuan Chhana, Lalhriat Zuala, D.P. Rai (2022). Surface half metallicity and thermodynamic stability of 001-plane Ti_2XSi (X=Mn, Co) Heusler alloys (HAs): A DFT approach. *Surfaces and Interfaces*, **28**, 101602(1-7). https://doi.org/10.1016/j.surfin.2021.101602. Online ISSN: 2468-0230. **IF = 6.137**

3. **Lalrinkima**, C.E. Ekuma, T.C. Chibueze, L.A. Fomin, I.V. Malikov, L. Zadeng, D.P. Rai (2021). Electronic, magnetic, vibrational and X-ray spectroscopy of inverse full-Heusler Fe_2IrSi alloy. *Physical Chemistry Chemical Physics*, **23**, 11876-11885. https://doi.org/10.1039/D1CP00418B. ISSN 1463-9076 (Print). **IF = 3.945**

4. **Lalrinkima**, L.A. Fomin, I.V. Malikov, Lalthakimi Zadeng, D.P. Rai (2020). Perpendicular magnetocrystalline anisotropy energy (MAE) of 111-surface slab of Fe_2CoAl. *Materials Research Express*, **7**, 064003(1-6). DOI 10.1088/2053-1591/ab97e4. Online ISSN: 2053-1591. **IF = 2.025**

5. **Lalrinkima Siakeng**, Gennady M Mikhailov, D.P. Rai (2018). Electronic, elastic and X-ray spectroscopic properties of direct and inverse full Heusler compounds Co_2FeAl and Fe_2CoAl, promising materials for spintronic applications: DFT+U approach. *Journal of Materials Chemistry C*, **6,** 10341-10349. https://doi.org/10.1039/C8TC02530D. ISSN: 20507534, 20507526. **IF = 8.067**

6. D.P. Rai, **Lalrinkima**, Lalhriatzuala, L.A. Fomin, I.V. Malikov, Adlane Sayede, Madhav Prasad Ghimire, R.K. Thapa, Lalthakimi Zadeng (2020). Pressure dependent half-metallic ferromagnetism in inverse Heusler alloy

Fe_2CoAl: a DFT+U calculations. *RSC Advances*, **10**, 44633-44640. https://doi.org/10.1039/D0RA07543D. ISSN 2046-2069 (Online). **IF = 4.036**

(II) Conference Proceedings:

1. **Lalrinkima**, Lalhriatzuala, D.P. Rai, Sunita Srivastava (2019). Strain dependence of electronic properties and effective masses of monolayer ZnO from density functional theory. AIP Conference Proceedings **2115**, 030093.

(III) Conferences/Workshop Attended

(a) National:

1. **Lalrinkima,** Lalhriatzuala, D.P. Rai, Sunita Strivastava (2018 Strain dependence of electronic properties and effective masses of monolayer ZnO from density functional theory. *63rd DAE Solid States Physics Symposium* (DAE-SSPS 2018), during 18th-22nd December , 2018. Guru Jambheshwar University of Science and Technology, Hisar, Haryana. (**Poster Presentation**)

2. **Lalrinkima**, D.P. Rai, Lalthakimi Zadeng (2018). Surface calculation of Fe_2CoAl from Density Functional Theory. *Mizoram Science Congress 2018*, during 4th-5th October, 2018, Pachhunga University College, Mizoram University, Aizawl. (**Oral Presentation**)

3. **Lalrinkima,** Lalthakimi Zadeng, D.P. Rai (2020). Electronics Structure and Perpendicular Magnetocrystalline Anisotropy Energy at the Inverse Full Heusler-Fe_2CoAl (111) Surface. *DST-SERB funded One Day workshop on 'Recent Advances in Theoretical and Condensed Matter Physics'*, on 26th February 2020, Pachhunga University College, Mizoram University, Aizawl. (**Oral Presentation**)

4. **Lalrinkima** (2019). *DST sponsored National Level Workshop on Quantum Science and Technology*, during 29th -31st July, 2019. Pachhunga University College, Mizoram University, Aizawl. **(Participated)**

5. **Lalrinkima** (2021). *Advanced Materials-Webinar Series 2021 (Event 5): Novel Magnetic Materials*, on 20th December 2021. St. Joseph's College (Autonomous), Tiruchirappalli, India. **(Participated)**

(b) International:

1. **Lalrinkima Siakeng,** Gennady M. Mikhailov, D.P. Rai (2018). First Principle Study of Direct and Inverse Full Heusler Compounds: Co_2FeAl and Fe_2CoAl. *International workshop on Evolution of Electronic Structure Theory & Experimental Realization (EESTER-2018)*, during September 11-15, 2018. SRM Institute of Science and Technology & Indian Institute of Technology Madras, Chennai, Tamil Nadu. (**Poster Presentation**)

2. **Lalrinkima,** D.P. Rai, L.A. Fomin, I.V. Malikov, Lalthakimi Zadeng (2019). Perpendicular magnetocrystalline anisotropy energy (MAE) of 111-surface slab of Fe_2CoAl. *International Conference on Nanoscience and Nanotechnology (ICNAN-2019)*, during 29th November-1st December, 2019. Centre for Nanotechnology Research (CNR), Vellore Institute of Technology, Vellore, Tamil Nadu. (**Poster Presentation**)

3. **Lalrinkima**, C.E. Ekuma, T.C. Chibueze, L.A. Fomin, I.V. Malikov, L. Zadeng, D.P. Rai (2021). Electronic, structural and Vibrational properties of Fe_2IrSi: A DFT+U Study. *Symposium on Magnetism and Spintronics (SMS-2021)*, during 25th – 27th November, 2021. NISER Bhubaneswar, India. **(Poster Presentation)**

4. **Lalrinkima** (2021). *First International Conference on Material Sciences and Applied Physics (ICMSAP-2021)*, during 22nd -24th November 2021. Pachhunga University College, Mizoram University, Aizawl. **(Participated)**

Abroad activities:

Visited *Institute of Microelectronics Technology and High Purity Materials RAS, 142432 Chernogolovka, Moscow Oblast, Russia* and presented an annual report of the joint Indo-Russia (DST-RFBR) project work on behalf of the Project Investigator (India) Dr. Dibya Prakash Rai, during 28th October – 2nd November, 2019. **(Oral Presentation)**

PCCP

ROYAL SOCIETY OF CHEMISTRY

PAPER

Cite this: *Phys. Chem. Chem. Phys.*, 2021, **23**, 11876

Electronic, magnetic, vibrational, and X-ray spectroscopy of inverse full-Heusler Fe_2IrSi alloy

Lalrinkima, [ab] C. E. Ekuma, *[c] T. C. Chibueze,[d] L. A. Fomin, [e] I. V. Malikov,[e] L. Zadeng[a] and D. P. Rai *[b]

Received 28th January 2021,
Accepted 21st April 2021

DOI: 10.1039/d1cp00418b

rsc.li/pccp

We report the electronic, magnetic, structural, vibrational, and X-ray absorption spectroscopy of the inverse full-Heusler Fe_2IrSi alloy. We employed state-of-the-art first-principles computational techniques. Our *ab initio* calculations revealed a ferromagnetic half-metallicity with a magnetic moment of $\sim$5.01 μ_B, which follows the Slater Pauling rule. We show rich magnetic behavior due to spin–orbit coupling through the entanglement of the Fe-3d/Ir-5d orbitals. The large extension of the Ir-5d orbital and the itinerant Fe-3d states enhanced spin–orbit and electron–electron interactions, respectively. The analyses of our results reveal that electron–electron interactions are essential for the proper description of the electronic properties while spin–orbit coupling effects are vital to accurately characterize the X-ray absorption and X-ray magnetic circular dichroism spectra. We estimate the strength of the spin–orbit coupling by comparing the intensity of the white-line features at the L_3 and L_2 absorption edges. This led to a branching ratio that deviates strongly from the statistical ratio of 2, indicative of strong spin–orbit coupling effects in the inverse full-Heusler Fe_2IrSi alloy.

1 Introduction

The manipulation of the spin degrees of freedom (spintronics) and its integration into devices has become the paradigm of frontier research for the advancement of next-generation technology. High-spin polarization and a high Curie temperature[1,2] are considered to be vital in achieving this goal. Materials with electronically active d-orbitals, such as Heusler alloys, have been identified as manifesting diverse physical and chemical properties. These properties include half-metallicity, topological insulators, shape memory, thermoelectricity, low Gilbert damping, high Curie temperature, and high spin polarization.[3–12] One of the most explored properties of the Heusler alloys is that they can act as half-metal ferromagnets (HMFs).[13–20] Half-metallic materials show metallic behavior in one spin channel while exhibiting semiconducting behavior in the other spin channel; they can provide a single-spin transport that could be important in future nanoelectronic devices. For practical applications, however, a spintronics material should possess a stable ferromagnetic half-metallic ground state and a high Curie temperature T_C beyond room temperature. In recent years, several theoretical and experimental studies have explored spintronics in Heusler-based compounds.[2,15–27] Gasi *et al.*[28] reported the T_C of some Fe-based inverse Heulser alloys: Fe_2CoGe (T_C, 925 K), Fe_2NiGe (T_C = 750 K), Fe_2NiGa (T_C = 845 K), Fe_2CuGa (T_C = 798 K), and Fe_2CuAl (T_C = 875 K). Dannenberg *et al.*[29] studied the structural ordering dependence of the T_C. These authors reported T_C values of $\sim$780 K and 770 K for the $L2_1$ and $L1_0$ phase of Fe_2CoGa, respectively.

In general, Heusler alloys can be grouped into a family of binary (X_3Z), ternary (X_2YZ), and quaternary (X_1X_2YZ) compounds, where X and Y are mainly transition metals and Z is the main group element. The ternary Heulser alloys have been shown to exist in two ordered structures: the conventional Cu_2MnAl-type exhibiting $Fm\bar{3}m$ symmetry[30] and the newly discovered Hg_2CuTi-type with the $F\bar{4}3m$ space group.[31] The former is generally referred to as a regular ($L2_1$) and the latter as an inverse (XA) Heusler alloy. We note that interest in the inverse equivalent of conventional materials is not only limited to the Heusler alloys (see, *e.g.*, ref. 32). The Wyckoff positions of the atomic system in both the XA and $L2_1$ phases of Fe_2IrSi are presented in Table 1. While the $L2_1$ phase has been studied (see, *e.g.*, the work of Krishnamurthy *et al.*[33]), the properties of the XA phase of Fe_2IrSi are relatively unexplored both experimentally and computationally. In the present study, we explore the electronic, magnetic, elastic, and X-ray spectroscopic properties of the less studied inverse full-Heusler Fe_2IrSi alloy using state-of-the-art first-principles computational approaches. Although both the $L2_1$ and XA Heusler

[a] *Department of Physics, Mizoram University, Aizawl-796004, India*
[b] *Physical Sciences Research Center (PSRC), Department of Physics, Pachhunga University College, Mizoram University, Aizawl-796001, India. E-mail: dibya@pucollege.edu.in*
[c] *Department of Physics, Lehigh University, Bethlehem, PA 18015, USA. E-mail: che218@lehigh.edu*
[d] *Department of Physics & Astronomy, University of Nigeria, Nsukka, 410001, Nigeria*
[e] *Institute of Microelectronics Technology and High Purity Materials, Russian Academy of Sciences (RAS), 142432, Chernogolovka, Russia*

Table 1 Whyckoff positions of inverse and regular full-Heusler Fe_2IrSi

Positions	x	y	z	Positions	x	y	z
XA phase				$L2_1$ phase			
Ir(4c)	0.25	0.25	0.25	Ir(4b)	0.50	0.50	0.50
Si(4a)	0.00	0.00	0.00	Si(4a)	0.00	0.00	0.00
Fe1(4d)	0.75	0.75	0.75	Fe(8c)	0.25	0.25	0.25
Fe2(4b)	0.50	0.50	0.50				

phase are highly ordered structures, our full structural optimization shows that the XA phase is energetically more stable by ~0.71 eV. Moreover, the predicted lattice constant of ~5.84 Å is in better agreement with structurally similar Fe-based compounds.[11,28,34–41] Using *ab initio* calculations, we predict a semiconducting ferromagnetic half-metallicity in inverse full-Heusler Fe_2IrSi with a rather high Curie temperature of ~911.7 K and a large melting temperature of ~2000 K. These properties support a half-metallicity that is stable well above room temperature. We hope that our results will motivate the future experimental investigation of the exotic properties of the inverse full-Heusler Fe_2IrSi alloy and related compounds.

2 Computational details

The unit cell of Fe_2IrSi with the XA structure belongs to the space group 216 ($F\bar{4}3m$) consisting of four interpenetrating face-centered cubic lattices. The Wyckoff positions of both the XA and $L2_1$ crystal structures are presented in Table 1. To model the physical properties of inverse full-Heusler Fe_2IrSi, we performed first-principles density functional theory (DFT)[42,43] calculations using the generalized gradient approximation (GGA) exchange–correlation functional of Perdew–Burke–Ernzerhof (PBE)[44] and screened Coulomb interactions (DFT+U) from the Lichtenstein approach.[45] The effective Coulomb potential is $U_{\text{eff}} \equiv U_{\text{Fe/Ir}} - J_{\text{Fe/Ir}}$. The effective interactions on the spin and orbitally polarized Ir d orbital are treated as a free parameter and U_{Ir} varies from 0 to 3.0 eV. However, J_{Ir} is not available in the literature so J_{Ir} = 0 eV is considered. We also varied U_{Fe} = 3.0–5.0 and adopted J_{Fe} = 0.50 eV for the exchange coupling parameter as $J_{3\text{d}}$ varies from 0.36 to 6.0 eV.[46,47] The result of electronic structures has a negligible impact within U_{Fe} = 3.0–5.0 eV and U_{Ir} = 1.0 eV. Therefore, we have estimated the interaction parameter $U_{\text{Fe}} \approx 3.52$ eV on Fe-d electrons and $U_{\text{Ir}} \approx 1.0$ eV on Ir-d electrons. Interestingly, this value of U = 3.52 eV for Fe in Fe_2IrSi is close to U_{Fe} = 3.8 eV in Co_2FeAl[48] and 3.1–3.83 eV for other 3d-electrons.[47] In our calculations, we used the Quantum Espresso electronic structure suite.[49] The electronic structure is obtained using a plane-wave basis set formalism with a cutoff energy of 100 Ryd and 16 × 16 × 16 k-points were used to sample the Brillouin zone. To obtain the exchange parameter, which is essential for determining the Curie temperature, we adopt the first-principles Green function-based Korringa–Kohn–Rostoker method using the SPRKKR code in its full potential, fully relativistic mode.[50,51] We used well-converged basis sets with dense Brillouin zone (BZ) sampling with a uniform grid of 250 k-points in the irreducible wedge of the BZ. The SPRKKR muffin-tin sphere radii were 2.60 bohr for Fe and Si, and 2.83 bohr for Ir. We treated the Fe-3d and 4s, Ir-4f, 5d and 6s, and Si-3s and 3p as valence electrons. The inclusion of the Ir-4f states has an insignificant impact on the calculated results; they are localized far away from the Fermi energy and, as such, we did not include them in subsequent calculations. The energy integrals were evaluated on a semicircular path withing the complex energy plane, using a Gaussian mesh of 50 points, and a maximum angular momentum $l_{\text{max}}^{\text{KKR}} = 3$ is used for the multipole expansion of the Green function. The SPRKKR code is also used to model the X-ray Absorption Spectra (XAS) and X-ray Magnetic Circular Dichroism (XMCD) using 1000 k-points to sample the irreducible wedge of the BZ. All input parameters in our calculations were checked for convergence.

3 Results and discussion

3.1 Structural and vibrational properties

An essential step in our calculations is establishing the ground state crystal structure of full-Heusler Fe_2IrSi, *i.e.*, whether Fe_2IrSi prefers $L2_1$ or XA symmetry [see Fig. 1(a and b)]. The experimental work of Krishnamurthy *et al.* studied the $L2_1$ crystal structure of Fe_2IrSi.[33] Consider a full-Heusler alloy with the chemical formula X_2YZ. In the regular, full-Heusler system, the electronegativity of the X atom is greater than that of the Y atom and *vice versa* for the inverse full-Heusler alloy. From this chemistry point of view, we expect Fe_2IrSi to be an inverse alloy because the Fe atom is less electronegative than the Ir atom. For full structural optimization of the lattice parameters, the energy and charge convergence criteria were set to 10^{-3} eV and 0.0001e, respectively. The Hellmann–Feynman forces experienced by all atoms in the cell are lower than 10^{-3} eV Å^{-1}. The initial structures (both for $L2_1$ and XA) were constructed using the experimental lattice constant a = 4.99 Å.[33] The most energetically stable structure is the one with the lowest ground state energy. We consider ferromagnetic (FM) and antiferromagnetic (AFM) configurations, respectively. The equilibrium lattice constant of each magnetic configuration is obtained by computing the total energy at the various lattice constants around the experimental lattice constants. We fit the calculated total energy (per unit cell)–lattice constant profile to the Murnaghan equation of state for both the $L2_1$ and XA structures. The obtained data are presented in Fig. 1(c). The calculated total energy difference $\Delta E = E_{\text{T}}^{\text{NM}} - E_{\text{T}}^{\text{FM/AFM}}$ and the corresponding magnetic moment for each atomic specie is presented in Table 2, where NM denotes the nonmagnetic state. From the energetic analysis, the XA phase with the FM configuration has the lowest ground state energy. This is due to the involvement of transition metal atoms in Heuslers with larger numbers of valence electrons and their interatomic distance. As it is well-known from the Bethe–Slater curve[52–54] when the late transition metal atoms like Fe, Co *etc.*, are at a certain interatomic distance the overlap of the wavefunctions is such that the ferromagnetic coupling is favored. In order to get antiferromagnetic coupling they should be much closer. In Fe_2IrSi the interatomic distance is comparable to Fe-bulk and thus

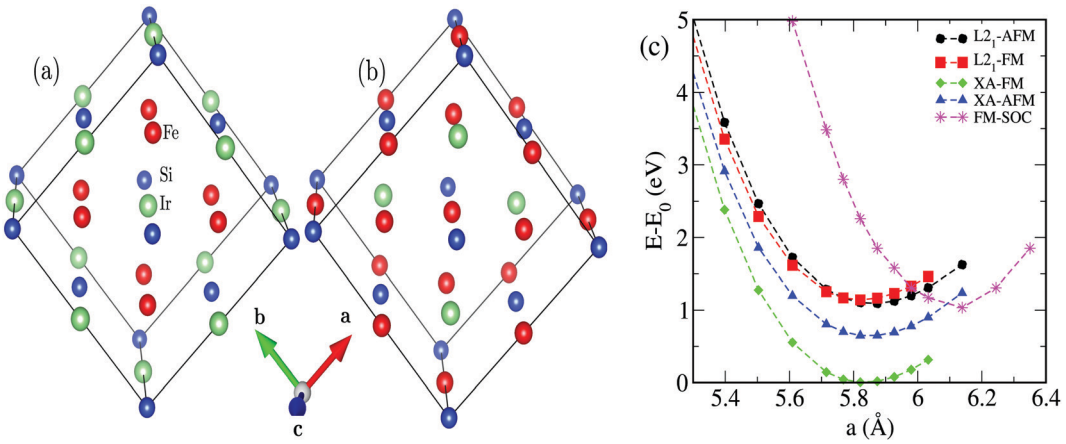

Fig. 1 The crystal structure of regular (a) and inverse (b) full-Heusler Fe_2IrSi. (c) Relative energy ($E - E_0$) per unit cell *versus* lattice constant profile of the various magnetic configurations calculated using the Quantum Espresso code.

Table 2 Magnetic moment of each atom in the XA and $L2_1$ structures, and the total energy (E_T) for the various magnetic configurations (MG) in full-Heusler Fe_2IrSi obtained with DFT. E_T is with respect to the nonmagnetic (NM) ground state, *i.e.*, $\Delta E = E_T^{NM} - E_T^{FM/AFM}$

MG	Fe1	Fe2	Ir	Si	ΔE (eV)
XA phase					
FM	1.89	2.88	0.30	−0.03	1.60
AFM	−2.47	2.08	−0.20	−0.07	0.91
$L2_1$ phase					
FM	2.01	2.01	0.62	−0.07	0.89
AFM	−2.29	2.29	0.0	0.0	0.98

ferromagnetism is favored. Also, magnetism of Fe dominates that of Ir giving rise to an itinerant-electron ferromagnet like behaviour. Thus the exchange interaction J increases with the number of conduction electrons, in fact the latter produce J *via* the Zener and de Gennes ferromagnetism mechanism. This favours ferromagnetism and dominates all other possible mechanisms.[55] We predict the lattice constant to be ∼5.84 Å. We note that the predicted lattice parameter is closer to structurally similar Fe-based Heusler compounds with a lattice constant of ≥5.80 ± 0.61 Å.[11,28,34–41]

To determine the dynamical stability of the predicted inverse full-Heusler alloy, we calculated the phonon and vibrational properties using density functional perturbation theory. The forces are calculated with Quantum Espresso.[49] The calculated phonon dispersion along the high symmetry points of the Brillouin zone, the corresponding phonon density and projected density of states, and the Raman spectra are presented in Fig. 2. We do not observe any imaginary frequency in the phonon dispersion, which confirms the dynamical stability. The atoms contribute to all the frequency scales with Si dominating at the mid-frequency regime of ∼20 meV. Surprisingly, there is a large density of Ir atoms in the high-frequency regime of ∼36 meV of the optical branch. This trend deviates from the simple trend observed in the diatomic linear chain model where the frequency scale of the acoustic (optical) phonon modes are dominated by atoms with larger (smaller) masses.[56] Inverse

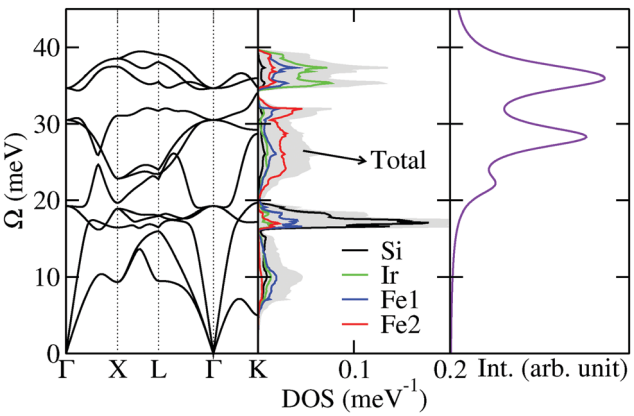

Fig. 2 Calculated phonon band structure along the various high symmetry points in the first Brillouin zone, the density and the projected phonon density of states, and the Raman spectra of inverse full-Heusler Fe_2IrSi obtained with the Quantum Espresso code.

full-Fe_2IrSi belongs to the point group T_d ($\bar{4}3m$) with four atoms in the primitive cell; this implies that there will be twelve normal vibrational modes at the zone center (Γ point). The irreducible representation of the vibrational modes at the Γ point is $\Gamma = 4T_2$. The first three low-frequency curves, which are the triply degenerate T_2 modes are the usual acoustic modes characterized by the transverse acoustic (TA), longitudinal acoustic (LA), and the out-of-plane transverse acoustic mode (ZA), respectively. The remaining nine curves belong to the optical mode. Using group theory analysis[57] with the Raman spectra, we predict Raman active modes at ∼20.80, 28.31, and 36.11 meV, which are all triply degenerate. We also observed a strong coupling between the acoustic and the optical branches; this may be due to the heavy Ir atom, which is a predominant feature of electron–phonon coupling.

3.2 Electronic and magnetic properties

We present in Fig. 3 the calculated electronic properties of inverse full-Heusler Fe_2IrSi employing various approximations. The electronic structure is studied using the Quantum Espresso

electronic structure codes. We determine the degree of the spin polarization at the Fermi energy E_F as $P = [N_\uparrow(E_F) - N_\downarrow(E_F)]/[N_\uparrow(E_F) + N_\downarrow(E_F)]$, where $N_\uparrow(E_F)$ and $N_\downarrow(E_F)$ are the number of density of states at E_F for spin-up and spin-down channels, respectively. Employing the GGA functional, we predict a metallic solution in both channels [Fig. 3(a and c)] with ~45% spin polarization. The dispersive band around E_F in the spin-down channel is due to the Fe2-d(↓) ($d - e_g + d - t_{2g}$) and the Fe1-d dominates that of the spin-up channel. The Fe1-d band lies at higher energy in both occupied and unoccupied states as compared with the Fe2-d bands, which fail to give the signature d–d hybridization between Fe1-d and Fe2-d orbitals as in the case of other half-metallic Heusler compounds.[2,15–19] This may be as a result of the insufficient treatment of electronic excitations, especially the highly polarizing Fe-d orbitals within the GGA approximation. To account for the electron–electron correlation effects, we employ the GGA+U functional [Fig. 3(b and d)]. Accounting for the electron–electron interactions, we predict a semiconducting behavior in the spin-down channel with an energy band gap of ~0.78 eV. Interestingly, the variation of U_{Ir} parameter (not shown) has an insignificant impact on the electronic band structures. This is not surprising since the large extensions of the Ir-d orbital support decreased itinerancy of the d electrons associated with the Ir atom. Hence, electron–electron correlation effects emanate mainly from the strongly polarizing Fe-d states. The origin of the energy bandgap in the spin-down channel is due to d–d hybridization, which results in the dominance of the doubly degenerated e_u and the triple t_{2u} orbitals that lie above the E_F.[18] The predicted semiconducting half-metallic behavior within our GGA+U calculations in inverse full-Heusler Fe_2IrSi has a characteristic spin polarization of ~99.9% at the E_F. We have also used spin–orbit coupling (SOC) along with GGA and GGA+U (U_{Ir} = 1.0 eV and U_{Fe} = 3.52 eV). The results of the density of states obtained from GGA + SOC and GGA+U + SOC is presented in Fig. 4(a and b), respectively. With the implementation of SOC the half-metallicity is lost and the system behaves like a magnetic metal. More bands are crossing the Fermi level with the majority of contributions from the Fe1-d, Fe2-d and Ir-d orbitals in the spin down channel.

The magnetic properties of Heusler compound depend mainly on the total number of valence electrons per unit cell,[2,15–18] as determined by the Slater Pauling (SP) rule.[18] The predicted total magnetic moment of the studied Heusler alloy follows the SP rule;[18] $M_t = (Z_t - 24)\ \mu_B$, where M_t is the total magnetic moment and Z_t is the total valence electrons. Since, Fe_2IrSi has 29 valence electrons, the corresponding total magnetic moment (M_t) is expected to be an integer number of 5.0 μ_B according to the SP rule. In the $L2_1$ phase, we observe ~0.62 μ_B for the Ir atom in the FM configuration and it is practically zero in the AFM configuration (see Table 2). In the XA structure, our simulation reveals that the Ir atom is ferromagnetically and antiferromagnetically coupled to the Fe atoms with an average magnetic moment of ~|0.25| μ_B in the FM and AFM states, respectively. The Si atom acquired a small but finite average magnetic moment, which depends weakly on U and antiferromagnetic coupling. As evident from Fig. 5 and Table 2, Fe1 and Fe2 have strikingly different magnetic moments; this is due to the different local coordination of their neighboring atoms. From the analysis of the magnetic coupling, we have gained a better understanding of the origin of the induced magnetic moment at the Ir-site. The ferromagnetic interatomic exchange interactions between the eight nearest neighbor 3d electrons of the Fe atom and the Ir-5d states are the main source of the induced magnetic moment on the Ir-site.

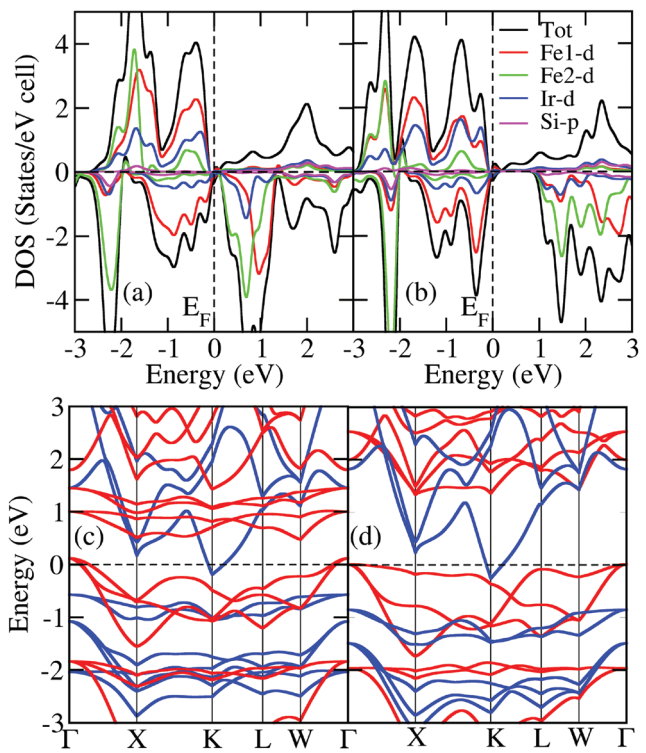

Fig. 3 Calculated total and partial density of states (a and b) and band structure along the high symmetry points of the Brillouin zone (c and d) of inverse full-Heusler Fe_2IrSi with GGA (left panel) and GGA+U (right panel) obtained using the Quantum Espresso code. The vertical dashed line (a and b) and the horizontal dashed-line (c and d) depicts the Fermi energy E_F, which has been set to zero at the top of the valence band. The blue and red curves in (c and d) correspond to the up and down spin channels, respectively.

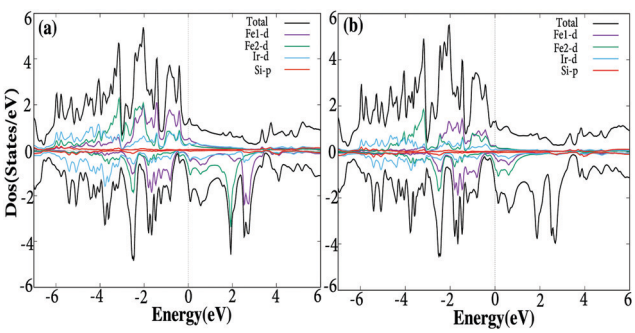

Fig. 4 Calculated total and partial density of states: (a) SOC (b) SOC+U (U_{Ir} = 1.0 eV and U_{Fe} = 3.52 eV).

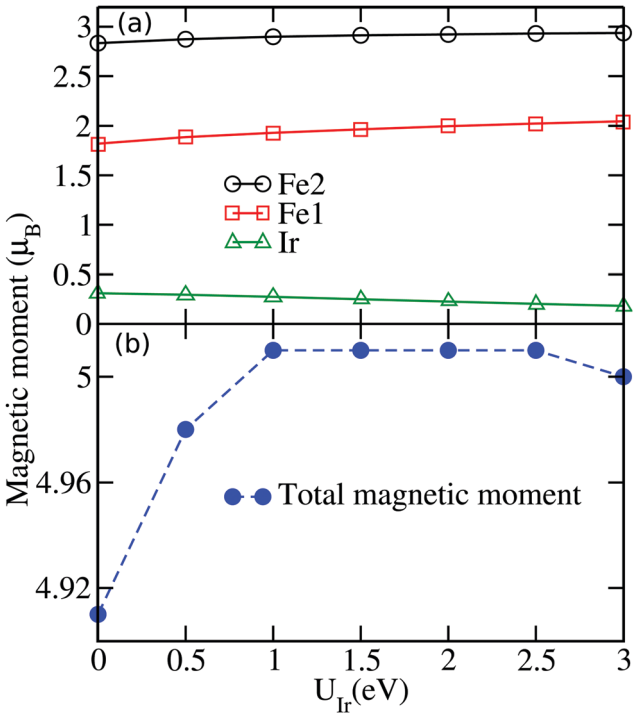

Fig. 5 Variation of the partial and total magnetic moment obtained using GGA+U (U_{Fe} = 3.52 eV, U_{Ir} = 0.0 eV to 3.0 eV) for the XA phase of full-Heulser Fe_2IrSi.

This observation is supported by the significant contribution of the 5d states to the density of states at the E_F. Our calculated GGA value, M_t = 4.91 μ_B, is within the numerical uncertainty of the expected value of 5.0 μ_B. The variation of the atomic moment obtained with the GGA and GGA+U is presented in Fig. 5(a). Observe that the magnetic moment of Fe1 and Fe2-atoms follows the same increasing trend as U_{Ir} value is increased, while that of Ir-atoms decreased slightly. The total magnetic moment as a function of U is presented in Fig. 5(b). If we include electron–electron interactions, the total magnetic moment increased to $\sim$5.01 μ_B and is almost independent of $U_{Ir} > 0.80$ eV, in good agreement with the SP-rule.

To gain further insights into the magnetic properties, we compute the strength of the magnetic interaction based on the Heisenberg model[17] using the SPRKKR code. The Hamiltonian of the extended Heisenberg model for a spin system is given by eqn (1),

$$H = -\sum_{ij} e_i e_j J_{ij} \quad (1)$$

here J_{ij} is the isotropic exchange-coupling related to unit vectors e_i and e_j pointing along the direction of the magnetic moment on the sites i and j, respectively. Using SPRKKR code we have computed the strength of the magnetic interaction J_{ij} by mapping the full system within a Heisenberg Hamiltonian model. The interaction between the atoms at i and j sites (pair exchange interaction parameter) as a function of distance is given by

$$J_{ij} = \frac{1}{4\pi}\int^{E_F} \mathrm{d}(E)\mathrm{Tr}_L\left\{\Delta_i T_\uparrow^{ij} \Delta_j T_\downarrow^{ji}\right\}, \quad (2)$$

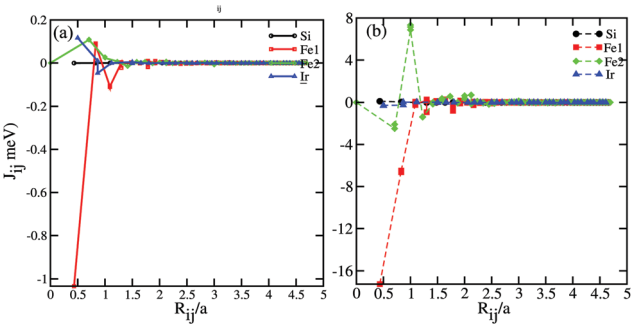

Fig. 6 Calculated exchange coupling parameter J_{ij} as a function of distance the R using GGA+U (U_{Fe} = 3.52 eV) for (a) U_{Ir} = 0.0 eV and (b) U_{Ir} = 1.0 eV obtained with the SPRKKR code.

where $\Delta_{ij} = t_{ij\uparrow}{}^{-1} - t_{ij\downarrow}{}^{-1}$, $t_{\uparrow\downarrow}{}^{-1}$ is the atomic t-matrix of the magnetic impurities at site i for the spin up/down state, $T_{\uparrow\downarrow}{}^{ij}$ is the scattering path operator between ij sites for the spin up/down state, and Tr_L is the trace over the orbital variables of the scattering matrices. The site i is assumed to be at the center of a cluster of radius $R^c = \max|R_i - R_j|$. J_{ij} is then calculated with respect to the atom at i defined by a cluster of radius R^c. We choose Fe2 as the center atom and use $R^c \approx 4.5$ Å. Other choices of $R^c \geq 2.5$ Å have negligible effect on J_{ij}. The calculated J_{ij} as a function of distance is presented in Fig. 6. Beyond 2 Å, J_{ij} is almost constant for all the atoms. We also present in Fig. 7(a) the calculated J_{ij} as a function of U_{Ir}; the variation in J_{ij} with U_{Ir} is rather small. With J_{ij} obtained, we calculate the T_C^{MFA} (see eqn (3)) within a mean-field approximation (MFA),[47,58]

$$\frac{3}{2}K_B T_C^{MFA}\langle e^\mu\rangle = \sum_\nu J_0^{\mu,\nu}\langle e^\nu\rangle \quad (3)$$

where $\langle e^\nu\rangle$ is the average z component of the unit vector e_r^ν pointing in the direction of the spin moment and K_B is the Boltzmann constant. The Curie temperature (T_C) can be obtained from the largest Eigenvalue matrix of $J_0^{\mu,\nu}$.[47,58] The variation of calculated T_C with respect to U_{Ir} is presented in Fig. 7(b). We observe a linear increase of T_C as the exchange interaction J_{ij} increases as denoted by the red dotted line in Fig. 7(b). At $U_{Ir} \approx 1$ eV, the T_C approaches a linear trend $T_C^{cal} = 23 + 181M_t$ [Fig. 7(b)], in agreement with the proposal of Wurmhel *et al.*[2,19] The crossing point $U_{Ir} \approx 1$ eV is also consistent with the point where the critical magnetic moment [lower panel of Fig. 5] is observed. Hence, $U_{Ir} \approx 1$ eV seems to be the optimal interaction strength of the Ir atom in the studied material. At the crossing point in Fig. 7(b), we obtain $T_C \approx 911.7$ K. The linear trend, which is independent of U_{Ir}, is due to the negligible dependence of the total magnetic moment on U_{Ir} (see Fig. 5). The crossing point of the mean-field approach and the linear relation could be said to depict the optimal T_C. Within the nearest-neighbor (NN) interactions and assuming that the exchange energy and spin magnetic moments are the same in both ferro- and antiferromagnetic states, *i.e.*, $|S_1| = |S_2| = S \sim \frac{3}{2}$ as the localized spin, which is the total moment on Fe^{2+} and $J_{AFM} = J_{FM} = J$, we estimate $J = \frac{\Delta E}{NS^2} \approx 153.33$ meV, where $\Delta E \approx 0.69$ eV is the total energy difference between the ferro- and anti-ferromagnetic configurations

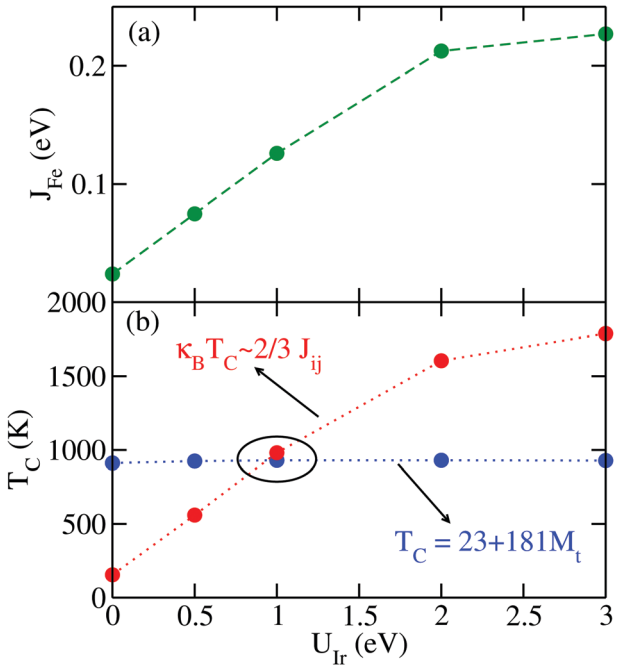

Fig. 7 Calculated (a) exchange-coupling parameter $J_{Fe} = \sum J_{Fe,i}$ for the Fe atom and (b) Curie temperature T_C within the mean-field approximation as a function of U_{Ir} with the GGA+U (U_{Fe} = 3.52 eV). Also plotted in figure (b) is the approximate relation T_C = 23 + 181M_t proposed by Wurmhel *et al.*[2,19]

and N = 2 is the total number of magnetic atoms. Using this, we obtain a NN mean-field Curie temperature $T_C^{MF} \approx 1186.29$ K, where κ_B is the Boltzmann constant. This value is larger than the one obtained using the exchange-coupling parameter within the KKR that accounted for the interactions beyond the NN. Beyond the NN, interactions are generally known to decrease the T_C. Overall we note, however, that mean-field theory usually overestimates T_C; it employs the average of the magnon energies in estimating the T_C, and, as such, does not take into account the local variations of the crystal lattice which could significantly affect the exchange coupling parameter. Nevertheless, the high T_C value suggests that the inverse full-Heusler Fe_2IrSi alloy could be a suitable material for spintronics and optoelectronic applications.

3.3 Elastic properties

The elastic properties determine the mechanical stability of solid materials and further confirm the dynamical stability. The elastic properties are key to ascertaining the stability of the material under applied external forces and serve as a guide on the potential device applications. In this regard, we compute the elastic parameters of the inverse full-Heusler Fe_2IrSi alloy by fitting the Murnaghan equation of states with the relaxation of atomic positions on the application of small strains using the Quantum Espresso code. The shear modulus G is obtained as the average of the Voigt–Reuss approximation: $G = (G_V + G_R)/2$, where $G_V = (C_{11} - C_{12} + 3C_{44})/5$, and $G_R = 5(C_{11} - C_{12})C_{44}/[4C_{44} + 3(C_{11} - C_{12})]$. The Young's modulus is obtained using $Y_M = 9B_MG/(3B_M + G)$, the bulk modulus as $B_M = (C_{11} + 2C_{12})/3$, and the Poisson ratio as $\nu = (3B_M - Y_M)/6B_M$. The calculated moduli of elasticity along with the elastic tensor C_{ij} are presented in Table 3; they satisfy the criteria of mechanical stability for a cubic structure, *i.e.*, $C_{11} - C_{12} > 0$, $C_{44} > 0$, $(C_{11} + 2C_{12}) > 0$. Significant is the large elastic anisotropy A_e of the Fe_2IrSi alloy obtained from eqn (4). This may be due to the intrinsic crystal lattice distortion, which seems to be a generic feature of Heulser alloys.

$$A_e = \frac{2C_{44} + C_{12}}{C_{11}} - 1 \quad (4)$$

Our calculations show an inverse relationship between the onsite Coulomb potential and the degree of anisotropy. This shows that accounting for electron–electron interactions in the d-electrons enhances the stability of the crystal structure. The calculated B/G ratio reveals a decrease in the ductility of Fe_2IrSi with an increase in U_{Ir}. However, at the critical U_{Ir} = 1.0 eV, we obtain a Pugh's modulus ratio (B/G) of ~3.41, which is well above the critical value of ~1.75 for ductility and even higher than the ~2.75 reported for Fe_2CoAl.[41]

The thermodynamical properties can be characterized by calculating the melting temperature T_M, the Debye temperature D_b, and the average sound velocity v_s. The average velocity (v_s) is obtained from eqn (5).

$$v_s = \left[\frac{1}{3}\left(\frac{1}{v_l^3} + \frac{2}{v_t^3}\right)\right]^{-1/3} \quad (5)$$

where $v_l = \sqrt{\frac{3B + 4G}{3\rho}}$ (longitudinal velocity), $v_t = \sqrt{\frac{G}{\rho}}$ (transverse velocity) and ρ is the density. We present the calculated thermodynamical properties in Table 4. A theoretical value of T_M has been determined as T_M (K) = [553 + (5.91)C_{11}] ± 300 K.[59] Our calculations show that inverse full-Heusler Fe_2IrSi exhibits a high $T_M \approx 2000 \pm 300$ K, which supports its stability at high temperatures. Concerning the calculated bulk and shear modulus,

Table 3 Calculated elastic tensor (C_{ij}), degree of elastic anisotropy (A_e), bulk modulus (B_M), modulus of rigidity (G), B/G, Young's modulus (Y_M), and the Poisson ratio (ν) at various onsite Coulomb potentials for the Ir atom

U_{Ir} (eV)	C_{11} (GPa)	C_{12} (GPa)	C_{44} (GPa)	A_e	B_M (GPa)	G (GPa)	B/G	Y_M (GPa)	ν
0.0	246.418	205.792	127.639	6.29	219.334	62.85	3.49	170.458	0.35602
0.5	242.025	205.246	128.728	7.00	217.506	61.23	3.55	166.003	0.35565
1.0	248.454	206.112	130.133	6.15	220.226	64.55	3.41	174.742	0.35361
1.5	244.963	198.477	130.948	5.63	215.639	69.28	3.11	186.432	0.34543
2.0	244.103	183.339	130.792	4.30	203.594	73.48	2.77	195.735	0.33193
2.5	244.877	178.150	129.780	3.89	200.392	75.70	2.65	200.871	0.32668
3.0	259.298	190.877	128.246	3.75	213.684	75.86	2.67	202.763	0.33647

Table 4 Calculated melting temperature T_M, Debye temperature D_b, sound velocity v_s (km s^{-1}), longitudinal velocity v_l (km s^{-1}) and transverse velocity v_t (km s^{-1}) at various onsite Coulomb potentials for the Ir atom

U_{Ir} (eV)	T_M (K)	D_b (K)	v_s	v_l	v_t
0.0	2009.33 ± 300	327.730	2.590	4.410	2.316
0.5	1983.37 ± 300	321.533	2.579	4.411	2.305
1.0	2021.36 ± 300	332.730	2.599	4.474	2.322
1.5	2000.73 ± 300	347.643	2.794	4.434	2.513
2.0	1995.65 ± 300	359.922	2.778	4.315	2.513
2.5	2000.22 ± 300	366.755	2.788	4.418	2.507
3.0	2085.45 ± 300	368.730	2.889	4.426	2.603

the longitudinal v_l, transverse v_t, and the average v_s sound velocities are also determined and presented in Table 4. Further, we obtain the Debye temperature $D_b = \frac{h}{\kappa_B} v_s \left(\frac{3nN_A\rho}{4\pi M}\right)^{1/3}$, where h is Planck's constant, N_A is the Avogadro number, n is the number of atoms in the unit cell, M is the molecular mass, and ρ is the density.[60]

3.4 X-Ray spectroscopy

Fig. 8 shows the calculated X-ray absorption spectra and the X-ray magnetic circular dichroism spectra at the Ir-$L_{2,3}$-edge of inverse full-Heusler Fe_2IrSi obtained using various levels of approximation within the SPRKKR code. The XAS and XMCD spectra were considered as the electron transition from the occupied p-orbital to the unoccupied d-orbital. We have considered the Ir-$L_{2,3}$ absorption edges ($2p_{\frac{1}{2},\frac{3}{2}} \rightarrow 5d$ transition) to examine the signatures of the Ir-5d states. Observe from Fig. 8(a) that relativistic spin–orbit coupling effects significantly impact the XAS spectra. Specifically, the inclusion of spin–orbit coupling led to a strong blueshift of the XAS and the emergence of a sharp, well-defined Ir-$L_{2,3}$ edge. The XMCD spectra are presented in Fig. 8(b). X-Ray magnetic circular dichroism is a useful tool to analyze the intrinsic magnetic properties of materials.[61–63] The contributions of spin and orbital moments can be qualitatively estimated *via* XMCD since it measures the difference between two X-ray absorption spectra in the presence of a magnetic field in two different polarizations directions.[61–63] The calculated spectra exhibit the essential features expected of XAS and XMCD: a sharp, atomic-like "white-line", a step-like edge, and a series of tiny fine structures. These features correspond to the 2p → 5d transition states, 2p → continuum excitations, and the oscillations emanating from the backscattering of photoelectrons off neighboring atoms.[64]

Similar to the electronic structure, we observe a substantial magnetization at the Ir site with a net magnetic moment of 0.28 μ_B per Ir atom. A key point to note is the positive sign of the Ir atom total magnetic moment; this unambiguously confirms a ferromagnetic coupling of the Ir atom to the strong ferromagnetic moment at the Fe sites. The presence of a threshold energy of ∼11 keV at the $L_{2,3}$ edges corresponds to the excitation of the 2p electrons to the 5d states at the X-ray energy. We observe a sharp and distinct X-ray absorption [Fig. 8(a)] and X-ray magnetic circular dichroism absorption [Fig. 8(b)] at both the L_2 $\left(2p_{\frac{1}{2}} \rightarrow 5d\right)$ and L_3 $\left(2p_{\frac{3}{2}} \rightarrow 5d\right)$ absorption edges, which

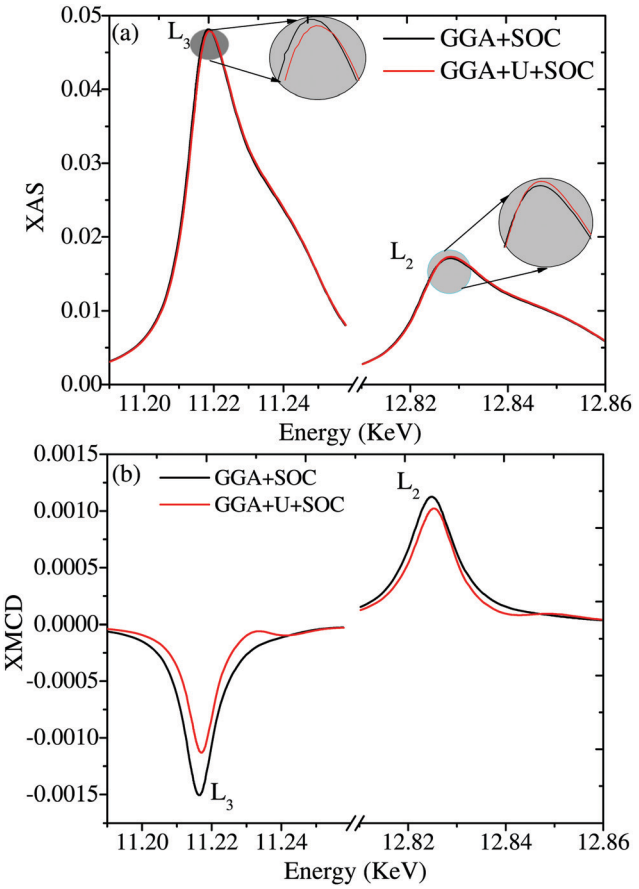

Fig. 8 Calculated (a) XAS and (b) XMCD of inverse full-Heusler Fe_2IrSi at various levels of approximation. We used the default U_{Fe} described in the text and U_{Ir} = 1.0 eV.

occur at energies of 11.10 keV and 12.72 keV, respectively. The predicted position of the Ir-$L_{2,3}$-edge is in basic agreement with the experiment that obtained the L_3 and L_2 edges at ∼11.12 keV and 12.83 keV, respectively, for the $L2_1$ crystal structure of full-Heusler Fe_2IrSi.[33,65] The calculated position of the L_3 peak is also in good agreement with ∼12.22 keV reported for Ir-based compounds.[64] The electric dipole transitions dictated by the selection rule determine the relative strength and, hence, the intensity of the white-lines at both the L_2 and L_3 absorption edges; this is also known as the branching ratio. To gain this understanding and determine the total angular momentum J of the available 5d hole states, we integrate the area of the white-line features, which is proportional to the local density of unoccupied final states.[66] For an allowed dipole transition, ΔJ must be 0 or ±1. As a consequence, the L_2 edge will mostly be sensitive to $5d_{\frac{3}{2}}$ hole excitations. On the other hand, the L_3 edge will be sensitive to both $5d_{\frac{1}{2}}$ and $5d_{\frac{3}{2}}$.[67] Overall, the main source of the different relative intensity of the white-line features could be attributed to the d-orbitals spin–orbit coupling, and multiplet effects due to the coupling of the 2p core states with the valence d electrons. Specifically, because of multiplet effects, the spectral weight transfer between the crystal field split t_{2g} and e_g peaks is approximately 25% and 5% at the L_3 and L_2 edge, respectively.[68] In the

absence of spin–orbit coupling, the selection rule dictates that the $J = 3/2$ and $J = 5/2$ multiplets will be degenerate. In this limit, only the density of the initial core-states will determine the transition probabilities of I_{L3} and I_{L2} excitations leading to a statistical branching ratio (BR), *i.e.*, the ratio of the L_3 and L_2 intensities, $BR = I_{L3}/I_{L2} \approx 2$.

However, as evident from Fig. 8, our data show strong white-line features that support a large local density of unoccupied d states. The intensity of the white-line features is larger at the L_3 absorption edge than the L_2 absorption edge. We obtain the FWHM for the L_3 absorption edge of 8.5 (8.9) eV using GGA + SOC (GGA+U + SOC) while that for the L_2 edge is 8.5 (8.9) eV with GGA + SOC (GGA+U + SOC). The linewidth is related to the intrinsic bandwidth of inverse full-Heusler Fe_2IrSi; it is affected by several factors including the lifetime of the core hole and the dipole-transition matrix element.[66] We determine the values of I_{L3} and I_{L2} from the XAS spectra following the method described in ref. 64. In the absence of spin–orbit coupling effects (not shown), BR $\approx$ 1.85; this ratio is $\sim$4.12 when we account for spin–orbit coupling effects. Electron–electron interactions have a negligible impact on the branching ratio. The over 120% increase in the branching ratio when we account for spin–orbit coupling effects in our calculations highlights the significant role it plays in the spectroscopic properties of inverse full-Heusler Fe_2IrSi. The predicted BR ratio is consistent with previous studies on Ir-based compounds that reported values that range from 2.40 eV to as high as 7.8 eV.[64,68–71] The deviation of the branching ratio from the statistical value suggests large spin–orbit coupling effects, which has been reported to enhance the BR in late 5d transition metal compounds due to charge transfer and crystal field effects.[69] We can quantify the strength of the spin–orbit coupling with the BR. Using the method proposed by Laan and Thole,[72,73] we can relate the branching ratio to the expectation value of the spin–orbit operator $\langle \mathbf{L}\cdot\mathbf{S}\rangle$ (in units of $\hbar^2$) as $BR = (2 + \zeta)/(1 - \zeta)$, where $\zeta = \langle \mathbf{L}\cdot\mathbf{S}\rangle/\langle n_h\rangle$ and $\langle n_h\rangle$ is the average number of 5d holes. We obtain $\langle \mathbf{L}\cdot\mathbf{S}\rangle \approx 2.07\hbar^2$; the $\langle \mathbf{L}\cdot\mathbf{S}\rangle$ value of $\sim 1.0\hbar^2$ for the Ir atom and $\sim 3.0\hbar^2$ has been reported for Ir-based compounds.[64]

4 Conclusion

In summary, we have studied the structural, electronic, magnetic, elastic, and X-ray spectroscopic properties of inverse full-Heusler Fe_2IrSi using first-principles calculations. We show that due to a strong correlation mainly from the Fe-3d states, including electron–electron interactions with the GGA+U formalism is essential to describe the electronic properties. We show that the GGA+U solution leads to a half-metallic behavior with a spin minority gap. The predicted magnetic moment of $\sim 5.01\ \mu_B$ agrees with the Slater Pauling rule, which supports the predicted half-metallicity. The calculated elastic and mechanical properties confirm both dynamical and structural stability with a melting temperature of $\sim 2000 \pm 300$ K, which supports a promising application of inverse full-Heusler Fe_2IrSi in devices operating above room temperature. We observe a rather large L_3/L_2 branching ratio that is more than twice the statistical branching ratio of $L_3/L_2 = 2$. The increased BR signifies the enhancement of the spin–orbit operator in inverse full-Heusler Fe_2IrSi.

Data availability

The data that support the findings of this study are available from the corresponding author upon reasonable request.

Conflicts of interest

There are no conflicts to declare.

Acknowledgements

D. P. R. acknowledges the Department of Science and Technology, New Delhi, Govt. of India vide Lett. No. INT/RUS/RFBR/P-264. I. V. M. acknowledges the Russian Foundation for Basic Research (RFBR), Russia, RFBR-17-57-45024. C. E. E. acknowledges the Lehigh University Start-up Grant. High-Performance Computing and computational resources are provided by the Lehigh University Center for Computing the Technology. D. P. R. extends condolence to the family of Prof. G. M. Mikhailov, an Indo-Russian project collaborator.

Notes and references

1 A. Fert, *Thin Solid Films*, 2008, **517**, 2.
2 S. Wurmehl, G. H. Fecher, H. C. Kandpal, V. Ksenofontov, C. Felser and H.-J. Lin, *Appl. Phys. Lett.*, 2006, **88**(3), 032503.
3 L. Bainsla and K. Suresh, *Appl. Phys. Lett.*, 2016, **3**, 031101.
4 X. Wang, Z. Cheng, J. Wang, X. Wang and G. Liu, *J. Mater. Chem. C*, 2016, **4**, 7176–7192.
5 T. Graf, C. Felser and S. Parkin, *Prog. Solid State Chem.*, 2011, **39**, 1–50.
6 S. Sanvito, C. Oses, J. Xue, A. Tiwari, M. Zic, T. Archer, P. Tozman, M. Venkatesan, M. Coey and S. Curtarolo, *Sci. Adv.*, 2017, **3**(4), e1602241, DOI: 10.1126/sciadv.1602241.
7 D. Bensaid, T. Hellal, M. Ameri, Y. Azzaz, B. Doumi, Y. Al-Douri, B. Abderrahim and F. Benzoudji, *J. Supercond. Novel Magn.*, 2016, **29**, 1843–1850.
8 I. Yahiaoui, A. Lazreg, Z. Dridi, Y. Al-Douri and B. Bouhafs, *J. Supercond. Novel Magn.*, 2016, **30**, 421–424.
9 F. Semari, F. Dahmane, N. Baki, Y. Al-Douri, S. Akbudak, G. Ugur, S. Ugur, A. Bouhemadou, R. Khenata and C. H. Voon, *Chin. J. Phys.*, 2018, **56**, 567–573.
10 F. Khelfaoui, M. Ameri, D. Bensaid, I. Ameri and Y. Al-Douri, *J. Supercond. Novel Magn.*, 2018, **31**, 3183–3192.
11 D. P. Rai, Sandeep, A. Shankar, R. Khenata, A. H. Reshak, C. E. Ekuma, R. K. Thapa and S.-H. Ke, *AIP Adv.*, 2017, **7**(4), 045118.
12 D. Wu, Z. Zhe, L. Li, Z. Zhang, H. Zhao, J. Wang, B. Ma and Q. Jin, *Sci. Rep.*, 2015, **5**, 12352.
13 R. A. de Groot, A. M. Kraan and K. H. J. Buschow, *J. Magn. Magn. Mater.*, 1986, **61**, 330.

14 K. H. J. Buschow and P. G. van Engen, *J. Magn. Magn. Mater.*, 1981, **25**, 90–96.
15 H. Kandpal, G. Fecher, C. Felser and G. Schonhense, *Phys. Rev. B: Condens. Matter Mater. Phys.*, 2006, **73**, 094422.
16 C. Felser, L. Wollmann, S. Chadov, G. Fecher and S. Parkin, *APL Mater.*, 2015, **3**, 041518.
17 A. Liechtenstein, M. Katsnelson, V. Antropov and V. Gubanov, *J. Magn. Magn. Mater.*, 1987, **67**(1), 65–74.
18 S. B. I. Galanakis, E. Sasoglu and K. Ozdogan, *Phys. Rev. B: Condens. Matter Mater. Phys.*, 2014, **90**, 064408.
19 X. Q. Chen, R. Podloucky and P. Rogl, *J. Appl. Phys.*, 2006, **100**, 113901.
20 P. E. M. A. Bansil, S. Kaprzyk and J. Tobola, *Phys. Rev. B: Condens. Matter Mater. Phys.*, 1999, **60**, 13396.
21 K. Kobayashi, R. Y. Umetsu, R. Kainuma, K. Ishida, T. Oyamada, A. Fujita and K. Fukamichi, *Appl. Phys. Lett.*, 2004, **85**(20), 4684–4686.
22 G. D. Liu, X. F. Dai, H. Y. Liu, J. L. Chen, Y. X. Li, G. Xiao and G. H. Wu, *Phys. Rev. B: Condens. Matter Mater. Phys.*, 2008, **77**, 014424.
23 X. Dai, G. Liu, G. H. Fecher, C. Felser, Y. Li and H. Liu, *J. Appl. Phys.*, 2009, **105**(7), 07E901.
24 Y. Du, G. Z. Xu, X. M. Zhang, Z. Y. Liu, S. Y. Yu, E. K. Liu, W. H. Wang and G. H. Wu, *EPL*, 2013, **103**(3), 37011.
25 Y. Du, G. Xu, E. Liu, G. Li, H. Zhang, S. Yu, W. Wang and G. Wu, *J. Magn. Magn. Mater.*, 2013, **335**, 101–104.
26 I. V. Malikov, L. A. Fomin, V. A. Berezin, A. V. Chernykh, D. P. Rai and G. M. Mikhailov, *Ferroelectrics*, 2019, **541**(1), 79–92.
27 A. Kumar and P. C. Srivastava, *Mater. Sci.*, 2013, **31**(4), 501–505.
28 T. Gasi, V. Ksenofontov, J. Kiss, S. Chadov, A. K. Nayak, M. Nicklas, J. Winterlik, M. Schwall, P. Klaer, P. Adler and C. Felser, *Phys. Rev. B: Condens. Matter Mater. Phys.*, 2013, **87**, 064411.
29 A. Dannenberg, M. Siewert, M. E. Gruner, M. Wuttig and P. Entel, *Phys. Rev. B: Condens. Matter Mater. Phys.*, 2010, **82**, 214421.
30 D. P. Rai, C. E. Ekuma, A. Boochani, S. Solaymani and R. K. Thapa, *J. Appl. Phys.*, 2018, **123**(16), 161509.
31 Y. Feng, B. Wu, H. Yuan, A. Kuang and H. Chen, 557, *J. Alloys Compd.*, 2013, 202–208.
32 Z. Fang, K. Terakura, H. Sawada, T. Miyazaki and I. Solovyev, *Phys. Rev. Lett.*, 1998, **81**, 1027–1030.
33 V. V. Krishnamurthy, J. L. Weston, G. J. Mankey, M. Suzuki, N. Kawamura and T. Ishikawa, *J. Appl. Phys.*, 2003, **93**(10), 7981–7983.
34 S. Ghosh and S. Ghosh, *Phys. Status Solidi B*, 2019, **256**(8), 1900039.
35 F. Aguilera-Granja, R. H. A. del Toro and J. L. Morán-López, *Mater. Res. Express*, 2019, **6**(10), 106118.
36 M. Meinert, M. P. Geisler, J. Schmalhorst, U. Heinzmann, E. Arenholz, W. Hetaba, M. Stöger-Pollach, A. Hütten and G. Reiss, *Phys. Rev. B: Condens. Matter Mater. Phys.*, 2014, **90**, 085127.
37 K. Endo, H. Matsuda, K. Ooiwa and K. Itoh, *J. Phys. Soc. Jpn.*, 1995, **64**(7), 2329–2332.
38 M. Friák, A. Slavik, I. Mihalikova, D. Holec, M. Vsianska, M. Sob, M. Palm and J. Neugebauer, *Materials*, 2018, **11**(9), 1732, DOI: 10.3390/ma11091732.
39 F. Dahmane, Y. Mogulkoc, B. Doumi, A. Tadjer, R. Khenata, S. B. Omran, D. P. Rai, G. Murtaza and D. Varshney, *J. Magn. Magn. Mater.*, 2016, **407**, 167–174.
40 N. Arkan, A. Iyigör, A. Candan, S. Uğur, Z. Charifi, H. Baaziz and G. Uğur, *J. Mater. Sci.*, 2014, **49**(12), 4180–4190.
41 L. Siakeng, G. M. Mikhailov and D. P. Rai, *J. Mater. Chem. C*, 2018, **6**, 10341–10349.
42 P. Hohenberg and W. Kohn, *Phys. Rev.*, 1964, **136**, B864–B871.
43 W. Kohn and L. J. Sham, *Phys. Rev.*, 1965, **140**, A1133–A1138.
44 J. P. Perdew, K. Burke and M. Ernzerhof, *Phys. Rev. Lett.*, 1996, **77**, 3865–3868.
45 S. L. Dudarev, G. A. Botton, S. Y. Savrasov, C. J. Humphreys and A. P. Sutton, *Phys. Rev. B: Condens. Matter Mater. Phys.*, 1998, **57**, 1505–1509.
46 M. Zipporah, P. Rohit, M. Robinson, M. Julius, S. Ralph and K. Arti, *AIP Adv.*, 2017, **7**, 055705, DOI: 10.1063/1.4973763.
47 E. Sasioglu, I. Galanakis, C. Friedrich and S. Blugel, 88, *Phys. Rev. B: Condens. Matter Mater. Phys.*, 2013, 134402; E. Sasioglu, I. Galanakis, L. M. Sandratskii and P. Bruno, *J. Phys.: Condens. Matter*, 2005, **17**, 3915–3930.
48 D. P. Rai, A. Shankar, Sandeep, L. R. Singh, M. Jamal, S. J. Hashemifar, M. P. Ghimire and R. K. Thapa, *Arm. J. Phys.*, 2012, **5**, 105–110.
49 P. Giannozzi, S. Baroni, N. Bonini, M. Calandra, R. Car, C. Cavazzoni, D. Ceresoli, G. L. Chiarotti, M. Cococcioni, I. Dabo, A. D. Corso, S. de Gironcoli, S. Fabris, G. Fratesi, R. Gebauer, U. Gerstmann, C. Gougoussis, A. Kokalj, M. Lazzeri, L. Martin-Samos, N. Marzari, F. Mauri, R. Mazzarello, S. Paolini, A. Pasquarello, L. Paulatto, C. Sbraccia, S. Scandolo, G. Sclauzero, A. P. Seitsonen, A. Smogunov, P. Umari and R. M. Wentzcovitch, *J. Phys.: Condens. Matter*, 2009, **21**(39), 395502.
50 D. K. H. Ebert and J. Minar, *Rep. Prog. Phys.*, 2011, **74**(9), 096501.
51 H. Ebert, *Fully Relativistic Band Structure Calculations for Magnetic Solids – Formalism and Application*, Springer Berlin Heidelberg, Berlin, Heidelberg, 2000, pp. 191–246.
52 J. C. Slater, *Phys. Rev.*, 1930, **36**(1), 57, DOI: 10.1103/PhysRev.36.57.
53 R. Cardias, A. Szilva, A. Bergman, I. Di Marco, M. I. Katsnelson, A. I. Lichtenstein, L. Nordström, A. B. Klautau, O. Eriksson and Y. O. Kvashnin, *Sci. Rep.*, 2017, **7**, 4058.
54 Y. J. Zhang, Z. H. Liu, Z. G. Wu and X. Q. Ma, *IUCrJ*, 2019, **6**, 610–618.
55 J. Kubler, *Phys. Rev. B: Condens. Matter Mater. Phys.*, 2007, **76**, 024414.
56 C. Ekuma, S. Najmaei and M. Dubey, *Mater. Today Commun.*, 2019, **19**, 383–392.
57 E. Kroumova, M. Aroyo, J. Perez-Mato, A. Kirov, C. Capillas, S. Ivantchev and H. Wondratschek, *Phase Transitions*, 2003, **76**(1–2), 155–170.

58 P. W. Anderson, *Solid State Physics*, Academic Press, 1963, vol. 14, pp. 99–214.
59 S. A. Khandy, I. Islam, D. C. Gupta, R. Khenata and A. Laref, *Sci. Rep.*, 2019, **9**, 1475.
60 X. Liu and H. Q. Fan, *R. Soc. Open Sci.*, 2018, **5**, 171921.
61 A. Juhin, P. Sainctavit, K. Ollefs, M. Sikora, A. Filipponi, P. Glatzel, F. Wilhelm and A. Rogalev, *J. Phys.: Condens. Matter*, 2016, **28**(50), 505202.
62 A. Rogalev and F. Wilhelm, *Phys. Met. Metallogr.*, 2015, **116**, 1285.
63 Y. Matsuda, J. Her, T. Inami, K. Ohwada, Z. Ouyang, K. Okada, H. Nojiri, A. Mitsuda, H. Wada, N. Kawamura and M. Suzuki, *J. Low Temp. Phys.*, 2010, **159**(1–2), 292–296.
64 J. P. Clancy, N. Chen, C. Y. Kim, W. F. Chen, K. W. Plumb, B. C. Jeon, T. W. Noh and Y.-J. Kim, *Phys. Rev. B: Condens. Matter Mater. Phys.*, 2012, **86**, 195131.
65 V. V. Krishnamurthy, N. Kawamura, M. Suzuki, T. Ishikawa, G. J. Mankey, P. Raj, A. Sathyamoorthy, A. G. Joshi and S. K. Malik, *Phys. Rev. B: Condens. Matter Mater. Phys.*, 2003, **68**, 214413.
66 T. K. Sham, *Phys. Rev. B: Condens. Matter Mater. Phys.*, 1985, **31**, 1888–1902.
67 J. Cheng, X. Sun, S. Liu, B. Li, H. Wang, P. Dong, Y. Wang and W. Xu, *New J. Phys.*, 2016, **18**(9), 093019.
68 F. M. F. de Groot, Z. W. Hu, M. F. Lopez, G. Kaindl, F. Guillot and M. Tronc, *J. Chem. Phys.*, 1994, **101**(8), 6570–6576.
69 D.-Y. Cho, J. Park, J. Yu and J.-G. Park, *J. Phys.: Condens. Matter*, 2012, **24**(5), 055503.
70 Y. Jeon, B. Qi, F. Lu and M. Croft, *Phys. Rev. B: Condens. Matter Mater. Phys.*, 1989, **40**, 1538–1545.
71 B. Qi, I. Perez, P. H. Ansari, F. Lu and M. Croft, *Phys. Rev. B: Condens. Matter Mater. Phys.*, 1987, **36**, 2972–2975.
72 G. van der Laan and B. T. Thole, *Phys. Rev. Lett.*, 1988, **60**, 1977–1980.
73 B. T. Thole and G. van der Laan, *Phys. Rev. B: Condens. Matter Mater. Phys.*, 1988, **38**, 3158–3171.

Surfaces and Interfaces 28 (2022) 101602

Contents lists available at ScienceDirect

Surfaces and Interfaces

journal homepage: www.sciencedirect.com/journal/surfaces-and-interfaces

Surface half metallicity and thermodynamic stability of 001-plane Ti_2XSi (X=Mn, Co) Heusler alloys (HAs): A DFT approach

Lalrinkima [a,b], Lalthakimi Zadeng [a], Lalmuan Chhana [a,b], Lalhriat Zuala [b], D.P. Rai [*,b]

[a] Department of Physics, Mizoram University, Aizawl, 796009, India
[b] Physical Sciences Research Center (PSRC), Department of Physics, Pachhunga University College, Mizoram University, Aizawl, 796001, India

ARTICLE INFO

Keywords:
GGA
Heusler alloys
Band structure
Surface
Half metal
Magnetic moment

ABSTRACT

We report the surface stability and surface half-metallicity of Ti_2XSi (X=Mn/Co) [001] slab with natural TiSi and TiX(X=Mn/Co) terminals from the first principles calculation. We started our calculation from the bulk optimization followed by the electronic and magnetic properties by adopting GGA exchange correlation for treating all electrons interaction. We have also analyzed the surface stability by calculating the surface energies as a function of constituents chemical potentials within the framework of *ab-initio* thermodynamics. Within the allowed chemical potentials range, $TiSi(Ti_2MnSi)$ terminated surface found to be the most energetically favorable thin film while the TiX terminated surfaces show strong molecular attraction. The bulk half metallicity is preserved in $TiSi(Ti_2MnSi)$ terminated surface with 100% spin polarization while the other terminal surfaces are metallic. The results of atomic site partial magnetic moments in the surface states along with their corresponding values in the bulk structure are also presented.

1. Introduction

The extensive theoretical and experimental studies on novel Heusler compounds [1] have been pursued after the discovery of peculiar half metal ferromagnetic (HMF) property by de Groot *et al.,* [2] from the band structure calculation in NiMnSb, where one of the spin channels is semiconducting and the other is metallic resulting 100% spin polarization at the Fermi level. The diverse functional properties of Heusler compounds includes HMF, high Curie temperature, large perpendicular magneto-anisotropy, low magnetic dumping, low saturation magnetization, tunneling magneto-resistance effect, Current-perpendicular-to-plane giant magneto-resistance etc., are crucial for the development of spin wave based spintronic device which explicitly rely on the degree of spin polarization at the Fermi level [3–5]. The components of spintronic application includes giant magneto-resistance (GMR) and magnetic random access memory(MRAM), spin injectors, spin computer applications and spin-transfer torque device [6–13]. In order to integrate the HMF property for the device application, it is very essential to fabricate the sample in nano-scale thin film. Epitaxial thin films growth technique is the prior pavement for device fabrications [14–18]. Regrettably, cleaving of surfaces or nano-structured Heusler alloys usually destroyed the bulk HMF property due to the breaking of bonds along the translation direction and release free conducting electrons on the surfaces [19]. As a result of which the preservation of the bulk half metallic nature in low dimensional thin film is highly challenging for its application in spintronic technology. It has been identified from the theoretical and the experimental work that Zincblende magnetic semiconductors also exhibit half-metallicity but they have low Curie Temperature (below room temperature) [20]. The thin film of rutile CrO_2 and perovskite $La_{0.7}Sr_{0.3}MnO_3$ shows half metallic nature with almost 100% spin polarization at low temperature as obtained from Andreev reflection measurement [21]. So, in this regard Heusler alloys (HAs) have comparatively high Curie temperature well above the room temperature for practical applications. However, there are no experimental report on the half metallicity (100% spin polarization) of Heusler alloys at the room temperature so far [22]. Interestingly, for the first time Jourdan *et al.* confirmed the direct half metallicity with 93% spin polarization in Co_2MnSi *in-situ* epitaxial thin film at room temperature using ultraviolet photoemission spectroscopy [23]. Nevertheless, the surface half metallicity for 001-surface of Co_2MnSi was predicted before the experiment from *ab-initio* density functional theory(DFT) investigation [24]. Therefore, predicting the nature of materials from first principles calculation is somewhat reliable to realise thin film growth in device application. The nature of low magnetic moment, high Curie temperature, low formation energy and mechanical stability

* Corresponding author.
E-mail address: dibya@pucollege.edu.in (D.P. Rai).

https://doi.org/10.1016/j.surfin.2021.101602
Received 22 September 2021; Received in revised form 7 November 2021; Accepted 11 November 2021
Available online 16 November 2021

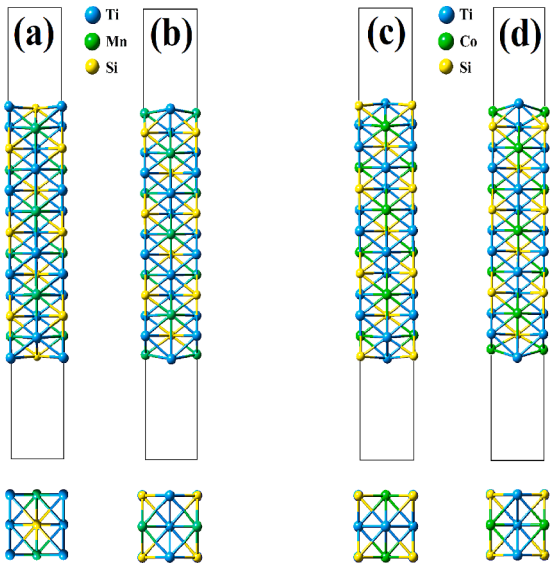

Fig. 1. Side view and top view of conventional slab model of 001-Ti_2MnSi (TMS) surfaces: (a)TiSi (b)TiMn terminations and 001-Ti_2CoSi(TCS) surfaces: (c)TiSi (d)TiCo terminations.

make Ti-based Heusler hetero-junction a potential candidate for current-perpendicular- to-plane (cpp) GMR devices and spin transfer torque MRAM applications [25–28].To the best of our knowledge, we have not come across any experimental study on the surface half metallicity of Ti-based Heusler alloys. Moreover, the surface half metallicity was predicted on *XA*-type Ti_2FeGe[001] [28] and Co-doped $Ti_2Fe_{1-x}Co_xSn$ [001] [29] from the first principles approach. We are also aware of the fact that no rigorous study (experiment and theory) have been performed on the surface states of Ti_2MnSi and Ti_2CoSi. Moreover, theoretical prediction of surface electronic structure of the analogous compounds of transition metal based Heusler alloys (HAs) with *XA* (Hg_2CuTi-type) structure have already been reported; Ti_2MnAl [001] where all the two natural Ti-Al, Ti-Mn terminals and three artificial modelled Ti-Ti, Mn-Mn and Al-Al terminations shown metallic character [30]. Ti_2CoSn [001] where TiSn terminal nearly gives the half metallicity with 94.2% spin polarization [31]. In this work, we have presented the surface electronic structure and thermodynamic stability of inverse *XA* (Hg_2CuTi-type) full Heusler alloy $Ti_2(X)Si$[001] slab. Motivated, with the aim of devices fabrication with HMF|semiconductor hetero-structures, the range of equilibrium lattice constant of $Ti_2XSi \approx 6.00$ Å is well matched with the varieties of semiconductors such as CdSe (6.05 Å), InAs (6.05 Å), ZnTe (6.10 Å) and GaSb (6.10 Å) without hard in-plane lattice perturbation at the interfaces, thus can enhance the interfacial spin polarisation and stability. By comparing the existing literature of the bulk structure, we briefly discuss about the bulk electronic structure calculated by using the equilibrium lattice constant. Further, we have presented the surface electronic structure and thermodynamic stability, also analyzed the effect of *sp*-elements in Ti-based Ti_2XSi [001] surfaces with their corresponding terminations.

2. Computational method

The first principles calculation were performed using DFT [32] based on the projector augmented wave (PAW) method which constitute the core ionic interaction as implemented and programmed in Vienna *ab-initio* Simulation Package (VASP) [33]. All electron interactions were treated using the electron correlation exchange energy within the generalized gradient approximation (GGA) within Perdew-Burke-Ernzerhof(PBE) formalism [34]. A plane wave cut off energy of 300 eV and 460 eV for the bulk and [001] surface, respectively. An explicit k-mesh of $8 \times 8 \times 8$ for the bulk system and $12 \times 12 \times 1$ for the surface were used within the Monkhorst pack grid [35] to integrate the first Brillouin zone. The self-consistent field calculation steps were performed till the energy difference reaches less than 10^{-5} eV. Structural relaxation was achieved via conjugate gradient(CG) algorithm as integrated in VASP [36] by minimizing the energy and atomic forces with a force tolerance of 0.02 eV/Å. A relaxed thin film of Ti_2XSi with [001]-surface slab having 13 diatomic layers have been constructed to study the effect of the thermodynamic stability and the surface electronic properties [see Fig. 1].

Table 1
The calculated optimized lattice constant *a*(Å), total and atomic partial magnetic moment with available literature.

Alloy	a_0	μ_B (Ti1)	μ_B (Ti2)	μ_B (X)	μ_B (Si)	μ_B (Total)
Ti_2MnSi	6.0084	1.042	0.63	-0.814	0.009	1.0145
	5.997[a]					1.050[b]
Ti_2CoSi	6.0022	1.545	0.795	0.407	0.012	3.0227
	6.02[b]					3.00[b]
	6.03[c]					3[c]

[a] Ref: [37].
[b] Ref: [38].
[c] Ref: [40].

3. Results and discussion

3.1. Bulk $Ti_2(X)Si$ (X=Mn, Co)

The equilibrium lattice parameter, total magnetic moment and atomic resolved magnetic moment of bulk structure of Ti-based inverse full Heusler Ti_2XSi (X= Mn, Co) calculated from GGA are presented in Table 1. Our calculated equilibrium lattice constants are in well-agreement with the previous reports with relatively negligible deviation.

In order to analyse the electronic properties of their bulk systems, we have presented the total and atomic resolved density of states (DOS) in Fig. 2. For both the bulk structures of Ti_2XSi with XA phases are HMF having finite band gap in the minority spin channel, while the spin up channel is characterized by the metallicity with dispersed bands around the Fermi level (E_F) as shown in Fig. 2(a,b). The blend of semiconducting and metallic behaviour in Ti_2XSi validate the half metal ferromagnet characteristic with ≈100% spin polarization at E_F. The calculated electronic and magnetic properties of Ti_2XSi are in close agreement with the previous reports [37,38]. There are some reports of possessing spin gapless semiconducting (SGS) behavior in Ti_2CoSi [39,40]. In Fig. 2(b), due to the presence of a minuscule electronic states (0.25 States/eV) in majority spin (↑) channel at around E_F, mainly contributed by the *d*-orbital states of Co; exhibiting a half metal ferromagnetic behaviour contrary to a SGS behaviour of Ti_2CoSi [39,40]. Our calculated electronic structure of Ti_2CoSi is well agreed with the available results, where 0.13 States/eV and 0.02 States/eV in the spin up channel reported within GGA and mBJ approximation, respectively [38]. Interestingly, a highly dominant states of Ti(1)-*d* orbital in the majority spin channel at around E_F (-1 eV to -0.1 eV) is followed by unanticipated strong coupled hybridization of $d-d$-orbitals which results an energy gap at around -1.3 to -1 eV. Below that energy range, the *d*-orbital states of Co atom imaged the total density of states for both the spin channel (Up or Down) as shown in Fig. 2(b). The formation of band gap in full Heusler rely on the $d-d$ hybridization of the transition elements. In Ti-based inverse Heusler, the shaping of $d-d$ band gap commenced from the coupling between the $2xe_g$ and $3xt_{2g}$ degenerated states of *d*-orbitals of the two inequivalent Ti atoms that prompting the bonding ($3xt_{2g}$, $2xe_g$) states and an anti-bonding ($3xt_u$, $2xe_u$) states. The coupled bonding states of Ti (1)$d-d$Ti(2) further undergone hybridization with the *d*-orbital degenerated states ($3xt_{2g}$, $2xe_g$) of X (Mn,Co) atom that resulted to the bonding states(3xt and 2xe) and anti-bonding states (3xt* and 2xu*).

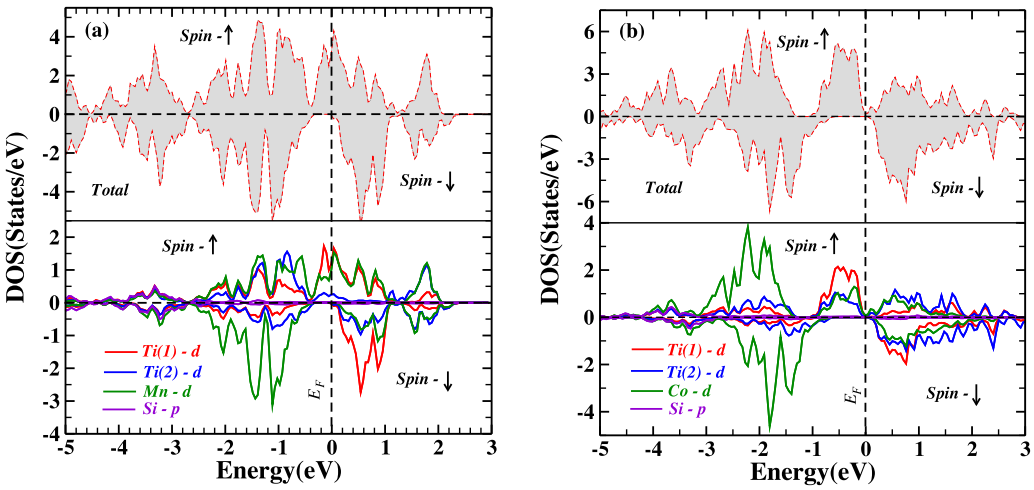

Fig. 2. Total Density of States (upper panel) and partial atomic resolved density of states (lower panel) of the bulk: (a)Ti_2MnSi (b)Ti_2CoSi compounds (↑-spin-up and ↓-spin-down).

The energy difference between the bonding state 3xt and anti-bonding state 3xt* induced from the hybridization of degenerated Mn *d* orbitals and bonding states of Ti-Ti coupled is the so called *d* −*d* band gap. The spin polarization at the Fermi level E_F is calculated using the applied formula;

$$P = \frac{N_\uparrow(E_F) - N_\downarrow(E_F)}{N_\uparrow(E_F) + N_\downarrow(E_F)} \quad (1)$$

where $N_\uparrow(E_F)$ and $N_\downarrow(E_F)$ are the density of states at the Fermi level E_F.

In spite of having the chemical formula of X_2YZ type Heusler alloys [41–43], the Ti-based inverse Full Heusler alloys Ti_2XSi follow the Slater-Pauling rule given by Eq. (2) [44]

$$\mu_t = Z_t - 18 \quad (2)$$

where total magnetic moment is denoted by μ_t and Z_t is the total number of valence electrons. Hence, the calculated magnetic moment per unit cell are associate well with the Slater-Pauling rule with an integer number 1 for Ti_2MnSi with 19 valence electrons and an integer 3 for Ti_2CoSi with 21 valence electrons. Thus, the total magnetic moments associated with Ti_2MnSi and Ti_2CoSi are expected to be $1\mu_B$ and $3\mu_B$, respectively. In Table 1, we have observed that the moment of Mn atom is anti-parallel to both the Ti atoms in Ti_2MnSi alloy. Therefore, a presence of non-zero magnetic moment despite having anti-ferromagnetic coupling between Mn-Ti revealed that Ti_2MnSi is a ferrimagnetic half metal, consistent with the previous report [37]. While, the parallel alignment of moment of Co atom with the neighbouring Ti atoms revealed the ferromagnetic character of Ti_2CoSi alloy. Further analysing the total and atomic partial moment, the sum of the local atomic magnetic moment is usually smaller than the total magnetic moment of the unit cell; the differences correspond to the contribution of the interstitial region.

3.2. Surface structural and relaxation

We have adopted the optimized bulk structure of Ti_2XSi and cleaved the [001] surfaces using supercell method. The surface [001] consist of two natural terminations; alternating planes of TiSi and TiMn terminals for Ti_2MnSi(TMS), while TiSi and TiCo terminated surfaces for Ti_2CoSi (TCS). We acquired each slabs with 13 diatomic layers and applied a vacuum of 15 Å on both the sides of the identical phases along the z-axis to prevent the unphysical interaction between the periodic slabs. The in-plane lattice parameter of these slabs are $a\sqrt{2}/2$, where $a = 6.0084$ Å is the optimized lattice constant of bulk Ti_2MnSi and 6.0022 Å for Ti_2CoSi.

Table 2
The relaxed atomic displacement (d_{i-f} in Å) and the atomic displacement (d_{i-f}) in percentage of optimized bulk lattice constant 'a_o'.

Alloy	Terminal	Layer	d_{i-f}(Å)	% of d_{i-f}
		Ti/Si (s)	-0.005/-0.130	-0.083/-2.16
		Ti/Mn(s-1)	0.040/-0.075	0.670/-1.250
	TiSi	Ti/Si(s-2)	-0.015/0.005	-0.250/0.080
Ti_2MnSi		Ti/Mn(s-3)	0.020/-0.035	0.330/-0.580
		Ti/Mn(s)	0.205/-0.120	3.410/-1.990
	TiMn	Ti/Si(s-1)	-0.010/-0.035	-0.17/-0.58
		Ti/Mn(s-2)	0.015/-0.060	0.25/-0.99
		Ti/Si(s-3)	0.005/-0.005	0.083/-0.083
		Ti/Si(s)	0.062/-0.088	1.04/-1.47
		Ti/Co(s-1)	0.083/-0.057	1.39/-0.95
	TiSi	Ti/Si(s-2)	-0.005/0.016	-0.09/0.26
Ti_2CoSi		Ti/Co(s-3)	0/0.026	0 /0.43
		Ti/Co(s)	0.213/-0.374	3.55/-6.24
	TiCo	Ti/Si(s-1)	0.010/0.042	0.17/0.69
		Ti/Co(s-2)	0.021/0	0.35 /0.000
		Ti/Si(s-3)	0.042/-0.005	0.69/-0.09

By considering the interfaces of both the sides of the slab, we have relaxed the top four layers of each slab with fixed core layers (5-layers). The results of relaxed parameters are presented in Table 2 in terms of atomic displacement (fourth column) and percentage of atomic displacement with respect to the bulk's lattice constant *a* (fifth column). The inward relaxation of both surface atoms (Ti, Si) are seen only in TiSi (TMS) terminal surface while the surface Ti-atom of other terminals are relaxed outward. The outward relaxation may be attributed to the metallicity of the surfaces, in which the surface layers tried to rearrange the displaced valence electron density [45]. The higher variation of atomic displacement among transition elements may be attributed to the *d-d* re-hybridization after reducing symmetry of the surfaces. In addition, Ti-X terminated surfaces for each compound give rise to strong relaxation due to the breaking of the bonds at the surface. One can noticed that TiSi(TMS) terminal surface generate the smallest relaxation among these terminals which is followed by TiSi(TCS) terminated surface. Consequently, TiSi(TMS) terminal surface is found to be the most stable surface structure out of the studied surfaces.

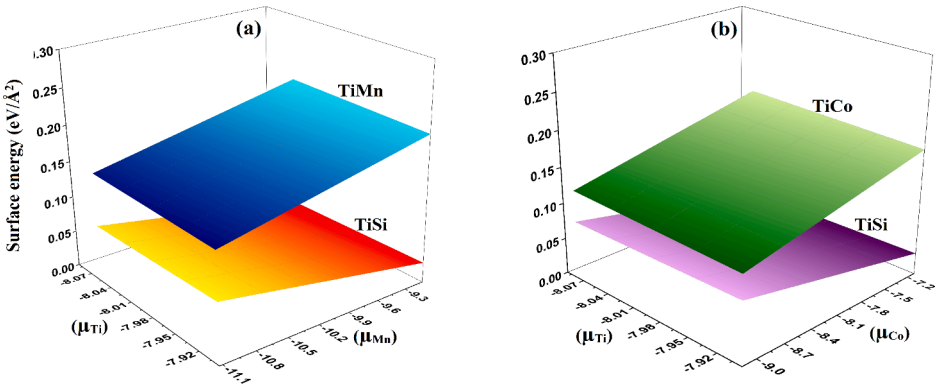

Fig. 3. Calculated surface energies (eV/Å^2) as a function of chemical potentials of (a) μ_{Ti} and μ_{Mn} (eV) for 001-surface of Ti_2MnSi and (b) μ_{Ti} and μ_{Co} (eV) for 001-surface of Ti_2CoSi.

3.3. Surface stability: ab-initio thermodynamic

As the surface stability is an important aspect in realization of thin films growth, we further study the stability of the adopted relaxed surfaces by calculating the surface energy as a function of the constituents atomic chemical potential within the framework of *ab-initio* thermodynamics [24,46,47]. The surface energy can be calculated as follows:

$$\gamma = \frac{1}{2A}\left[G - \sum_i (N_i \mu_i)\right] \tag{3}$$

where A and G are the surface area and total energy of the relaxed slab respectively. N_i and μ_i; the total number and chemical potential of the constituent i^{th} atom in the slab. Since the chemical potential of the constituent elements in the compounds are not independent, the sum of the chemical potentials are equal to the total energy of the bulk Ti_2XSi; $G_{Ti_2(X)Si}$ where $X = Mn, Co$:

$$2\mu_{Ti} + \mu_{(X)} + \mu_{Si} = G_{Ti_2(X)Si} (X = Mn, Co) \tag{4}$$

By rearranging the Eq. (4) and substituting the μ_{Si} in Eq. (3), we obtained the surface energy as a function of μ_{Ti} and $\mu_{(X)}$. The maximum value of chemical potential for Ti and X (Mn,Co) can be obtained from the total energy of their bulk structure; the minimum allowed chemical potentials were set on to a certain extent that by diminishing μ_{Ti} and $\mu_{(X)}$ till Ti and X(Mn,Co) leave the structure and T_2Si and X(Mn,Co)Si were formed. Where as the boundary conditions of μ_{Ti} and $\mu_{(X)}$ are given by:

$$\frac{1}{2}(G_{Ti_2(X)Si} - G_{(X)Si}) \le \mu_{Ti} \le G_{Ti} \tag{5}$$

$$G_{Ti_2(X)Si} - G_{Ti_2Si} \le \mu_{(X)} \le G_{(X)} \tag{6}$$

where $G_{(X)Si}$, G_{Ti}, G_{Ti_2Si} and $G_{(X)}$ are the total energy of the bulk (X)Si, Ti, T_2Si and (X), respectively. To obtain the allowed chemical potentials for μ_{Ti} and $\mu_{(X)}$, we adopted the available data of the above mentioned total energies except G_{Ti} from the authentic web (www.materialsproject.org) [48] those data were obtained from the similar computational approaches.

In Fig. 3, we have presented the surface energies of different slabs as a function of μ_{Ti} and $\mu_{(X)}$ within the allowed ranges. TiSi terminal surfaces possibly favorable than Ti(X) terminal surfaces from their respective compounds due to the presence of lower surface energies which agrees well with the smaller structural relaxation as discussed in the preceding subsection. Interestingly, the Ti-X terminated surfaces show strong molecular attraction as their chemical potentials μ_{Mn} and μ_{Co} increases. From the practical point of view; the instability of the surfaces can be handle by deploying non-equilibrium epitaxial thin film growth technique.

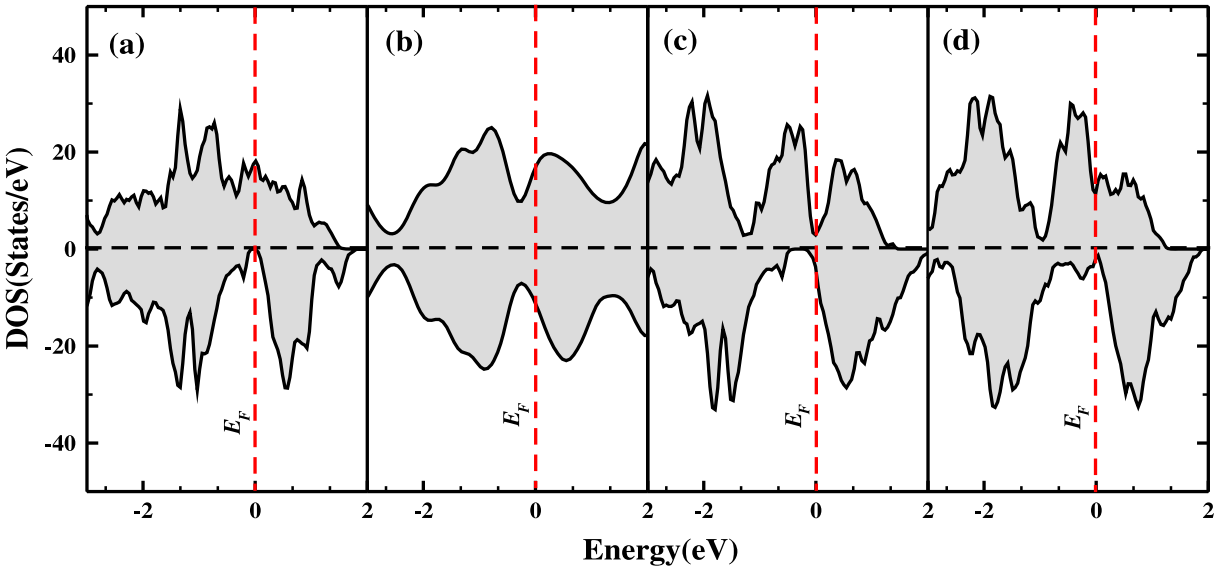

Fig. 4. Total DOS of Ti_2MnSi (001) [(a)TiSi (b)TiMn-terminal] and Ti_2CoSi (001) [(c)TiSi (d)TiCo terminal].

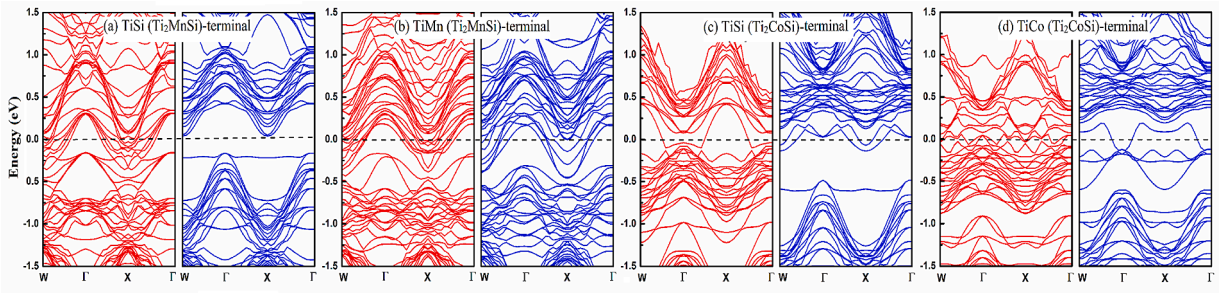

Fig. 5. Calculated Band structures of Ti_2MnSi (001)[(a)TiSi (b)TiMn-terminal] and Ti_2CoSi (001)[(c)TiSi (d)TiCo terminal](↑-spin-up and ↓-spin-down).

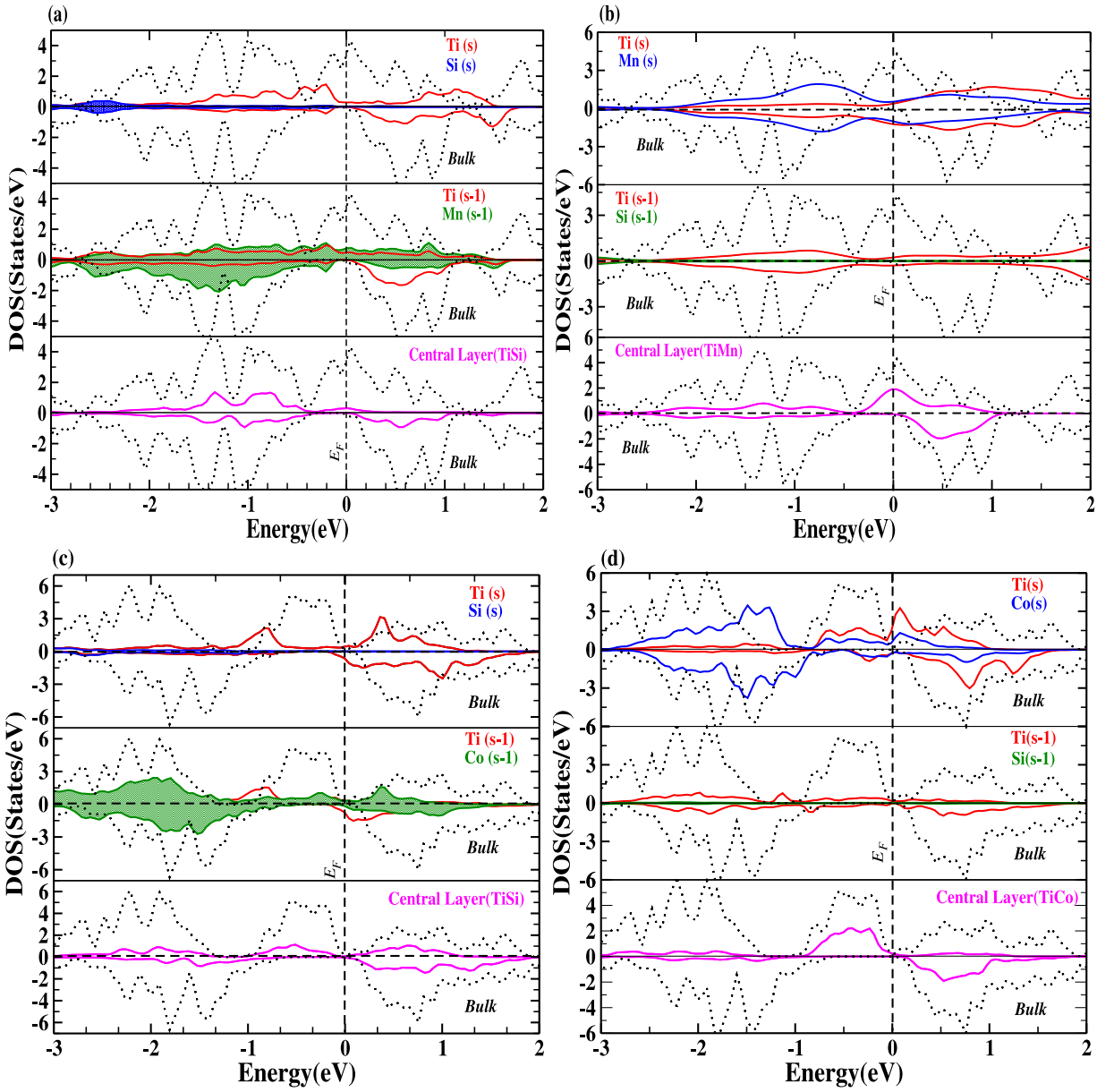

Fig. 6. Spin resolved partial density of states :(a)TiSi(TMS), (b)TiMn, (c)TiSi(TCS) and (d)TiCo terminal surfaces (↑-spin-up and ↓-spin-down).

3.4. Surface electronic and magnetic properties

To analyze the surface electronic structures, we have presented the calculated DOS and energy band structures of TiSi, TiMn terminal of Ti_2MnSi (001) slab and TiSi, TiCo terminal of Ti_2CoSi (001) surface in (Figs. 4 and 5), respectively. In order to gain the detail insight of the surface electronic configuration, the atomic partial DOS of surface layer (s) were presented. The second layer(s-1) and central layer for each particular film as well as their respective bulk electronic DOS were also displayed in Fig. 6. In Ti_2MnSi (001) surface, we can noticed that the

Table 3
Calculated atomic magnetic moment (in μ_B) of surface (s), sub-surface (s-1). central layer (C.L) and corresponding calculated values in their respective bulk structure.

Ti_2MnSi (units are in μ_B)					Ti_2CoSi (units are in μ_B)				
Term	Ti	Mn	Si	C.L	Term	Ti	Co	Si	C.L
TiSi	1.112(s)	-1.182(s-1)	-0.033(s)	0.605(Ti) 0.009(Si)	TiSi	0.997(s)	0.263(s-1)	-0.022(s)	0.780(Ti) 0.011(Si)
TiMn	-1.324(s)	2.738(s)	-006(s-1)	0.957(Ti) -1.001(Mn)	TiCo	1.13(s)	0.012(s)	-0.006(s-1)	1.532(Ti) 0.394(Co)
Bulk	1.042(Ti1) 0.63(Ti2)	-0.814	0.009		Bulk	1.545(Ti1) 0.795(Ti2)	0.407	0.012	

bulk half metallic character is degenerated in TiMn terminal with complete metallic character as seen in Fig. 4(b), while it is preserved in TiSi terminal with the presence of distinct bandgap in the spin down channel and the overlapped of the valence and the conduction bands with the E_F crossing over it in the spin up states are as shown in Fig. 4(a). TiSi termination of Ti_2CoSi (001) surface, exhibit the spin gapless semiconducting phase (SGS) over the half metal [see Fig. 6(c)]. Furthermore, one can observed from Fig. 5(c) and Fig. 6(c), the presence of surface delocalized states derived from *d*-orbitals of the surface Ti(s) and Co(s-1) atoms around the Fermi level destroyed the HMF nature. This may be attributed to the electrostatic potential declined towards the vacuum region which has lifted these states up to the E_F as the Ti(s) atom relaxed towards vacuum [24]. For TiCo termination, the weak hybridization between the *d* states of Ti(s) and Co(s) may induced zero energy splitting which results surface states at the E_F due to the lowering of symmetry at the surface. Hence, the half metallic properties are lost.

However, it is clearly seen that the partial DOS contributed from the central layer atoms of all terminals are well matches with the bulk electronic properties as displayed in bottom pannel of Fig. 6(a, b, c and d). These figures demonstrated that the chosen slabs thickness are sufficient enough to investigate the surface electronic properties. 100% spin polarization is an ideal factor for spin injected device application, we further calculate the spin polarization of all terminal surfaces using Eq. (3). We have found that an excellent 100% spin polarization for TiSi terminal in Ti_2MnSi surface only, whereas TiMn terminal shows the metallic character. For TiSi terminal of Ti_2CoSi surface, we have found the flip of spin polarization of -33.4% due to the presence of spin gapless semiconducting like behaviour with more dense states at the spin down channel. Meanwhile, we report 89.1% spin polarization of TiCo terminal surface.

To explore the surface effect of the magnetic properties, the calculated atomic magnetic moment of the surface, sub-surface (s-1) and central layer (C.L) atoms for each terminals surface and corresponding calculated moment in their respective bulk structures are presented in Table 3. By comparing the corresponding partial moments in the bulk structure, we have observed the enhanced magnetic moment of the surface atoms. The increased in the magnetic moment of surface atoms may be due to the release of the free electrons owing to the breaking of translations symmetry (breaking of bond) during the surface formation [24,28,47,49]. However, the value of bulk atomic site moment are nearly retained in the central region. The anti-parallel spin moment of Si atom in each surface and sub-surface layer may be attributed to the Ruderman-Kittel-Kasuya-Yosida (RKKY) exchange interaction between Mn atoms [28,50–52]. For TiMn termination, the occurrence of anti-ferromagnetic super-exchange [53] between the surface atoms Ti and Mn possibly enhancing spin moment value as compared to the bulk phase.

4. Conclusion

The first principles calculation based on density functional theory (DFT) have been performed to study the structural stability, electronic and magnetic properties of (001) surfaces of inverse $Ti_2(X)Si$ (X=Mn,Co) full Heusler alloy having XA-phase. The 001 surface with four terminated faces have been exfoliated theoretically. Out of the four explored terminal surfaces, TiSi(TMS) is the most stable with lowest surface energy which agrees well with its smallest surface relaxation. However, the TiX(X=Mn/Co) terminated surfaces from both Ti_2MnSi and Ti_2CoSi compounds are less stable as compared to respective adjacent TiSi terminated surfaces. We have observed that for TiMn, TiSi (TCS) and TiCo terminal surfaces, the presence of surface states at the Fermi level destroying their respective bulk half metallic properties. A significant surface half metallicity is observed in TiSi(TMS) terminal surface. We expect that our present work will invigorate the experimental work for the realization of surface half-metallicity in Ti_2MnSi with TiSi termination.

Data availability

The data that support the findings of this study are available from the corresponding author upon reasonable request.

CRediT authorship contribution statement

: Writing – original draft, Writing – review & editing. **Lalthakimi Zadeng:** Conceptualization, Data curation, Formal analysis, Validation, Writing – original draft, Visualization. **Lalmuan Chhana:** Formal analysis, Data curation, Investigation, Methodology. **Lalhriat Zuala:** Formal analysis, Data curation, Investigation. **D.P. Rai:** Writing – original draft, Methodology, Resources, Validation, Formal analysis, Visualization, Validation, Writing – review & editing.

Declaration of Competing Interest

The authors declare that they have no known competing financial interests or personal relationships that could have appeared to influence the work reported in this paper.

Acknowledgements

Lalrinkima acknowledges the Department of Science and Technology (DST), New Delhi, Government of India for INSPIRE Fellowship vide Dy. Order No. DST/INSPIRE Fellowship/2018/IF180550.

References

[1] F. Heusler, W. Starck, E. Haupt, Verh. Dtsch. Phys. Ges. 5 (1903) 220–223.
[2] R.A. de Groot, F.M. Mueller, P.G. van Engen, K.H.J. Buschow, New class of materials: half-Metallic ferromagnets, Phys. Rev. Lett. 50 (25) (1983) 2024, https://doi.org/10.1103/PhysRevLett.50.2024.
[3] H.C. Kandpal, G.H. Fecher, C. Felser, G. Schönhense, Correlation in the transition-metal-based heusler compounds <span class, Phys. Rev. B 73 (9) (2006) 094422, https://doi.org/10.1103/PhysRevB.73.094422.
[4] L.E. Nistor, B. Rodmacq, S. Auffret, B. Dieny, Pt/co/oxide and oxide/co/pt electrodes for perpendicular magnetic tunnel junctions, Appl. Phys. Lett. 94 (1) (2009) 012512, https://doi.org/10.1063/1.3064162.
[5] I. Galanakis, K. Özdoğan, E. Şaşoğlu, S. Blügel, Conditions for spin-gapless semiconducting behavior in mn2coal inverse heusler compound, J. Appl. Phys. 115 (9) (2014) 093908, https://doi.org/10.1063/1.4867917.
[6] C. Felser, L. Wollmann, S. Chadov, G.H. Fecher, S.S.P. Parkin, Basics and prospective of magnetic heusler compounds, APL Mater. 3 (4) (2015) 041518, https://doi.org/10.1063/1.4917387.

[7] K.H. Buschow, P.G. van Engen, Magnetic and magneto-optical properties of heusler alloys based on aluminium and gallium, J. Magn. Magn. Mater. 25 (1) (1981) 90–96, https://doi.org/10.1016/0304-8853(81)90151-7.

[8] D.P. Rai, Lalrinkima, Lalhriatzuala, L.A. Fomin, I.V. Malikov, A. Sayede, M. P. Ghimire, R.K. Thapa, L. Zadeng, Pressure dependent half-metallic ferromagnetism in inverse heusler alloy fe2coal: a DFT+u calculations, RSC Adv. 10 (73) (2020) 44633–44640, https://doi.org/10.1039/D0RA07543D.

[9] I. Galanakis, K. Özdoğan, E. Şaşoğlu, B. Aktaş, Doping of <span class, Phys. Rev. B 75 (9) (2007) 092407, https://doi.org/10.1103/PhysRevB.75.092407.

[10] L. Siakeng, G.M. Mikhailov, D.P. Rai, Electronic, elastic and X-ray spectroscopic properties of direct and inverse full heusler compounds co2feal and fe2coal, promising materials for spintronic applications: a DFT+u approach, J. Mater. Chem. C 6 (38) (2018) 10341–10349, https://doi.org/10.1039/C8TC02530D.

[11] I.V. Malikov, L.A. Fomin, V.A. Berezin, A.V. Chernykh, D.P. Rai, G.M. Mikhailov, Study of the fe2coal heusler alloy films growth on the R-plane sapphire substrate by scanning probe microscopy, Ferroelectric 541 (1) (2019) 79–92, https://doi.org/10.1080/00150193.2019.1574647.

[12] S. Idrissi, H. Labrim, S. Ziti, L. Bahmad, Structural, electronic, magnetic properties and critical behavior of the equiatomic quaternary heusler alloy cofetisn, Phys. Lett. A 384 (24) (2020) 126453, https://doi.org/10.1016/J.PHYSLETA.2020.126453.

[13] S. Idrissi, H. Labrim, S. Ziti, L. Bahmad, Investigation of the physical properties of the equiatomic quaternary heusler alloy coycrz (z = si and ge): a DFT study, Appl. Phys. A 2020 1263 126 (3) (2020) 1–12, https://doi.org/10.1007/S00339-020-3354-6.

[14] H. Bach, K. Westerholt, U. Geiersbach, Thin-film epitaxial growth of the heusler alloy cu2almn, J. Cryst. Growth 237–239 (1–4 III) (2002) 2046–2049, https://doi.org/10.1016/S0022-0248(01)02308-9.

[15] J.A. Logan, T.L. Brown-Heft, S.D. Harrington, N.S. Wilson, A.P. McFadden, A. D. Rice, M. Pendharkar, C.J. Palmstrøm, Growth, structural, and magnetic properties of single-crystal full-Heusler co2tige thin films, J. Appl. Phys. 121 (21) (2017) 213903, https://doi.org/10.1063/1.4984311.

[16] S. Idrissi, H. Labrim, S. Ziti, L. Bahmad, Characterization of the equiatomic quaternary heusler alloy zncdrhmn: structural, electronic, and magnetic properties, J. Supercond. Nov. Magn. 2020 3310 33 (10) (2020) 3087–3095, https://doi.org/10.1007/S10948-020-05561-8.

[17] C. Guillemard, S. Petit-Watelot, T. Devolder, L. Pasquier, P. Boulet, S. Migot, J. Ghanbaja, F. Bertran, S. Andrieu, Issues in growing heusler compounds in thin films for spintronic applications, J. Appl. Phys. 128 (24) (2020) 241102, https://doi.org/10.1063/5.0014241.

[18] M. Mouatassime, Y. Selmani, S. Idrissi, L. Bahmad, F. Goumrhar, H. Labrim, A. Benyoussef, Magnetic properties and half metallic behavior of the full-Heusler co2fege alloy: DFT and monte carlo studies, J. Solid State Chem. 304 (2021) 122534, https://doi.org/10.1016/J.JSSC.2021.122534.

[19] I. Galanakis, Surface properties of the half-and full-Heusler alloys, J. Phys. Condens. Matter 14 (25) (2002) 6329, https://doi.org/10.1088/0953-8984/14/25/303.

[20] T. Dietl, H. Ohno, F. Matsukura, J. Cibert, D. Ferrand, Zener model description of ferromagnetism in zinc-blende magnetic semiconductors, Science 287 (5455) (2000) 1019–1022, https://doi.org/10.1126/SCIENCE.287.5455.1019.

[21] R.J. Soulen, J.M. Byers, M.S. Osofsky, B. Nadgorny, T. Ambrose, S.F. Cheng, P. R. Broussard, C.T. Tanaka, J. Nowak, J.S. Moodera, A. Barry, J.M. Coey, Measuring the spin polarization of a metal with a superconducting point contact, Science 282 (5386) (1998) 85–88, https://doi.org/10.1126/SCIENCE.282.5386.85.

[22] K. Elphick, W. Frost, M. Samiepour, T. Kubota, K. Takanashi, H. Sukegawa, S. Mitani, A. Hirohata, Heusler alloys for spintronic devices: review on recent development and future perspectives, Sci Technol Adv Mater 22 (1) (2021) 235–271, https://doi.org/10.1080/14686996.2020.1812364.

[23] M. Jourdan, J. Minár, J. Braun, A. Kronenberg, S. Chadov, B. Balke, A. Gloskovskii, M. Kolbe, H. Elmers, G. Schönhense, H. Ebert, C. Felser, M. Kläui, Direct observation of half-metallicity in the heusler compound co2mnsi, Nat. Commun. 2014 51 5 (1) (2014) 1–5, https://doi.org/10.1038/ncomms4974.

[24] S.J. Hashemifar, P. Kratzer, M. Scheffler, Preserving the half-metallicity at the heusler alloy co 2Mnsi(001) surface: a density functional theory study, Phys. Rev. Lett. 94 (9) (2005), https://doi.org/10.1103/PHYSREVLETT.94.096402.

[25] S. Ikeda, K. Miura, H. Yamamoto, K. Mizunuma, H.D. Gan, M. Endo, S. Kanai, J. Hayakawa, F. Matsukura, H. Ohno, A perpendicular-anisotropy cofeB-Mgo magnetic tunnel junction, Nat. Mater. 2010 99 9 (9) (2010) 721–724, https://doi.org/10.1038/nmat2804.

[26] Lalrinkima, C.E. Ekuma, T.C. Chibueze, L.A. Fomin, I.V. Malikov, L. Zadeng, D. P. Rai, Electronic, magnetic, vibrational, and X-ray spectroscopy of inverse full-Heusler fe2irsi alloy, Phys. Chem. Chem. Phys. 23 (20) (2021) 11876–11885, https://doi.org/10.1039/D1CP00418B.

[27] R. Vadapoo, A. Hallal, H. Yang, M. Chshiev, First-principles investigation of magnetocrystalline anisotropy at the <span class, Phys. Rev. B 94 (10) (2016) 104418, https://doi.org/10.1103/PhysRevB.94.104418.

[28] Y. Hu, J.M. Zhang, First-principles study on the thermodynamic stability, magnetism, and half-metallicity of full-Heusler alloy ti2fege (001) surface, Phys. Lett. A 381 (18) (2017) 1592–1597, https://doi.org/10.1016/J.PHYSLETA.2017.02.050.

[29] I. Muhammad, J.-M. Zhang, A. Ali, M. Mushtaq, S. Muhammad, Stable half-metallicity in the (001)-oriented thin films of co-doped full-Heusler alloys ti2fe1xcoxsn (x=0.00, 0.25, 0.50, 0.75 or 1.00), J. Phys. Condens. Matter 32 (32) (2020) 325001, https://doi.org/10.1088/1361-648X/AB832D.

[30] Q.L. Fang, X.M. Zhao, J.M. Zhang, K.W. Xu, Magnetic properties and half-metallic in bulk and (001) surface of ti2mnal heusler alloy with hg2cuti-type structure, Thin Solid Films 558 (2014) 241–246, https://doi.org/10.1016/J.TSF.2014.03.007.

[31] P.L. Yan, J.M. Zhang, K.W. Xu, First-principles study on the magnetic and half-metallic properties in bulk and (001) surface of ti2cosn heusler alloy, Thin Solid Films 609 (2016) 19–24, https://doi.org/10.1016/J.TSF.2016.04.029.

[32] W. Kohn, L.J. Sham, Self-Consistent equations including exchange and correlation effects, Phys. Rev. 140 (4A) (1965) A1133, https://doi.org/10.1103/PhysRev.140.A1133.

[33] J. Hafner, Ab-initio simulations of materials using VASP: density-functional theory and beyond, J Comput Chem 29 (2008) 2044–2078, https://doi.org/10.1002/jcc.21057.

[34] J.P. Perdew, K. Burke, M. Ernzerhof, Generalized gradient approximation made simple [Phys. Rev. Lett. 77, 3865 (1996)], Phys. Rev. Lett. 78 (7) (1997) 1396, https://doi.org/10.1103/PhysRevLett.78.1396.

[35] H.J. Monkhorst, J.D. Pack, Special points for brillouin-zone integrations, Phys. Rev. B 13 (12) (1976) 5188, https://doi.org/10.1103/PhysRevB.13.5188.

[36] G. Kresse, J. Furthmüller, Efficient iterative schemes for ab initio total-energy calculations using a plane-wave basis set, Phys. Rev. B 54 (16) (1996) 11169, https://doi.org/10.1103/PhysRevB.54.11169.

[37] Q.L. Fang, J.M. Zhang, K.W. Xu, Magnetic properties and origin of the half-metallicity of ti2mnz (z=al, ga, in, si, ge, sn) heusler alloys with the hg2cuti-type structure, J. Magn. Magn. Mater. 349 (2014) 104–108, https://doi.org/10.1016/J.JMMM.2013.08.030.

[38] D.J. Mokhtari, I. Jum'h, H. Baaziz, Z. Charifi, T. Ghellab, A. Telfah, R. Hergenröder, Structural, electronic, magnetic and thermoelectric properties of inverse heusler alloys ti2cosi, mn2coal and cr2znsi by employing ab initio calculations, Philos. Mag. 100 (12) (2020) 1636–1661, https://doi.org/10.1080/14786435.2020.1731926.

[39] L. Zhang, S. Dong, J. Du, Y.-L. Lu, H. Zhao, L. Feng, First-Principles forecast of gapless half-Metallic and spin-Gapless semiconducting materials: case study of inverse ti2cosi-Based compounds, Appl. Sci. 10 (3) (2020) 782, https://doi.org/10.3390/APP10030782.

[40] M. Amiri, H. Akbari, B. Nedaee-shakarab, A. Boochani, A. Aminian, Y. Zangeneh, S. Naderi, Thermodynamic stability, half-Metallic and optical properties of sc2cosi [001] film: a DFT study, Commun. Theor. Phys. 71 (4) (2019) 455, https://doi.org/10.1088/0253-6102/71/4/455.

[41] M. Gilleßen, R. Dronskowski, A combinatorial study of inverse heusler alloys by first-principles computational methods, J Comput Chem 31 (3) (2009) 612–619, https://doi.org/10.1002/jcc.21358.

[42] D.P. Rai, J. Hashemifar, M. Jamal, et al., Study of co_2mnal heusler alloy as half metallic ferromagnet, Indian J. Phys. 84 (2010) 717–721, https://doi.org/10.1007/s12648-010-0077-0.

[43] D.P. Rai, Sandeep, A. Shankar, A.P. Sakhya, T.P. Sinha, R. Khenata, M.P. Ghimire, R.K. Thapa, Electronic and magnetic properties of x_2YZ and XYZ heusler compounds: a comparative study of density functional theory with different exchange-correlation potentials, Mater. Res. Express 3 (2016) 075022, https://doi.org/10.1088/2053-1591/3/7/075022.

[44] S. Skaftouros, K. Özdoğan, E. Şaşoğlu, I. Galanakis, Generalized slater-Pauling rule for the inverse heusler compounds, Phys. Rev. B 87 (2) (2013) 024420, https://doi.org/10.1103/PhysRevB.87.024420.

[45] V. Chis, B. Hellsing, Surface relaxation influenced by surface states, Phys. Rev. Lett. 93 (22) (2004) 226103, https://doi.org/10.1103/PhysRevLett.93.226103.

[46] R.A. Faregh, A. Boochani, S.R. Masharian, F.H. Jafarpour, The surface effect on the thermodynamic stability, half-metallic and optical properties of co2mnga(001) films: a DFT study, Int. Nano Lett. 2019 94 9 (4) (2019) 339–348, https://doi.org/10.1007/S40089-019-00289-3.

[47] H. Han, Z. Bai, K.L. Yao, Half-metallicity of bulk and (111) surface for full-Heusler alloy co2val: a density functional study, J. Alloys Compd. 576 (2013) 93–97, https://doi.org/10.1016/J.JALLCOM.2013.04.145.

[48] A. Jain, S.P. Ong, G. Hautier, W. Chen, W.D. Richards, S. Dacek, S. Cholia, D. Gunter, D. Skinner, G. Ceder, K.A. Persson, Commentary: the materials project: a materials genome approach to accelerating materials innovation, APL Mater. 1 (1) (2013) 011002, https://doi.org/10.1063/1.4812323.

[49] Lalrinkima, L.A. Fomin, I.V. Malikov, L. Zadeng, D.P. Rai, Perpendicular magnetocrystalline anisotropy energy (MAE) of 111-surface slab of fe2coal, Mater. Res. Express 7 (6) (2020) 064003, https://doi.org/10.1088/2053-1591/AB97E4.

[50] M.A. Ruderman, C. Kittel, Indirect exchange coupling of nuclear magnetic moments by conduction electrons, Phys. Rev. 96 (1) (1954) 99, https://doi.org/10.1103/PhysRev.96.99.

[51] E. Şaşoğlu, L.M. Sandratskii, P. Bruno, Role of conduction electrons in mediating exchange interactions in mn-based heusler alloys, Phys. Rev. B 77 (6) (2008) 064417, https://doi.org/10.1103/PhysRevB.77.064417.

[52] T. Kim, I.H. Cha, Y.J. Kim, G.W. Kim, A. Stashkevich, Y. Roussigné, M. Belmeguenai, S.M. Chérif, A.S. Samardak, Y.K. Kim, Ruderman-Kittel-Kasuya-Yosida-type interfacial dzyaloshinskii-Moriya interaction in heavy metal/ferromagnet heterostructures, Nat. Commun. 12 (1) (2021) 1–10, https://doi.org/10.1038/s41467-021-23586-y.

[53] E. Şaşoğlu, L.M. Sandratskii, P. Bruno, Role of conduction electrons in mediating exchange interactions in mn-based heusler alloys, Phys. Rev. B 77 (6) (2008) 064417, https://doi.org/10.1103/PhysRevB.77.064417.

Materials Research Express

PAPER • OPEN ACCESS

Perpendicular magnetocrystalline anisotropy energy (MAE) of 111-surface slab of Fe_2CoAl

To cite this article: Lalrinkima *et al* 2020 *Mater. Res. Express* **7** 064003

Materials Research Express

PAPER

Perpendicular magnetocrystalline anisotropy energy (MAE) of 111-surface slab of Fe_2CoAl

Lalrinkima[1,3], **L A Fomin**[2], **I V Malikov**[2], **Lalthakimi Zadeng**[1] and **D P Rai**[3]

[1] Department of Physics, Mizoram University Aizawl 796009, India
[2] Institute of Microelectronics Technology and High Purity Materials RAS, 142432 Chernogolovka, Russia
[3] Physical Sciences Research Center (PSRC), Department of Physics, Pachhunga University College Aizawl 796001, India

E-mail: dibya@pucollege.edu.in

Keywords: GGA, GGA+U, magnetocrystalline anisotropy energy, spin orbit coupling, band structure

OPEN ACCESS

RECEIVED
1 May 2020

ACCEPTED FOR PUBLICATION
29 May 2020

PUBLISHED
5 June 2020

Abstract

We have analyzed the surface stability of different orientations(111, 001, 011) of Fe_2CoAl (FCA) slabs. Among all the slabs, the orientation with 111-surface is found to be most stable with minimum energy. The surface electronic and magnetic properties along with the atomic orbital resolved magneto-crystalline anisotropy energy (MAE) has been performed by using first principles density functional theory (DFT). We have reported the surface metallicity with dispersed electronic bands around the fermi energy (E_F) in all the three terminals Fe/Co/Al. This may be the result of translational broken symmetry in which metallic bonds are broken with the release of free conducting electrons on the surface. We have observed the presence of both the in-plane MAE and the out-plane MAE characterized by the distribution of total MAE over an atomic sites for each Al-, Co- and Fe-terminal. The total MAE favors in-plane magnetization in case of antiferromagnetic configured Al-terminal (MAE = 0.034 meV) and Fe-terminal (0.68 meV) whereas out-plane total MAE is observed in ferromagnetic configured Co-terminal.

1. Introduction

The magnetic materials with half-metallic, large perpendicular magnetic anisotropy, high thermal stability and low critical current, magnetic damping etc, always fascinates the scientific research due to their potential application in spintronics. They also possess high magnetization density, high density spin transfer torque under applied magnetic field which are crucial for implementation in magnetic random access memory (STT-MRAM) and logic devices [1–4]. For materials to device applications size compatibility with preserving the functional properties are always an issue. In most cases, the half-metallicity and other physical properties are destroyed when cleaveged to low dimension surface slab and 2D thin film from the bulk materials. The nano-scale object loses its magnetic stability with the lowering of size scaled [5]. The stabilization of surface magnetization and magnetic crystalline anisotropy of the magnetic materials at its nano-scale, thin film and surface level for successful device application is an outmost challenge. In tetragonal Heusler compounds large magneto-crystalline anisotropy can be easily produced by positioning the Fermi energy at the van Hove singularity in one of the spin channels, while the ferromagnetic cubic Heusler alloys exhibit small magneto-crystalline anisotropy energy (MAE) mainly due to the higher dominating magnetization [6]. So for that reason, the usage of low magnetization materials such as ferrimagnetic and antiferromagnetic materials with large MAE preferred over highly magnetized ferromagnetic materials to reduce critical current density and enhanced the thermal stability in magnetic tunnel junctions (MTJs) [7, 8]. Several results of high values of MAE has been reported in the metal-semiconductor hetero-junction. For example, full Heusler alloy and semiconductor heterostructure (Co_2FeAl)|MgO have been found to exhibit large interfacial perpendicular magnetic anisotropy energy (PMA) value of 1.31 mJ m^{-2} [3], 1.28mJ m^{-2} [9] for Co-terminated in Co_2FeAl|MgO interfaces and a PMA value of 0.428 erg cm^{-2} for FeAl-terminal [10]. Wen *et al* [11] experimentally achieved PMA densities around

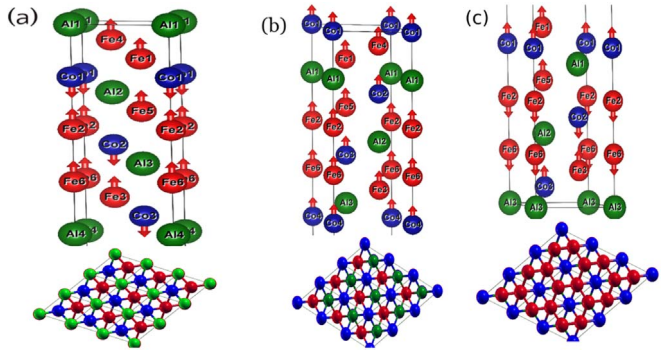

Figure 1. Conventinal slab model (Top-view and Side-view) for (a) Antiferromagnetic (AFM1) Al-terminal (b) Ferromagnetic Co-terminal and (c) Antiferromagnetic(AFM2) Fe-terminal.

2–3 $\times$ 10^6erg cm^{-3} within CFA|MgO and MgO|CFA structures. Interestingly, a large negative perpendicular uniaxial anisotropy has also been observed in CFA|Mgo(001) [12].

In this paper, we have presented the surface electronic and perpendicular magnetic anisotropy energy (PMA) for non-periodic slab (111) of inverse (XA-type) cubic full Heusler alloy Fe_2CoAl. To the best of our knowledge, neither experimental nor theoretical studied have been performed for PMA of free standing Fe_2CoAl 111-surface. However, numbers of work on the analogous composite $L2_1$ structured Co_2FeAl have already been reported. For electronic structure calculation, we have treated strongly correlated electron-electron interaction by including Hubbard parameter (U) [13] ($U_{Fe} = 3.82$ eV and $U_{Co} = 3.89$ eV) as GGA+U calculation in addition to GGA.

2. Computational detail

Different FCA surface slabs with orientations [(001), (110), (111)] have been cleavage from the cubic bulk Fe_2CoAl with lattice constant $a = 5.703$ Å[14]. A vacuum of 15 (Å) is applied along the z-axis to avoid periodic layer interactions. We have performed the first principles DFT [15] calculation using Quantum Espresso (QE) [16] package considering the electron exchange energy within the generalized gradient approximation (GGA) proposed by Perdew–Burke–Ernzerhof(PBE) [17]. We used 250 Rydberg for the kinetic cut off energy and a mesh of 16 $\times$ 16 $\times$ 1 within Monkhorst pack [18] for K-point to integrate the first Brillouin zone. Stuctural relaxation was achieved with a force tolerance of 0.0136eV/Å. We deployed the force theorem [5] as implemented in QE; by performing the self-consistent-field calculation (SCF) without the spin–orbit coupling (SOC) within the scalar pseudopotentials method we obtained the charge density and spin magnetic moment. Then, two types non-SCF calculation are executed with the spin polarized fully relativistic pseudopotentials (with SOC). In which we have considered spin moment with angle 0° in xy-plane for parallel and 90° in z-axis for perpendicular direction. The difference of the band energy between the two spin moment directions (90° and 0°) is the the total MAE.

3. Results and discussion

Among the three different slab orientations (001, 110 and 111) the 111-surface slab with thirteen atomic monolayers have been found to be the most stable with the minimum ground state energy. We have performed the magnetic configuration dependent ground state energy calculation from the 111-surface slab. The 111-surface slabs of Fe_2CoAl are again categorized with three different terminal atoms like Fe-, Co- and Al-terminals as shown in figure 1. The seven magnetic configurations are considered including one ferromagnetic (FM) and six types of antiferromagnetic (AFM) orientations (see tables 1, 2, 3) for each Fe-, Co and Al-terminal, respectively. In terms of their minimum ground state energy with corresponding magnetic configurations; Al-terminal is stable with AFM1-configuration, Fe-terminal with AFM2 configuration and Co-terminal with FM configuration (see tables 1, 2, 3).

3.1. Electronic and magnetic properties

In figures 2, 3, we have presented the spin-resolved partial density of states (DOS) and energy band stuctures of 111-surface slab of Fe_2CoAl, calculated from GGA and GGA+U ($U_{Fe} = 3.82$ eV and $U_{Co} = 3.89$ eV) [13] to study the electronic properties. For each terminal, we considered the surface-, subsurface1- and subsurface2

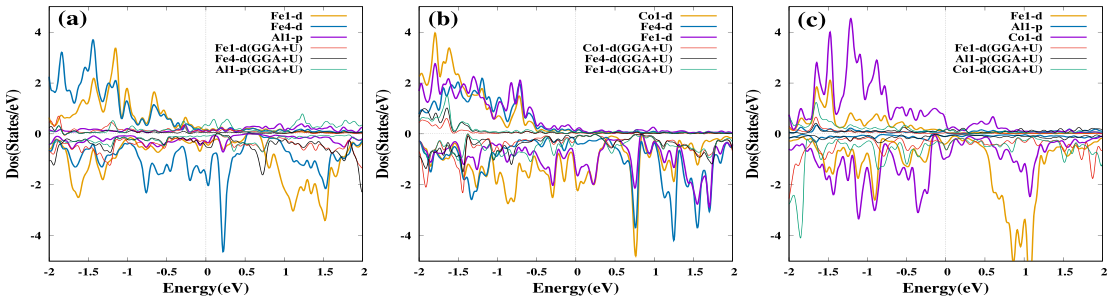

Figure 2. Calculated partial DOS of Fe_2CoAl from GGA and GGA+U: (a) Al-terminal, (b) Co-terminal and (c) Fe-terminal.

Table 1. Magnetic Configuration on magnetic atomic sites (six Fe- and three Co-atoms) and energy difference (E_{FM}-E_{AFM}) in Ry for Al-terminated surface.

Config.	Fe1	Fe2	Fe3	Fe4	Fe5	Fe6	Co1	Co2	Co3	E_{FM}-E_{AFM}(Ry)
FM	↑	↑	↑	↑	↑	↑	↑	↑	↑	0.00
AFM1	↑	↑	↑	↑	↑	↑	↓	↓	↓	0.009
AFM2	↑	↓	↑	↓	↑	↓	↑	↓	↑	−0.040
AFM3	↑	↑	↓	↓	↑	↑	↑	↑	↓	−3.889
AFM4	↓	↓	↑	↑	↓	↓	↓	↓	↑	−2.438
AFM5	↑	↓	↓	↑	↓	↓	↑	↓	↓	−0.004
AFM6	↓	↑	↑	↓	↑	↑	↓	↑	↑	−0.004

Table 2. Magnetic Configuration on magnetic atomic sites (six Fe- and four Co-atoms) and energy difference (E_{FM}-E_{AFM}) in Ry for Co-terminated surface.

Config.	Fe1	Fe2	Fe3	Fe4	Fe5	Fe6	Co1	Co2	Co3	Co4	E_{FM}-E_{AFM}(Ry)
FM	↑	↑	↑	↑	↑	↑	↑	↑	↑	↑	0.000
AFM1	↑	↑	↑	↑	↑	↑	↓	↓	↓	↓	−4.762
AFM2	↑	↓	↑	↓	↑	↓	↑	↓	↑	↓	−6.889
AFM3	↑	↑	↓	↓	↑	↑	↑	↑	↓	↓	−5.101
AFM4	↓	↓	↑	↑	↓	↓	↓	↓	↑	↓	−3.690
AFM5	↑	↓	↓	↑	↓	↓	↑	↓	↓	↑	−4.798
AFM6	↓	↑	↑	↓	↑	↑	↓	↑	↑	↓	−4.797

Table 3. Magnetic Configuration on magnetic atomic sites (seven Fe- and three Co-atoms) and energy difference (E_{FM}-E_{AFM}) in Ry for Fe-terminated surface.

Config.	Fe1	Fe2	Fe3	Fe4	Fe5	Fe6	Fe7	Co1	Co2	Co3	E_{FM}-E_{AFM}(Ry)
FM	↑	↑	↑	↑	↑	↑	↑	↑	↑	↑	0.000
AFM1	↑	↑	↑	↑	↑	↑	↑	↓	↓	↓	−0.314
AFM2	↑	↓	↑	↓	↑	↓	↑	↑	↓	↑	3.551
AFM3	↑	↑	↓	↓	↑	↑	↓	↑	↑	↓	−0.678
AFM4	↓	↓	↑	↑	↓	↓	↑	↓	↓	↑	2.586
AFM5	↑	↓	↓	↑	↓	↓	↑	↑	↓	↓	3.520
AFM6	↓	↑	↑	↓	↑	↑	↓	↓	↑	↑	−2.105

atomic layer to reveal the electronic properties. We observed a metallic behaviour in both the spin channels with dispersed bands around the fermi level due to the breaking of metallic bonding when the non-periodic surface slab is cleavaged from the periodic bulk system and also the DOS decreases from GGA to GGA+U calculation in all cases (See figures 2(a), (b) and (c)). In Al-terminated surface, as shown in figure 2(a), all the Fe1-*d*, Al-*p* and Fe4-*d* spin-up and spin-down states are dispersed around the Fermi level (E_F) within GGA and GGA+U calculation. The higher occupation of Fe4-*d* states prior to Fe1-*d* states around the E_F in the spin-down channel may be due to the absence of $d - d$ hybridization between Fe4-*d* and Fe1 -*d* states. A higher peak of Fe4-*d* spin down states likely reveals the surface reconstruction [19, 20]. Interestingly, we observed a small spin-down band gap (0.19 eV) between 0.55 eV–0.74 eV in the conduction band from GGA calculation. By treating electron-

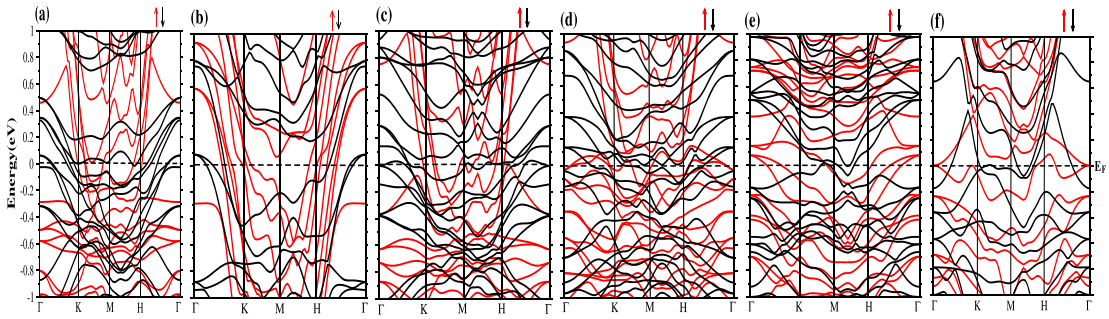

Figure 3. Calculated band structures:(a) Al-terminal(GGA), (b) Al-terminal(GGA+U), (c) Co-terminal(GGA), (d) Co-terminal(GGA +U), (e) Fe-terminal(GGA) and (f) Fe-terminal(GGA+U).

Table 4. Comparision between surface/subsurface atomic sites magnetic moment with their corresponding moment in the bulk Fe_2CoAl.

	Atomic site	μ_B (GGA)	μ_B (GGA+U)
Al-terminal	Fe4	2.45	2.68
	Fe1	2.43	2.53
Co-terminal	Co1	1.80	1.90
	Fe4	2.67	2.77
	Fe1	2.25	2.48
Fe-terminal	Fe1	3.00	3.01
	Co1	0.83	1.35
Bulk	Fe1	2.56	2.76
	Fe2	1.64	2.16
	Co	1.18	0.89

electron interactions in GGA+U calculation, free electrons abruptly reduced which results lesser population states. The presence of small hybridization between Co1-*d* and Fe1-*d* in spin-down states results in coupled states at the E_F in FM Co-terminated surface, the similar trend of results are obtained for AFM1 Al-terminated and AFM2 Fe-terminal electronic structure. We have calculated the total spin polarization degree for each terminal using the relation equation (1) [21]

$$P = \frac{N_{\uparrow}(E_F) - N_{\downarrow}(E_F)}{N_{\uparrow}(E_F) + N_{\downarrow}(E_F)} \tag{1}$$

where $N_{\uparrow}(E_F)$ and $N_{\downarrow}(E_F)$ are the densities of states at E_F for spin-up and spin-down channels respectively. We estimated the polarization degree 65% (GGA) and 21.7% (GGA+U) for Al-terminal, 62.4% (GGA) and 36.5% (GGA+U) for Co-terminal, where a comparatively low polarization degree with 40% (GGA) and 5% (GGA+U) for Fe-terminal.

The calculated total magnetic moments are found to be 18.9 μ_B (GGA) and 20.46 μ_B (GGA+U) for ferromagnetic Co-terminal and comparatively higher than antiferromagnetic Al-terminal [5.32 μ_B (GGA) and 9.73 μ_B (GGA+U)] and Fe-terminal [0.03 μ_B (GGA) and 3.5 μ_B (GGA+U)]. The calculated values of magnetic moment of the surfaces, sub-surfaces atoms in each terminals along with the partial magnetic moments of the corresponding magnetic moment of the bulk Fe_2CoAl [14] is shown in Table 4. The moment of Fe4 atoms in sub-surface1 for Al- and Co-terminals are comparable with the moment of Fe1 site in the bulk whereas, the Fe1 moment of the sub-surface2 are likely within the range of Fe1 and Fe2 sites in the bulk stucture. But, the values of magnetic moment of Co1 atom in Co-terminal surface is fractionally higher as compared to that of the Co1 atom at sub-surface1 of the Fe-terminal and the bulk within both GGA and GGA+U calculation. The atomic sites magnetic moment from GGA and GGA+U calculation are also presented in figure 4. The anti-parallely configured three Co-atoms of Al-terminal experienced parallel magnetization along with Fe-atoms from GGA calculation, this may be due to the strong coupling between Co-atoms and Fe-atoms within the core-region of the slab. The magnetic atoms (Fe and Co) in the FM Co-terminal shows parallel magnetization as expected where the moment of magnetic atoms in the AFM2 Fe-terminal oscillate around zero.

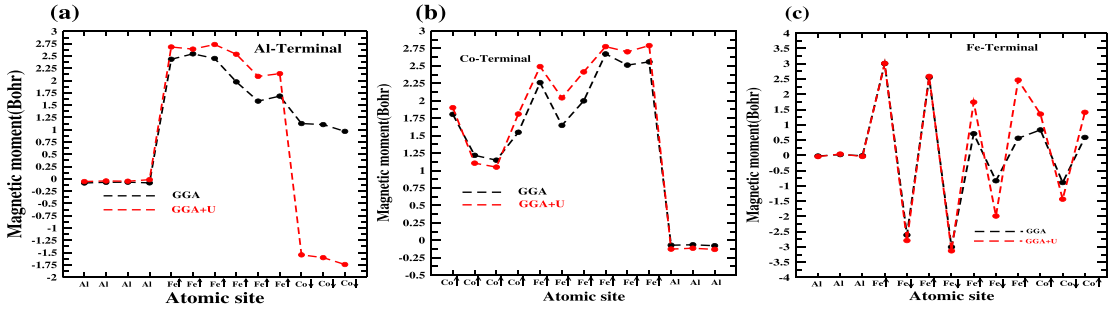

Figure 4. Calculated Atomic site magnetic moment(a) Al-terminal and (b) Co-terminal and (c) Fe-terminal.

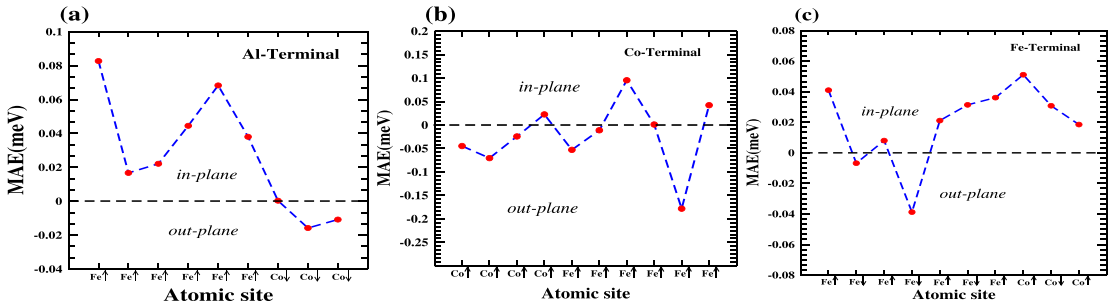

Figure 5. Calculated Atomic resolved MAE (a) Al-terminal and (b) Co-terminal and (c) Fe-terminal.

3.2. Perpendicular Magnetocrystalline anisotropy

We calculated the energy required to switch the magnetization direction from easy(*xy*)axis to the perpendicular direction(*z*) of the crystal axis for each terminal, which is usually termed as perpendicular magnetocrystalline anisotropy energy (MAE). We estimated the total in-plane MAE values 0.034 meV/cell and 0.68 meV/cell for the two antiferromagnetic Al(AFM1)- and Fe-(AFM2)terminated surfaces respectively, whereas the out-plane total MAE −0.087 meV/cell for ferromagnetic Co-terminated surface. The distribution of total MAE over an atomic sites *i* is given by equation (2) [5]

$$MAE_i = \int^{E_F^1} (E - E_F) n_i^1(E)\, dE - \int^{E_F^2} (E - E_F) n_i^2(E)\, dE \tag{2}$$

where E_F is the Fermi energy of obtained from non-SCF calculation with SOC and subtracted from all the eigen values to produce correct local decomposition of MAE. Figure 5 shows the atomic resolved MAE for different terminals. In case of antiferromagnetic Al-terminal(AFM1) and Fe-terminal(AFM2), we have noticed the dependence of total MAE on the atomic resolved surface and sub-surfaces. Incase of Co-terminal, the out-plane favours the surface, whereas the sub-surfaces are ferromagnetic. The major contribution to the total out-plane MAE is neither dominated by surface nor by sub-surface atoms rather from the core-region. This may be due to the cancellation between surface and sub-surface atomic moments [5]. Usually the cubic bulk structure exhibit negligibly small MAE per atom, but it is possible to get higher measurable values of MAE (more likely inmeV) in nanostructures [22, 23] due to reducibility of dimension or miniature in sizescale. Unfortunately, we do not have sufficient reported data to compare our results.

4. Conclusion

We have studied the surface electronic and perpendicular magnetocrystalline anisotropy of 111-surface slab of inverse Heusler alloy Fe_2CoAl using the first principles calculation. Adopting the different atomic terminals we have calculated the minimum ground state energy for various magnetic configurations (FM and AFM). The slab with different atomic-terminals and energetically stable ground states are AFM1:Al-terminal, FM:Co-terminal and AFM2:Fe-terminal. All the terminals are magnetic metals with finite value of total magnetic moments and dispersed bands around E_F in both the spin channels from GGA as well as GGA+U approaches. We have observed the decrease in the degree of the total spin polarization from the GGA to GGA+U calculation in all cases. This may be due to the large number of free conducting charges dispersed on the surface and another

reason might be the irrelevant choice of the Hubbard potential (U) to incorporate the surface atoms. In fact, we have observed a small spin-down energy gap (0.19 eV) between 0.55 eV–0.74 eV in Al-terminal within GGA calculation. By varying the cell parameters it may be possibly tuned the Fermi level in the spin band gap to get the surface half-metallicity. The perpendicular magnetocrystalline anisotropy energy (PMA) calculation were performed using force theorem as implemented in Quantum Espresso. We observed both in-plane and out-plane mixed-up character for atomic-layer resolved MAE. However, Al- and Fe-terminal favor the in-plane while Co-terminal is subjected to out-plane total MAE.

Acknowledgments

D P Rai acknowledges Department of Science and Technology (DST) New Delhi, Govt. of India vide Lett. No. INT/RUS/RFBR/P-264. Prof. I V Malikov acknowledges Russian Foundation for Basic Research (RFBR), Russia, RFBR-17-57-45024. Obituary to Prof. G M Mikhailov (RAS).

ORCID iDs

Lalrinkima https://orcid.org/0000-0002-3534-7325
D P Rai https://orcid.org/0000-0002-3803-8923

References

[1] Nistor L E, Rodmacq B, Auffret S and Dieny B 2009 Pt/Co/oxide and oxide/Co/Pt electrodes for perpendicular magnetic tunnel junctions *Appl. Phys. Lett.* **94** 012512
[2] Ikeda S, Miura K, Yamamoto H, Mizunuma K, Gan H D, Endo M, Kanai S, Hayakawa J, Matsukura F and Ohno H 2010 A perpendicular-anisotropy CoFeB-Mgo magnetic tunnel junction *Nat. Mater.* **9** 721
[3] Vadapoo R, Halal A, Yang H and Chshiev M 2016 First principle investigation of magnetocrystalline anisotropy at the $L2_1$ full Heusler| MgO interfaces and tunnel junction *Phys. Rev.* B **94** 104418 (5-1)
[4] Malikov I V, Fomin L A, Berezin V A, Chernykh A V, Rai D P and Mikhailov G M 2019 Study of the Fe_2CoAl heusler alloy films growth on the R-plane sapphire substrate by scanning probe microscopy *Ferroelectrics* **541** 79–92
[5] Li D, Barrateau C, Castell M R, Silly F and Smogunov A 2014 Out- versus in-plane magnetic anisotropy of free Fe and Co nanocrystal: Tight-binding and first-principle studies *Phys. Rev.* B **90** 205409 (7-1)
[6] Felser C, Wollman L, Chadov S, Fecher G H and Parkin S P S 2015 Basics and prospective of magnetic Heusler compounds *APL Mater* **3** 041518 (8-1)
[7] Odkhuu D, Rhim S H, Park N, Nakamura K and Hong S C 2018 Jahn-Teller driven perpendicular magnetocrystalline anisotropy in metastable ruthenium *Phys. Rev.* B **98** 094408 (8-1)
[8] Loth S, Baumann S, Lutz C P, Eigler D M and Heinrich A J 2014 Bistability in atomic-scale antiferromagnets *Science* **335** 196–9
[9] Tsujikawa M, Mori D, Miura Y and Shirai M 2013 Perpendicular magnetic anisotropy and its electrical modulation of MgO/Co_2FeAl interface: a first-principles study *Proceeding of MML 2013—The VIII International Symposium on Metallic Multilayers (MML2013) (Kyoto, Japan, May 19-24)*
[10] Bai Z, Shen L, Cai Y, Wu Q, Zeng M, Han G and Feng Y P 2014 Magnetocrystalline anisotropy and its electric-field-assisted switching of Heusler-compound-based perpendicular magnetic tunnel junctions *New J. Phys.* **16** 103033 (18-1)
[11] Wen Z, Sukegawa H, Mitani S and Inomata K 2011 Perpendicular magnetization of Co_2FeAl full Heusler alloy films induced by MgO interface *Appl. Phys. Lett.* **98** 242507 (3-1)
[12] Belmeguenai M, Tuzcuoglu H, Gabor M S, Petrisor T Jr., Tiusan C, Berling D, Zighem F, Chauveau T, Cherif S M and Moch P 2013 Co 2 FeAl thin films grown on MgO substrates: correlation between static, dynamic, and structural propertie *Phys. Rev.* B **87** 184431 (11-1)
[13] Rai D P, Shankar A, Sandeep, Singh L R, Jamal M, Hashemifar S J, Ghimire M P and Thapa R K 2012 Calculation of coulomb repulsion (U) for 3d transition elements in Co2YAl type Heusler alloys *Arm. J. Phys.* **5** 105-110 (http://ajp.asj-oa.am/511/)
[14] Siakeng L, Mikhailov G and Rai D P 2018 Electronic, elastic and x-ray spectroscopic properties of direct and inverse full Heusler compounds Co_2FeAl and Fe_2CoAl, promising materials for spintronic applications: a DFT+U approach *J. Mater. Chem.* C **6** 10341–9
[15] Kohn W and Sham L J 1965 Self-Consistent equations Including Exchange and Correlation Effects *Phys. Rev.* **140** A1133–8
[16] Giannozzi P, Baroni S, Bonini N, Calandra M, Car R, Cavazzoni C, Ceresoli D, Chiarotti G L, Cococcioni M and Dabo I 2009 QUANTUM ESPRESSO: a modular and open-source software project for quantum simulations of materials *J. Phys. Condens. Mat.* **21** 395502
[17] Perdew J P, Burke K and Ernzerhof M 1996 Generalized gradient approximation made simple *Phys. Rev. Lett.* **77** 3865–8
[18] Monkhorst H J and Pack J D 1976 Special points for brillouin zone integrations *Phys. Rev.* B **13** 5188–92
[19] Galanakis I 2002 Surface properties of the half-and full-Heusler alloys *J. Phys.: Condens. Matt.* **14** 6329–40
[20] Paudel R and Zhu J 2019 Investigation of half-metallicity and magnetism of bulk and (111)-surfaces of Fe_2MnP full Heusler alloy *Vacuum* **164** 336–42
[21] Soulen R J Jr *et al* 1998 Measuring the spin polarization of a metal with a superconducting point contact *Science* **282** 85–8
[22] Gambardella P, Rusponi S, Veronese M, Dhesi S S, Grazioli C, Dallmeyer A, Cabria I, Zeller R, Dederichs P H and Kern K 2003 Giant magnetic anisotropy of single cobalt atoms and nanoparticles *Science* **300** 1130–3
[23] Rusponi S, Cren T, Weiss N, Epple M, Buluschek P, Claude L and Brune H 2003 The remarkable difference between surface and step atoms in the magnetic anisotropy of two-dimensional nanostructures *Nat. Mater.* **2** 546–51

PARTICULARS OF THE CANDIDATE

NAME OF THE CANDIDATE:		LALRINKIMA
DEGREE	:	DOCTOR OF PHILOSOPHY
DEPARTMENT	:	PHYSICS
TITLE OF THESIS	:	STUDY OF SURFACE HALF METALLICITY OF FULL HEUSLER COMPOUNDS USING AB-INITIO APPROACH
DATE OF ADMISSION	:	14.08.2018

APPROVAL OF RESEARCH PROPOSAL

1.	DRC	:	28.03.2019
2.	BOS	:	15.04.2019
3.	SCHOOL BOARD	:	08.05.2019
4.	MZU REGISTRATION No.	:	3443 of 2010-11
5.	Ph.D REGISTRATION No.	:	MZU/Ph.D./1261 of 14.08.2018
6.	EXTENSION (IF ANY)	:	NIL

(Prof. Zaithanzauva Pachuau)

Head

Department of Physics

ABSTRACT

STUDY OF SURFACE HALF-METALLICITY OF FULL-HEUSLER COMPOUNDS USING *AB INITIO* APPROACH

AN ABSTRACT SUBMITTED IN PARTIAL FULFILLMENT OF THE REQUIREMENTS FOR THE DEGREE OF DOCTOR OF PHILOSOPHY

LALRINKIMA

MZU REGISTRATION NO.: 3443 of 2010-11

Ph.D REGISTRATION NO.: MZU/PH.D./1261 of 14.08.2018

DEPARTMENT OF PHYSICS

SCHOOL OF PHYSICAL SCIENCES

NOVEMBER, 2022

STUDY OF SURFACE HALF-METALLICITY OF FULL-HEUSLER COMPOUNDS USING *AB INITIO* APPROACH

BY

Lalrinkima

Department of Physics

Name of Supervisor: Dr. Lalthakimi Zadeng

Name of Joint Supervisor: Dr. Dibya Prakash Rai, PUC

Submitted

In partial fulfillment of the requirement of the Degree of Doctor of Philosophy in Physics of Mizoram University, Aizawl

ABSTRACT

The extensive investigation of full Heusler compounds from ab-initio (First principle) calculation had been performed rigorously to study mainly electronic and magnetic properties within different phases such as bulk symmetric, non-periodic slab or thin film and an extended the study to spin quantum transports in device realm by modelling Heusler electrode based magnetoresistance tunnelling junction (MTJ) device.

The XA phase of Fe_2IrSi with ferromagnetic configuration exhibited its lowest form of ground state energy from our theoretical energetic analysis. The absence of imaginary frequency in phonon dispersion curve revealed its dynamical stability and we observed a strong coupling between the acoustic and the optical branches; this may be due to the heavy Ir-atom, which is a predominant feature of electron-phonon coupling. We predicted metallic nature in both the spin channel with ~ 45% spin polarization from GGA calculation in inverse full-Heusler Fe_2IrSi. The dispersive bands around E_F in the spin down channel is due to the Fe2-d(↓) [d-e_g+d-t_{2g}] states. The predicted semiconducting half-metallic behavior within our GGA+U calculations has a characteristic of indirect band gap along Γ-X symmetry point in minority channel with a spin polarization of ~ 99.9% at the E_F. We, appropriately treat relativistic effect since the presence of 4d-element (Ir-atom) by deploying spin‑orbit coupling (SOC) along with GGA and GGA+U (U_{Ir} =1.0eV and U_{Fe} =3.52eV). With the implementation of SOC the half metallicity is lost and the system behaves like a magnetic metal. The predicted magnetic moment for 29 valence electrons system Fe_2IrSi strongly obeyed Slater-Pauling rule M_t = (Z_t - 24) with the total magnetic moment with 5.01μ_B. The calculated elastic and mechanical properties confirm both dynamical and structural stability with a melting temperature of ~ 2000±300 K, which supports a promising application of inverse full-Heusler Fe_2IrSi in devices operating above room temperature.

The prediction for crystallization of Ti_2XSi (X=Mn, Co) inverse Heusler in XA phase is well agreed with available previous reports. The blend of semiconducting minority channel and metallic majority channel behavior in Ti_2XSi validate the half metallic characteristic with ≅100% spin polarization at E_F. Both the compounds

followed Slater-Pauling rule with a moment of 1.01μ_B and 3.02μ_B for Ti_2MnSi and Ti_2CoSi respectively. The presence of non-zero magnetic moment despite having anti-ferromagnetic coupling between Mn-Ti revealed that Ti_2MnSi is a ferrimagnetic half metal, whereas Ti_2CoSi is predicted to be ferromagnetic half metal. The calculated elastic constants matrix and non-negative twelve modes of phonon dispersion relation revealed the mechanical and thermodynamical stability of Ti_2XSi (X=Mn, Co) compounds.

A first principles density functional theory calculation based on PAW and LCAO method revealed the ferrimagnet half-metallic nature of the bulk Mn_2CoSi(MCS) within GGA and GGA+U exchange-correlation potential. The higher accuracy treatment of electron-electron interactions has been incorporated with the inclusion of the on-site Hubbard potential as GGA+U which enhanced the band gap. The calculated lattice constant from the aforementioned two method are slightly smaller as compared with the experiment report with absolute uncertainty about 3.1% for the former and 2.88% for the later method.

The values obtained from GGA and GGA+U under applied pressures. We have shown that the strong correlation mainly comes from the Fe-3d and Co-d states, and the inclusion of electron–electron interactions within GGA as the GGA+U formalism is essential to describe the electronic properties. The implementation of GGA+U along with compressive pressure ($5 < P < 60$GPa) leads to half-metallic behavior with the opening ofa spin minority band gap. The predicted integer value of the total magnetic moment in the inverse full-Heusler alloy Fe_2CoAl, ~ 4.0μ_B at 30 GPa, is in accordance with the Slater–Pauling rule, which supports the half-metallicity. The T_C calculated from equation (4) is 747 K at 30 GPa, in good agreement with the results of other Fe-based inverse full-Heusler compounds. However, the results from MFA are overestimated. The calculated cohesive energy confirmed the ground state stability of the system under different applied pressures.

The non-periodic thin film of 001 surface with four terminated faces have been exfoliated from the optimized bulk Ti_2XSi(X=Mn,Co) structure. Out of the four explored terminal surfaces, TiSi(TMS) is the most stable with lowest surface energy which agrees well with its smallest surface relaxation. However, the TiX(X=Mn/Co) terminated surfaces from both Ti_2MnSi(TMS) and Ti_2CoSi(TCS) compounds are less

stable as compared to respective adjacent TiSi terminated surfaces which were revealed by the ab-initio atomistic thermodynamic calculation. We have observed from the electronic structure calculations that for TiMn, TiSi (TCS) and TiCo terminal surfaces, the presence of surface states at the Fermi level destroying their respective bulk half metallic properties. A significant surface half metallicity is observed in TiSi(TMS) terminal surface. We expect that our present work will invigorate the experimental work for the realization of surface half-metallicity in Ti_2MnSi with TiSi termination.

We have studied the surface electronic and perpendicular magnetocrystalline anisotropy of 111-surface slab of inverse Heusler alloy Fe_2CoAl using the first principles calculation. Adopting the different atomic terminals we have calculated the minimum ground state energy for various magnetic configurations - Ferromagnetic (FM) and antiferromagnetic (AFM). The slab with different atomic-terminals and energetically stable ground states are AFM1: Al-terminal, FM: Co-terminal and AFM2: Fe-terminal. All the terminals are magnetic metals with finite value of total magnetic moments and dispersed bands around EF in both the spin channels from GGA as well as GGA+U approaches. We have observed the decrease in the degree of the total spin polarization from the GGA to GGA+U calculation in all cases. This may be due to the large number of free conducting charges dispersed on the surface and another reason might be the irrelevant choice of the Hubbard potential (U) to incorporate the surface atoms. In fact, we have observed a small spin-down energy gap (0.19 eV) between 0.55 eV – 0.74 eV in Al-terminal within GGA calculation. By varying the cell parameters or doping it may be possibly tuned the Fermi level in the spin band gap to get the surface half-metallicity.

For Mn_2CoSi surfaces study, among two ideal terminations the energetically favored MnSi-terminal to MnCo-terminal. From the analysis of surface electronic structure via spin resolved partial density and band structure; MnSi-terminal surface is found to be exhibited half metallic nature with a minority gap in the spin down channel while MnCo-terminal revealed the metallic character with a dispersed bands around Fermi level in both the spin channel. This may be attributed to the weak d-d re-hybridization after losing half of their respective nearest neighbor atoms which in turn may did not induced sufficient energy splitting of hybridized e_u-t_{1u} states at

around E_F. The surface half metallicity of MnSi-terminal is further confirmed using LCAO method, this most likely attributed to even after the reduction of co-ordination number, Mn(s)-d states governed a sufficiently strong d-d re-hybridization with sub-surface atoms; Co(s1)-d states, which induced and energy splitting between the bonding and antibonding states; perceiving a well-defined band gap characterized by the subsurface atoms Co(s1) and Mn(s1). This may possibly indicated that a negligible surface effect on strong covalent hybridization between Mn(s1) and Co(s1) and Mn(s) d-d states which turned out energy splitting between e_u-t_{1u} states to open up band gap around E_F. The enhancement of localized spin moment of surface atom Mn(s) in MnSi terminated surface is revealed from both the calculation approach. The presence of broken translational symmetry at the non-periodic surface tends to rearrange the displaced valence electrons that leads to a strong intra-atomic exchange interaction, induced a larger localized spin magnetic moment of Mn(s) as compared to the respective magnetic moment in bulk. The anti-parallel spin moment of surface Si(s) atom had slightly increases which may be due to the direct exchange between p-orbital from Si(s) and d orbital of the subsurface Mn(s1) atoms. The subsurface Co atom has less experienced surface effect with a negligibly variation from the bulk value. In MnCo surface, the Mn2 site of the bulk structure is terminated and unexpectedly a parallel spin is observed between Mn(s) and Mn(s1), so for that reason it can be obvious that the antiparallel moment induced in Si(s1) arises from the second subsurface Mn atom. The complexity of surface and subsurface atoms magnetic structure may be due to the presence of competition between direct exchange and antiferromagnetic super exchange interaction.

The quantum transport in half metallic ferrimagnet Mn_2CoSi based MTJ have been studied with the aim of developing ferrimagnet spintronic material. The spin dependent transport properties have been studied within non-equilibrium Green function-density functional theory [NEGF-DFT]; in view of miniaturization the resistance product area, the lattice matching semiconductor Calcium-Chalcogen (CaS) is used as non-magnetic spacer in our ferrimagnet MTJ device. The spin dependent transmission value is comparatively low which may be due to the only contribution from spin-flip scattering, which is inherently small due to the half-metallic electrode. However, a large TMR value is observed at equilibrium. We found a drastic change is

TMR under applied bias voltage, which further oscillates at increasing voltage, which is reasonably attributed to the non-monotonic energy of transmission coefficients which further split in molecular field. We concluded that our proposed half metallic electrode (spin injector) for further study especially in experimental characterization for ferrimagnetic spintronic. It will also be very useful to explore the tunneling anisotropic magnetoresistance, spin texture and spin dynamics for future spintronic application.